Gilbert KNAPP

Dissertation

Gilbert KNAPP

Dissertation

Characterization and optimization of polymer membranes for acoustic applications

May 2015

Polymer Competence Center Leoben GmbH

Department Polymer Engineering and Science, University of Leoben

About the Dissertation

This Dissertation was authored by

DI Gilbert KNAPP
born 14. Mai 1986
in Mittersill (Salzburg, Republik Österreich)

Submitted to

Materials Science and Testing of Polymers
Department Polymer Engineering and Science
University of Leoben

Conducted at

Polymer Competence Center Leoben GmbH

Supervisor

Dr. Gernot OREŠKI
Polymer Competence Center Leoben GmbH

Academic Supervisor

Univ.-Prof. Dr. Gerald PINTER
Materials Science and Testing of Polymers
Department Polymer Engineering and Science
University of Leoben

Affidavit

I declare in lieu of oath, that I wrote this thesis and performed the associated research myself, using only literature cited in this volume.

Gilbert KNAPP
Leoben (Steiermark, Republik Österreich) — May 2015

Funding

The majority of the research work of this Dissertation was performed within the COMET-projects ”Advanced multi-layer films for acoustic applications” (grant-no.: 824191) and ”Characterization of thin polymer loudspeaker films” (grant-no.: 843276) at the Polymer Competence Center Leoben GmbH (PCCL, Austria) within the framework of the COMET-program of the Federal Ministry for Transport, Innovation and Technology and Federal Ministry of Economy, Family and Youth. The PCCL is funded by the Austrian Government and the State Governments of Styria and Upper Austria.

Competence Centers for
Excellent Technologies

Acknowledgement

First of all I want to thank the supervisors I had during my thesis, Dr. Michael Buder-Stroißnigg, Dr. Gerald Pilz and Dr. Gernot Oreški. Especially Gernot, who supervised the project I worked in in the last four years, was a great mentor for me, trusted in my scientific skills and encouraged self-independent scientific working. Whenever I came with a new idea he supported me in my scientific curiosity.

I want to express my gratitude to Univ.-Prof. Dr. Gerald Pinter for his scientific guidance, especially in the field of fracture mechanics. He significantly contributed in further improving my academic skills. Furthermore thanks go to Univ.-Prof. Dr. Walter Friesenbichler for his support in the field of polymer processing and Mag. Martin Payer for enabling the project within this thesis was done.

Special thanks go to Michael Berer and Peter Guttmann. I took a great benefit from their experience in the field of fracture mechanics and dynamic mechanical analysis, respectively. In many fruitful discussions they often provided me different perspectives.

Furthermore I had the honor to supervise the bachelor thesis of Martin Leyrer, who also supported me as a junior researcher for nearly three years. His conscientiously and precise way to work significantly contributed to our scientific success.

I also want to thank my colleagues and also friends at the PCCL and the University of Leoben for the friendly working environment and numerous convivial evenings. The team of our working group with Gernot, Bettina, Marlene, Astrid, Marko, Antonia and Sandra I want to thank for our lively discussions during coffee breaks and joint leisure time activities and their team spirit. Especially I want to thank Arno Hoffmann, Archim Wolfberger, Gloria Thürschmid, Florian Müller, Anna Felsner, Andreas Hausberger, Lisa Neumann, Bernd Schrittesser, Tobias Struklec, Nina Steiner, Martin Auer and Andreas Weber for their friendship and support. Also thanks go to my long lasting friends in Salzburg with Hans-Peter, both Christophs, Elisa, Franz, Korbinian, Birgit, Stefan, Christian, Daniel and Bernhard.

Special thanks also go to the family of my wife Karina with Josi, Ernst, Johannes, Michael, Teresa and Jana for their support and friendliness.

I want to express my deepest gratitude to my parents, Gertrude and Klaus, my brother Christoph, my sister Ursula, my grandparents Maria and Rudolf Vötter and Maria and Johann Knapp. The greatest gift my parents gave me was to support me in becoming a self-responsible person. Also special thanks go to my uncle Stefan and his family for their support, especially during my Ph.D. thesis.

Finally I owe much to my wife Karina. Without whose love, support and patience the successful finalization of this thesis would not have been possible.

Kurzfassung

Der Aufstieg von Smartphones und Tablets und deren wesentliches Designmerkmal einer geringen Dicke, hat zu einer signifikanten Erhöhung der zyklischen Belastungen in deren Miniaturlautsprechern geführt. Ein wesentliches Strukturbauteil dieser Lautsprecher ist die Polymermembran, die zwei Hauptanforderungen erfüllen muss. Als erstes muss ein adäquates Dämpfungsvermögen gewährleistet sein, damit eine gute Klangqualität erreicht wird und die Membran vor Bruch bei hohen dynamischen Lasten im Resonanzfall geschützt wird. Weiters wird eine gute Risszähigkeit benötigt, damit den hohen zyklischen Lasten in der Anwendung standgehalten wird. Als Konsequenz ist das Wissen um diese Parameter für eine erfolgreiche Lautsprecherkonstruktion unbedingt notwendig.

Der Stand der Technik in der Charakterisierung der genannten Parameter für Miniaturlautsprecher sind Bauteiltests. Diese sind zwar wichtig in einer abschließenden Abstimmung der Lautsprecherkonstruktion, jedoch für eine frühe Materialauswahl und fokusierte Studie von Designparametern der Lautsprechermembran sind Prüfmethoden direkt an den Folien sowohl zeit- als auch kosteneffizienter. Da zur Zeit vorhandene Prüfmethoden nicht geeignet sind, um die Materialcharakterisierung auch bei anwendungsrelevanten Bedingungen durchzuführen, werden in der vorliegenden Arbeit neue Methoden vorgestellt.

In monotonen bruchmechanischen Versuchen wurde bei einer Reihe von Lautsprecherfolien spröde Versagensmuster festgestellt, wodurch linear

elastische bruchmechanische (LEBM) Methoden als anwendbar eingeschätzt wurden. Da jedoch keine Korrelation zu Bauteiltests gefunden wurde, wurde in weiterer Folge ein zyklischer Ermüdungsversuch unter Zugbeanspruchung mit einer sehr hohen Prüffrequenz von 100 Hz aufgebaut, basierend auf Wöhler- und Risskinetikversuchen (fatigue crack growth tests, FCG). Um die Anwendbarkeit von LEBM für das zyklische Versagensverhalten von dünnen Lautsprecherfolien zu überprüfen, wurde das Rissähnlichkeitsprinzip angewendet. Hierzu wurden Versuche mit zwei unterschiedlichen Prüfkörpergeometrien, doppelt gekerbte (double edge notched tension, DENT) und zentral gekerbte (center cracked tension, CCT) Zugproben durchgeführt und Risskinetikkurven von unterschiedlichen 4.5 µm bis 10 µm dicken Polymerfolien verglichen. Für Polyarylat (PAR), Polyethersulfon (PESU) und Polyethylentherephthalat (PET) wurde die Anwendbarkeit des Rissähnlichkeitsprinzips nachgewiesen.

In weiterführenden Versuchen wurden Effekte der Temperatur, des Mehrlagenaufbaus und des anisotropen Materialverhaltens auf das Versagensverhalten von Lautsprecherfolien untersucht. Bei temperaturabhängigen Ermüdungsversuchen mit PET Folien wurde ein Maximum in deren Ermüdungsfestigkeit bei 60 °C und somit unterhalb deren Glasübergangstemperatur festgestellt. Weiters wurde nachgewiesen, dass Delaminationsprozesse im Ermüdungsverhalten von Mehrschichtlaminaten für Miniaturlautsprecher nur eine untergeordnete Rolle haben. Hierzu wurden T-Peel und Ermüdungsversuche durchgeführt und bezüglich deren Bruchenergien ausgewertet. Jedoch wurde entdeckt, dass die Dämpfungsschichten in den Mehrlagenfolien die Rissspitzen in den steifen Außenschichten vor äußeren Lasten möglicherweise abschirmen, was zu einer scheinbaren Erhöhung des Risswachstumswiederstandes gegenüber Monofolien führen kann. Abschließend wurde das richtungsabhängige Versagensverhalten von extrudierten Folien untersucht. Hierbei wurde eine Ablenkung des Risswachstums durch die Molekülausrichtung in eine Richtung mit niedrigem Risswachstumswiederstand beobachtet. Dieses Verhalten konnte durch die bevorzugte

Ausrichtung der Molekülketten in Extrusionsrichtung der Folien erklärt werden.

Zur Charakterisierung des Dämpfungsverhaltens von Miniaturlautsprecherlaminaten wurden zwei Messmethoden erstellt, beide basierend auf der Methode der dynamisch mechanischen Analyse (DMA) unter erzwungener Schwingung. Die erste sogenannte “Speaker” Mode Methode wurde der Sickengeometrie von Miniaturlautsprechermembranen nachempfunden. Basierend auf dem DMA Dual Cantilever Modus wurden aus den Laminaten die Sickengeometrien symmetrisch zwischen der Antriebswelle und den beiden äußeren Einspannungen ausgeformt. Der große Vorteil hierbei ist, dass zusätzlich zur Charakterisierung des Dämpfungsvermögens der Dämpfungsschichten, auch Effekte durch die Steifigkeitsverhältnisse zwischen den weichen Dämpfungs- und steifen Außenschichten beschreibbar waren. Die zweite Methode basiert auf dem DMA Schermodus und wurde für die Charakterisierung von Dämpfungsschichten in constrained layer damping (CLD) Laminaten optimiert. Da beide Methoden hinsichtlich der erreichbaren maximalen Prüffrequenz eingeschränkt sind, wurde das Zeit-Temperatur-Superpositionsprinzip angewandt. Damit wurde es möglich Extrapolationen bis zu anwendungsrelevanten Frequenzen von bis zu 1000 Hz durchzuführen. Weiters wurde die Auswertung mittels des im anwendungsrelevanten Temperaturbereich gemittelten integralen Durchschnitts des Verlustfaktors, $\overline{tA}$, eingeführt. Mit diesem wurde die vergleichende Bewertung von Lautsprechlaminaten hinsichtlich ihres Dämpfungsvermögens signifikant erleichtert. Die Anwendbarkeit des DMA “Speaker” Modes wurde durch Tests mit Monofolien und free layer damping (FLD) und constraint layer damping (CLD) Laminaten verifiziert. In Übereinstimmung mit der Literatur wurde das beste Dämpfungsverhalten beim CLD Laminat festgestellt, gefolgt vom FLD Laminat und der Monofolie. In einem weiteren Schritt wurde der Einfluss der steifen Außenschichten und auch des Adhäsionsverhaltens zwischen Außen- und Dämpfungsschichten in CLD Laminaten im DMA Schermodus untersucht. Dafür wurden vier Laminate mit technischen Kunst-

stoffen und ein Laminat mit Trennfolien als Außenschichten charakterisiert. Wenn eine ausreichende Haftung, wie bei den untersuchten technischen Polymeren, gegeben war, war kein Einfluss auf die Dämpfungscharakterisierung feststellbar. Abschließend wurde der Einfluss der Dicke der Dämpfungsschichten in CLD Laminaten im DMA Schermodus untersucht. Übereinstimmend mit der Literatur, wo Dämpfungsschichten mit mehreren Millimeter Dicke auf Metallfolien untersucht wurden, zeigten die Lautsprecherlaminate einen proportionalen Zusammenhang zwischen Dämpfungshöhe und Dämpfungsschichtdicke.

Abstract

The rise of smartphones and tablets with one of their main design goals to be very thin has led to a significant increase of the cyclic loads in their miniature loudspeakers. One of their key structural elements are the polymer membranes which have to fulfill two main tasks. First of all an adequate damping performance is required in order to ensure an excellent sound quality and to prevent the membranes from failing due to otherwise occurring high dynamic loads at resonance. Furthermore a high fracture toughness is needed to ensure a long service life by withstanding the cyclic fatigue loads during application. As a consequence the knowledge of these parameters is indispensable for a successful loudspeaker design.

State of the art in the characterization of the material parameters of miniature speaker membranes are component tests. Although they are essential for a final adjustment of the loudspeaker design, it is more time and cost efficient to have an early material selection and focused optimization of design parameters of the miniature loudspeaker membranes with tests on the film level. Since state of the art test methods on the film level are not capable of performing experiments at application-relevant conditions new approaches are presented in this thesis.

In monotonic fracture mechanical tests it was found that state of the art thin films for miniature speakers exhibit predominantly brittle fracture modes and therefore linear elastic fracture mechanics (LEFM) seemed applicable. Since in monotonic tests also no correlation was found to component tests

a fatigue test was setup at a high frequency of 100 Hz based on Wöhler and fatigue crack growth (FCG) tests. In order to verify the applicability of LEFM for the cyclic fatigue of thin loudspeaker films the crack tip similitude concept was applied by comparing the FCG behavior of double edge notched tension (DENT) and center cracked tension (CCT) specimens with different polymer films with thicknesses between 4.5 µm and 10 µm. For polyarylate (PAR), polyether sulfone (PESU) and polyethylene therephthalate (PET) films the applicability of the crack similitude concept was verified.

In further investigations effects due to temperature, the multilayer design and anisotropic material behavior were investigated. Temperature-dependent fatigue tests with PET films revealed a maximum of their fatigue strength below their glass transition at approximately 60 °C. Furthermore it was observed that delamination processes in multilayer miniature speaker laminates only play a minor role in their fatigue behavior. This was discovered by performing monotonic T-peel delamination and cyclic fatigue crack growth tests and comparing the calculated energies involved in both processes. But it was found that the damping adhesives might shield the crack growth in the stiff outer layers and therefore might contribute to an increase in crack growth resistance over monolayer films. Finally extrusion induced molecular orientations were identified as the cause for an anisotropic fatigue behavior of extruded films. Here crack growth was deflected by the molecular orientation in a direction of lower crack growth resistance.

In order to characterize the damping behavior of miniature speaker laminates two methods based on forced frequency dynamic mechanical analysis (DMA) were established. In the first so-called ”speaker” mode the supports of loudspeakers were mimicked between the clamps of a modified dual cantilever DMA setup. The great advantage of this setup was that effects of the damping performance of both the damping layer itself and also effects due to different stiffness ratios between the stiff base and soft damping layers were characterizable. The second method is based on a DMA shear mode setup and is optimized for the characterization of damping adhesives in con-

strained layer damping laminates. Since both methods are limited in their frequency range the time temperature superposition principle (TTSP) was applied in order to enable extrapolations to application-relevant frequencies of up to 1000 Hz. Furthermore with the calculation of the integrated average of the mechanical loss factor $\overline{tA}$ in the application-relevant temperature range an factor was introduced which simplified the ranking of laminates regarding their damping performance. The applicability of the DMA "speaker" mode was verified by characterization of a monolayer, a FLD and CLD laminate. In concordance with the literature the CLD laminate exhibited the best damping performance, followed by the FLD laminate and the monolayer film. In a next step the influences due to different constraining layers and also the adhesion between the damping and the stiff outer layers to the damping performance in CLD laminates was investigated in DMA shear mode. Therefore laminates with different technical polymers and one laminate with release films as outer layers were characterized. It was found that, as long as sufficient adhesion and therefore sufficient coupling to the damping layer was ensured, no influence on the damping performance existed. Finally the effect of the damping layer thickness on the damping performance of CLD laminates in DMA shear mode was evaluated. Consistent with the literature, where several millimeter thick damping layers on metal sheets were characterized, the laminates exhibited an increase in the damping performance proportional with the damping layer thickness.

Contents

Affidavit **v**

Funding **vii**

Acknowledgement **ix**

Kurzfassung **xi**

Abstract **xv**

1 Introduction, Objectives and Structure **1**
1.1 Main challenges 1
1.2 Structure of the thesis 2

2 State of the art **5**
2.1 Production process of miniature speakers 5
2.2 Materials 7
2.2.1 Naming scheme 9
2.3 Fracture characterization of thin films 9
2.3.1 Component tests 9
2.3.2 Tests on the film level 11
2.4 Damping characterization of thin films 15
2.4.1 Component tests 18
2.4.2 Tests on the film 19
2.5 Main Objectives 20

3 Fracture toughness testing of thin polymer films for acoustic applications 31
3.1 Introduction . . . 31
3.2 Background . . . 32
3.2.1 Linear elastic fracture mechanics . . . 33
3.2.1.1 Energy release rate G . . . 33
3.2.1.2 K concept . . . 35
3.2.1.3 Interrelation between G and K . . . 38
3.2.1.4 Crack tip plastic zone . . . 38
3.2.1.5 Plane stress/plane strain . . . 39
3.2.1.6 Multilayer fracture mechanics . . . 41
3.2.2 Delamination . . . 44
3.3 Methodology . . . 47
3.3.1 Objectives . . . 47
3.3.2 Specimen geometries . . . 48
3.3.3 Monotonic fracture . . . 49
3.3.4 Cyclic fatigue . . . 51
3.3.4.1 Stress based approach . . . 52
3.3.4.2 Fracture mechanical approach . . . 54
3.3.5 Fatigue test setup . . . 56
3.3.6 T-Peel tests . . . 60
3.4 Results and Discussion . . . 61
3.4.1 Monotonic fracture mechanical tests . . . 61
3.4.2 Applicability of linear elastic fracture mechanics to cyclic fatigue of polymer films . . . 67
3.4.3 Effect of temperature . . . 85
3.4.4 Effect of the multilayer design . . . 91
3.4.5 Effect of anisotropy . . . 117
3.5 Summary . . . 122

4 Damping characterization of thin polymer films for acoustic applications 139
4.1 Introduction . . . 139

4.2 Background 140
4.2.1 Undamped structures 143
4.2.2 Free layer damping (FLD) 143
4.2.3 Constrained layer damping (CLD) 144
4.2.4 Interrelation between different damping measures . . . 145
4.2.5 Frequency-temperature behavior of glass and secondary transitions 146
4.3 Methodology 149
4.3.1 Objectives 149
4.3.2 Dynamic mechanical analysis (DMA) in bending mode . 150
4.3.3 Dynamic mechanical analysis (DMA) in shear mode . . . 155
4.3.4 Application of the time temperature superposition principle (TTSP) 161
4.3.5 Normalized loss factor tA 162
4.4 Results and Discussion 162
4.4.1 Effect of damping design under bending deformation . 162
4.4.2 Effect of outer layers in CLD laminates in DMA shear mode 173
4.4.3 Effect of the damping layer thickness in CLD laminates 187
4.5 Summary 196

5 Conclusion and Outlook 207

1 Introduction, Objectives and Structure

1.1 Main challenges

Miniature speakers have grown in importance in recent years, not least due to the rise of smartphones and tablets. One of the key features of these devices, compared to ordinary cellular phones, is their thinness, hence the main challenges for the speakers have been transformed [1], [2]. Not only are clear sound and therefore good acoustics are required any longer. Due to the thinness of the devices also the mechanical requirements for the speaker membranes have increased [3]. A schematic representation of a miniature speaker is shown in Figure 1.1.

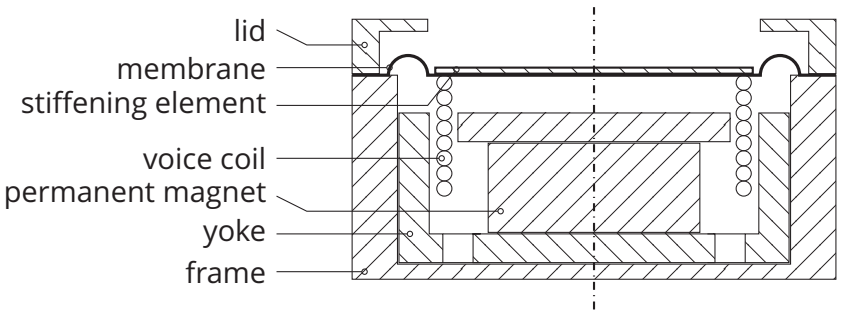

Figure 1.1: Schematic of a miniature speaker, according to [2]–[6].

The most important parts are the membrane with a stiffening element, the voice coil attached to it, the magnet and the yoke. In contrast to traditional loudspeakers, miniature speakers do not have a spider due to space and size

constraints. As a result the suspension system of miniature speakers consists of the polymer membrane alone [2], [4]. The resulting main challenges for the membrane are, on the one hand to exhibit an adequate damping behavior to ensure a high sound quality and on the other hand, a high fracture toughness to resist high fatigue loads. In order to fulfill both requirements, multilayer laminates with thicknesses of about 50 µm used as membranes are state of the art in miniature speaker designs. A high fracture toughness and fatigue resistance is ensured by one or two tough base layers which are laminated with a damping layer on top or in between.

1.2 Structure of the thesis

Based on the main requirements of a high fracture toughness and a good damping behavior of the polymeric laminates in the present thesis, methods are introduced to characterize them directly at the film level. The thesis is divided into the following five parts:

1. Introduction, Objectives and Structure
2. State of the art
3. Fracture toughness testing of thin polymer films
4. Damping characterization of thin polymer films
5. Conclusion and outlook

In the first part a short overview of the main challenges of miniature loudspeakers with their main structural parts is given.

In the second part the state of the art of polymer membranes for miniature speakers and how their fatigue and damping behavior is commonly characterized is presented. At first the main polymer film types used in miniature

speaker membranes are introduced and their key features and main advantages and disadvantages are discussed. This is followed by the state of the art in fracture and damping characterization. Both parts are divided into methods on the component and on the film level. Since current test methods on the film level are not appropriate for performing experiments in application relevant conditions, finally the derived main objectives for establishing new test methods are presented at the end of this chapter.

The third part begins with an introduction to the basic concepts of linear elastic fracture mechanics (LEFM) and methods to characterize the monotonic and cyclic fracture toughness of thin polymeric laminates. In a first step the monotonic fracture toughness of different polymer films and laminates is evaluated. Since only minor differentiation can be found with this test but in loudspeakers significant differences are obvious, in further investigations the cyclic fatigue behavior of the films and laminates is tested. In a next step the applicability of LEFM for cyclic fatigue of thin polymer films is investigated. Also effects of the adhesion between layers in multilayer laminates, effects of anisotropy and effects of temperature to the cyclic fatigue behavior of polymer films and laminates are investigated.

In the fourth part the basic concepts of passive damping designs are explained. This is followed by the introduction of two adapted methods for the damping characterization of thin polymer laminates via dynamic mechanical analysis (DMA) with the ”speaker” and the shear mode. Furthermore the drawback of the limited frequency range of the DMA setups is overcome by using the time temperature superposition principle (TTSP). Finally the damping behavior of different laminates is rated by the frequency dependent normalized loss factor $\overline{tA}$ in the application-relevant temperature range. The new methods then are used to determine the effects of different damping designs in DMA ”speaker” mode and effects of different outer layers and different damping layer thicknesses in DMA shear mode.

In the fifth part conclusions are drawn from the key findings. In the outlook, main challenges which were not covered in this work and possible paths for succeeding works are discussed.

References

[1] S. J. Pawar, S. Weng, and J. Huang, "Total harmonic distortion improvement for elliptical miniature loudspeaker based on suspension stiffness nonlinearity," *IEEE Transactions on Consumer Electronics*, vol. 58, no. 2, pp. 221–227, 2012, ISSN: 0098-3063. DOI: 10.1109/TCE.2012.6227416.

[2] C. Chang, S. J. Pawar, S. Weng, Y. Shiah, and J. Huang, "Effect of nonlinear stiffness on the total harmonic distortion and sound pressure level of a circular miniature loudspeaker-experiments and simulations," *IEEE Transactions on Consumer Electronics*, vol. 58, no. 2, pp. 212–220, 2012, ISSN: 0098-3063. DOI: 10.1109/TCE.2012.6227415.

[3] W. Klippel, *Nonlinear damping in micro-speakers*, Dresden, DE. [Online]. Available: http://www.klippel.de/fileadmin/klippel/Files/Know_How/Literature/Papers/Nonlinear%20Damping%20in%20Micro-Speakers_Klippel.pdf.

[4] J. H. Huang, H.-C. Her, Y. C. Shiah, and S.-J. Shin, "Electroacoustic simulation and experiment on a miniature loudspeaker for cellular phones," *Journal of Applied Physics*, vol. 103, no. 3, p. 033 502, 2008, ISSN: 00218979. DOI: 10.1063/1.2837112.

[5] A. Kesisyan, "Optimierungsmöglichkeiten für den akustischen einbau von kleinlautsprechern in telekommunikationsanwendungen," Master's thesis, Fachhochschule Technikum Wien, Wien, AUT, 1.09.2008.

[6] M. Papakyriacou and S. Windischberger, "Diaphragm for a micro loudspeaker," pat. EP2268058 (A1), 2010.

2 State of the art

2.1 Production process of miniature speakers

In order to obtain the stiff monolayer films for loudspeaker membranes, which are required to guarantee a high fracture toughness, two main production processes are used. On the one hand thin polymer films are produced via solvent casting. Here in a first step a dope is prepared by dissolving the polymer in a solvent such as acetone, methanole, methylene cloride or water, which is then mixed and filtered. In a next step the dope is casted on a stainless steel belt or drum with widths of up to 2 m, where the drying process begins for which various drying techniques are available. If the residual solvent content is low enough, to ensure mechanical stability of the films, they are taken of and further dried finally from both sides for instance in a roller cabinet. Crucial for this production process is the recovery of the solvent from the process air, since the solvents are often harmful for both employees and the environment. Therefore the solvent casting is also a closed process. The main advantage of this process is the nearly isotropic material behavior of the produced films because no predominant molecular orientation is created within the films with this process, but this is accompanied by a high price due to the complex process [7].

The second wide spread manufacturing process for thin films is extrusion. Here the polymer in form of a powder or a granulate is molten and homogenized in an extruder.The melt then is transferred from a round shape in

the extruder to a rectangular film shape in the die. After the die the films are axially drawn in order to obtain the desired thicknesses of under 10 µm, before they get in contact with a chill roll. In a last step the films are rolled with a winder [8]. The main disadvantage of this process is that the films have to be significantly drawn after the die in order to reach the desired low thicknesses, which consequently leads to a strong molecular orientation of the polymer chains along the processing direction. As a result a significant anisotropic material behavior is obtained. The upside is the low resulting price of the films due to the economic efficiency of the process

In order to ensure a high damping capacity and therefore excellent acoustic properties of the membranes in a next step the monolayer films are laminated together with a soft damping layer in between two monolayer films or on one monolayer film on top. The desired speaker geometry is then obtained via deep drawing of these laminates. Finally the membrane is cut out and assembled in a miniature speaker. In Figure 2.1 an overview of the processes involved and their corresponding products from a monolayer film to the final miniature loudspeaker in form of a flow diagram is shown.

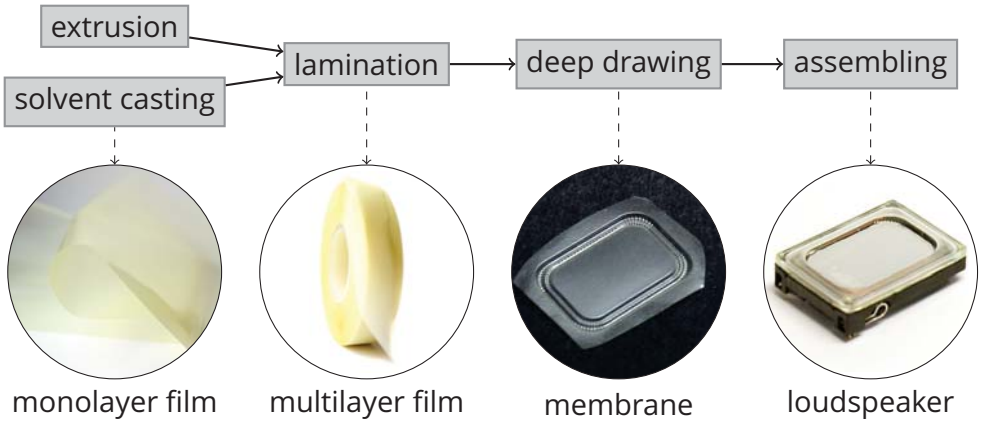

Figure 2.1: Flow diagram of the production steps and their corresponding products of miniature loudspeakers.

2.2 Materials

The standard material in recent years for the stiff outer layers in laminates for miniature speakers has been polyarylate (PAR). These films are produced via solvent casting, feature thicknesses starting from 6 µm and exhibit a high temperature stability (T_G up to 192 °C) [9], [10]. Since the low fracture toughness of PAR has become a significant problem due to rising loads in miniature speakers, alternatives have to be found. Possible polymers which also can be solvent cast are polycarbonate (PC), polyetherimide (PEI) and polyethersulfone (PESU). All of them provide a similar temperature stability to PAR but according to the literature, a higher fracture toughness [11]–[14]. Nevertheless the main disadvantage remains the high price.

Other thin polymer films on the market with an even higher fracture toughness like polyethyleneterephthalate (PET), polyethylenenaphthalate (PEN) and polyetheretherketone (PEEK) are produced via extrusion. Since PET has its glass transition T_G at approximately 70 °C this prohibits its application in highly stressed speaker designs where even higher temperatures may occur. PEN is a derivative of PET and is better suited for such applications with its T_G at 121 °C but does not provide the same level of fracture toughness [15]. PEEK has gained significant attention in recent years due to its outstanding fracture toughness and high temperature stability with its T_G at 143 °C [16]. In Table 2.1 a brief overview of the key values of these films from the literature is listed with their glass transition temperature T_G, their tensile modulus E and their fracture toughness K_{IC}. When no data about the listed parameters was available for the films, generic data for the same polymer type was taken from the literature.

Table 2.1: Main polymer types for miniature loudspeakers.

Material		PAR	PC	PEEK	PEI	PEN	PESU	PET
Polymer		Polyarylate	Poly-carbonate	Polyether-etherketone	Polyether-imide	Polyethylene-naphthalate	Polyether-sulfone	Polyethylene-terephthalate
Morphology		amorphous	amorphous	semi-crystalline	amorphous	amorphous	amorphous	semi-crystalline
Production process		solvent casting	solvent casting	extrusion	Solvent casting	extrusion	solvent casting	extrusion
T_G	[°C]	193[a]	157[b]	143[c]	217[d]	121[e]	186-192[f]	68-80[f]
E	[GPa]	2.1[a]	2.2[b]	2.6[c]	3.0[d]	6.08[e]	2.6-2.8[f]	5.5[g]
K_{IC}	[MPa m$^{0.5}$]	1.28-2.13[h]	2.1-2.3[f]	6[i]	2.93[i]	3.4-3.8[f]	3.54[i]	4.8-5.3[f]

[a] [11] [b] [12] [c] [16] [d] [13] [e] [15] [f] Cambridge Engineering Selector (Granta Design Ltd., Cambridge, UK) [g] [17] [h] [18] [i] [14]

2.2.1 Naming scheme

The naming scheme for the tested materials in this thesis is as follows with examples shown in the following list. At first the number of layers is given in bold face with a subscripted indication of the overall thickness of the laminate in µm. After that each layer is listed with the abbreviation of its polymer type followed by the subscripted thickness. Base or constraining layers are in black, damping layers in red color. For symmetrical layer designs for 3- and 5-layer laminates, the layer stack up is mirrored at the last listed layer.

1L$_{10}$-PAR$_{10}$

2L$_{38}$-PEEK$_8$TPE(b)$_{30}$

3L$_{46}$-PEEK$_8$I$_{30}$

5L$_{50}$-PAR$_{10}$C$_9$PET(b)$_{12}$

2.3 Fracture characterization of thin films

2.3.1 Component tests

State of the art in fatigue testing of new membrane materials for miniature speakers are component tests. For these a large number of speakers are tested under one and the same load until failure occurs. As a result a statistical estimation of the probability of failure $F(t)$ of a speaker as a function of time t or load cycles N is obtained, based on the Weibull test. This method is based on the assumption that a structure fails when the weakest part of it fails, which is expressed in Equation 2.1,

$$F(t) = 1 - e^{(t-t_0/a)^b} \tag{2.1}$$

with the fraction failing $F(t)$, the failure time t, the time before the first failure occurs t_0, the scale parameter or characteristic life a and the shape

parameter or slope b [19]–[21]. An example of a Weibull evaluation is shown in Figure 2.2 for a rotating beam test with St-37 steel, with a scale parameter a of 62 080.2 and a shape parameter b of 2.63 [20], [22]. In the probability density function PDF the probability of failure as function of the cycles to failure N_f is described. Together with the related shape parameter b it is possible to distinguish between failure types of infant mortality ($b = 0.5$), random failures ($b = 1$), early wearout ($b = 3$) and old age wearout ($b = 6$). The cumulative density function CDF provides an assumption of the percentage of failed specimens as a function of the cycles to failure N_f.

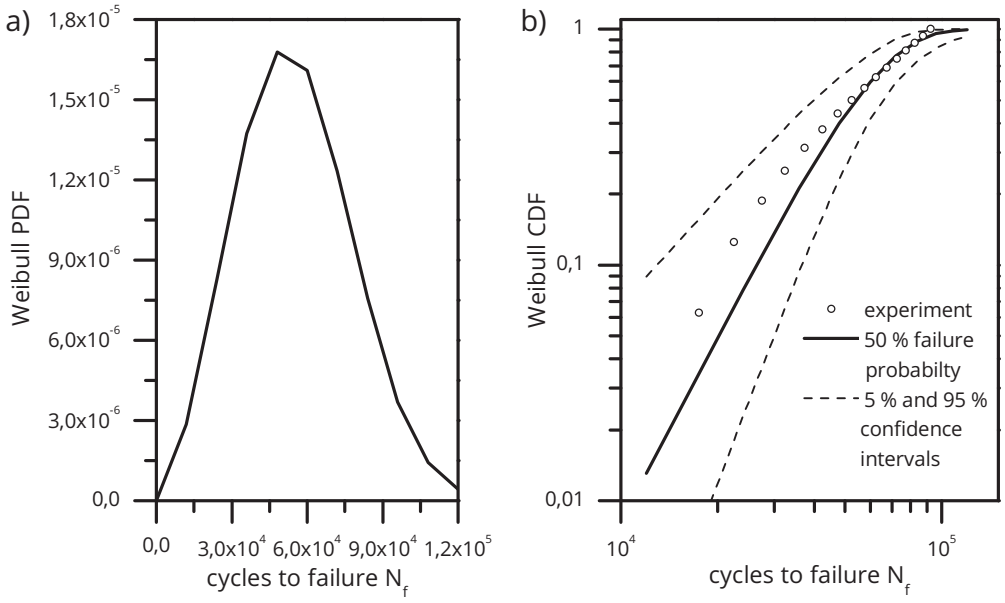

Figure 2.2: Weibull evaluation of St-37 steel in a rotating beam test at $\pm 32\,\mathrm{kg\,mm^{-2}}$ with a scale parameter a of 62 080.2 and a shape parameter b of 2.63, a) the probability density function (PDF) and b) the cumulative density function (CDF), both as function of the cycles to failure N_f, according to [20], [22].

In order to test new membrane film materials, therefore, in a first step laminates and in a second step a large number of speakers have to be produced on a production line prior to the tests. Since this is neither time nor cost efficient for comprehensive research on new speaker membrane materials, a test directly on the film is introduced in this thesis.

2.3.2 Tests on the film level

Thin polymer films are described in the literature as showing predominantly ductile fracture behavior and large plastic zones; the crack tip is surrounded by plastic flow most of which is not involved in crack growth. Therefore concepts like linear elastic fracture mechanics, which were developed for the characterization of brittle fatigue modes, are described as not applicable [23]. On the other hand, for the fracture characterization of polymer films and ductile materials in general the concept of essential work of fracture (EWF) has gained wide attention in recent years. It was first introduced by Cotterell and Reddel for thin steel sheets [24] based on the concept of Broberg [25]–[27]. Following their idea, the non-elastic region at the crack tip is dividable into two parts. One part is involved in the fracture process, which is characterized by the essential work of fracture w_e. In the other, surrounding, part plastic deformation occurs, which is characterized by the non-essential work of fracture w_p. Both are shown schematically in Figure 2.3 [24]–[27].

Wu and Mai have shown, that w_e is independent of the specimen geometry for a defined thickness as long as plane stress conditions prevail and is therefore a material property . On the other hand the non-essential work of fracture w_p depends as well on the material itself and on the stress state in front of the crack, which is different in each specimen geometry [27], [29]. The essential work of fracture w_e acts along the fracture line, is proportional to the fracture area and therefore also proportional to the length of the ligament L. The non-essential work of fracture w_p depends on the volume of the plastic zone surrounding the crack, which is proportional to the square of the ligament length L^2. As a result, for the total work of fracture W_f follows:

$$W_f = w_e BL + \beta w_p BL^2 \tag{2.2}$$

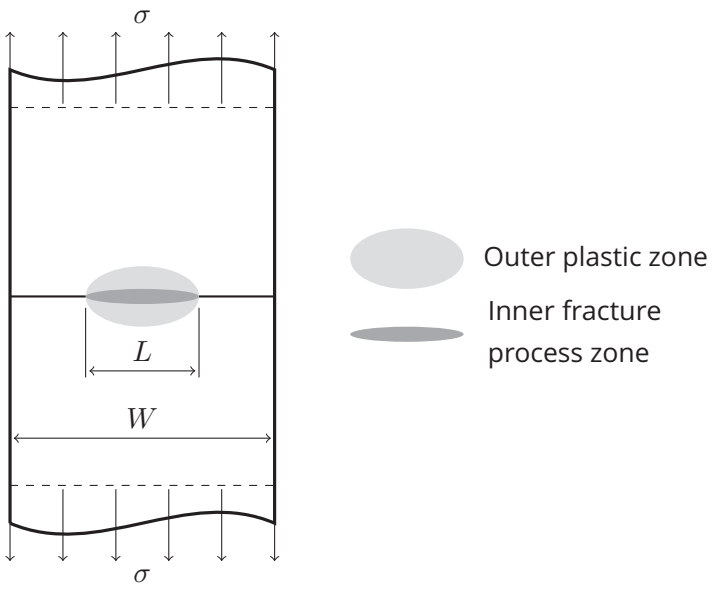

Figure 2.3: Schematic diagram of a DENT specimen with the outer plastic zone and the inner fracture process zone with the width of the specimen W, the ligament length L and the tension load σ, according to [28].

with the ligament length L, the thickness of the specimen B and the shape factor β which describes the dimension of the plastic zone normal to the crack line. This is usually normalized to the fracture area BL and the specific work of fracture w_f is obtained [27].

$$w_f = \frac{W_f}{BL} = w_e + \beta w_p L \tag{2.3}$$

In order to determine the two parts of fracture energy, load vs. displacement curves with single (SENT) or double edge notched tension (DENT) specimens at several ligament lengths are recorded. To ensure validity of the measurements, the specimen has to meet two requirements. First it has to be in plane stress state, which is guaranteed with a ligament length 3 to 5 times larger than the specimen thickness B. Second the plasticity in the ligament has to be fully developed which is guaranteed with a maximum ligament

length smaller than double the plastic zone size in the DENT specimens, following:

$$2r_p = \frac{1}{\pi}\left(\frac{Ew_e}{\sigma_{ys}^2}\right) > L > 3 - 5B \tag{2.4}$$

with the plastic zone size r_p and the Young's modulus E [23], [24], [30]. Calculating the area under the load displacement curves leads to the specific work of fracture w_f, which is plotted as a function of the ligament length L. As long plane stress prevails, a linear relationship between w_f and L is obtained. Following Equation 2.3 in a linear regression fit the essential work of fracture w_e is determined by calculation of the work of fracture at zero ligament length. The slope of the fit is the non-essential work of fracture w_p [28].

The method of EWF was applied for the first time to polymer films by Mai and Cotterell for 4.8 mm thick polyamide 66 (PA 66) and two types of 3 mm thick polyethylene (PE) sheets in 1986 [31]. Starting with 1990 EWF began to spread. Saleemi and Nairn tried to extend the concept to determine the plane strain fracture toughness of two rubber-toughened PA and three PE types with sheets with thicknesses of 1.587 mm and 3.175 mm [32]. Paton and Hashemi investigated the effect of specimen geometry, specimen size and specimen orientation to the EWF parameters of polycarbonate (PC). Using DENT and SENT specimens of varying sizes they showed that for PC also w_e is a material parameter for a given thickness. Furthermore they discovered with tests with the crack path in different directions relative to the process direction of the films that w_e is able to describe the direction-dependent fracture toughness. Similar work was done by Chan and Williams, who studied the effects of specimen geometry with two PA types and the effects of specimen width and strain rate with PE, polyethylenetherephthalate (PET) and polyimide (PI) films [33]. Hashemi and different co-workers studied various polymers and effects on the fracture behavior of them, such as the effect of the specimen width on the EWF parameters for a PC film [34],

the effect of thickness and degree of crystallinity on polyetheretherketone (PEEK) films and they made an attempt to calculate EWF parameters from crack tip opening displacement (COD) measurements [23], the validity of EWF for polyethylenetherephthalate (PET), polyethylenenaphthalate (PEN), polyetheretherketone (PEEK), polycarbonate (PC), polybutyleneterephthalate (PBT), cellulose acetate (CA), polyetherimide (PEI) and polyimide (PI) films [28], the effect of temperature and deformation rate to the work of fracture of PC films [35], the effect of temperature and film thickness to PBT films [36], [37], effects of specimen geometry, loading rate and temperature for a PET and a PEN film [38], [39], the effect of temperature for PC, PEEK, PET, PEN and PBT films [39]–[42], effects of gauge length and width of the specimen, anisotropy, loading rate and temperature of a HIPS film [43] and the effects of temperature and anisotropy of biaxially oriented PET (BOPET) films [44]. Karger-Kocsis and co-workers studied the fracture of amorphous copolyester (aCOP) films and influences of the film thickness. The have shown that aCOP meets the basic requirements of EWF with full ligament yielding prior to crack growth and, as a result, w_e became independent of the specimen thickness as long as plane stress conditions are ensured. Secondly they suggested splitting the work of fracture into two parts, one related to yielding (w_{eI} and w_{pI}) and the other related to necking and fracture (w_{eII} and w_{pII}) [45]. In further work they studied the influence of the intrinsic viscosity (IV) and the mean entanglement length (M_e) of aCOP films on the work of fracture [46], the effect of the deformation rate to aCOP [47] and the plain strain fracture toughness of aCOP under impact loading [48]. Maspoch and co-workers successfully applied the EWF concept to a thermoplastic elastomer (TPE) [49], they studied effects of specimen height, width and thickness and deformation rate of a isotactic polypropylene (iPP) [50] and characterized the fracture behavior of a polypropylene (PP) homopolymer and ethylene-propolyene (EPBC) block copolymers with different ethylene content (EC) as a function of temperature [51]. Pegoretti and Ricco characterized temperature and deformation rate effects of semicrystalline PET films [26] and Light and Lesser did the same for PET films [52]. Lach, et al. studied

the applicability of EWF to nanostructured polystyrene-polybutadiene block copolymers using in situ testing devices combining a tensile test and an optical strain-field measuring system [53]. Zhao and Li studied the anisotropic fracture behavior of PEEK films of different thicknesses [54]. Williams and Rink described results of a round robin test within the European Structural Integrity Society - Technical Comittee 4 (ESIS TC4) with ethylene-propylene 100 µm films [55]. Bárány, Czigány and Karger-Kocsis published a review of the application of the EWF concept for polymers, blends and composites [30]. Most recently Rink et al. investigated the correlation between EWF parameters to that of the concept of J-integral for different polymers [56].

The advantage of EWF is that it accounts well for probable large plastic deformations which may occur in thin polymer films and enables the characterization of their fracture toughness in an efficient manner because it is based on monotonic experiments. Although this seems promising, the major disadvantage is that effects due to cyclic loads at high frequencies, which may occur in miniature loudspeaker membranes, are not reproduced. Since cyclic loads at high frequencies may also lead to high strain rates in the loudspeaker films, a transition to brittle fracture modes might also take place. An example of a transition from ductile to brittle fracture modes at high loading rates was shown by Ching et al. for 0.5 mm thick PET films [57]. In conclusion, the implementation of a cyclic fatigue test for a detailed study of the cyclic fracture behavior of thin polymer films for miniature loudspeakers directly on the film may be necessary to reproduce the conditions during use.

2.4 Damping characterization of thin films

One of the key features of the speaker membrane is to provide adequate damping to the loudspeaker in order to ensure a high sound quality and

to keep the loudspeaker from failure due to high displacements at resonance. Before we go more into detail, first basic concepts of speakers have to be explained. A schematic overview of the sound pressure level SPL and corresponding displacement of the membrane x vs. frequency f for a hypothetical loudspeaker is shown in Figure 2.4a and 2.4b, respectively. In region A the displacement x of the membrane is controlled by the stiffness of the supports and therefore stays at a constant level. The sound pressure increases from low levels with 12 dB per octave (forth power of the frequency f^4). The resonance frequency f_R of the loudspeaker lies in region B where both sound pressure level SPL and displacement x of the membrane exhibit their maximum [5], [58]. An inadequately low damping at the resonance frequency f_R results in high displacements of the membrane and consequently a low sound quality caused by distortion from nonlinear deformation of the membrane, from the membrane hitting the miniature speaker housing and also early failure resulting from high mechanical loads in the membrane. Above f_R lies region C which features a constant SPL level and a decrease of x with 12 dB. Area C is used as the application area of the loudspeaker. The second resonance and the following sound pressure decrease with −12 dB form the upper limit of the application area [5], [58], [59].

Consequently the damping design has to ensure that the system does not undergo high displacements during resonance in order to prohibit the membrane from

- mechanical failure due to high cyclic loads,
- hitting the housing, consequentially giving bad sound quality and damage of the membrane,
- nonlinear behavior and, consequentially, distorted sound [60], [61].

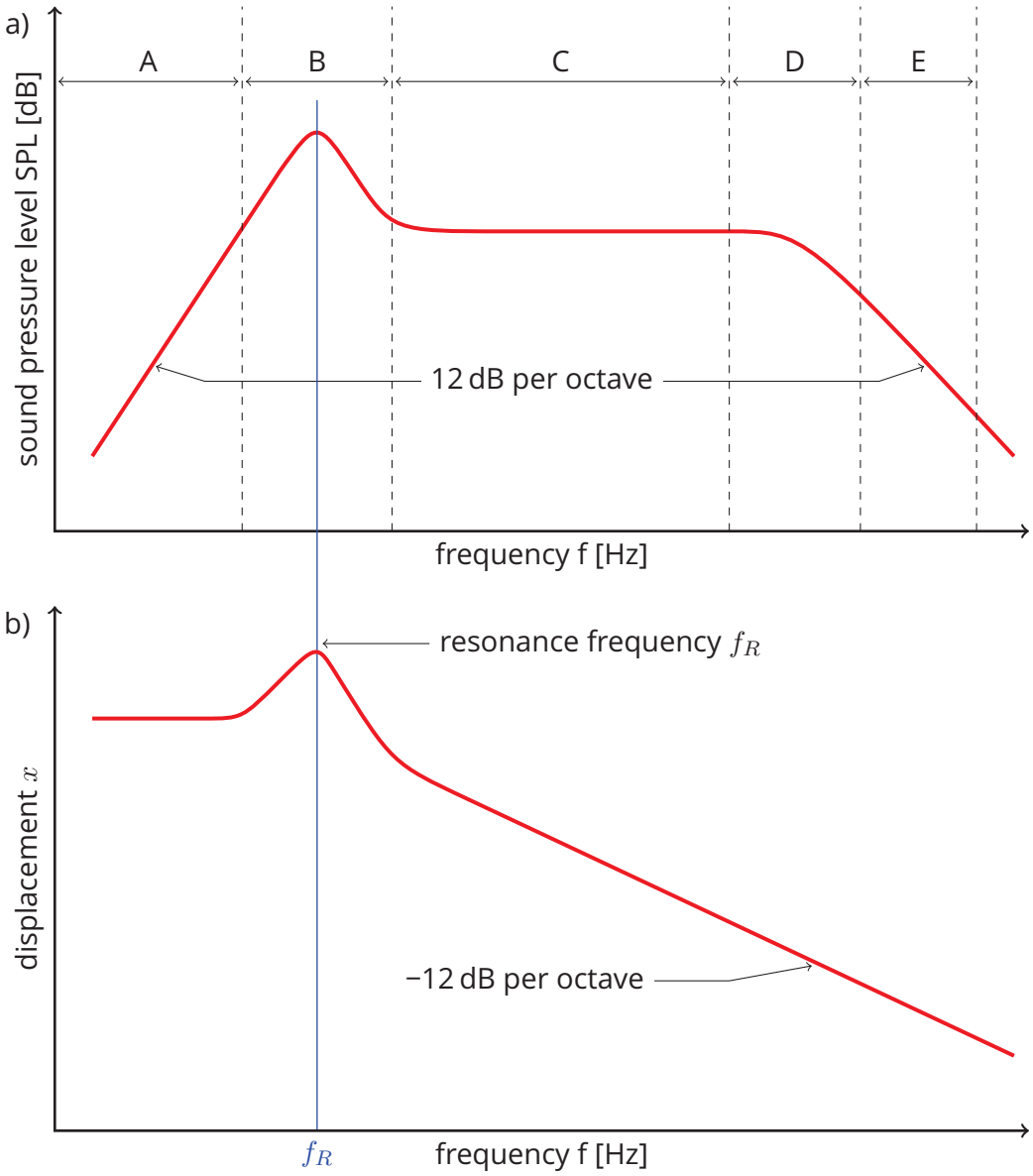

Figure 2.4: Schematic a) sound pressure level SPL and b) displacement x as a function of frequency f of a loudspeaker with low damping, according to [5], [58], [59].

2.4.1 Component tests

State of the art in characterizing the damping behavior of loudspeaker membranes are, on the one hand the full acoustic characterization in component tests and on the other hand, tests on the film level via free resonance dynamic mechanical analysis (DMA) using a modified Oberst beam test [5], [62], [63]. In the component tests the damping of the loudspeaker is described with the quality factor Q which exhibits a reciprocal proportionality to the amount of damping [64]–[66]. The quality factor of the total system Q_{TS} consists of the electrical quality factor Q_{ES} and the mechanical quality factor Q_{MS}[65]–[67]. Q_{ES} depends on the electrical resistance of the voice coil R_{DC}, the force factor of the electro-dynamical system $B \cdot l$, the ratio of the mechanical compliance C_{MS} and the mass of the dynamic system M_{MS} (Equation 2.5) [65], [66]. Q_{MS} describes the energy relationships of the mechanical system with the ratio of energy which is elastically stored in deformation of the material and the energy which is dissipated into heat [5]. The mechanical quality factor depends on the mechanical resistance R_{MS} of the loudspeaker suspension which is, in the case of miniature loudspeakers, the polymeric loudspeaker membrane. R_{MS} is defined as the mechanical equivalent to the electrical resistance R_{DC} (Equation 2.6). Consequently the damping behavior of the loudspeaker membrane is characterized with Q_{MS} [5].

$$Q_{ES} = \frac{2\pi f_r \cdot M_{MS} \cdot R_{DC}}{(B \cdot l)^2} = \frac{R_{DC}}{(B \cdot l)^2} \cdot \sqrt{\frac{M_{MS}}{C_{MS}}} \tag{2.5}$$

$$Q_{MS} = \frac{2\pi f_r \cdot M_{MS}}{R_{MS}} = \frac{1}{R_{MS}} \cdot \sqrt{\frac{M_{MS}}{C_{MS}}} \tag{2.6}$$

$$Q_{TS} = \frac{Q_{ES} \cdot Q_{MS}}{Q_{ES} + Q_{MS}} = \frac{R_{DC}}{(B \cdot l)^2 + R_{MS} \cdot R_{DC}} \sqrt{\frac{M_{MS}}{C_{MS}}} \tag{2.7}$$

The evaluation of Q_{MS} is done by measuring the impedance Z of the loudspeaker as a function of the frequency, as shown schematically in Figure 2.5. In a next step Q_{MS} is evaluated using the following correlation:

$$Q_{MS} = \frac{f_r \cdot \sqrt{r_0}}{f_2 - f_1} \tag{2.8}$$

with the free air resonance frequency f_R, the maximum resistance at resonance frequency r_0, and the frequencies at $\sqrt{r_0}$, named f_1 and f_2 [65], [66], [68].

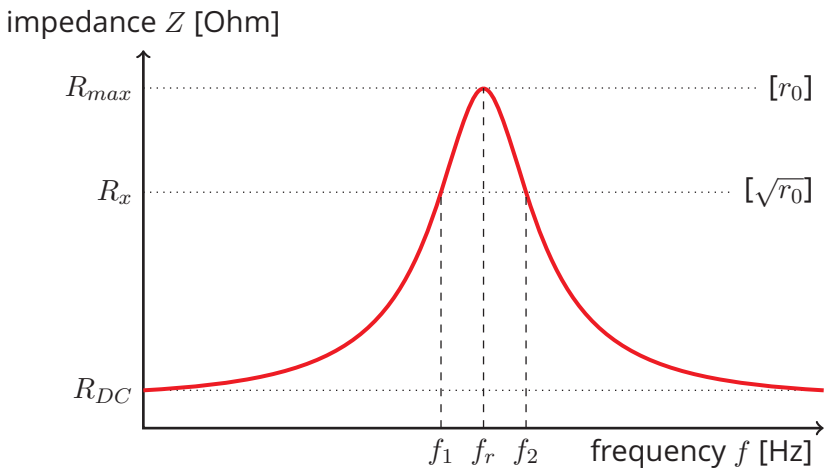

Figure 2.5: Schematic impedance curve of a loudspeaker with the maximum of the impedance r_0 at resonance frequency f_R and the frequencies at $\sqrt{r_0}$ f_1 and f_2, according to [65], [66], [68].

2.4.2 Tests on the film

State of the art in characterizing the damping behavior of FLD and CLD designs on the specimen is a modified Oberst beam test, with the basic method described in ASTM E756 [62], [63], [69]–[72]. In this variation of a free resonance dynamic mechanical analysis (DMA) the specimen in the form of a beam is clamped at one end and excited passively around its first or upper resonance frequencies. Both excitation force F and displacement x are recorded as functions of the frequency f. Based on basic beam theory which is extended for FLD and CLD designs material parameters such as Young's modulus E and loss factor η are calculated [62], [70], [72], [73]. A

special test setup for the characterization of thin loudspeaker membranes is schematically shown in Figure 2.6 [63].

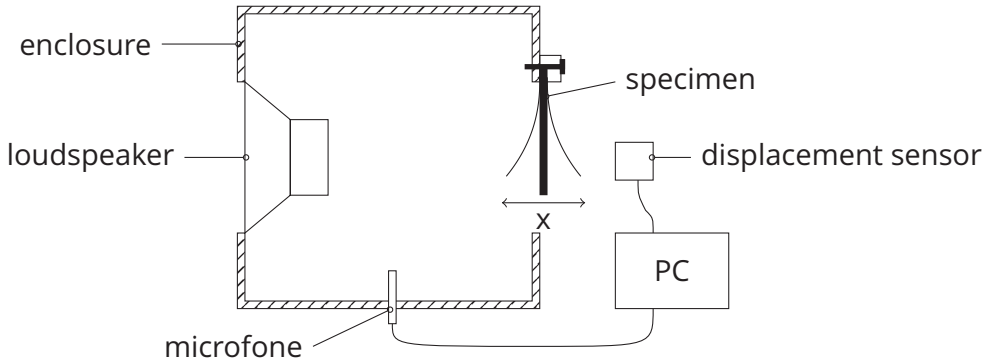

Figure 2.6: Schematic of a setup to characterize thin loudspeaker membranes, according to [63].

In order to measure the material properties as a function of frequency, the specimen length and therefore its resonance frequencies are varied [73]. Since the membranes in miniature speakers exhibit thicknesses of about 50 µm, their stiffness and therefore resonance frequencies f_R are very low and also at significantly lower frequencies than the application frequency range of the loudspeakers. Furthermore state of the art setups for thin loudspeaker membranes are not capable of characterizing material parameters as a function of the temperature. Since the application temperatures for miniature loudspeakers range from temperatures below freezing up to temperatures, significantly above room temperature, an extended temperature range for the damping characterization of the membranes is required.

2.5 Main Objectives

The state of the art in the detailed characterization of both the fatigue and damping behavior of membranes for miniature loudspeaker are component tests. In order to perform the tests beforehand loudspeakers have to be built on a fully automatic production line. Although component tests are of great

importance for the final adjustment of the loudspeaker design, they are neither time nor cost effective for an early material selection. Consequently tests on the films themselves are favored for a material selection. Current systems for the characterization of the damping behavior of thin membranes are limited to tests at ambient temperatures and to frequencies significantly below the application range of miniature loudspeakers. Consequently in the present work new methods were to be established for the characterization of the fracture and damping behavior of miniature speaker membranes with the following goals:

Characterization of the fracture behavior:

- evaluation and implementation of a fracture mechanical test for thin acoustic films,
- characterization of the fracture behavior of thin films at application-relevant temperatures and frequencies.

Characterization of the damping behavior:

- dynamic-mechanical characterization of loudspeaker membranes with respect to frequency and temperature,
- extending the characterization range of both temperature and frequency to application-relevant conditions.

References

[5] A. Kesisyan, “Optimierungsmöglichkeiten für den akustischen einbau von kleinlautsprechern in telekommunikationsanwendungen,” Master’s thesis, Fachhochschule Technikum Wien, Wien, AUT, 1.09.2008.

[7] U. Siemann, "Solvent cast technology – a versatile tool for thin film production," in *Scattering methods and the properties of polymer materials*, ser. Progress in Colloid and Polymer Science, N. Stribeck, W. Ruland, and B. Smarsly, Eds., vol. 130, Berlin and New York: Springer, 2005, pp. 1–14, ISBN: 978-3-540-25323-5. DOI: 10.1007/b107336.

[8] P. G. Lafleur and B. Vergnes, *Polymer extrusion*, ser. Materials science series. John Wiley & Sons, Inc., 2014, ISBN: 978-1-84821-650-1.

[9] Lofo High Tech Film GmbH, "Membranes made of cast polyarylate film," pat. WO 2004/003062 A1.

[10] Lofo High Tech Film GmbH, *Aryphan: Product information*, 26.11.2014. [Online]. Available: http://www.lofo.com/fileadmin/user_upload/pdfs/produktseiten_produktinformationen/englisch/lofo_productinformation_aryphan_v01.pdf.

[11] Lofo High Tech Film GmbH, *Aryphan N 681 EM: Technical data*.

[12] Lofo High Tech Film GmbH, *Pokalon N 470 EM: Technical data*.

[13] Lofo High Tech Film GmbH, *Sonophan N 670 EM: Technical data*.

[14] J. P. Trotignon, J. Verdu, C. Martin, and E. Morel, "Fatigue behaviour of some temperature-resistant polymers," *Journal of Materials Science*, vol. 28, no. 8, pp. 2207–2213, 1993, ISSN: 0022-2461. DOI: 10.1007/BF00367585.

[15] Teijin DuPont Films U.S. Ltd., *Film type Teonex Q51*, 27.02.2015. [Online]. Available: www.iec-international.com/pdf/PEN_TeonexQ51.pdf.

[16] Victrex plc, *Victrex PEEK polymer for films*.

[17] Mitsubishi Polyester Film GmbH, *Hostaphan TT*, 26.11.2014. [Online]. Available: http://www.m-petfilm.com/upload/Europe_131ENG.pdf.

[18] K. Humer, E. K. Tschegg, and H. W. Weber, "Tensile, fracture and thermal properties of polyarylates at room and cryogenic temperatures," *Cryogenics*, vol. 33, no. 7, pp. 686–691, 1993, ISSN: 0011-2275. DOI: 10.1016/0011-2275(93)90020-D.

[19] W. Weibull, *The phenomenon of rupture in solids*. Generalstabens Litografiska Anst, 1939.

[20] W. Weibull, "A statistical distribution function of wide applicability," *Journal of applied mechanics*, vol. 18, pp. 293–297, 1951.

[21] R. B. Abernethy, J. E. Breneman, C. H. Medlin, and G. L. Reinman, *Weibull analysis handbook*, U.S. Air Force AFWAL-TR-83-2079, Ed., 1.01.1983.

[22] H. Müller-Stock, "Der einfluß dauernd und unterbrochen wirkender, schwingender überbeanspruchung auf die entwicklung des dauerbruchs," *Mitteilungen Kohle- und Eisenforschung*, 1938.

[23] S. Hashemi and D. O'Brien, "The essential work of plane-stress ductile fracture of poly(ether-ether ketone) thermoplastic," *Journal of Materials Science*, vol. 28, no. 15, pp. 3977–3982, 1993, ISSN: 0022-2461. DOI: 10.1007/BF00351217.

[24] B. Cotterell and J. K. Reddel, "The essential work of plane stress ductile fracture," *International Journal of Fracture*, vol. 13, no. 3, pp. 267–277, 1977, ISSN: 0376-9429. DOI: 10.1007/BF00040143.

[25] K. B. Broberg, "On stable crack growth," *Journal of the Mechanics and Physics of Solids*, vol. 23, no. 3, pp. 215–237, 1975, ISSN: 00225096. DOI: 10.1016/0022-5096(75)90017-4.

[26] A. Pegoretti and T. Ricco, "Rate and temperature effects on the plane stress essential work of fracture in semicrystalline pet," in *Fracture of polymers, composites, and adhesives II*, ser. ESIS publication, Blackman, B. R. K, A. Pavan, and J. G. Williams, Eds., vol. 32, Amsterdam and Boston: Elsevier, 2003, pp. 89–100, ISBN: 9780080441955. DOI: 10.1016/S1566-1369(03)80086-9.

[27] E. Clutton, "Essential work of fracture," in *Fracture mechanics testing methods for polymers, adhesives, and composites*, ser. ESIS publication, D. R. Moore, A. Pavan, and J. G. Williams, Eds., vol. 28, Amsterdam and New York: Elsevier, 2001, pp. 177–195, ISBN: 9780080436890. DOI: 10.1016/S1566-1369(01)80033-9.

[28] S. Hashemi, "Fracture toughness evaluation of ductile polymeric films," *Journal of Materials Science*, vol. 32, pp. 1563–1573, 1997, ISSN: 0022-2461. DOI: 10.1023/A:1018582707419.

[29] J. Wu and Y.-W. Mai, "The essential fracture work concept for toughness measurement of ductile polymers," *Polymer Engineering & Science*, vol. 36, no. 18, pp. 2275–2288, 1996, ISSN: 00323888. DOI: 10.1002/pen.10626.

[30] T. Bárány, T. Czigány, and J. Karger-Kocsis, "Application of the essential work of fracture (ewf) concept for polymers, related blends and composites: A review," *Progress in Polymer Science*, vol. 35, no. 10, pp. 1257–1287, 2010, ISSN: 00796700. DOI: 10.1016/j.progpolymsci.2010.07.001.

[31] Y.-W. Mai and B. Cotterell, "On the essential work of ductile fracture in polymers," *International Journal of Fracture*, vol. 32, no. 2, pp. 105–125, 1986, ISSN: 0376-9429. DOI: 10.1007/BF00019787.

[32] A. S. Saleemi and J. A. Nairn, "The plane-strain essential work of fracture as a measure of the fracture toughness of ductile polymers," *Polymer Engineering and Science*, vol. 30, no. 4, pp. 211–218, 1990. DOI: 10.1002/pen.760300404.

[33] W. Chan and J. G. Williams, "Determination of the fracture toughness of polymeric films by the essential work method," *Polymer*, vol. 35, no. 8, pp. 1666–1672, 1994, ISSN: 00323861. DOI: 10.1016/0032-3861(94)90840-0.

[34] S. Hashemi, "Plane-stress fracture of polycarbonate films," *Journal of Materials Science*, vol. 28, pp. 6178–6184, 1993, ISSN: 0022-2461. DOI: 10.1007/BF00365040.

[35] S. Hashemi, "Temperature and deformation rate dependence of the work of fracture in polycarbonate (pc) film," *Journal of Materials Science*, vol. 35, no. 23, pp. 5851–5856, 2000, ISSN: 0022-2461. DOI: 10.1023/A:1026704323702.

[36] S. Hashemi, "Temperature dependence of work of fracture parameters in polybutylene terephthalate (pbt)," *Polymer Engineering & Science*, vol. 40, no. 6, pp. 1435–1446, 2000, ISSN: 00323888. DOI: 10.1002/pen.11273.

[37] S. Hashemi, "Fracture of polybutylene terephthalate (pbt) film," *Polymer*, vol. 43, no. 14, pp. 4033–4041, 2002, ISSN: 00323861. DOI: 10.1016/S0032-3861(02)00204-5.

[38] A. Arkhireyeva and S. Hashemi, "Determination of fracture toughness of poly (ethylene terephthalate) film by essential work of fracture and j integral measurements," *Plastics, Rubber and Composites*, vol. 30, no. 7, pp. 337–350, 2001. DOI: 10.1179/146580101322913257.

[39] A. Arkhireyeva and S. Hashemi, "Fracture behaviour of polyethylene naphthalate (pen)," *Polymer*, vol. 43, no. 2, pp. 289–300, 2002, ISSN: 00323861. DOI: 10.1016/S0032-3861(01)00623-1.

[40] S. Hashemi and J. G. Williams, "Temperature dependence of essential and non-essential work of fracture parameters for polycarbonate film," *Plastics, Rubber and Composites*, vol. 29, no. 6, pp. 294–302, 2000. DOI: 10.1179/146580100101541102.

[41] S. Hashemi and A. Arkhireyeva, "Influence of temperature on work of fracture parameters in semi-crystalline polyester films," *Journal of Macromolecular Science, Part B*, vol. 41, no. 4, pp. 863–880, 2002. DOI: 10.1081/MB-120013070.

[42] S. Hashemi, "Effect of temperature on fracture toughness of an amorphous poly(ether-ether ketone) film using essential work of fracture analysis," *Polymer Testing*, vol. 22, no. 5, pp. 589–599, 2003, ISSN: 01429418. DOI: 10.1016/S0142-9418(02)00162-9.

[43] S. Hashemi, "Work of fracture of high impact polystyrene (hips) film under plane stress conditions," *Journal of Materials Science*, vol. 38, no. 14, pp. 3055–3062, 2003, ISSN: 0022-2461. DOI: 10.1023/A:1024752508458.

[44] S. Hashemi and Y. Xu, "Thermal effects on fracture of biaxial-oriented poly(ethylene terephthalate) (bopet) film," *Journal of Materials Science*, vol. 42, no. 15, pp. 6197–6204, 2007, ISSN: 0022-2461. DOI: 10.1007/s10853-006-1157-6.

[45] J. Karger-Kocsis, T. Czigány, and E. J. Moskala, "Thickness dependence of work of fracture parameters of an amorphous copolyester," *Polymer*, vol. 38, no. 18, pp. 4587–4593, 1997, ISSN: 00323861. DOI: 10.1016/S0032-3861(96)01061-0.

[46] J. Karger-Kocsis and E. J. Moskala, "Relationships between molecular and plane-stress essential work of fracture parameters in amorphous copolyesters," *Polymer Bulletin*, vol. 39, no. 4, pp. 503–510, 1997. DOI: 10.1007/s002890050179.

[47] J. Karger-Kocsis, T. Czigány, and E. J. Moskala, "Deformation rate dependence of the essential and non-essential work of fracture parameters in an amorphous copolyester," *Polymer*, vol. 39, no. 17, pp. 3939–3944, 1998, ISSN: 00323861. DOI: 10.1016/S0032-3861(98)00029-9.

[48] J. Karger-Kocsis and D. Ferrer-Balas, "On the plane-strain essential work of fracture of polymer sheets," *Polymer Bulletin*, vol. 46, no. 6, pp. 507–512, 2001. DOI: 10.1007/s002890170039.

[49] M. L. Maspoch, O. O. Santana, J. Grando, D. Ferrer, and A. B. Martinez, "The essential work of fracture of a thermoplastic elastomer," *Polymer Bulletin*, vol. 39, no. 2, pp. 249–255, 1997. DOI: 10.1007/s002890050145.

[50] M. L. Maspoch, D. Ferrer, A. Gordillo, O. O. Santana, and A. B. Martinez, "Effect of the specimen dimensions and the test speed on the fracture toughness of ipp by the essential work of fracture (ewf) method," *Journal of Applied Polymer Science*, vol. 73, no. 2, pp. 177–187, 1999, ISSN: 00218995. DOI: 10.1002/(SICI)1097-4628(19990711)73:2<177::AID-APP5>3.0.CO;2-{\#}.

[51] D. Ferrer-Balas, M. L. Maspoch, A. B. Martinez, E. Ching, Li, R. K. Y, and Y.-W Mai, "Fracture behaviour of polypropylene films at different temperatures: Assessment of the ewf parameters," *Polymer*, vol. 42, no. 6, pp. 2665–2674, 2001, ISSN: 00323861. DOI: 10.1016/S0032-3861(00)00603-0.

[52] M. E. Light and A. J. Lesser, "Effect of test conditions on the essential work of fracture in polyethylene terephthalate film," *Journal of Materials Science*, vol. 40, no. 11, pp. 2861–2866, 2005, ISSN: 0022-2461. DOI: 10.1007/s10853-005-2430-9.

[53] R. Lach, K. Schneider, R. Weidisch, A. Janke, and A. Knoll, "Application of the essential work of fracture concept to nanostructured polymer materials," *European Polymer Journal*, vol. 41, no. 2, pp. 383–392, 2005. DOI: 10.1016/j.eurpolymj.2004.09.021.

[54] H. Zhao and R. K. Li, "Fracture behaviour of poly(ether ether ketone) films with different thicknesses," *Mechanics of Materials*, vol. 38, no. 1-2, pp. 100–110, 2006, ISSN: 01676636. DOI: 10.1016/j.mechmat.2005.05.013.

[55] J. G. Williams and M. Rink, "The standardisation of the ewf test," *Engineering Fracture Mechanics*, vol. 74, no. 7, pp. 1009–1017, 2007. DOI: 10.1016/j.engfracmech.2006.12.017.

[56] M. Rink, L. Andena, and C. Marano, "The essential work of fracture in relation to j-integral," *Engineering Fracture Mechanics*, vol. 127, pp. 46–55, 2014. DOI: 10.1016/j.engfracmech.2014.05.006.

[57] E. C. Y. Ching, R. K. Y. Li, and Y.-W. Mai, "Effects of gauge length and strain rate on fracture toughness of polyethylene terephthalate glycol (petg) film using the essential work of fracture analysis," *Polymer Engineering & Science*, vol. 40, no. 2, pp. 310–319, 2000, ISSN: 00323888. DOI: 10.1002/pen.11164.

[58] L. L. Beranek, *Acoustics*. Woodbury NY.: American Inst. of Physics, 1996, ISBN: 088318494X.

[59] A. D. Nashif, D. I. G. Jones, and J. P. Henderson, *Vibration damping*. New York: Wiley, 1985, ISBN: 0471867721.

[60] W. Klippel, *Prediction of speaker performance at high amplitudes*, Dresden, DE. [Online]. Available: http://www.klippel.de/fileadmin/klippel/Files/Know_How/Literature/Papers/Prediction_of_speaker_performance_at_high_amplitudes_01.pdf.

[61] W. Klippel, *Distributed mechanical parameters describing vibration and sound radiation of loudspeaker drive units*, Dresden, DE. [Online]. Available: https://www.klippel.de/fileadmin/klippel/Files/Know_How/Literature/Papers/Distributed%20parameter.pdf.

[62] H. Oberst and K. Frankenfeld, "Über die dämpfung der biegeschwingungen dünner bleche durch festhaftende beläge," *Acustica*, vol. 2, no. 4, pp. 181–194, 1952.

[63] Klippel GmbH, *Klippel product brochure*, Dresden, DE. [Online]. Available: http://www.klippel.de/uploads/media/KLIPPEL_Brochure_RnD_QC_CTR.pdf.

[64] E. E. Ungar, "Damping of panels," in *Noise and vibration control*, L. L. Beranek, Ed., New York: McGraw-Hill, 1971, pp. 434–474, ISBN: 0-9622072-0-9.

[65] N. Thiele, "Loudspeakers in vented boxes: Part 2," *J. Audio Eng. Soc*, vol. 19, no. 6, pp. 471–483, 1971. [Online]. Available: http://www.aes.org/e-lib/browse.cfm?elib=2163.

[66] R. Small, "Direct-radiator loudspeaker system analysis," *IEEE Transactions on Audio and Electroacoustics*, vol. 19, no. 4, pp. 269–281, 1971, ISSN: 0018-9278. DOI: 10.1109/tau.1971.1162200.

[67] J. Eargle, *Loudspeaker Handbook*, Second edition. Boston, MA: Springer US, 2003, ISBN: 978-1-4757-5678-4.

[68] R. H. Small, "Closed-box loudspeaker systems-part 1: Analysis," *J. Audio Eng. Soc*, vol. 20, no. 10, pp. 798–808, 1972. [Online]. Available: http://www.aes.org/e-lib/browse.cfm?elib=2022.

[69] D. I. G. Jones and M. L. Parin, "Technique for measuring damping properties of thin viscoelastic layers," *Journal of Sound and Vibration*, vol. 24, no. 2, pp. 201–210, 1972, ISSN: 0022-460X. DOI: 10.1016/0022-460X(72)90949-2.

[70] American Society for Testing and Materials ASTM E 756 - 05, *Test method for measuring vibration-damping properties of materials*, West Conshohocken, PA, 2010. DOI: 10.1520/E0756-05R10.

[71] H. Koruk and K. Y. Sanliturk, "On measuring dynamic properties of damping materials using oberst beam method," in *Proceedings of the ASME 2010 10th biennal conference on engineering systems design and analysis - ESDA 2010*, 2010. [Online]. Available: http://web.itu.edu.tr/sanliturk/Publications/ESDA2010-24452.pdf.

[72] P. P. Hujare and A. D. Sahasrabudhe, "Experimental investigation of damping performance of viscoelastic material using constrained layer damping treatment," *Procedia Materials Science*, vol. 5, pp. 726–733, 2014, ISSN: 22118128. DOI: 10.1016/j.mspro.2014.07.321.

[73] G. W. Ehrenstein, G. Riedel, and P. Trawiel, *Thermal analysis of plastics: Theory and practice*. Munich: Carl Hanser Verlag, 2004, ISBN: 978-1569903629.

3 Fracture toughness testing of thin polymer films for acoustic applications

3.1 Introduction

The fatigue behavior of thin polymer films used as membranes in miniature loudspeakers is one of their key features in order to guarantee a long service life, as explained in section 2.3. In order to ensure a good speaker design therefore, the knowledge of the fracture and cyclic fatigue behavior is indispensable. Since state of the art systems cannot provide detailed insights into the fracture and cyclic fatigue behavior of these films at application relevant conditions at both high frequencies and a wide temperature range (2.3.2), in this work new methods are introduced to overcome this drawback.

In monotonic fracture mechanic tests it was found that, contrary to results from the literature described in section 2.3.2, the characterized miniature speaker films exhibited brittle fatigue modes. Consequently instead of the concept of essential work of fracture (EWF), which is usually applied to describe ductile fatigue modes of thin films, for the miniature loudspeaker films linear elastic fracture mechanics (LEFM) seemed applicable.

As a consequence in section 3.2 an introduction is given into the basics of linear elastic fracture mechanics (LEFM) (3.2.1) with a special focus on multilayer fracture mechanics (3.2.1.6). Furthermore the theoretical basis of the delamination behavior of multilayer films is explained (3.2.2). The

methods used to characterize the monotonic and cyclic fracture behavior of the films are then explained in section 3.3 beginning with the objectives to clarify the goals of each test. Then the specimen geometries (3.3.2) are introduced followed by the test and evaluation methods for monotonic (3.3.3) and cyclic fracture (3.3.4). The latter splits up into the stress based Wöhler approach (3.3.4.1) and the fracture mechanical fatigue crack growth test (3.3.4.2). Finally the T-peel test is explained (3.3.6).

The results section begins with a description of tests (3.4.1) where we try to characterize the fracture behavior of polymer films and laminates for miniature loudspeakers with monotonic fracture mechanical tests based on linear elastic fracture mechanics (LEFM). Based on this a fatigue test is setup and the applicability of LEFM to describe the fatigue behavior of these films is checked (3.4.2). In the next section the characterization of temperature effects on the fatigue behavior of thin PET monolayer films is described. Furthermore the effect of the multilayer design, and consequently delamination processes, on the fatigue behavior of the loudspeaker laminates is determined (3.4.4). The results section then is closed by the characterization of the anisotropic fatigue behavior due to the manufacturing process of extrusion in section 3.4.5 followed by the summary and outlook.

3.2 Background

Excellent literature is available for the following theoretical topics so only a short overview of the most essential concepts of the fracture toughness evaluations for polymeric films are given in order to provide a basic understanding of the following investigations [74]–[79].

3.2.1 Linear elastic fracture mechanics

Already at the end of 19th century Larmor described that a main driving factor of failure in engineering structures is the presence of flaws [77], [80]. These flaws act as the starting point for crack growth. Driven by the motivation to find a correlation between size, shape and type of the flaws and load conditions which lead to failure, the concept of fracture mechanics was developed in the last century [77]. The failure modes of brittle materials are described by two different perspectives. On the one hand in the approach of Griffith the driving factor for crack growth is the imbalance between the energy necessary for creating new surfaces and the potential energy from external forces and internal strain energy. This has led to the introduction of the energy release rate G as a measure for the fracture toughness of materials, described in chapter 3.2.1.1 [77], [78], [81]. On the other hand the analytical description by Irwin and others of the stress state in the surroundings of crack tips has led to the definition of the stress intensity factor K with which the crack tip conditions are completely described [77], [78], [82]–[85]. For both, predominantly linear elastic material behavior is required which led to the designation linear elastic fracture mechanics (LEFM) [77].

3.2.1.1 Energy release rate G

The starting point for the method of Griffith is a body with a flaw inside which is elastically stressed by external forces P_i and therefore contains elastic strain energy (Figure 3.1). When crack growth occurs the body is subjected to deformation which also causes the application points of the external forces to move a distance δ. Consequently the stored elastic energy is changed [77].

According to Griffith crack growth only occurs when the total energy decreases or remains constant following Equation 3.1 [77], [78].

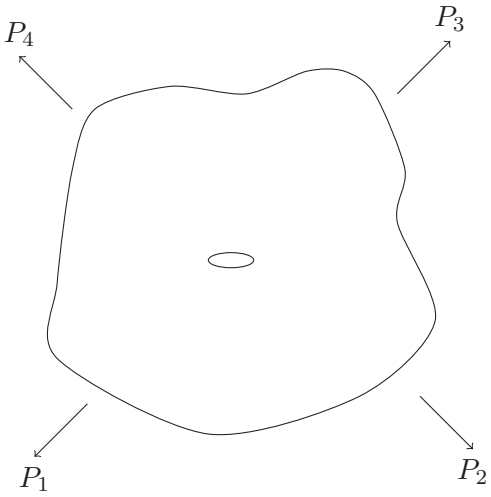

Figure 3.1: Free body diagram of a structure containing a flaw, according to [77].

$$\delta U + \delta W - \delta F \leq 0 \tag{3.1}$$

where $F = \sum P_i \cdot \delta_i$ is the potential energy due to the displacement δ_i of the application points of the external forces F_i, U is the elastically stored strain energy and W is the work needed to form new surfaces and for plastic deformation if the latter occurs. Rearranging Equation 3.1 leads to the criterion for crack growth, that the work of the external forces has to be greater than the sum of U and W according to Equation 3.2 [77], [78].

$$\delta F > \delta U + \delta W \tag{3.2}$$

In a next step, based on the work of Inglis [86], Griffith calculated that crack growth occurs if a critical stress is reached for both extrema with crack growth at constant load, and at constant displacement (Equation 3.3). Therefore it also has to be valid for all situations in between [77], [78], [87].

$$\sigma \geq \sqrt{\frac{2Ee_s}{\pi a}} \tag{3.3}$$

with the applied stress σ, the elastic modulus E, the surface energy per unit area e_s and the crack length a. Irwin introduced an equivalent approach with the energy release rate G as a measure of fracture toughness of a material [78], [88]. G is defined as energy available for an incremental crack growth and stands in direct correlation to the criterion of Griffith.

$$G = -\left(\frac{dU}{dA} - \frac{dF}{dA}\right) = \frac{\pi\sigma^2 a}{E} \tag{3.4}$$

with the crack surface A [77], [78]. The crack resistance to form new crack surfaces is called R which equals $dW = 2e_s$ from Griffith's criterion since two surfaces are generated at crack growth. Accordingly crack growth occurs when G reaches R [77], [78].

3.2.1.2 K concept

In the stress analysis of crack tips a distinction is made between three deformation modes of crack extension. These are crack opening (Mode I), in-plane shear (Mode II) and antiplane shear (Mode III) [74]–[79]. Since predominantly Mode I and II are of importance for loudspeaker membranes, the other modes are left out in the following description. Based on the work of Westergaard, the following formulation for the stress distribution in Mode I was established with the corresponding definition of the coordinate system in Figure 3.2 [77], [78], [82].

$$\begin{aligned}
\sigma_{xx} \quad & \frac{K_I}{\sqrt{2\pi r}} \cos\left(\frac{\theta}{2}\right)\left[1 - \sin\left(\frac{\theta}{2}\right)\sin\left(\frac{3\theta}{2}\right)\right] \\
\sigma_{yy} \quad & \frac{K_I}{\sqrt{2\pi r}} \cos\left(\frac{\theta}{2}\right)\left[1 + \sin\left(\frac{\theta}{2}\right)\sin\left(\frac{3\theta}{2}\right)\right] \\
\tau_{xy} \quad & \frac{K_I}{\sqrt{2\pi r}} \cos\left(\frac{\theta}{2}\right)\sin\left(\frac{\theta}{2}\right)\cos\left(\frac{3\theta}{2}\right) \\
\sigma_{zz} \quad & \begin{cases} 0 & \text{(plane stress)} \\ \nu(\sigma_{xx} + \sigma_{yy}) & \text{(plane strain)} \end{cases} \\
\tau_{xz}, \tau_{yz} \quad & 0
\end{aligned} \tag{3.5}$$

For mode II the following formulation was established [77], [78].

$$\begin{aligned}
\sigma_{xx} \quad & -\frac{K_{II}}{\sqrt{2\pi r}} \sin\left(\frac{\theta}{2}\right)\left[2+\cos\left(\frac{\theta}{2}\right)\cos\left(\frac{3\theta}{2}\right)\right] \\
\sigma_{yy} \quad & \frac{K_{II}}{\sqrt{2\pi r}} \sin\left(\frac{\theta}{2}\right)\cos\left(\frac{\theta}{2}\right)\cos\left(\frac{3\theta}{2}\right) \\
\tau_{xy} \quad & \frac{K_{II}}{\sqrt{2\pi r}} \cos\left(\frac{\theta}{2}\right)\left[1-\sin\left(\frac{\theta}{2}\right)\sin\left(\frac{3\theta}{2}\right)\right] \\
\sigma_{zz} \quad & \begin{cases} 0 & \text{(plane stress)} \\ \nu(\sigma_{xx}+\sigma_{yy}) & \text{(plane strain)} \end{cases} \\
\tau_{xz}, \tau_{yz} \quad & 0
\end{aligned} \tag{3.6}$$

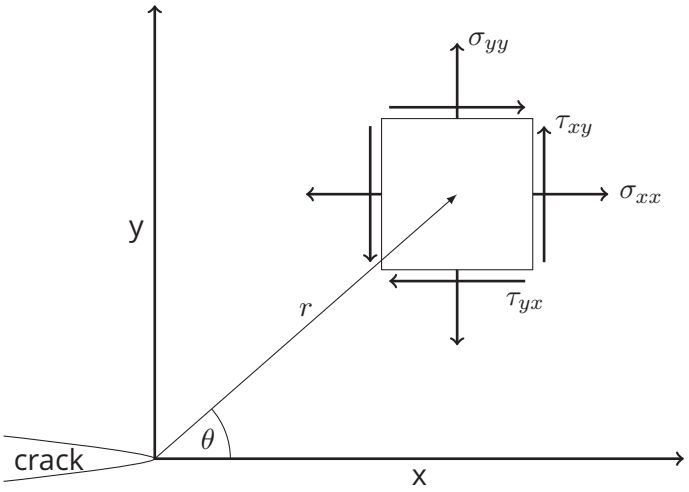

Figure 3.2: Coordinate system starting directly at the crack tip with the z-axis normal to the page, according to [78].

with the stress intensity factor K which is a measure for the amplification of the global stress field directly at the crack tip and the Poisson's ratio ν. The stress varies proportionally with $1/\sqrt{r}$ and becomes infinite directly at the crack tip which is therefore defined as stress singularity. Considering a mixed mode stress state, the individual contributions add up to the total stress:

$$\sigma_{ij}^{total} = \sigma_{ij}^{I} + \sigma_{ij}^{II} + \sigma_{ij}^{III} \tag{3.7}$$

In the crack plane ($\theta = 0$) Equation 3.5 shortens to following relationship:

$$\sigma_{xx} = \sigma_{yy} = \frac{K_I}{\sqrt{2\pi r}} \qquad \text{and} \qquad \tau_{xy} = 0 \tag{3.8}$$

Whereas in proximity of the crack tip the stress field is defined by the stress singularity, stresses remote from it are governed by the global boundary conditions. Consequently Equations 3.5 to 3.8 are only valid in the zone dominated by the stress singularity. Since with the knowledge of K_I it is possible to completely characterize the crack tip conditions, it is also possible to define a critical value where failure occurs at a critical combination of stress and strain. This critical stress intensity K_c is used as the measure for the fracture toughness of a material [78].

In order to determine K, the load and boundary conditions and the geometry of a structure have to be determined. For simple cases, closed form solutions are available in the literature [78], [89]. The basic case is a through crack in an infinite plate in pure mode I conditions for which the following relation was established [78]:

$$K_I = \sigma\sqrt{\pi a} \tag{3.9}$$

If a through crack is aligned at a certain angle $\beta \neq 0$ to the stress axis, combined Mode I and II occurs at the crack tip. This also may be the case in an anisotropic polymer film when the stress axis does not coincide with the machine direction of the film. By tilting the coordinate system into the crack plane this problem resolves into normal and shear components. The stress intensity factors for both mode I and II for an angled through crack in an infinite plate follow as [78]:

$$K_I = \sigma_{y'y'}\sqrt{\pi a} = \sigma\cos^2\beta\sqrt{\pi a} \tag{3.10}$$

$$K_{II} = \tau_{x'y'}\sqrt{\pi a} = \sigma\sin\beta\cos\beta\sqrt{\pi a} \tag{3.11}$$

Generally for all cases K is described in the form given in Equation 3.12 with Y as a dimensionless constant depending on geometry and load conditions [78], [87]. For the case of an infinite plate with a through crack under tensile load perpendicular to the crack plane (pure Mode I) $Y = 1$ [78].

$$K_{(I,II,III)} = Y\sigma\sqrt{\pi a} \tag{3.12}$$

3.2.1.3 Interrelation between G and K

Within the framework of linear elastic fracture mechanics (LEFM) two measures of fracture toughness were defined with the energy release rate G and the stress intensity factor K. The first describes the global loss in potential energy due to an incremental crack growth, the latter defines the local stress distribution in proximity of the crack tip. Irwin has shown that for linear elastic materials the following relationship between G and K is valid [78], [84].

$$G = \frac{K^2}{E} \tag{3.13}$$

with the elastic modulus E for plane stress conditions. In the case of plane strain conditions E has to be replaced with $E/(1-\nu^2)$ [78], [87].

3.2.1.4 Crack tip plastic zone

Linear elastic fracture mechanics (LEFM) predict the stresses to reach infinity at a infinitely sharp crack tip. Since real materials are not capable of bearing infinite stresses and their crack tips have finite sizes different approaches were introduced to overcome this. Above the yield strength ($\sigma_{yy} > \sigma_{ys}$) in a material, plastic deformation occurs [78]. An estimation of the size of the plastic deformation at the crack tip for plane stress conditions was given

by Irwin through substituting σ_{ys} into Equation 3.5 [78], [90]. The forces truncated above σ_{ys} which cannot be carried in a real material then are redistributed in the plastic zone for which the first estimation is corrected and leads to the known expressions for the plastic zone sizes in plane stress conditions (Equation 3.14). In plane strain conditions due to the triaxial stress state, yielding is hindered which leads to smaller plastic zone sizes (Equation 3.15) [78].

$$\text{plane stress} \qquad r_p = \frac{1}{\pi} \cdot \left(\frac{K_I}{\sigma_{ys}} \right)^2 \tag{3.14}$$

$$\text{plane strain} \qquad r_p = \frac{1}{3\pi} \cdot \left(\frac{K_I}{\sigma_{ys}} \right)^2 \tag{3.15}$$

where r_p is the plastic zone size for plane stress and plane strain conditions and σ_{ys} is the yield stress [76], [78], [90], [91]. Dugdale proposed the strip-yield model where at the crack tips of a slender through crack, crack closing yield stresses occur. For this case the plastic zone size is calculated according to Equation 3.16.

$$\text{Dugdale model} \qquad l_c = \frac{\pi}{8} \cdot \left(\frac{K_I}{\sigma_{ys}} \right)^2 \tag{3.16}$$

where l_c is the length of the plastic zone [78], [92].

3.2.1.5 Plane stress/plane strain

In the interior of a material in proximity to the crack tip, stresses normal to the crack plane are significantly higher than in remote regions. Thus in this region the material tries to contract but is hindered by the surrounding material. This leads to the occurrence of stress components in the thickness direction σ_{zz} and therefore a triaxial stress state which is commonly referred as ”plane strain” stress state. In regions near the surface the hindrance, and therefore also σ_{zz} decreases which leads to low triaxiality. But pure plane

stress conditions are only found directly at the surface as schematically shown in Figure 3.3 [78].

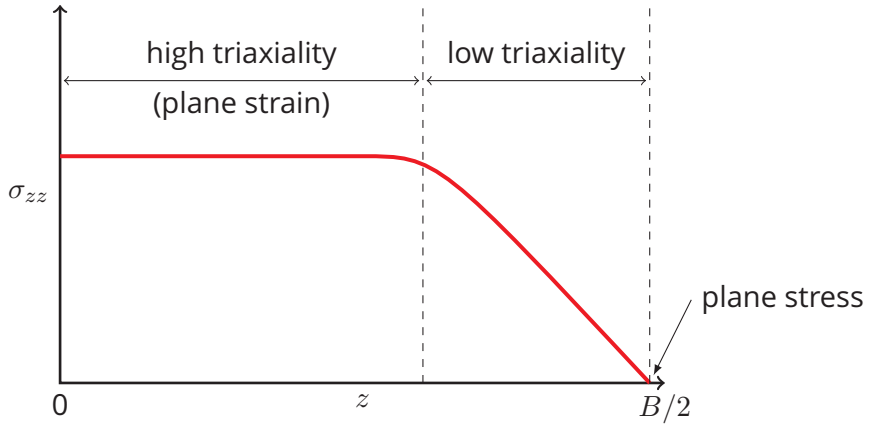

Figure 3.3: Schematic diagram of the stress component in thickness direction σ_{zz} as function of the position relative to the thickness in proximity of the crack tip, according to [78].

This additional stress component σ_{zz} leads to a higher load at the crack tip. As a result in thick structures where the zone with high triaxiality dominates the fracture behavior lower fracture toughness values are measured than in thin structures [78]. Since as long as the triaxial stress state dominates the fracture toughness it stays constant and therefore is regarded as a material parameter in academic research, K_I is preferably determined at plane strain conditions [28]. The requirement for both the crack length a and the thickness t to ensure valid plane strain conditions according to equation 3.17 was found empirically by Brown and Srawley and is also mentioned as a requirement in ASTM E399 and ASTM D5045 [23], [28], [75], [78], [87], [93]–[95].

$$a, B, W - a \geq 2.5 \left(\frac{K_c}{\sigma_{ys}} \right)^2 \tag{3.17}$$

with the crack length a, the specimen thickness B, the specimen width W, the critical value of the stress intensity factor K_c and the yield stress σ_{ys}.

Since with thin films these requirements cannot be met, according to the literature it may not be possible to determine their geometry-independent plain strain fracture toughness [28], [96]. Another method to determine the region of plane strain fracture toughness is to perform thickness-dependent experiments. If a plateau with lower fracture toughness values is reached at higher specimen thicknesses, plane strain fracture dominates and the thickness-independent plane strain fracture toughness is measured [78].

3.2.1.6 Multilayer fracture mechanics

State of the art membranes for miniature loudspeakers exhibit a multilayer design in order to provide both a high fracture toughness and a good damping behavior and this has to be taken into account when describing their fracture behavior. It is thought that in the membranes crack growth starts at an inherent failure in a locally highly stressed part of the membrane. Here in just one of outer layers the threshold for crack growth may be reached first, as described in section 3.3.4.2. When further crack growth takes place, then the load may increase locally high enough in the other stiff outer layer which also may be amplified by an existing flaw in that and here another crack may nucleate. The further crack nucleation process is assumed to consume further energy and therefore increases the crack growth resistance of the films. Due to the low stiffness of the damping adhesive it is thought that here only low stresses and stress intensities below the threshold for crack growth occur. Therefore it may play only a minor role here, except that it acts as spacer between the outer layers. This configuration is called in the literature a ”crack arrester” configuration (Figure 3.4a) [75], [97]–[99]. Since this behavior is hard to test with thin films, in this theses the focus lies on the situation where a through crack already exists. Crack growth then occurs perpendicular to the thickness of the laminates as shown in Figure 3.4b. This is referred as ”crack divider” configuration in literature [75], [97]–[100].

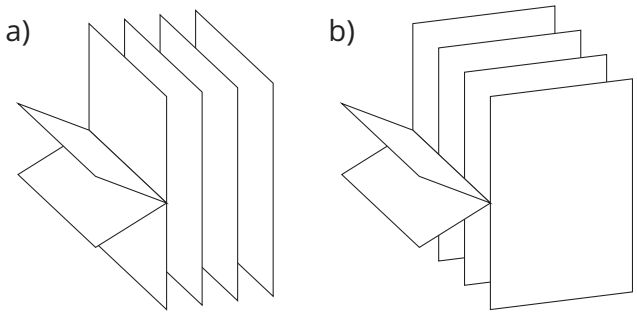

Figure 3.4: Schematic diagram of a) a crack arrester and b) a crack divider configuration, according to [75], [97]–[100].

The following description is based on the ”crack divider” configuration with an existing through crack. Whereas the stiff outer layers in the loudspeaker laminates exhibit moduli between 2 GPa to 6 GPa (see Table 2.1) at room temperature for the soft damping adhesives, moduli between 0.1 MPa to 10 MPa were measured in DMA experiments. Therefore the damping adhesives are approximately 10^3 to 10^5 times softer than the stiff outer layers. In order to simplify the analysis a pure tensile load σ_t and an equally distributed strain $\varepsilon_1 = \varepsilon_2$ in all layers throughout the thickness is assumed. Following the modulus ratio between the layers, also 10^3 to 10^5 lower stress σ_i and therefore also with the same factor lower stress intensity values K_I^i are expected in the soft adhesive damping layers than in the stiff outer layers. A schematic diagram of the laminate under tensile loads and the resulting strain ε_i, stress σ_i and stress intensity K_I^i for each layer i is shown in Figure 3.5.

As a result when a generic loudspeaker laminate is dynamically excited it is expected that at loads where in the stiff outer layers already crack growth occurs, depending on the fracture toughness of each layer, in the soft damping adhesive K_I may stay well below the threshold for crack growth. This phenomenon is called ”crack tunneling” in the literature [97]–[100]. The remaining uncracked region in the soft adhesive layer then shields the growing crack in the outer layers and consequently an apparent higher

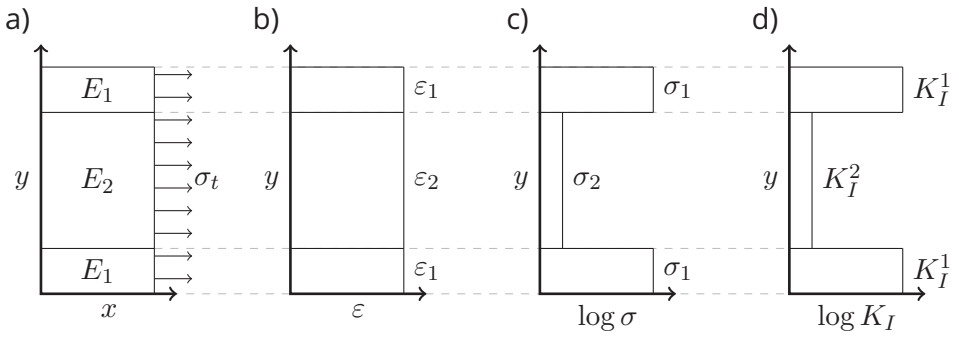

Figure 3.5: Schematic diagram of a laminate for miniature loudspeaker membranes with a symmetrical design with two stiff outer layers of high modulus E_1 of 2 GPa to 6 GPa and a soft adhesive layer with a low modulus E_2 of 0.1 MPa to 10 MPa with a) an overview of the laminate design, b) an evenly distributed strain ε_i in all layers under predominant tensile deformation σ_t, c) the resulting distribution of stresses σ_i due to the differences in the modulus E_i of the different layers and d) the resulting stress intensities K_I^i due to the differences in the stress distribution.

fracture toughness is obtained which is referred as ”crack bridging”. An estimation of the shielding contribution caused by crack bridging is obtained by a weight function method as shown in Equation 3.18 [97], [99], [101]–[106].

$$K_b = \int_L \sigma(x) h(a,x) \mathrm{d}x \tag{3.18}$$

with the traction as a function of the distance behind the crack tip $\sigma(x)$, the weight function $h(a,x)$ and the length of the bridging zone L [97]–[99]. Here the closing forces due to the bridging ligaments are integrated over the bridging zone length using a weighting function which appropriately weights the traction forces for each point behind the crack tip x depending on the specimen geometry, as shown in Figure 3.6 for a crack arrester configuration [98]. Consequently for a crack divider configuration L spans from the crack tip in the brittle layer back to the crack tip in the ductile layer in which crack growth has lagged behind.

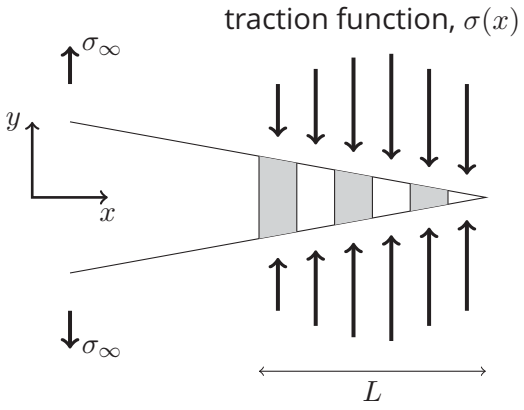

Figure 3.6: Schematic diagram of the model to predict the shielding contribution due to crack bridging with the external stress σ_∞ for a crack arrester configuration, according to [98].

The apparent fracture toughness K_{app} is obtained by superposing the shielding contribution K_b onto the intrinsic fracture toughness K_0 of the stiff outer layers according to Equation 3.19 [97]–[99].

$$K_{app} = K_0 + K_b \tag{3.19}$$

For a first estimation a constant traction over the ligament can be taken by replacing $\sigma(x)$ with a constant function $f\sigma_{ys}$, with the reinforcement volume fraction f and the constrained yield stress σ_{ys} [97], [107]. The stiffness difference between the stiff outer and the soft damping layers also might lead to delamination stresses normal to the thickness direction of the laminates. Delamination processes are described theoretically in the following section.

3.2.2 Delamination

Kinloch, Moore, Williams and coworkers established a concept for the description of delamination processes via the adhesive fracture energy G_A which is based on a energy balance as follows:

$$G_A = \frac{1}{B}\left(\frac{\mathrm{d}U_{ext}}{\mathrm{d}a} - \frac{\mathrm{d}U_s}{\mathrm{d}a} - \frac{\mathrm{d}U_{dt}}{da} - \frac{\mathrm{d}U_{db}}{\mathrm{d}a}\right) \tag{3.20}$$

with the width of the specimen B, the external work $\mathrm{d}U_{ext}$, the stored strain energy in the peeling arms $\mathrm{d}U_s$, the energy dissipated during irreversible tensile deformation of the peeling arms $\mathrm{d}U_{dt}$ and the energy dissipated during irreversible bending of the peeling arms near the peel front $\mathrm{d}U_{db}$ [108]–[115]. Generally peeling is related to breaking of bonding forces. In the macroscopic conceptual description of the peeling process this is ascribed to either adhesion, cohesion or a mixture of both. Since on the microscopic scale the crack runs through matter, the peel fracture toughness in reality has to be always ”cohesive” according to Moore and Williams [111]. The first term in Equation 3.20 is related to the kinetic energy in the moving peel arms which could be eliminated by performing a slow peel test. The next term U_S relates to the stored strain energy in the peel arms which stands in a reciprocal relation to the thickness of the peel arms [111].

For the theoretical case of a peel arm with infinite modulus and therefore where strain energy is negligible and also purely elastic bending deformation occurs, the adhesive fracture energy is calculated as follows:

$$G_A = G_A^{\infty E} = \frac{P}{B}\left(1 - \cos\theta\right) \tag{3.21}$$

with the peel force P, the thickness of the laminate B and the peel angle θ [109], [111]. Since in reality this is not the case, terms of irreversible tensile deformation G_A^{eb} and irreversible bending deformation G_A^{db} also have to be taken into account, as shown in Equations 3.22 to 3.25 [111].

$$G_A = G_A^{eb} - G_A^{db} \tag{3.22}$$

where (3.23)

$$G_A^{eb} = \frac{P}{B}(1 + \varepsilon - \cos\theta) - h\int_0^{\varepsilon} \sigma \mathrm{d}\varepsilon \tag{3.24}$$

$$G_A^{db} = \frac{1}{B}\frac{\mathrm{d}U_{db}}{\mathrm{d}a} \tag{3.25}$$

In order to account for all terms, two experiments have to be performed:

1. a peel test where the peel angle is controlled,
2. a tensile test of a peel arm up to fracture [111].

For a T-peel test additional factors have to be considered. If the peel arms exhibit different stiffnesses, the peel angle will take the angles θ and $180 - \theta$, respectively, as shown in Figure 3.7 where peel arm 2 is stiffer. Since there

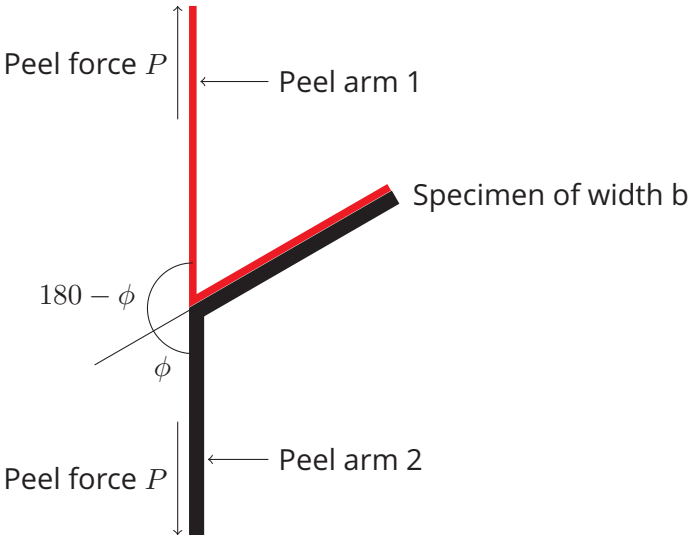

Figure 3.7: Schematic diagram of a T-peel test with a stiffer lower peel arm 2 and the resulting peel angle θ, according to [111].

are two peels arms in the T-peel test the adhesive fracture energy splits up into two parts, each for one peel arm (Equation).

$$G_A = G_A^1 + G_A^2 \tag{3.26}$$

$$G_A^1 = G_A^{\infty E} = \frac{P}{B}(1 + \cos\theta) \tag{3.27}$$

$$G_A^2 = G_A^{\infty E} = \frac{P}{B}(1 - \cos\theta) \tag{3.28}$$

The terms for elastic corrections and dissipated energy also split up to account for the presence of two peel arms as follows:

$$G_A^1 = \left(G_A^{eb}\right)^1 - \left(G_A^{db}\right)^1 \tag{3.29}$$

$$G_A^2 = \left(G_A^{eb}\right)^2 - \left(G_A^{db}\right)^2 \tag{3.30}$$

3.3 Methodology

3.3.1 Objectives

The starting situation for the characterization of loudspeaker film membranes is their low thickness of about 50 µm, different damping designs and a temperature range in application from 0 °C to 60 °C and the highest loads significantly above 100 Hz. Consequently the main challenges in characterizing their fracture and fatigue behavior are the handling of the thin films, achieving an appropriate reproducibility and experiments in conditions close to application over a wide temperature range at high frequencies. The most basic method to determine fracture toughness values of materials are monotonic tests with notched specimens based on fracture mechanics. Depending on the fracture modes of a material, different concepts like LEFM (section 3.2.1) and EWF (section 2.3.2) are applicable which allow achieving first estimations for several materials within one test day. Since loudspeakers are dynamically loaded, for a detailed investigation of the fracture modes of their polymeric membranes, cyclic fatigue tests are mandatory. Whereas

with standard Wöhler tests only the total life time as a function of the applied load is observed, with fracture mechanical concepts like the fatigue crack growth curves information about crack growth kinetics before the ultimate break down can also be obtained [116]. By using specimens with a defined crack geometry it is possible to optimize the reproducibility. The resulting main challenges for the fracture characterization of loudspeaker membranes on the film level are:

- implementation of monotonic fracture mechanical tests to achieve a first overview of the fracture toughness of the main polymeric film types,
- implementation of cyclic fatigue tests based on:
  - a Wöhler test to achieve an insight into the load dependence of the total lifetime,
  - a fatigue crack growth (FCG) test to track the crack growth kinetics.
- achieving an appropriate reproducibility,
- performing experiments at application-near conditions over a wide temperature range and high frequencies.

3.3.2 Specimen geometries

Two different specimen geometries were used in this thesis, double edge notched tension (DENT) and center cracked tension (CCT) specimens as shown in Figure 3.8. Both were prepared by cutting strips using a commercially available roll cutter. The double edge notches were brought in symmetrically using templates of glass with a predefined crack length and razorblades as shown in Figure 3.9. The center cracks were cut using an optical microscope and a scalpel. The calculation of the stress intensities K_I (Equations 3.31) was based on the appropriate geometry factors with

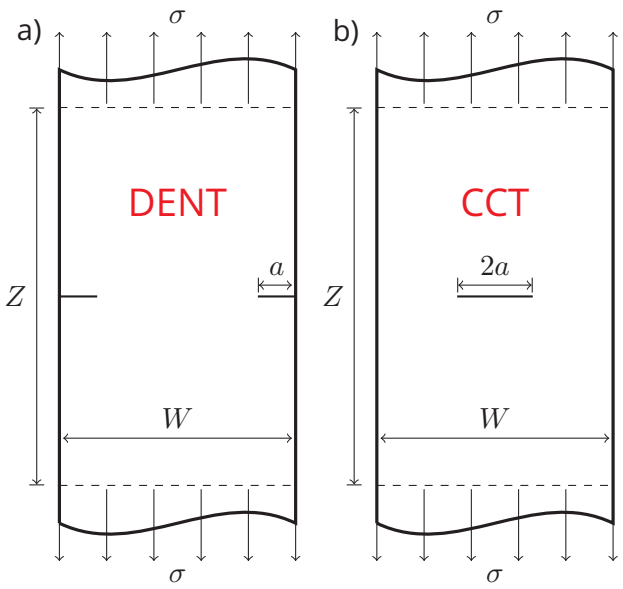

Figure 3.8: Schematic of the specimen geometries with a) the double edge notched tension (DENT) and b) the center cracked tension (CCT) geometry, according to [89].

Equation 3.33 for DENT specimens and Equation 3.34 for CCT specimens [78], [89], [117]–[119].

$$K_I = \sigma\sqrt{\pi a} \cdot Y_I(\alpha) \tag{3.31}$$

$$\alpha = \frac{2a}{W} \tag{3.32}$$

$$Y_I^{DENT} = \left(1 + 0.122cos^2\left(\frac{\pi\alpha}{2}\right)\right)\sqrt{\frac{2}{\pi\alpha}\tan\left(\frac{\pi\alpha}{2}\right)} \tag{3.33}$$

$$Y_I^{CCT} = \sqrt{\sec\left(\frac{\alpha\pi}{2}\right)} \cdot \left(1 - 0.025\alpha^2 + 0.06\alpha^4\right) \tag{3.34}$$

3.3.3 Monotonic fracture

For the monotonic fracture toughness tensile tests with notched specimens are performed and a critical load F_Q is determined. For brittle materials with only low nonlinear elasticity F_{max} is taken as F_Q. Polymers with viscoelastic

Figure 3.9: Templates made of glass for the preparation of DENT specimens with a defined crack length of 0.5 mm.

and strong ductile behavior exhibit linear behavior only over a very narrow displacement range thus the critical load for them is defined as the intersection of the load-displacement curve with the 5 % secant line. This is a line from the origin with a slope of 95 % of the initial elastic loading slope as shown in Figure 3.10 [78], [94], [116].

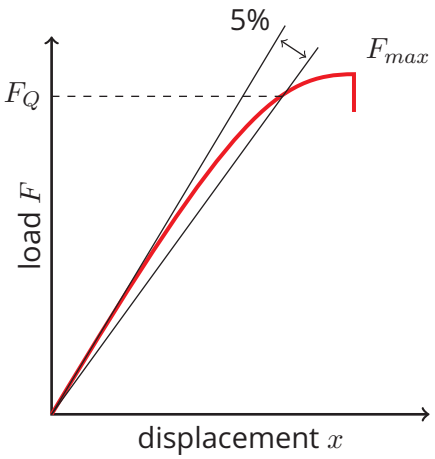

Figure 3.10: Schematic of the evaluation of the critical load F_Q, according to [78], [94].

With the specimen geometry known, the critical fracture toughness K_{IC} then can be calculated according to Equation 3.12. In order to obtain a valid

plane strain fracture toughness according to ASTM E399 the requirements for the crack length a, the specimen width B and the ligament length $W - a$ in Equation 3.17, the ratio of the crack length to the specimen width a/W in Equation 3.35 and the ratio between the critical and maximum load in Equation 3.36 have to be met [78], [94], [116]. With thin films the requirements in Equation 3.17 cannot be reached and therefore instead the plane stress fracture toughness K_c is calculated [120].

$$0.45 \leq \frac{a}{W} \leq 0.55 \tag{3.35}$$

$$\frac{F_{max}}{F_Q} \leq 1.1 \tag{3.36}$$

The tests for this thesis were performed with DENT specimens on a universal test machine Zwick Z010 (Zwick/Roell GmbH & Co. KG, Ulm, DE) with a 500 N load cell and unperforated clamps to prohibit failure of the specimens near the clamps. Double edge notched tension (DENT) specimens with 15 mm $\times$ 75 mm $\times$ 3.5 mm widths $W\times$ clamping length $Z\times$ crack length a were prepared as described in section 3.3.2. The experiments were conducted at standard conditions and a cross head speed of 100 mm min^{-1}. Critical stress intensities K_{IC} were then calculated from force F - displacement x curves according to Equation 3.31 to 3.33 [89], [117].

3.3.4 Cyclic fatigue

Since polymer membranes in miniature speakers have to fulfill their service life under cyclic loads at high frequencies, it is necessary to also determine their failure modes under cyclic fatigue loads in order to obtain a detailed insight. In contrast to monotonic loads, material failure under cyclic loads occurs at significantly lower stress levels than their monotonic strength [116], [120]. The schematics of a sinusoidal fatigue load over time is shown in Figure 3.11 with an indication of the most important parameters with the stress maximum σ_{max}, the stress minimum σ_{min}, the mean stress σ_m and

the stress amplitude $\Delta\sigma$. In order to characterize the fatigue behavior of

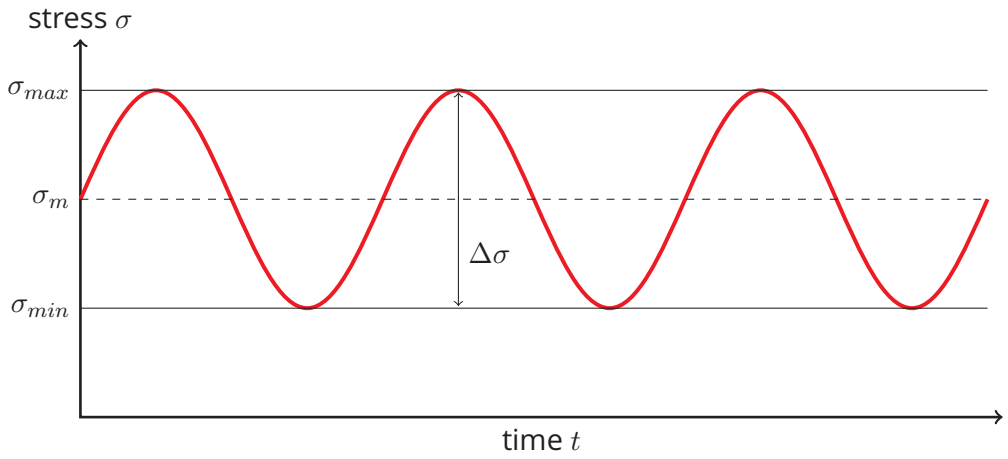

Figure 3.11: Schematic of a cyclic fatigue load σ as function of time t, according to [75], [116], [121], [122].

materials two main concepts were established. In the stress based approach, explained in section 3.3.4.1 the time to failure is determined as a function of the applied load. Section 3.3.4.2 covers the fracture mechanical approach where the crack growth kinetics are traced. For a better understanding some parameters have to be defined first:

cyclic stress range	$\Delta\sigma = \sigma_{max} - \sigma_{min}$	(3.37)
mean stress	$\sigma_m = (\sigma_{max} - \sigma_{min})/2$	(3.38)
stress ratio	$R = \sigma_{min}/\sigma_{max}$	(3.39)

with the maximum and the minimum stress level σ_{max} and σ_{min}, respectively [75], [116], [121], [122].

3.3.4.1 Stress based approach

In 1860 Wöhler first described the load dependence of the service life of railroad car wheels [116], [123]. The diagram in which the relationship

between the magnitude of a cyclic load and the cycles to failure is depicted, therefore, is called Wöhler diagram. A schematic description is shown in Figure 3.12. Here an increased fatigue strength shows as a shift of the curve

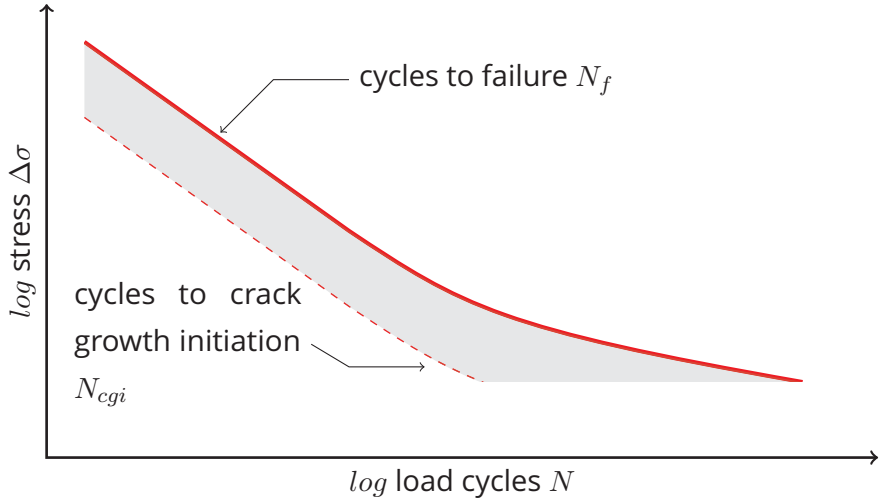

Figure 3.12: Schematic of a Wöhler curve with the cycles to crack growth initiation N_{cgi} and cycles to failure N_f as function of the stress $\Delta\sigma$, according to [75], [116].

to higher endurable loads at higher cycles to failure. It was observed that for most materials over the so called finite life fatigue strength in a half- or double logarithmic diagram, a linear relationship can be found. One of the most used mathematical descriptions of the finite life fatigue strength was introduced by Basquin in 1910 in the following form:

$$\log N_f = a - b \cdot \log \sigma \tag{3.40}$$

with the fit parameters a and b [121], [124], [125]. At lower stress levels for ferrous metals, a limit can be determined under which no failure occurs. For non-ferrous metals and polymers often only a flattened area at lower levels may be found [116]. Commonly fatigue is seen as a three-stage process

starting with an area before which no crack growth occurs, which is marked in Figure 3.12 with the cycles to crack growth initiation N_{cgi}. This is followed by the crack propagation region and final failure marked by the line for cycles to failure N_f. In the presence of flaws, the initiation time may be shortened significantly [75].

Since fatigue tests often show significant scatter, several statistical methods were introduced which consider both the planning of the experiments and the analysis of the results. Standard methods for Wöhler-tests are covered in several standards such as ASTM E 739 and DIN 50100 [122], [125]. In this thesis the $\arcsin\sqrt{P}$-method after Dengel was applied since it provides advantages in both the number of experiments needed at each load level and its statistical robustness [126]–[128]. Wöhler tests were done both as a function of the load level $\Delta\sigma$ and/or temperature T in order to clarify different effects. For both, at least three experiments at each of three load or temperature levels were done.

In order to obtain a more detailed picture of the fatigue behavior of the films, both the cycles to failure N_f and the cycles to crack growth initiation N_{cgi} were determined. This was done by evaluating the onset of the deviation of the strain span $\Delta\varepsilon$ ($\Delta\epsilon = \epsilon_{max} - \epsilon_{min}$), as shown in Figure 3.13, which was then double-checked with an optical documentation of crack growth. The scatter in the strain span $\Delta\varepsilon$ in Figure 3.13 was caused by the resolution limit of the displacement sensor of the testing machine. More details regarding the experimental procedure are explained in section 3.3.5.

3.3.4.2 Fracture mechanical approach

In fracture mechanics it is assumed that every structure contains a certain number of flaws of finite size. Thus the flaws act as sites of stress concentration and therefore, when a threshold stress intensity ΔK_{th} is reached, as an initial point for crack growth as explained in section 3.2.1 [116]. Under cyclic

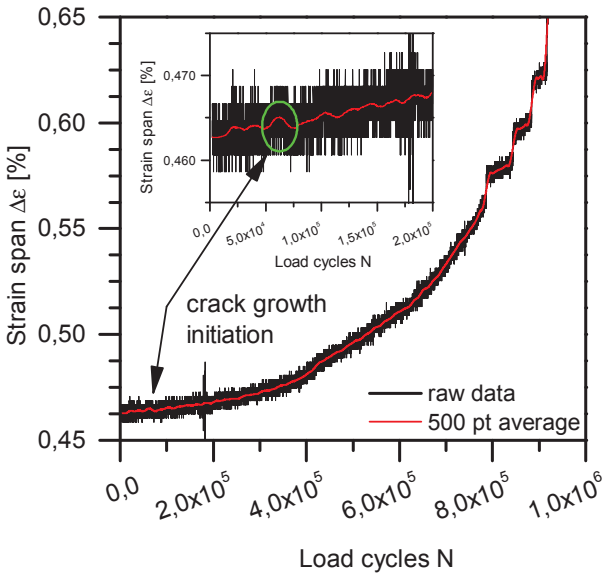

Figure 3.13: Evaluation of the cycles to crack growth initiation N_{cgi} via the onset of the deviation of the strain span $\Delta\varepsilon$ for a PC film at $\Delta\sigma$=12.87 MPa.

loading $\Delta K = K_{max} - K_{min}$ acts as the driving force for crack growth. The crack growth rate da/dN then is described as a function of ΔK, for which Paris and Erdogan found the following form empirically:

$$da/dN = A \cdot \Delta K^m \tag{3.41}$$

in which da/dN is the crack growth rate, A and m are material constants that depend on various conditions such as the material and environment and test conditions [74], [75], [78], [116], [129], [130]. A schematic diagram of the crack growth rate da/dN as a function of the stress intensity span ΔK is shown in Figure 3.14 [116].

Generally the crack growth behavior is divided into three sections. Region I marks the threshold region. At lower values than ΔK_{th} no crack growth occurs. This is followed by Region II where stable crack growth occurs which is described mathematically by the power law of Paris and Erdogan

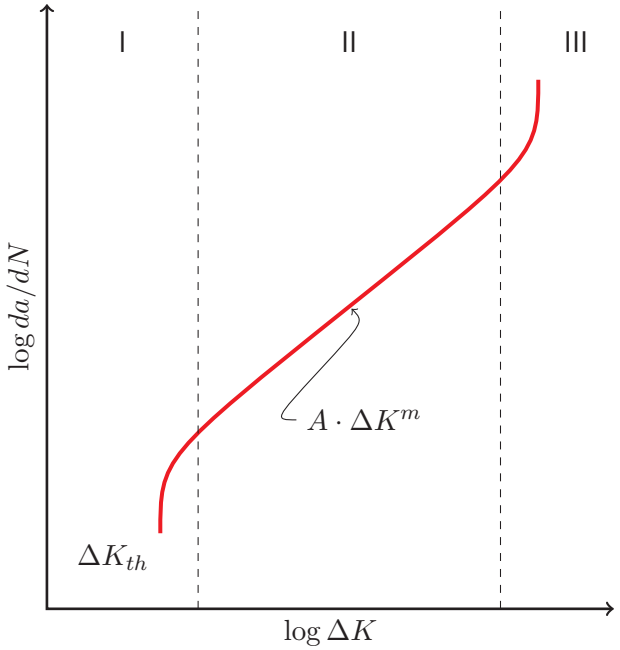

Figure 3.14: Schematic description of a fatigue crack growth (FCG) curve with the crack growth rate da/dN as function of the stress intensity span ΔK, according to [75], [116].

(Equation 3.41). Unstable accelerating crack growth with final rupture forms the upper limit within region III [75], [78], [116]. An improved material behavior shows then in a shift of the curve to lower crack growth rates da/dN at higher endurable stress intensities ΔK [120].

3.3.5 Fatigue test setup

Standard machines for fatigue tests are hydraulically driven and therefore not capable of providing high displacement amplitudes at frequencies of 100 Hz and above. Nevertheless these requirements have to be fulfilled in order to perform fatigue tests with thin polymeric loudspeaker films with thicknesses down to 4.5 µm at conditions near the application. To overcome this an electrically driven fatigue test, a Bose 3230 (Bose Corp., Eden Prairie, USA) was used (Figure 3.15). In order to prevent the thin films

Figure 3.15: Fatigue test setup consisting of an electrically driven fatigue test machine Bose 3230 with special unperforated lightweight aluminum clamps, an optical system PixeLink B959 and high output LEDs.

from failure due to clamping conditions, unperforated clamps were designed. Additionally, to enable high frequency tests for which low moving masses are required, these were made of aluminum (Figure 3.16). As specimen

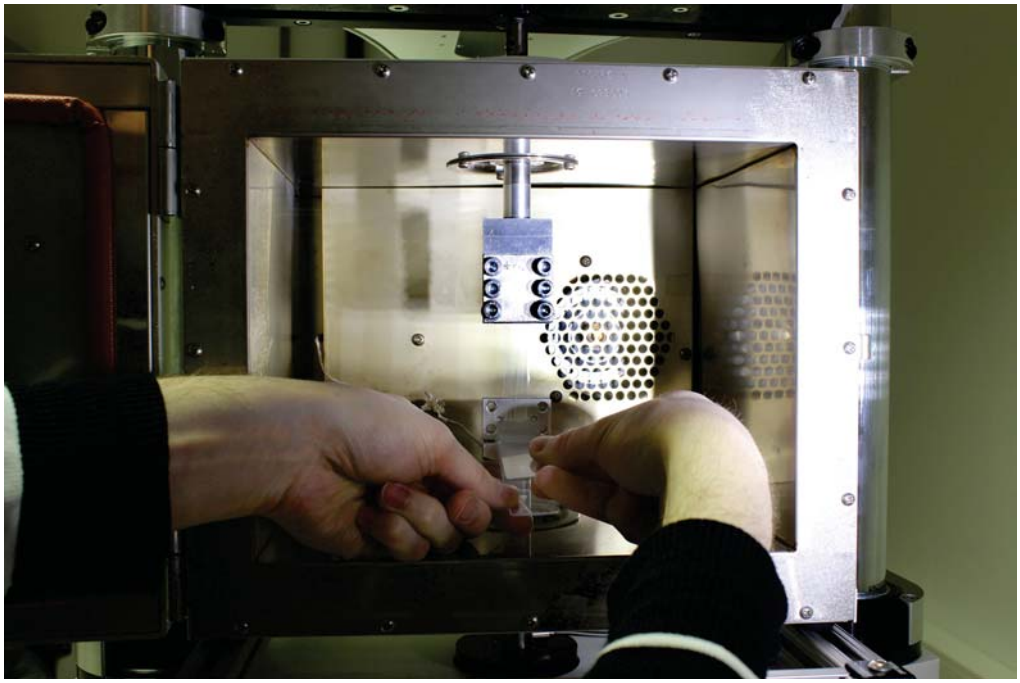

Figure 3.16: Method to clamp and align the thin films properly to the load axis by attaching a small piece of adhesive tape to one end of the specimen and then sticking it to the clamps by using two microscope glass slides. By attaching the films to the clamps with a planar edge of the glass slide and also ensuring a perfect alignment, a uniform stress distribution is guaranteed throughout the specimen.

geometry both double edge notched tension (DENT) with a crack length a of 0.5 mm and center cracked tension (CCT) specimens with a crack length a of 1.5 mm were used with dimensions of 15 mm $\times$ 45 mm (width W x clamping length Z) according to ASTM E647 where a clamping length of at least $1.7W$ is recommended to ensure a homogeneous stress distribution in the fracture plane [131]. More details about the specimen geometries are found in section 3.3.2.

One of the most crucial factors for a successful experiment is to clamp the film strips appropriately. Here both a perfect alignment of the films to the load axis and also a uniform stress distribution in the specimens has to be ensured. Otherwise one crack will experience higher loads which results in unsymmetrical and accelerated crack growth and as a consequence results in low quality of the tests. In order to fulfill these requirements, in a first step the films are attached to the clamps and properly aligned by taking advantage of their electrostatic charge. Then they are clamped at the upper side. In order to ensure uniform stress distribution a small strip of adhesive tape is attached uniformly at the lower end of the specimen using two microscope glass slides as shown in Figure 3.16. Since the films are very thin they show ripples under tension which is therefore used to perfectly align the specimens in the setup by ensuring that the ripples are aligned in the load direction. Finally the film strip is affixed to the lower clamp with the adhesive tape and clamped by attaching the aluminum bracket. Also the thin films have to be prevented from fluttering in the clamps due to manufacturing tolerances of the clamps, which is done by attaching small pieces of paper between the clamps and the specimens.

In order to determine the crack growth kinetics, an optical system PixeLINK B959 (PixeLINK, Ottawa, CAN) and six high-output LEDs were attached to the fatigue testing machine to ensure sharp images at short exposure times (Figure 3.15). Subsequently the crack length was evaluated as function of the load cycles N and the associated crack growth rates da/dN and stress intensity ΔK were calculated using equation 3.42 and the appropriate geometry factors Y described in section 3.3.2. For the calculation of FCG curves of one specimen, approximately 30 pictures equally spaced between test begin and N_f were evaluated.

$$\frac{da}{dN} = \frac{\Delta a}{\Delta N} = \frac{a_i - a_{i-1}}{N_i - N_{i-1}} \tag{3.42}$$

When machine data of high enough quality from the fatigue tests with peak/valley load F and displacement d pairs was available, so that it was possible to calculate more detailed FCG curves. In this method, introduced by Berer and based on ISO 15850, ASTM E 647-11 and the works of Novotny and Zahnt, the dynamic specimen compliance C_{dyn} is calculated as a function of the load cycles N, according to Equation 3.43, from peak/valley load and displacement pairs, which were recorded every 1000 cycles during the tests [131]–[136].

$$C_{dyn} = |C^*| = \frac{d_{max} - d_{min}}{F_{max} - F_{min}} \tag{3.43}$$

with the absolute value of the complex dynamic compliance $|C^*|$ and the peak/valley data d_{max}, d_{min}, F_{max} and F_{min} of the dynamic displacement and the dynamic force, respectively. The goal, then, is to calibrate the compliance data of C_{dyn} vs. N to the measured crack lengths a vs. N from the optical documentation of the crack growth kinetics in order to obtain a function in the following form [132]:

$$a = \text{function}\,(C_{dyn}) \tag{3.44}$$

Based on the calculated data of crack length as a function of the load cycles a vs. N in a next step crack growth rates da/dN as a function of the stress intensities ΔK are determined. More detailed information about this method is available in [132].

3.3.6 T-Peel tests

For T-Peel tests rectangular laminated specimens are used where there is a region of unadhered material of approximately 30 mm. This was achieved by dissolving the laminates in methyl ethyl ketone for 30 min, peeling them a little apart for a length of approximately 30 mm and placing a strip of release

film in between. In a next step laminate strips with a width B of 15 mm were cut using a commercially available roll cutter. The overall length was approximately 80 mm. T-peel tests were performed also on the Bose 3230 (Bose Corp., Eden Prairie, USA) with a clamping length Z of 50 mm at a test speed of 5 mm min^{-1} for a peel length of 12.5 mm. During the tests the peel force P displacement x curves were recorded and the peel angle was measured at least three times for each experiment, one at the beginning of the peeling process, one in the middle and one near the end. For the following calculations of G_A then the average propagation peel force P and the average peel angle θ were determined. For each configuration at least two experiments were performed.

In order to correct the adhesive fracture toughness G_A for irreversible tensile and bending deformation of the peel arms, as described in section 3.2.2, stress-strain curves of the peel arms were recorded with film strips ($B \times Z$ = 15 mm $\times$ 50 mm) at a strain rate $\mathrm{d}\varepsilon/\mathrm{d}t$ of 10 % min^{-1} which corresponds to 5 mm min^{-1}. Both data sets of the peel and the tensile curves were then used in the software "IC Peel" (Imperial College London, London, UK) from the adhesion and adhesives group from the Imperial College London [137].

3.4 Results and Discussion

3.4.1 Monotonic fracture mechanical tests

Based on the findings in the literature, monotonic fracture mechanical tests were carried out, using DENT specimens with three different monolayer films, two monolayers with symmetrically attached adhesive damping layers and five 5-layer laminates, all of which are state of the art in miniature loudspeakers. For the monolayer films a 10 µm solvent cast polyarylate (PAR) film, a 12 µm extruded polyethylene therephthalate (PET) film and a 20 µm extruded polyetheretherketone (PEEK) film were chosen as test

materials. The two tested 3-layer films consisted of 12 µm extruded PET and 12 µm polyethylennaphtalate (PEN) films, respectively, and symmetrically attached adhesive damping layers with a thickness of 9 µm on each side. The 5-layer laminates featured a symmetrical sandwich design with the outer layers consisting of the same solvent cast 10 µm PAR films as the tested monolayers, varying 12 µm extruded PET and PEN middle layers and varying 9 µm damping adhesives in between. An detailed overview of the test materials is given in Table 3.1.

Table 3.1: Test materials with an overview of the polymers and adhesives in each layer and their corresponding thicknesses.

Laminate	Layer type			Thickness t [µm]		
	1/5	2/4	3	1/5	2/4	3
1L$_{10}$-PAR$_{10}$	PAR	-	-	10	-	-
1L$_{12}$-PET(a)$_{12}$	PET(a)	-	-	12	-	-
1L$_{20}$-PEEK$_{20}$	PEEK	-	-	20	-	-
3L$_{30}$-A$_9$PET(b)$_{12}$	-	adhesive A	PET(b)	-	9	12
3L$_{30}$-B$_9$PEN$_{12}$	-	adhesive B	PEN	-	9	12
5L$_{50}$-PAR$_{10}$C$_9$PET(b)$_{12}$	PAR	adhesive C	PET(b)	10	9	12
5L$_{50}$-PAR$_{10}$D$_9$PET(a)$_{12}$	PAR	adhesive D	PET(a)	10	9	12
5L$_{50}$-PAR$_{10}$E$_9$PET(c)$_{12}$	PAR	adhesive E	PET(c)	10	9	12
5L$_{50}$-PAR$_{10}$F$_9$PET(c)$_{12}$	PAR	adhesive F	PET(c)	10	9	12
5L$_{50}$-PAR$_{10}$G$_9$PEN$_{12}$	PAR	adhesive G	PEN	10	9	12

DENT specimens were cut along the machine direction of the films with 15 mm $\times$ 75 mm $\times$ 3.5 mm width $W\times$ clamping length $Z\times$ crack length a and tested at a high crosshead speed of 100 mm min^{-1} or 133 % min^{-1} as described in section 3.3.3. The high deformation rates were chosen in order to reflect the conditions in application where also high deformation rates occur due to the high frequencies. Representative individual results with the measured load F as a function of the displacement x for the test series with

monolayers and monolayers with attached damping adhesives are shown in Figure 3.17a.

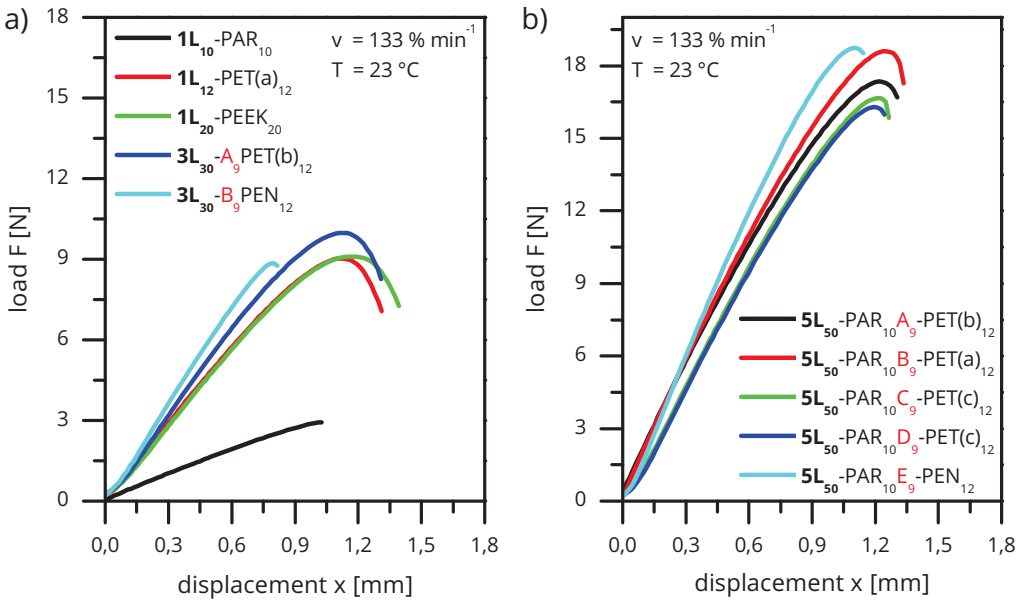

Figure 3.17: Results of monotonic fracture mechanical tests with the load F as a function of the displacement x with DENT specimen for a) monolayer films and monolayers with attached damping layers and b) 5-layer laminates.

Significant differences were found between the monolayers and the monolayer films with attached damping layers. It is worth noting that the influence of the different thicknesses of the films is not taken into account in the load/displacement curves. The PAR monofilm exhibited very linear deformation behavior with brittle fracture. **1L$_{12}$**-PET(a)$_{12}$ and **1L$_{20}$**-PEEK$_{20}$ also showed brittle fractures accompanied by small plastic deformation after the maximum load F_{max} was reached. Comparing results of the PET and PEN monolayers with attached adhesive damping layers with **1L$_{12}$**-PET(a)$_{12}$ it is quite interesting that there are only small differences. Therefore it is possible to deduce that the adhesive damping layer has only a negligible influence to the monotonic fracture behavior of the laminates. In contrast to **3L$_{30}$**-A$_9$PET(b)$_{12}$, the PEN film showed nearly no plastic deformation whereas

the PET film featured more plastic deformation and higher F_{max}. These findings are at odds with the literature where films of the same polymer types were characterized with the concept of EWF. There these films are described to feature a predominant ductile material behavior with large plastic deformations. Consequently it has been concluded in the literature that LEFM would not be applicable for them [23], [26], [28], [30], [38], [39], [41], [42], [52], [54], [96], [138]. In the load-displacement curves for the 5-layer laminates similar results were obtained, which could be explained by the similar constituents of the laminates (Figure 3.17b). All laminates featured the same PAR outer layers and very similar PET middle layers, except of **5L$_{50}$**-PAR$_{10}$G$_9$PEN$_{12}$ with PEN as the middle layer. For all the 5-layer laminates very similar results with brittle fatigue behavior was found with only small plastic zones, hence LEFM seems applicable to describe the fracture behavior of both monolayers and multilayer laminates [78], [87].

In a next step K_{IC} values were calculated based on the load F - displacement x curves as described in section 3.3.3. Since the films behaved in a very brittle manner with only a low amount of nonlinearity, F_{max} was taken as critical load F_Q. Results for the tested films are depicted in Figure 3.18 where for the multilayer films an apparent fracture toughness $K_{IC,app}$ was calculated for the whole cross section of the specimens. Generally a very high reproducibility with only small scatter was obtained. Significant differences regarding their fracture toughness were found for the monolayer films. PAR has shown comparable results to those found in the literature, with a high reproducibility at low toughness levels [18]. The fracture toughness of the tested PEEK films exhibited values between the PAR and the **1L$_{12}$**-PET(a)$_{12}$ film and lower values than found in the literature [14], [139]–[142]. Since the 5-layer laminates consisted of two additional 10 µm thick PAR outer layers compared to **3L$_{30}$**-A$_9$PET(b)$_{12}$ and **3L$_{30}$**-B$_9$PEN$_{12}$ but featured almost the same $K_{IC,app}$ values, it was concluded that the PET and PEN middle layers dominate the fracture toughness of these 5-layer laminates.

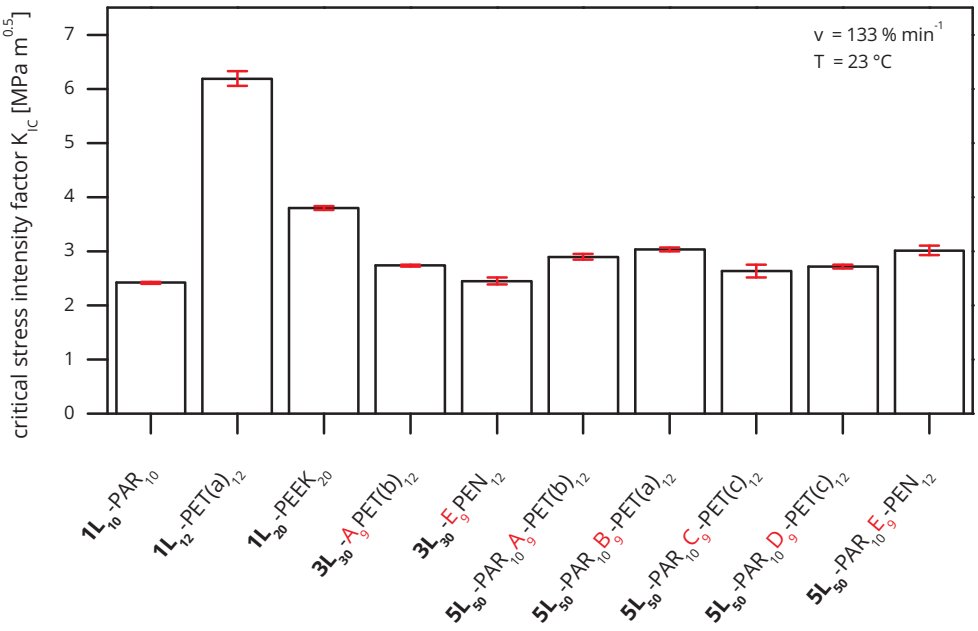

Figure 3.18: Evaluation of the critical stress intensity factor K_{IC} with DENT specimens for monolayer films, monolayers with attached damping layers and 5-layer laminates with K-values with the load averaged over the whole cross section of the films and laminates.

In Figure 3.19 results are shown with $K_{IC,app}$-values with the load calculated for the cross section without the soft damping adhesives for the 3- and 5-layer laminates. This evaluation is based on the assumption that due to the approximately 10^3 to 10^5 times lower modulus of the soft adhesive damping layers compared to the stiff outer layers, the damping layers bear only a negligible part of the load (see also section 3.2.1.6). The adhesive damping layers may therefore have only little effect on the monotonic fracture toughness of the laminates. Here both PET and the PEN films showed similar results with a small advantage for PET and a significantly higher fracture toughness than all other films, which is in good agreement with values from the literature [143]–[147]. In the comparison between results of mono- and multilayer films the multilayer laminates showed their fracture toughness at values right in between the PET films and the PAR monolayers. This verified

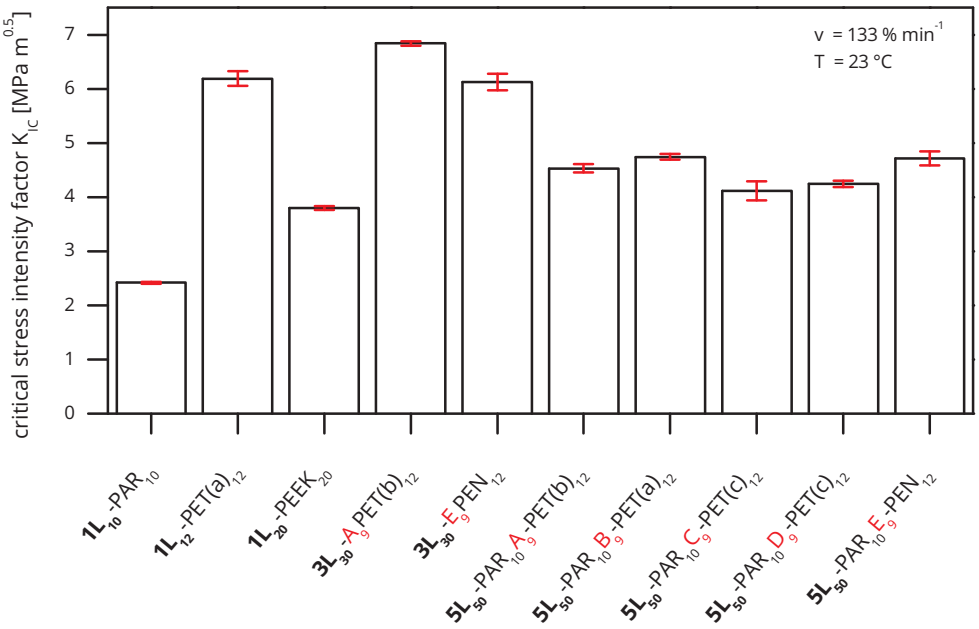

Figure 3.19: Evaluation of the critical stress intensity factor K_{IC} with DENT specimens for monolayer films, monolayers with attached damping layers and 5-layer laminates with K-values with the load calculated for the cross section without the soft damping adhesives for the 3- and 5-layer laminates.

the assumption that the adhesive damping layers bore only a negligible part of the load in monotonic tests. Furthermore it is obvious, that the PAR outer layers are the weakest part in the 5-layer laminates and therefore worsen the fracture toughness of the laminate.

The findings from the static fracture mechanical tests with only small differences between the tested 5-layer laminate stand in contrast to results of fatigue tests with miniature speakers where significant differences between these 5-layer laminates were obtained. Therefore it was subsequently concluded that a cyclic fracture mechanical test had to be made.

3.4.2 Applicability of linear elastic fracture mechanics to cyclic fatigue of polymer films

Based on findings from monotonic pretests, a fatigue test at a frequency of 100 Hz was set up to determine the fatigue behavior of thin miniature speaker films with linear elastic fracture mechanics (LEFM). In the literature LEFM is said to be not applicable for thin polymer films, in this part the applicability, LEFM for cyclic fatigue of thin polymer films is tested. One main feature of LEFM is the crack tip similitude concept. It states that the stress state in the surroundings of a crack tip are similar in both structure components and in fracture mechanics specimens and are in both cases describable by the so-called stress intensity factor K [78], [148]. The same applies to different specimen geometries. This was utilized in the present work to verify the applicability of LEFM for thin polymer films under cyclic tensile loads. If differences between the specimen geometries are found, LEFM might still be applicable but no material parameters are measured. However, it still can be used to rank materials as long as the same specimen geometry is used. Fatigue crack growth (FCG) tests with two different specimen geometries, double edge notched tension (DENT) and center cracked tension (CCT) specimens (Fig. 3.8), were performed at standard conditions and 100 Hz. The specimens were cut along the machine direction of the films with 15 mm $\times$ 45 mm $\times$ 0.5 mm (DENT) and 15 mm $\times$ 45 mm $\times$ 1.5 mm (CCT) width $W\times$ clamping length $Z\times$ crack length a. During the fatigue tests the crack growth was traced via an optical system and subsequently described via FCG curves according to the Paris law (eq. 3.41) [129].

Evidence for the applicability of LEFM is the process zone size. Therefore for each polymer film type, fatigue tests were stopped shortly after crack growth initiation. With polarization light microscopy crack tips were discernible and the process zone sizes were measured accurately. In a next step these values were compared with theoretical calculations according to the models for plane strain (eq. 3.15), plane stress conditions (eq. 3.14) and the Dugdale

model (eq. 3.16) using the measured yield strength σ_{ys} from tensile tests with each material.

Polymer films of five selected model materials were investigated. These films were produced via solvent casting and extrusion, respectively, and had thicknesses between 4.5 µm and 10 µm. First estimations of the fracture toughness of the used polymer types were obtained from the literature and the Cambridge Engineering Selector (Granta Design Ltd., Cambridge, UK). Details of the model materials are shown in Table 3.2 with material data for the glass transition temperature T_G, tensile modulus E and fracture toughness K_{IC}. If no data about the listed parameters was available for the films, generic data for the same polymer type was taken from literature.

Table 3.2: Test materials with five variations of constraining and damping layers.

Film	Polymer	Thickness t [µm]	fracture toughness K_{IC} [MPa m$^{0.5}$]
1L$_{10}$-PAR$_{10}$	PAR	10	2.42[a]
1L$_{10}$-PC$_{10}$	PC	10	2.1-2.3[b]
1L$_{7}$-PEI$_{7}$	PEI	7	2.93[c]
1L$_{10}$-PESU$_{10}$	PESU	10	3.54[c]
1L$_{4.5}$-PET(c)$_{4.5}$	PET(c)	4.5	4.8-5.3[b]

[a] Section 3.4.1 [b] Cambridge Engineering Selector (Granta Design Ltd., Cambridge, UK) [c] [14]

Fatigue crack growth (FCG) curves for PAR, PC, PEI, PESU and PET with a comparison between results with center cracked tension (CCT) and double edge notched tension (DENT) specimens are shown in Figure 3.20a) to 3.20e) with an indication of the monotonic fracture toughness K_{IC} values from Table 3.2. The crack growth kinetics were optically tracked with images shot every 1000 cycles. As a result especially at unstable crack growth before ultimate failure the image frequency was too low to record the crack

growth kinetics accurately. Therefore data points of several experiments for each material and specimen geometry, respectively, are plotted in the FCG evaluations. For DENT specimens results from start values from ΔK= 0.42 MPa m$^{0.5}$ to 0.83 MPa m$^{0.5}$ for PAR, PC, PEI and PESU films and from 1.10 MPa m$^{0.5}$ to 2.28 MPa m$^{0.5}$ for PET films were evaluated for the FCG curves. With CCT specimens for PAR and PC tests were performed at a start value of ΔK= 0.63 MPa m$^{0.5}$, for PEI and PESU at 0.45 MPa m$^{0.5}$ and for PET at 1.41 MPa m$^{0.5}$. An overview of results with DENT specimens for all tested materials is depicted in Figure 3.20f. Results with CCT specimens were left out in Figure 3.20f, since they show nearly the same picture, but would distract from the clarity of the comparison.

Three main reasons are thought to have led to partial significant scatter in the FCG evaluations. At first symmetrical crack growth was often not achieved, since already the slightest misalignment of the specimens in the fatigue setup led to asymmetrical crack growth. For instance, according to ASTM E647 in CCT specimens the crack lengths on both sides should not exceed a difference of 0.025 W [131]. Furthermore often discontinuous crack growth occurred, which led to faster crack growth rates when the crack jumped. Finally PAR and PESU showed zig-zag crack paths and therefore, according to Equations 3.10 and 3.11, also superimposed mode II loads. Strictly speaking, for these measurements the requirements of pure mode I loading for the validity of the calculations of ΔK_I according to Equations 3.31, 3.33 and 3.34 then were violated.

ΔK values before ultimate failure and K_{IC} values from Table 3.2 correlated well for all films. FCG curves with PAR, PESU and PET films showed good agreement between both specimen geometries; in contrast, PC and particularly PEI exhibited significant deviations with, in both cases, higher crack growth rates at the same stress intensities for the CCT compared to the DENT specimen geometry. PET has shown superior crack growth resistance with significantly higher stress intensities K_I at the same crack growth rates da/dN than the other films. PAR and PC showed rather similar results with

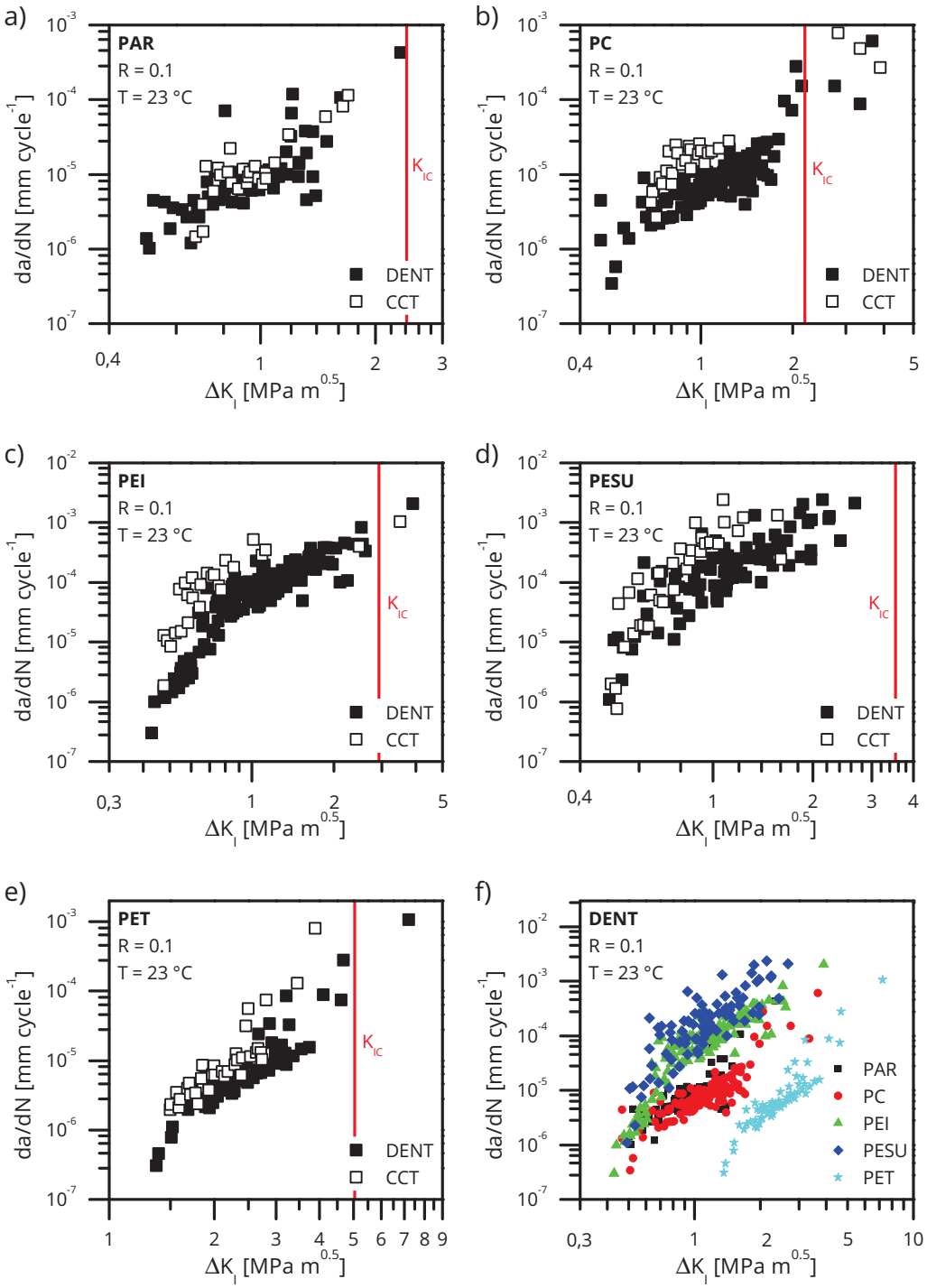

Figure 3.20: Fatigue crack growth behavior of the a) PAR, b) PC, c) PEI, d) PESU and e) PET films with results with DENT and CCT geometries and an indication of monotonic fracture toughness K_{IC} values from Table 3.2 and f) a comparison of results with DENT specimens and different films.

a lower crack growth resistance than PET for both films and with a slight advantage for PC. The lowest crack growth resistance was found for PESU and PEI with also very similar curves but with slightly higher crack growth rates and significantly higher scatter for PESU.

Based on the findings in the FCG analysis, an explanation for the deviation between curves with DENT and CCT specimens for PC and PEI films was sought. One idea was that in these two polymers the crack tip similitude concept does not apply and therefore differences in the process zone may be observable. In order to justify this hypothesis three tests were stopped with each material at the same stress intensity level for both specimen geometries soon after crack growth was discernible. Subsequently process zones sizes were measured using polarized light microscopy. Since slight deviations in the width of the specimens and the length of the cracks are unavoidable, standard deviation values for ΔK of about 0.05 MPa m$^{0.5}$ in both specimen geometries were measured. Furthermore ΔK values in the specimens were approximately 0.1 MPa m$^{0.5}$ higher for all materials in CCT specimens than in DENT specimens when the tests were stopped. Finally it has to be mentioned that overall differences in the color appearance of the micrographs is due to slightly different angles of the polarizers in order to maximize the visibility of the observed effects, but has no influence the general result. In a next step the measured values were compared to theoretical ones based on LEFM for plane stress and plane strain conditions and the Dugdale model according to eq. 3.14 to 3.16, respectively, for which yield stresses σ_{ys} were determined in tensile tests. The tensile tests were performed with the same test machine as the fatigue tests with film strips (15 mm $\times$ 50 mm, width $W\times$ clamping length Z) at a strain rate of 20 % min^{-1}.

In Figure 3.21 the optical documentation of the fatigue crack growth behavior of a PAR and a PC film with a DENT specimen at a start value of ΔK= 0.43 MPa m$^{0.5}$ is depicted. Pictures are shown for the initial state, at the cycles of crack growth initiation N_{cgi}, at the cycles of failure N_f and also two

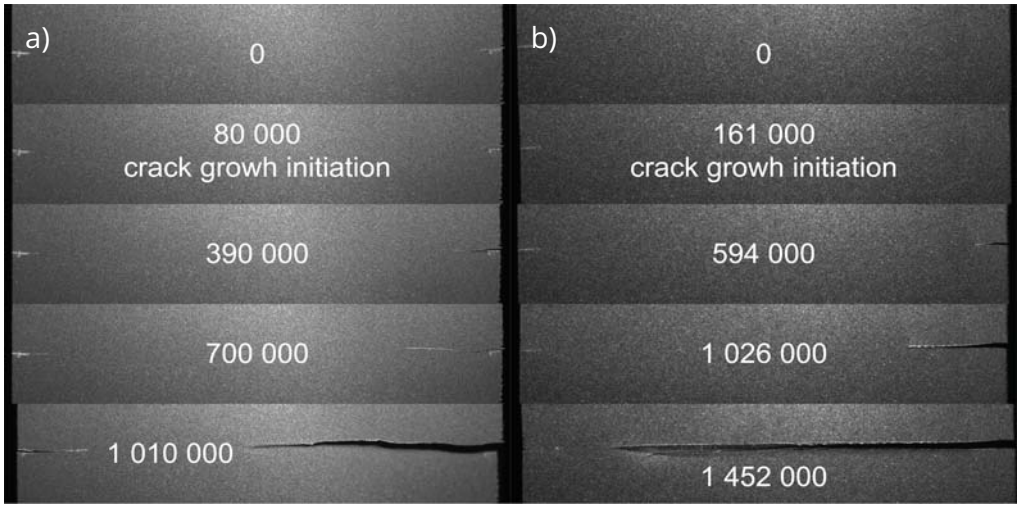

Figure 3.21: Optical documentation of the fatigue crack growth behavior of a) a PAR and b) a PC film with a DENT geometry at a start value of ΔK = 0.43 MPa $m^{0.5}$, respectively.

pictures during crack growth, which are equally spaced between N_{cgi} and N_f. For PAR a predominantly brittle fatigue behavior was found with rather coarse fracture surfaces and crack paths with a slight zig-zag pattern.

Figure 3.22 shows polarized light microscopical images with magnifications of 50x and 200x of crack tips from PAR films with a) a DENT and b) a CCT specimen, respectively, after crack growth initiation at a ΔK value of approximately 1.00 MPa $m^{0.5}$. Also in the micrographs, the crack path direction showed slight deviations. In the last 200 µm of the crack path in the DENT specimen very localized highlighted birefringence effects with a width of approximately 50 µm were found under polarized light, which were attributed to a process zone surrounding the crack tip. In the middle of the region line-like patterns along the crack plane were observed which were regarded as already broken material. Evidence for the validity of the assumption was obtained with the comparison of the theoretical plastic zone size with the measured process zone size in DENT specimens in front of the broken material (Figure 3.30a). Here the measured mean values of 60 µm fitted quite well the theoretical ones for plane stress conditions and showed only

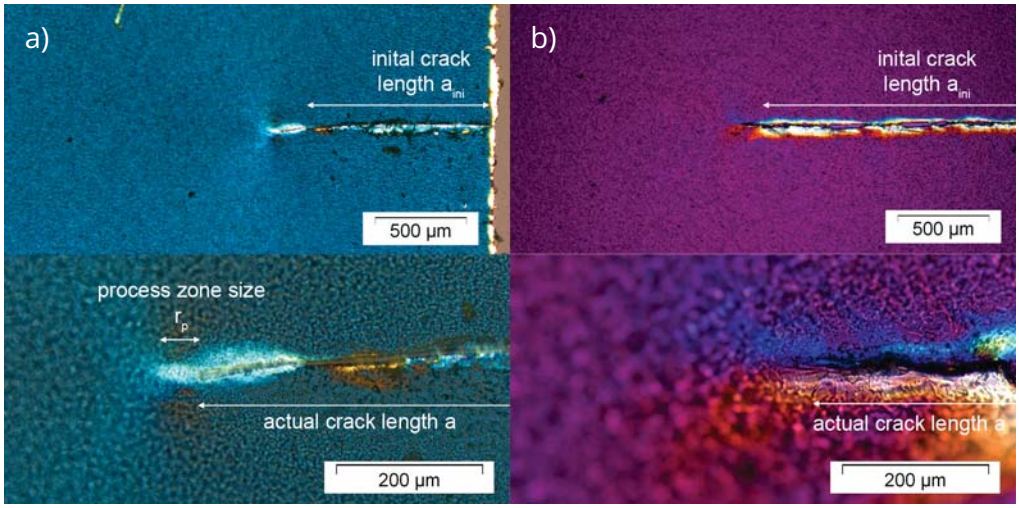

Figure 3.22: Polarized light microscopical images with magnifications of 50x and 200x of crack tips from PAR film specimens with a) a DENT and b) a CCT geometry, respectively, where the test was stopped after crack growth initiation at $\Delta K \sim 1.00\,\mathrm{MPa\,m^{0.5}}$.

minor scatter. For CCT specimens, process zone sizes could not be evaluated because the birefringence patterns gradually faded in front of the crack tips (Figure 3.30). Still the approximate shape of the birefringence effects matched well the plastic zone shapes estimated by the "dogbone" model for elastic solutions in mode I according to Anderson and Dodds et al. and plastic zones near the surface in high density polyethylene (HDPE) reported by Friedrich [78], [149], [150]. Although process zone shapes and sizes differed for both specimen geometries the evaluation of the FCG curves suggested validity of the crack tip similitude concept.

The PC films showed brittle fracture modes too, but with smoother broken surfaces than in PAR (Figure 3.21b). In micrographs of DENT specimens (Figure 3.23a) the process zone shape was analogical to that described by Dugdale and therefore was described according to the Dugdale model with the plastic zone size l_c (eq. 3.16), which fitted well with the theoretical model (Figure 3.30). This is in accordance with the literature where applicability of the Dugdale model for PC was reported [34], [151]–[155]. Similar to PAR

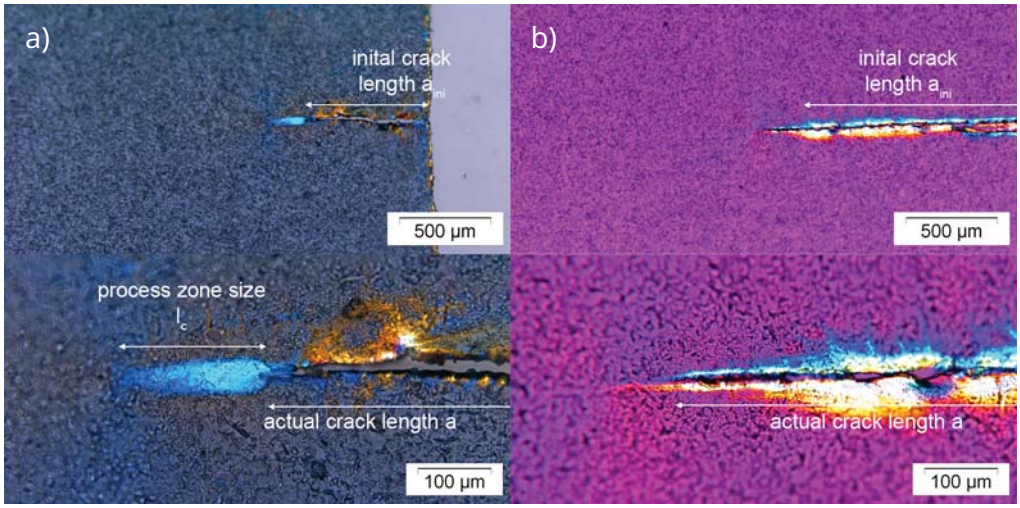

Figure 3.23: Polarized light microscopical images with magnifications of 50x and 200x of crack tips from PC film specimens with a) a DENT and b) a CCT geometry, respectively, where the test was stopped after crack growth initiation at $\Delta K \sim 1.05$ MPa m$^{0.5}$.

also in PC in the CCT specimens process zones were not discernible due to gradually vanishing birefringence effects (Figure 3.23b). This difference of the process zones between DENT and CCT specimens was regarded as the cause for the different fatigue crack growth behaviors of these two geometries with PC films. To sum up: both in the FCG curves and in the evaluation of the process zone significant differences were found for PC and therefore the applicability of the crack tip similitude concept was not verified for the characterized PC films.

The optical documentation of PEI films in Figure 3.24a) moreover has revealed a brittle fatigue behavior with crack paths almost perpendicular to the load direction. In both specimen geometries the crack path was surrounded by highlighted birefringence patterns, which also here were referred to as regions of plastically deformed material (Figure 3.25). Only a very small process zone in front of the crack tip was found with a length of 60 µm for the DENT specimens and 100 µm for the CCT specimens, which matched the theoretical size according to LEFM (Figure 3.30). The larger process

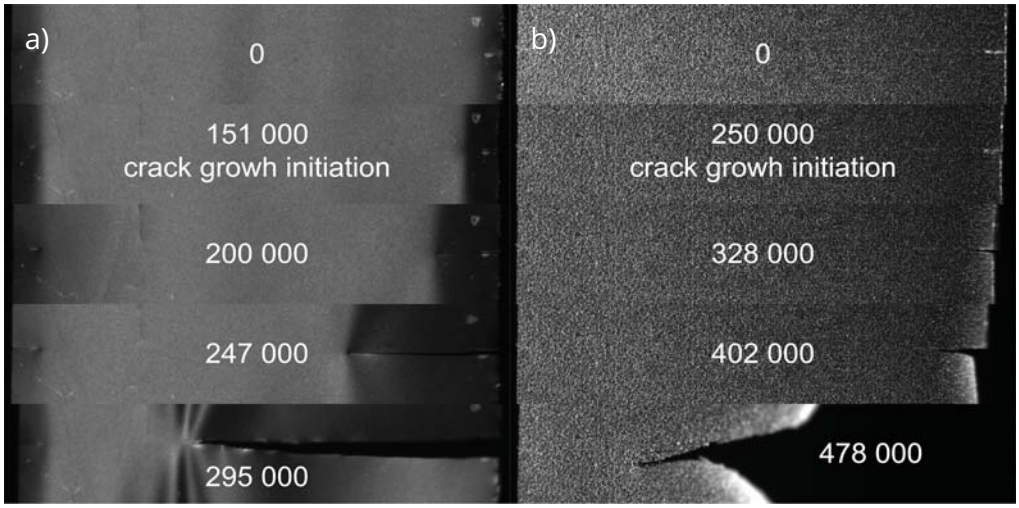

Figure 3.24: Optical documentation of the fatigue crack growth behavior of a) a PEI and b) a PESU film with a DENT geometry at a start value of ΔK= 0.43 MPa m$^{0.5}$, respectively.

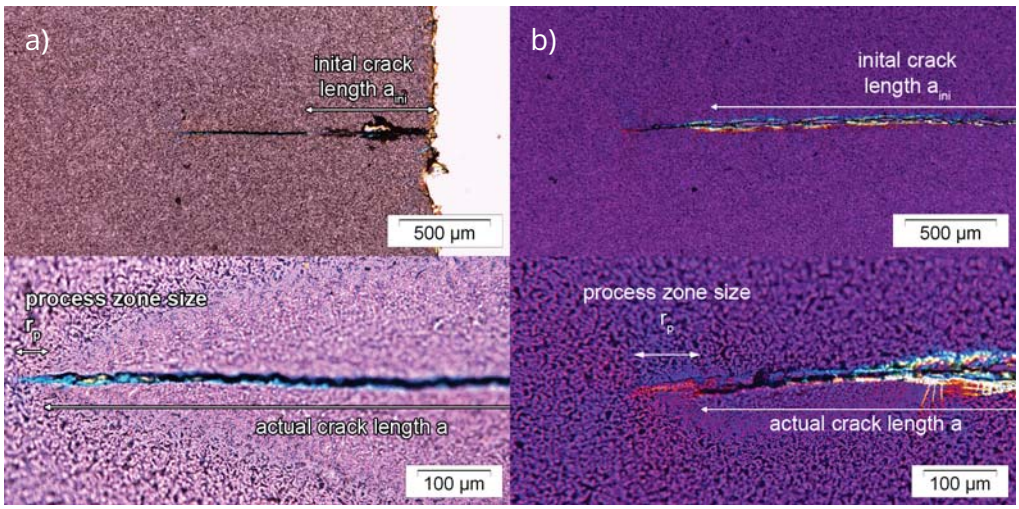

Figure 3.25: Polarized light microscopical images with magnifications of 50x and 200x of crack tips from PEI film specimens with a) a DENT and b) a CCT geometry, respectively, where the test was stopped after crack growth initiation at ΔK~1.45 MPa m$^{0.5}$.

zone sizes measured for CCT specimens contradicted the results from FCG measurements with higher crack growth rates at the same stress intensities for the CCT geometry. Although the PAR films showed nearly the same process zone sizes for both geometries, the PEI films showed significantly higher scatter, which may have caused the differences in the FCG behavior between the DENT and CCT specimen. As for the PC films, also for PEI films differences both in the FCG and the process zone size evaluation were found and therefore the applicability of the crack tip similitude concept for the PEI films was not verified.

PESU has shown the most coarse fracture surfaces of all tested films even with torn out parts in the crack path (Figure 3.24b). Both specimen geometries showed a similar behavior in micrographs with also a coarse surface structure and a very complex branched structure of the cracks (Figure 3.26). Although a defined process zone was not discernible it was always possible

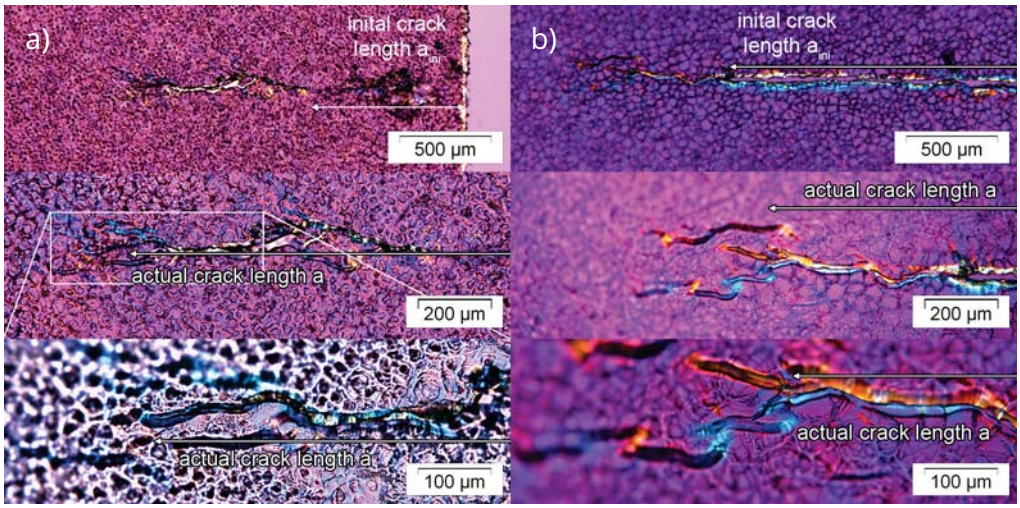

Figure 3.26: Polarized light microscopical images with magnifications of 50x, 100x and 200x of crack tips from PESU film specimens with a) a DENT and b) a CCT geometry, respectively, where the test was stopped after crack growth initiation at $\Delta K \sim 1.10\,\mathrm{MPa\,m^{0.5}}$.

to identify the crack tips. The occurrence of multiple crack fronts is also regarded as the cause for the higher scatter of PESU in FCG tests. Therefore

on the one hand the theoretical requirements of LEFM with one defined crack tip is broken for the PESU film, but on the other hand the requirement of crack tip similitude is fulfilled for both the FCG tests and the evaluation of the process zone shapes. Consequently LEFM was regarded as applicable for the PESU films.

PET films featured high crack growth resistance, but nevertheless brittle fatigue behavior under cyclic loads with crack paths strictly perpendicular to the load direction (Figure 3.27). Along the crack path birefringence effects

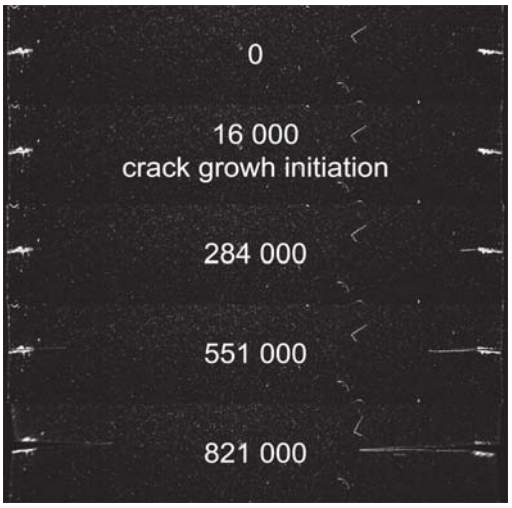

Figure 3.27: Optical documentation of the fatigue crack growth behavior of a PET film with a DENT specimen at a start value of ΔK = 1.38 MPa $m^{0.5}$.

on both sides were found (Figure 3.28). Here process zones sizes were not discernible in either of the geometry. A reason for this might be that the PET films showed a bi-linear yield behavior without a defined yield stress and therefore the requirements for the formation of a plastic zone are not met (Figure 3.29). For the PET films both FCG curves and evaluation of the process zones suggest applicability of LEFM.

Figure 3.30 shows comparisons of process zone sizes from tests which were stopped when crack growth was discernible for a) the DENT and b) the CCT geometry and theoretical values according to LEFM for plane stress and

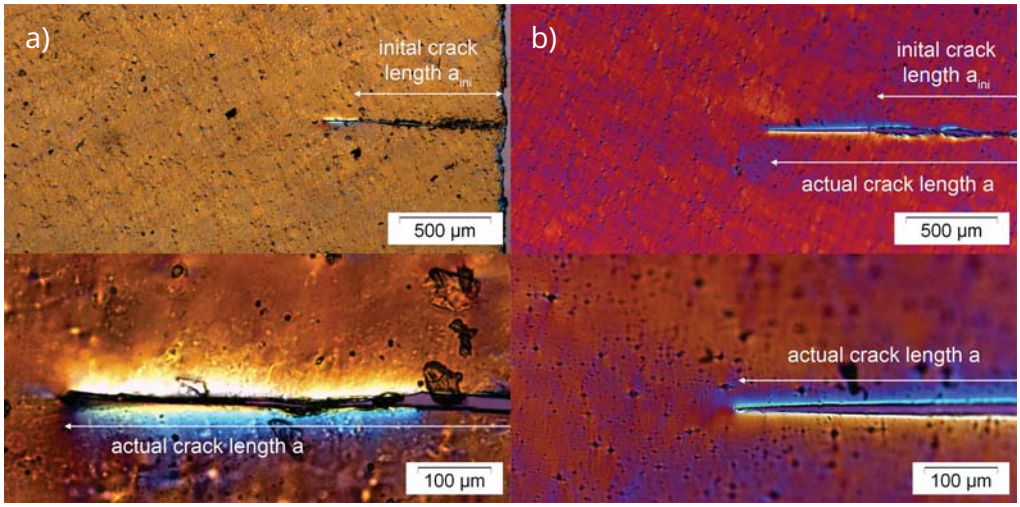

Figure 3.28: Polarized light microscopical images with magnifications of 50x and 500x of crack tips from PET film specimens with a) a DENT and b) a CCT geometry, respectively, where the test was stopped after crack growth initiation at $\Delta K \sim 3.40\ \mathrm{MPa\,m^{0.5}}$.

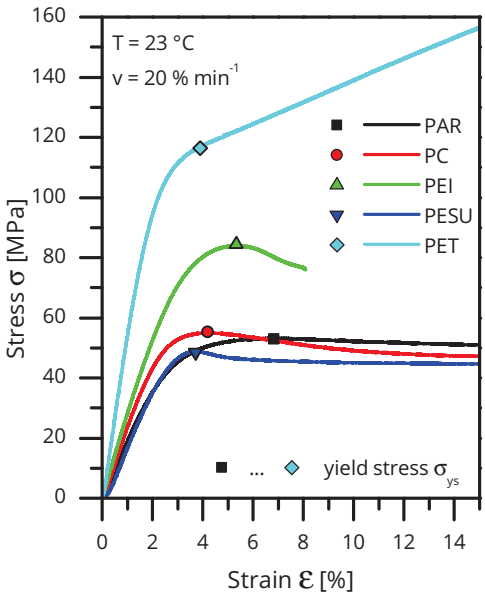

Figure 3.29: Tensile curves at standard conditions and a strain rate v of 20 % min^{-1} with the evaluation of the yield stress σ_{ys} for PAR, PC, PEI, PESU and PET films.

plane strain conditions for all materials and for PC additionally according to the Dugdale model [76], [90]–[92]. In PESU and PET in both specimen geometries and in PAR and PC in CCT specimens the process zones were not discernible, therefore for these only the calculated ones are depicted. One important result is that the measured process zone sizes were approximately one order of magnitude larger than the thicknesses of the films. Therefore the requirement of LEFM that the process zones have to be small compared to the length dimensions of the specimens or structures is violated [78]. For PAR with DENT and PEI with both specimen geometries, a good agreement of the measured values to the theoretical ones for plane stress conditions, according to Equation 3.14, was found. For PEI films larger process zone sizes were measured with CCT specimens which contradicts the results from FCG measurements with higher crack growth rates at the same stress intensities for the CCT geometry. In contrast, PC has shown three times larger process zone sizes than those predicted by plane stress conditions. Since in micrographs process zone shapes similar to those described by Dugdale were observed, also a comparison was made with theoretical process zone sizes according to the Dugdale model (Equation 3.16) [78], [92]. Here a significant better correlation between measured an theoretical process zone sizes was observed.

In order to clarify why differences in the process zone shapes were found, especially in the PC films, elasto-plastic fracture mechanical finite element (FEM) simulations for all materials and both specimen geometries were done. Comparability to the microscopic process zone evaluations was achieved by applying the same loads and therefore also the same stress intensities. In Figure 3.31 an overview of the stress distribution (von Mises stress) at $\Delta K \sim 1.05\,\mathrm{MPa\,m^{0.5}}$ in PC films for both a) a DENT and b) a CCT specimen is shown. For the material data, results from the tensile tests were taken. It clearly can be seen that the overall stress state differs significantly with higher loads throughout the specimen for the DENT geometry and there is more localized behavior in CCT specimens. The main reason for this

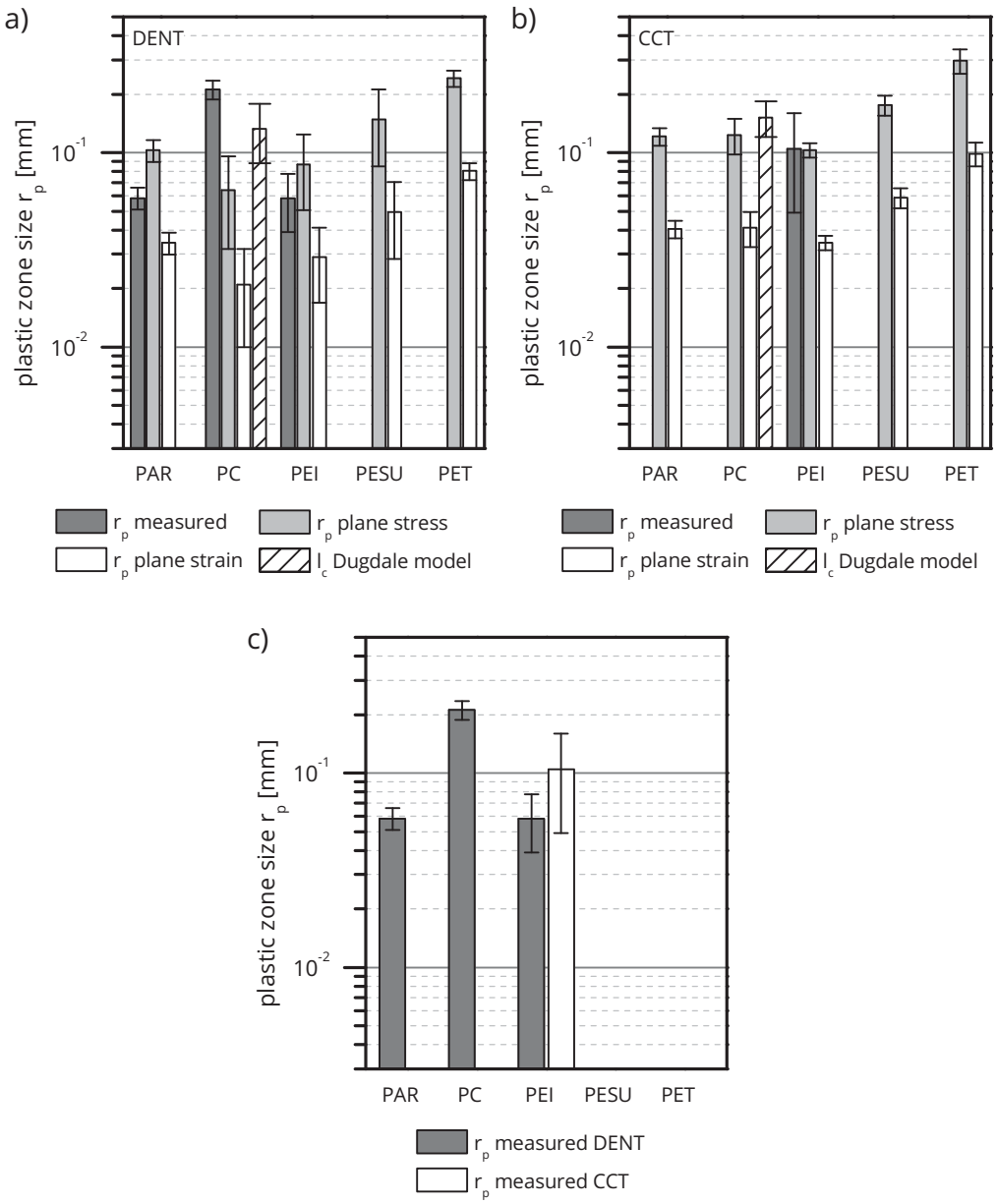

Figure 3.30: Comparison of measured process zone sizes from micrographs of stopped tests right after crack growth initiation with a) DENT and b) CCT specimens and theoretical values according to LEFM for plane stress and plane strain conditions for all materials and the Dugdale model additionally for PC and c) a comparison of measured process zone sizes for both specimen geometries [76], [90]–[92].

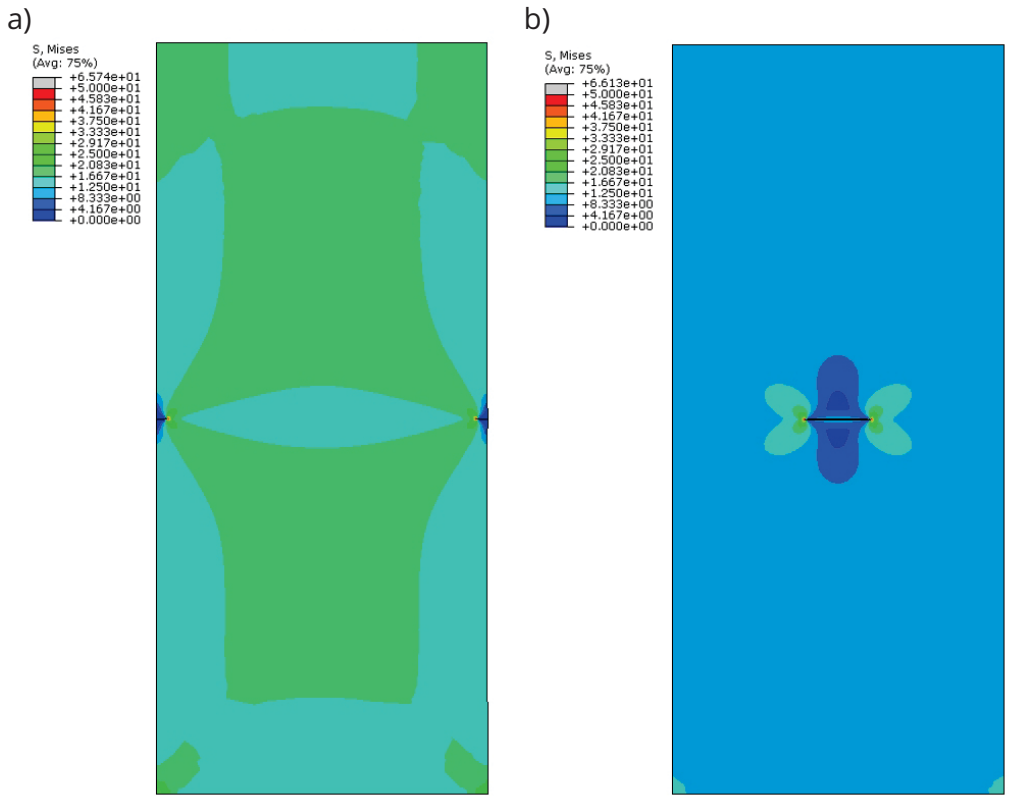

Figure 3.31: Simulation results with an overview of the stress distributions at $\Delta K \sim 1.05\,\mathrm{MPa\,m^{0.5}}$ in a) a DENT specimen with a crack length a of 0.5 mm and b) a CCT specimen with a crack length a of 1.5 mm for PC films.

might be the short crack length of 0.5 mm in DENT compared to 1.5 mm in CCT specimens. As a result the stress amplification at the crack tip is significantly higher in the latter. Similar stress distributions to those in the CCT specimen were reported by Brinson and MIlls also for center cracked tension specimens with PC [151], [156].

Detailed views of the stress distribution (von Mises stress) near the crack tip in PC films are shown in Figure 3.32 for a) a DENT and b) a CCT specimen. Here similar stress distributions are obtained for both geometries as proposed by LEFM, but again more localized in the CCT geometry. LEFM proposes that if the crack tip similitude concept applies, the crack tip near

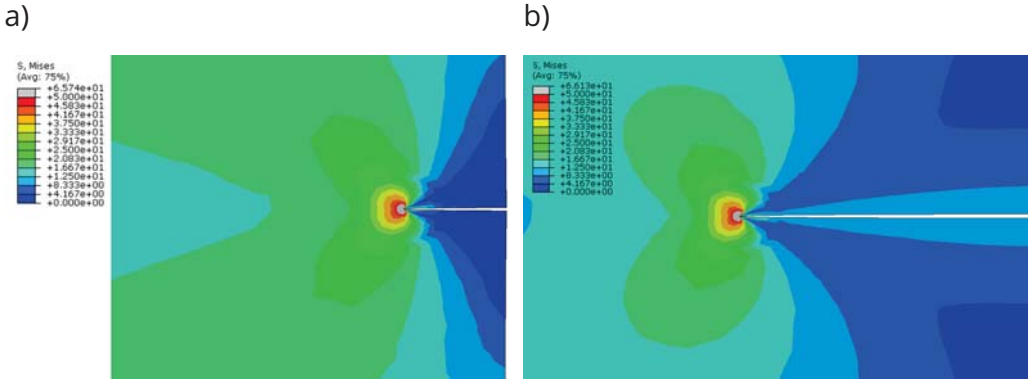

Figure 3.32: Simulation results with a detail of the stress distributions at $\Delta K \sim 1.05\,\mathrm{MPa\,m^{0.5}}$ in a) a DENT specimen with a crack length a of 0.5 mm and b) a CCT specimen with a crack length a of 1.5 mm for PC films.

field is controlled by the stress intensity factor K and therefore independent of the geometry. As a result by comparing simulations with different specimen geometries the boundary between the regions where the stress distributions are controlled by the stress intensity factor K and the global tensile stresses should be obtained. An evaluation of the simulation results for PC with the crack opening stress σ_{yy} as a function of the distance from the crack tip x for both DENT and CCT specimen geometries from the fatigue tests at stress intensities at the crack tips of $K_I = 1\,\mathrm{MPa\,m^{0.5}}$ is shown in Figure 3.33. Since different crack lengths of 0.5 mm in DENT compared to 1.5 mm in CCT specimens were used in the fatigue tests, the loads had to be chosen accordingly to achieve matching stress intensities. Therefore in the far field region different global tensile loads were also obtained in the simulations. Nevertheless as proposed by LEFM up to a distance of approximately 0.25 mm almost identical stress curves were obtained. This suggests that up to this point the stress distribution at the crack tip is controlled by the stress singularity and therefore by the stress intensity factor. Since in PC the process zones have similar sizes, especially in DENT specimens, the requirement might be violated, that according to LEFM the process zones have to be confined to a small region around the crack tip.

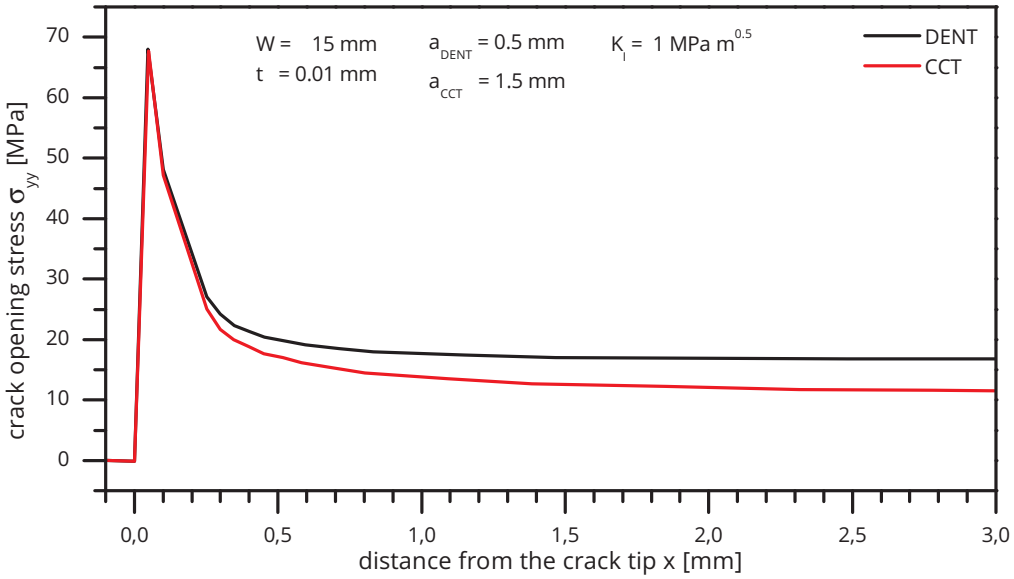

Figure 3.33: Simulation results for PC with the crack opening stress σ_{yy} as function of the distance from the crack tip x for both DENT and CCT specimen geometries at a stress intensity of $K_I = 1\,\mathrm{MPa\,m^{0.5}}$.

Further effects which may influence the applicability of LEFM are hysteretic effects due to high frequency dynamic loads and the effect of path or load history according to Lang et al. [148]. Based thereupon thermographic evaluations of the hysteretic heat up directly at the crack tip during fatigue pretests with PAR films were done using an IR camera SC7500 (FLIR System, Inc., Wilsonville, USA). These have shown that, during stable crack growth, the temperature increase does not exceed 2 °C to 3 °C. One of the main reasons for such small heat up might be the thinness and therefore a high aspect ratio of these films. Consequently heat is quickly transferred to the relatively large surface and taken away by convection. One further aspect which may lead to differences in the fatigue behavior in different specimen geometries is the path or history dependence. Under cyclic fatigue the crack has to grow through material which has observed a higher number of cycles. This might lead to changes in both the viscoelastic state and also the yield behavior of the material over the crack path [148]. If a material shows a

dependence on such so-called far field effects, the stress state at the crack tip is not solely dependent of the stress intensity K and therefore LEFM might be not applicable.

In conclusion the applicability of LEFM for cyclic fatigue of PAR, PC, PEI, PESU and PET polymer films with thicknesses from 4.5 µm to 10 µm at 100 Hz was investigated using the crack similitude concept by comparing fatigue crack growth tests with DENT and CCT specimens. Furthermore measured and calculated process zone sizes from stopped tests with all materials and both specimen geometries were compared. The applicability of LEFM seemed given for PAR, PESU and PET films but not for PC and PEI films. The latter showed both differences between DENT and CCT specimen geometries in the fatigue crack growth and the polarized light microscopic process zone evaluations. It also was found that for PAR, PC and PEI the process zone sizes were approximately one order of magnitude larger than the thickness of the films. Therefore the requirement of LEFM that the process zones have to be small compared to the length dimensions of the specimen or structure might have been violated. In order to clarify the deviations in PC films, elasto-plastic fracture mechanical simulations were done and evaluated regarding the global and local stress distributions at the crack tip. It was found that for PC at up to 0.25 mm behind the crack tip, identical stress distributions of the crack opening stress σ_{yy} prevail in both DENT and CCT specimens. Therefore it was concluded that up to this point the stress distributions should be singularly controlled by the stress intensity K. Since the measured process zone sizes for PC are of a similar size, the requirement for LEFM, that the process zones should be confined to a small region around the crack tip, was regarded as violated for PC. Finally it was concluded that in PC also far field effects might have occurred which led to crack growth which is not any longer solely dependent on K and therefore the requirements of LEFM might have not been met.

3.4.3 Effect of temperature

Due to the decreasing thickness of smartphones and tablets the mechanical loads in the polymer membranes of their miniature loudspeakers have increased significantly. One of their main challenges is to provide a long service life even at elevated temperatures. The temperatures loads are caused by the heat up of the voice coil and intensified by the tight packaging of components in the devices in which the speakers are built in. In order to determine the temperature loads, pretests were done using an IR camera SC7500 (FLIR System, Inc., Wilsonville, USA) on a generic miniature loudspeaker which was loaded with a voltage signal derived from component fatigue tests. The loudspeaker was tested in free air and therefore the temperature loads of built-in speakers should be even higher than the measured heat up of 40 °C above room temperature.

Two of the commonly used polymer films for miniature speakers are polyethylene therephthalate (PET) and polyether ether ketone (PEEK) films. A main advantage of these films is their high fracture toughness, as already pointed out in sections 2.2 and 3.4.2. But this is accompanied by a low glass transition temperature of PET of approximately 70 °C. As a result the use of PET films for highly stressed miniature speakers with even higher temperature loads might be inadvisable. Instead PEEK films are favored since they provide both a high fracture toughness and also a high temperature stability with their glass transition at approximately 143 °C [16]. Usually fracture toughness evaluations of PET and PEEK films are done by the method of EWF. Here the nonelastic region is divided into the region which is involved in the fracture process and a region were plastic deformation occurs. The former is characterized as the essential work of fracture w_e and the latter by the non-essential work of fracture w_p, as explained in detail in section 2.3.2. Temperature-dependent EWF characterizations with PET films were already reported by Arkhireyeva and Hashemi [38], [41] and Pegoretti and Ricco [26]. They found that, whereas w_e is rather independent of temperature

from 23 °C to 80 °C followed by a maximum at 120 °C, w_p shows a significant maximum at 80 °C. Arkhireyeva and Hashemi reported also temperature-dependent EWF tests with PEEK films [138].

In order to clarify the influence of temperature on the fatigue behavior of PET and PEEK films Wöhler and fatigue crack growth (FCG) tests in the machine direction of the films were done using DENT specimens at a frequency of 100 Hz and a temperature range from −20 °C to 100 °C at stress spans $\Delta\sigma$ of 26 MPa, 33 MPa and 42 MPa for the PET films. PEEK films were tested at a temperature range from 23 °C to 80 °C at $\Delta\sigma$ of 48 MPa. Here the same PET films as in section 3.4.2 were used. The specimens were cut along the machine direction of the films with a thickness of 4.5 µm and a geometry of 15 mm $\times$ 45 mm $\times$ 0.5 mm (width W $\times$ clamping length Z $\times$ crack length a). An overview of the test materials is given in Table 3.3 with an indication of their thickness and also fracture toughness K_{IC} values from monotonic tests in section 3.4.1 for films consisting of the same polymer types.

Table 3.3: Test materials with indications for the contained polymer types, film thicknesses and fracture toughness values from monotonic fracture mechanic tests in section 3.4.1.

Film	Polymer	Thickness t [µm]	fracture toughness K_{IC} [MPa m$^{0.5}$]
1L$_{4.5}$-PET(c)$_{4.5}$	PET(c)	4.5	6.2-6.8
1L$_8$-PEEK$_8$	PEEK	8	3.8

[a] Section 3.4.1 [b] Cambridge Engineering Selector (Granta Design Ltd., Cambridge, UK) [c] [14]

This section is focused on the more detailed results with PET films. Since only minor influence from temperature to the fatigue results with the PEEK films were found, these results are covered in the following section 3.4.4

where the correlation between temperature dependent T-peel and fatigue tests of PEEK multilayer films is discussed.

Results for the PET films from temperature dependent and load dependent Wöhler tests are shown in Figure 3.34. For all loads significant temperature dependencies were found with a maximum of the cycles to failure N_f at 60 °C for stress spans $\Delta\sigma$ of 27 MPa and 33 MPa and at 40 °C for 42 MPa. At 27 MPa and −20 °C N_f of approximately 10^6 cycles were measured, which increased by four times when the temperature was increased to 60 °C. By further increasing the temperature to 100 °C, N_f fell below 10^5 cycles. The temperature-dependence for higher load levels of 33 MPa and 42 MPa were slightly lower with an approximate 3 fold increase of N_f at their maximum at 60 °C and 40 °C respectively. This difference results mostly from the higher scatter of the 27 MPa curves at 40 °C and 60 °C, as shown in the fits of 5 % and 95 % probabilities of failure.

The load-dependent evaluations are shown in Figures 3.34b and 3.34c. Here again a maximum of the fatigue strength was found at 60 °C with the highest cycles to failure N_f in Figure 3.34b, the lowest slopes k of the Wöhler curves and the highest endurable stress spans at 10^7 cycles $\Delta\sigma_e$. Noda et al. reported a similar behavior of a minimum in the slope k in temperature dependent Wöhler tests at the glass transition of glass fiber reinforced polyamide 66 (PA 66). They have related this minimum to a change of the fracture mechanism at T_G [157]. A comparison of the Wöhler curves with a dynamic mechanical characterization of the films in tensile mode at frequencies of 1 Hz, 10 Hz and 100 Hz reveals a good agreement of the crack growth resistance maximum at 60 °C with the onset temperature of the glass transition, as shown in Figure 3.35a. Similar behavior of a maximum in the fatigue strength for semi crystalline polymers was reported by Novotny. Here polyether etherketone (PEEK), polyether ketone ether ketone ketone (PEKEKK), polyamide 6.6 (PA 6.6) and polyamide 6 (PA 6) showed a maximum in their fatigue strength down to 70 °C below their glass transition T_G. It was supposed that the achieved molecular mobility in the glass transition of the

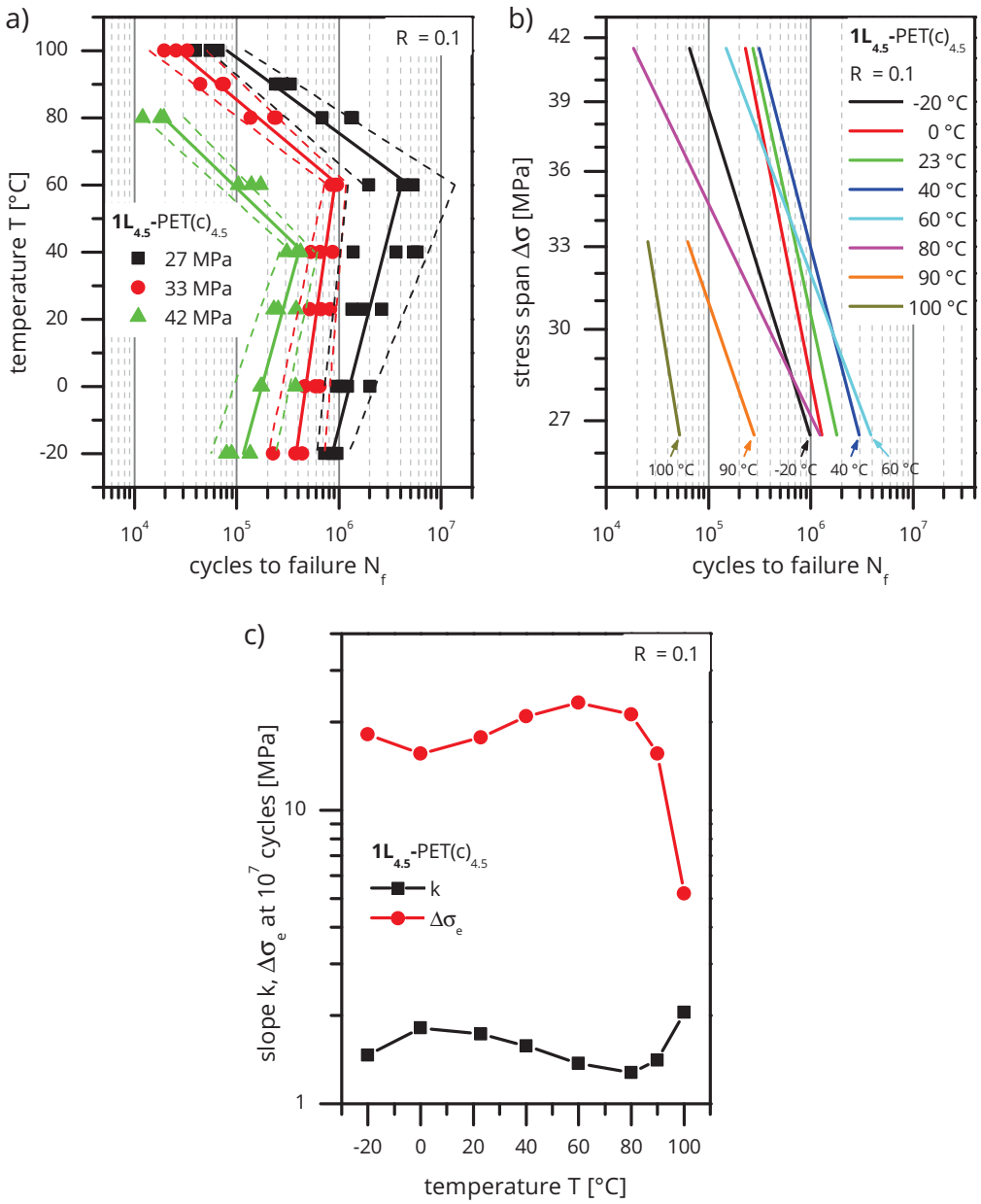

Figure 3.34: Results of Wöhler test for **1L$_{4.5}$**-PET(c)$_{4.5}$ as function of a) the temperature T for probabilities of failure of 5 %, 50 % and 95 % and b) the load $\Delta\sigma$ for a probability of failure of 50 % and c) an evaluation of the slope k for a probability of failure of 50 % and the endurable stress span $\Delta\sigma_e$ at 10^7 cycles.

amorphous phase in semi crystalline polymers contributed to an enhanced crack tip plasticity [158]. In the fatigue tests with PET films at higher temperatures, their glass transitions occurred which resulted in a drop of the modulus of over one order of magnitude, as shown in Figure 3.35a. The resulting drop in fatigue strength at temperatures above its glass transition, therefore, followed from the loss of mechanical stability.

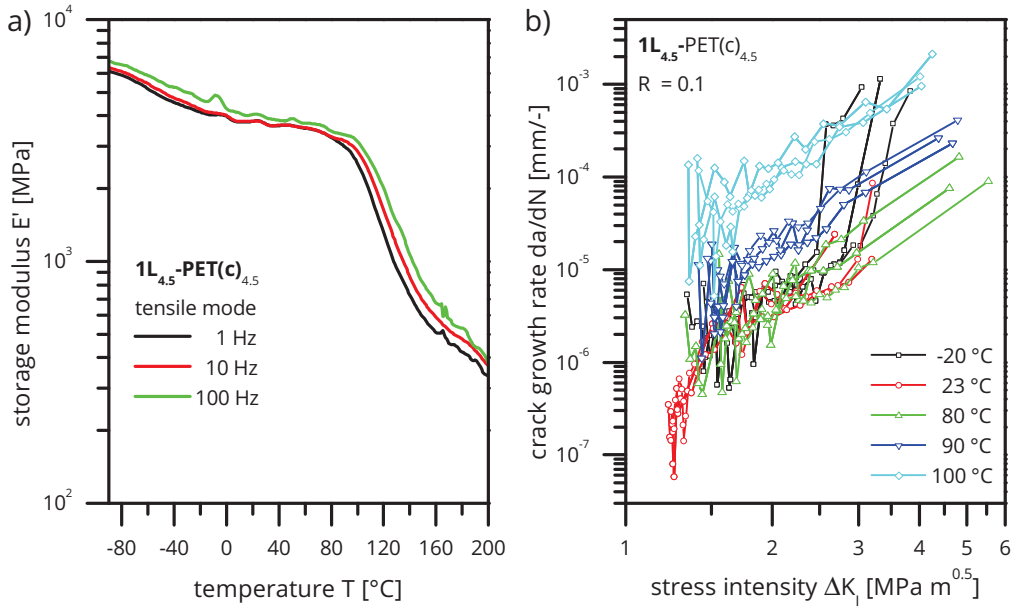

Figure 3.35: Results of a) dynamic mechanical analysis (DMA) evaluations in tensile mode with the storage tensile modulus E' as function of the temperature T at frequencies of 1 Hz, 10 Hz and 100 Hz at a heating rate of 2 K min^{-1} and b) temperature dependent fatigue crack growth (FCG) tests with **1L$_{4.5}$**-PET(c)$_{4.5}$ for temperatures from −20 °C to 100 °C.

An evaluation of the fatigue crack growth behavior of the PET films is depicted in Figure 3.35b. For this the optical documentation of the crack growth kinetics from Wöhler tests at 27 MPa was used and was subsequently evaluated for each of three experiments at each temperature, as explained in section 3.3.5. For all temperatures only low scatter in the FCG curves was found with the area of stable crack growth reaching from ΔK values of approximately 1.7 MPa m$^{0.5}$ to 3 MPa m$^{0.5}$. From −20 °C to 80 °C no significant

differences between the FCG curves were found but higher crack growth rates da/dN at the same stress intensities ΔK at temperatures above that.

A deeper insight into the fracture behavior of the PET films was achieved by polarized light microscopical images with magnifications of 50x of the broken surfaces from specimens which were tested at temperatures from −20 °C to 100 °C, which are shown in Figures 3.36 and 3.37. As it can clearly be seen, it was hardly ever possible to achieve symmetrical crack growth from both sides, since the specimens reacted very sensitively to slight misalignments from the clamping process. If this were the case, crack growth began in a slight angle. In the transition zone to perpendicular crack growth often coarser fracture surfaces were observed. This transition zone did not change its position but its roughness changed over temperature with a maximum in roughness in good correlation to the maximum fatigue strength at 40 °C and 60 °C. It is thought that the transition to standard crack growth perpendicular to the load axis took place when an evenly distributed stress distribution was reached. Especially at lower temperatures at −20 °C and 0 °C after the transition zone until final failure the cracks grew in a strict straight line. This indicates brittle fatigue modes, which correlates well with the lower fatigue strength measured at these temperatures in Wöhler tests. With rising temperatures, sections directly at the crack front which show birefringence effects (brightened up in red, yellow and light blue) increased significantly in width. It is assumed that this stems from softening of the material with increasing temperatures, as shown in Figure 3.35a, which therefore led to an increasingly localized plastic deformation, which led in turn to a higher fatigue strength. With elevated temperatures, especially at 80 °C and 100 °C and therefore in the modulus drop of the glass transition, large plastic deformations took place across the entire sample. These global plastic deformations were thought to have yielded from the ongoing softening due to the glass transition which led therefore also to a drop in the mechanical stability and fatigue resistance. The global plastic deformations are in good agreement with findings from the literature were a maximum in the non-

essential work of fracture w_p from 60 °C to 100 °C is described, which relates to the fracture energy which is dissipated in the plastic deformation far from the crack tip [26], [38], [41].

In conclusion the temperature and load dependent fatigue behavior of 4.5 µm thin PET films was investigated with Wöhler and fatigue crack growth tests at load levels of 27 MPa, 33 MPa and 42 MPa and temperatures from −20 °C to 100 °C. A maximum in the crack growth resistance at 60 °C was found in the Wöhler tests which was also accompanied by a decrease in the slope of the load dependent Wöhler curves at 60 °C and above. In FCG tests up to temperatures of 80 °C almost identical curves were obtained with a decreasing crack growth resistance at temperatures above that. Both the drops in fatigue life in both Wöhler and FCG evaluations correlate well with DMA experiments in tensile mode at frequencies of 1 Hz, 10 Hz and 100 Hz, where the onset of the glass transitions lies at approximately 60 °C. As seen in polarized light microscopic evaluations, with an increase in the temperature there was also an increase of plastic deformations directly at the crack fronts and also in remote areas across the test specimens. The increased local deformations are thought to have also led to an increased fracture energy consumption for crack growth and therefore have contributed to an increase in the fatigue strength. The latter are thought to stem from a global softening of the material above its glass transition and therefore have led to a loss of mechanical stability and, as a result, to a lower fatigue strength. The increased global plastic deformations are in good agreement with fracture toughness tests found in the literature, where a maximum in the non essential work of fracture w_p from 60 °C to 100 °C is described [26], [38], [41].

3.4.4 Effect of the multilayer design

The state of the art in polymeric membranes for miniature loudspeakers are multilayer films. Since this may influence the fatigue behavior, in this

Figure 3.36: Polarized light microscopic images of fracture surfaces from temperature dependent fatigue tests with **1L$_{4.5}$**-PET(C)$_{4.5}$ at a) −20 °C, b) 0 °C and c) 23 °C.

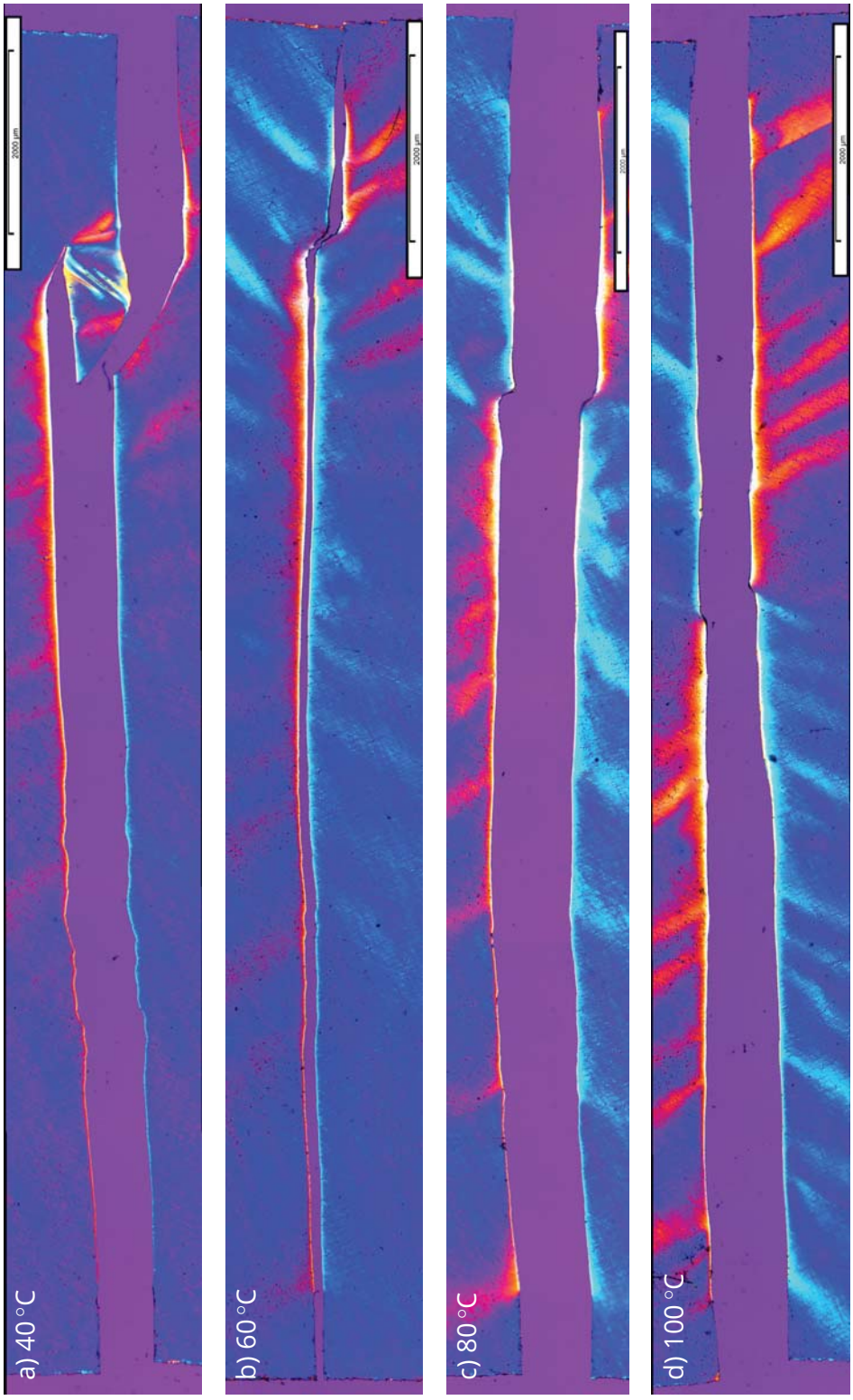

Figure 3.37: Polarized light microscopic images of fracture surfaces from temperature dependent fatigue tests with **1L$_{4.5}$**-PET(c)$_{4.5}$ at a) 40 °C, b) 60 °C, c) 80 °C and d) 100 °C.

section effects originating from the multilayer design are investigated. As described in sections 3.2.1.6 and 3.2.2, two main processes such as crack bridging and delamination might occur and influence the fatigue behavior of the laminates. Since crack bridging effects are hard to determine in this evaluation the focus lies on describing the influence of delamination effects to the fatigue behavior of these laminates. This is done by calculating and comparing the dissipated energies involved in both processes. Therefore on the one hand fatigue tests with an evaluation of both Wöhler kind tests and FCG curves were performed and on the other hand T-peel tests were done to examine their delamination properties. Finally based on data from the experiments the adhesive fracture energy G_A from delamination tests and the energy release rate G from fatigue tests were calculated and compared.

Due to the fact that miniature speakers often have to endure loads at elevated temperatures the tests were performed over a temperature range from 23 °C to 80 °C to also take a certain amount of heat brought in by the voice coil into consideration. Therefore for the Wöhler tests instead of the load dependence, the temperature dependence of the cycles to failure at a fixed load was investigated. Two 3-layer laminates with damping adhesives with different stiffnesses were chosen as model materials. They consist of a symmetrical design with two of the same polyetheretherketone (PEEK) outer layers with thicknesses of 8 µm and an adhesive damping layer in between with a thickness of 30 µm. **3L$_{46}$**-PEEK$_8$I$_{30}$ contains a soft and **3L$_{46}$**-PEEK$_8$J$_{30}$ contains a stiff adhesive layer. Specimens with 15 mm × 50 mm (width W × clamping length Z) and a peel distance of 13 mm were cut along the machine direction of the films as described in Subsection 3.3.6. The results of temperature dependent T-peel tests for both laminates with 15 mm wide T-peel samples at a test speed v of 5 mm min^{-1} are shown in Figure 3.38.

3L$_{46}$-PEEK$_8$I$_{30}$ with a soft adhesive (Figure 3.38a) showed relatively low peel forces with moderate scatter in tests at each temperature. Starting with 0.37 N at 23 °C, the peel force already halved at 40 °C and decreased down to 0.06 N at 80 °C. In the optical documentation of the T-peel tests, peel angles

Table 3.4: Test materials.

Laminate	Layer type		Thickness t [µm]	
	1/3	2	1/3	2
1L$_8$-PEEK$_8$	PEEK	-	8	-
3L$_{46}$-PEEK$_8$I$_{30}$	PEEK	adhesive I	8	30
3L$_{46}$-PEEK$_8$J$_{30}$	PEEK	adhesive J	8	30

between 79° to 87° were measured with no distinct difference between the test temperatures. In Figure 3.39a) an image taken during a test at 40 °C is shown with the peel angle θ slightly deviating from 90°. This deviation of the expected value of 90° was partly attributed to gravitation, but also to the low adhesion forces in **3L$_{46}$**-PEEK$_8$I$_{30}$. A detailed evaluation of the peeled surfaces is shown in light microscopic images in Figures 3.40a) to d). Most of the times the adhesive was found with the majority on one peel arm and only a small portion on the other, but the adhesive never was found on both peel arms at the same position. Also marks of the start of the T-peel tests 6.25 mm away from the remaining unpeeled laminate part were observable on both peel arms, which became more visible at higher temperatures. Since throughout all the tests and temperatures stable delamination was found and the remaining adhesive always just on one peel arm at the same position it was concluded that in this laminate adhesion fracture occurred.

3L$_{46}$-PEEK$_8$J$_{30}$ with a stiff adhesive showed significantly higher peel forces of 2.33 N at 23 °C down to 0.29 N at 80 °C (Figure 3.38b). Whereas at 23 °C and 40 °C higher scatter with rougher curves were obtained, at higher temperatures they became smooth. The mean values of the peel angles with **3L$_{46}$**-PEEK$_8$J$_{30}$ were almost exactly 90° for all temperatures, but significant differences in the standard deviations were found. Whereas for 23 °C and 40 °C standard deviations below 1.6° were measured, at 60 °C it had increased already to 4.6° and reached 9.9° at 80 °C. The significant differences in both roughness of the curves and differences in the standard deviations

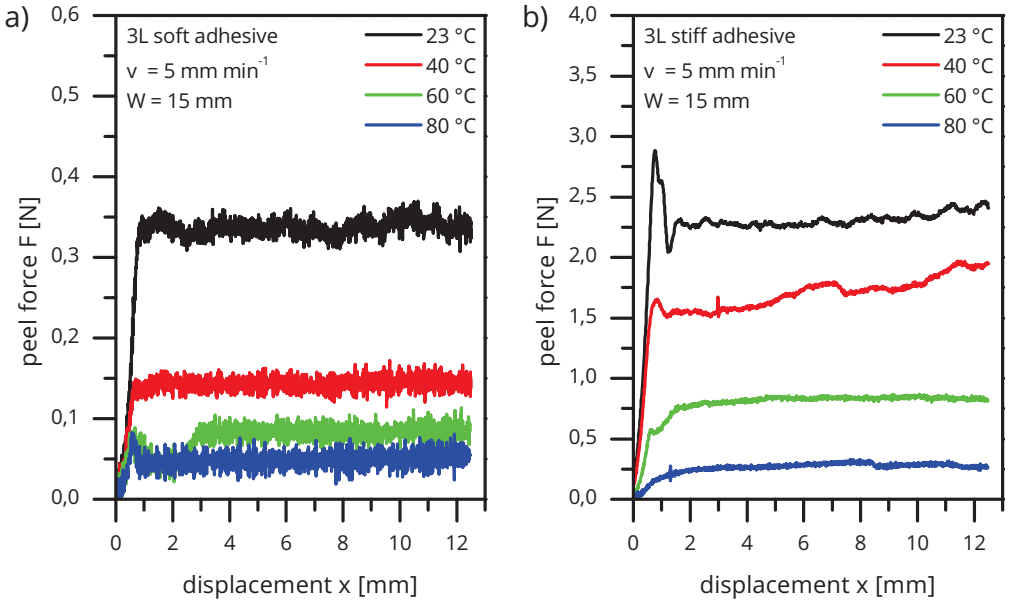

Figure 3.38: Results of temperature dependent T-peel tests at temperatures from 23 °C to 80 °C with two 3-layer laminates, a) **3L$_{46}$**-PEEK$_8$I$_{30}$ with a soft and b) **3L$_{46}$**-PEEK$_8$J$_{30}$ with a stiff adhesive.

of the peel angles were attributed to differences in the peel processes as light microscopic evaluations of the peeled surfaces revealed, shown in Figures 3.40e) to h). Here on specimens which were peeled at 23 °C and 40 °C remains of the adhesive were found on both peel arms at the same positions and therefore cohesive fracture occurred. Also marks of the starting of the peel process were hard to determine in specimens which were tested at these temperatures. For specimens which were peeled at higher temperatures at the same positions, only on one peel arm were remains of the adhesive found and therefore adhesive fracture took place. Furthermore the starting marks became more visible.

A comparison of the temperature-dependent peel forces per millimeter of width for **3L$_{46}$**-PEEK$_8$I$_{30}$ with a soft adhesive and **3L$_{46}$**-PEEK$_8$J$_{30}$ with a stiff adhesive is depicted in Figure 3.41a). Here a difference of the peel forces of approximately one order of magnitude at the same temperatures was observed

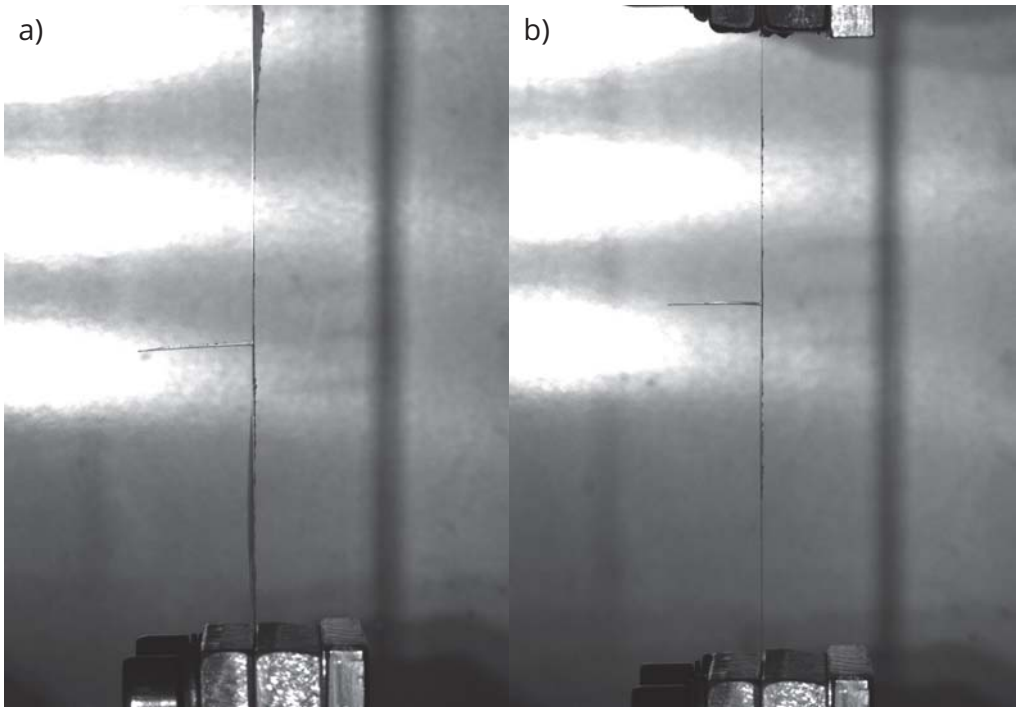

Figure 3.39: Images taken during the T-peel tests at 40 °C for a) **3L$_{46}$**-PEEK$_8$I$_{30}$ with a soft and b) **3L$_{46}$**-PEEK$_8$J$_{30}$ with a stiff adhesive.

with values from $2.5 \cdot 10^{-2}$ N mm^{-1} to $3.4 \cdot 10^{-3}$ N mm^{-1} for **3L$_{46}$**-PEEK$_8$I$_{30}$ with a soft adhesive and from $1.6 \cdot 10^{-1}$ N mm^{-1} to $1.9 \cdot 10^{-2}$ N mm^{-1} for **3L$_{46}$**-PEEK$_8$J$_{30}$ with a stiff adhesive for temperatures between 23 °C to 80 °C. In comparison, Oreški and Wallner reported for 5-layer backsheet films (polyvinyl flouride - adhesive - polyethylene therephthalate - adhesive - polyvinyl flouride) for the encapsulation of solar cells peel forces between 5 N mm^{-1} and 7 N mm^{-1} [159]. Zhou has measured values between 0.5 N mm^{-1} and 3.6 N mm^{-1} for coextruded films consisting of PC and PC-based copolymers [160].

The curves from T-Peel tests fit well to results from DMA tests in shear mode (Figure 3.42) were **3L$_{46}$**-PEEK$_8$J$_{30}$ revealed a significantly stiffer material behavior over the whole measured temperature range than **3L$_{46}$**-PEEK$_8$I$_{30}$ and both exhibited a drop in modulus between 23 °C and 80 °C of nearly one or-

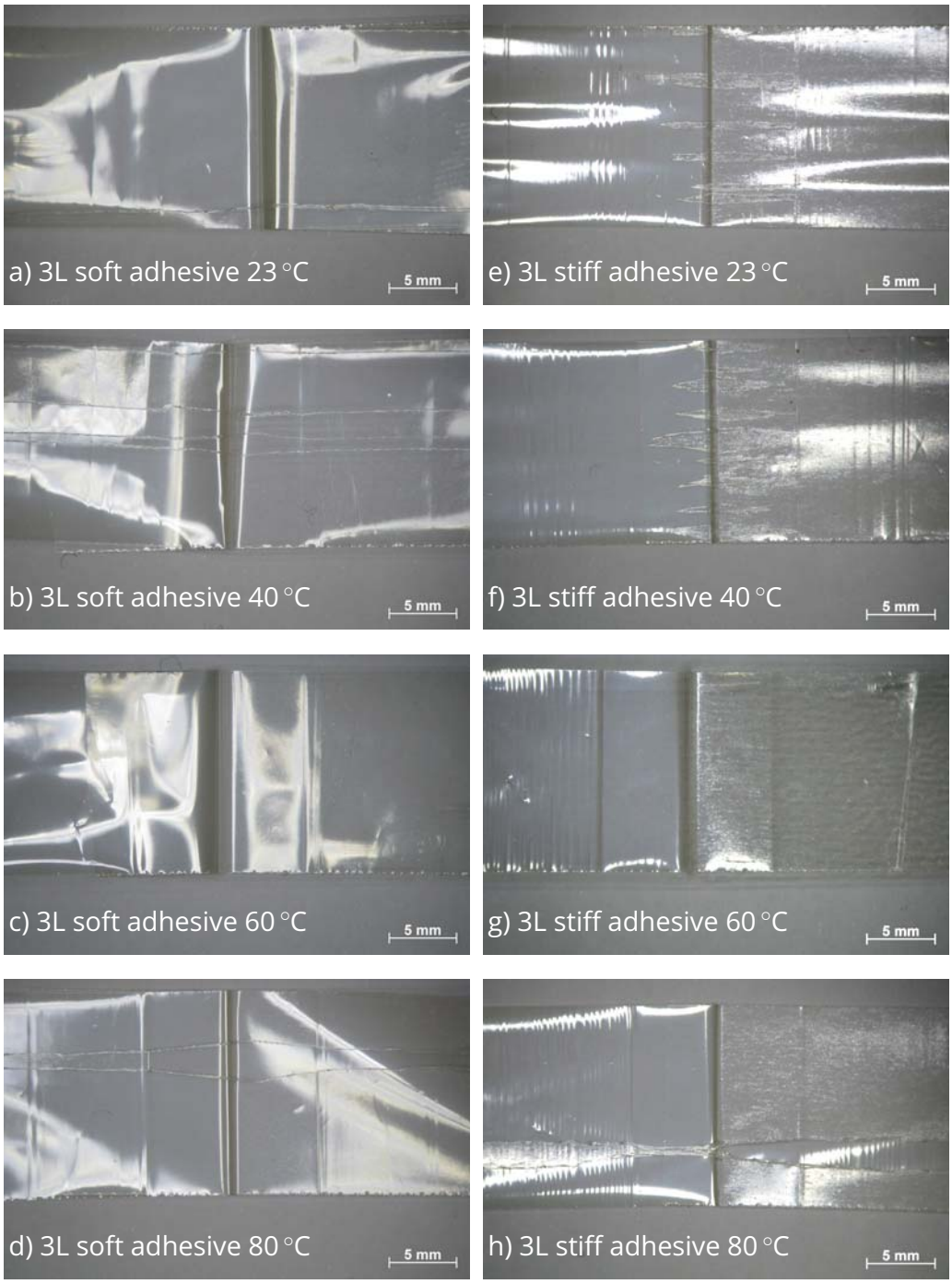

Figure 3.40: Light microscopic images of the peeled surfaces of **3L$_{46}$**-PEEK$_8$I$_{30}$ with a soft adhesive and **3L$_{46}$**-PEEK$_8$J$_{30}$ with a stiff adhesive which where peeled at temperatures from 23 °C to 80 °C.

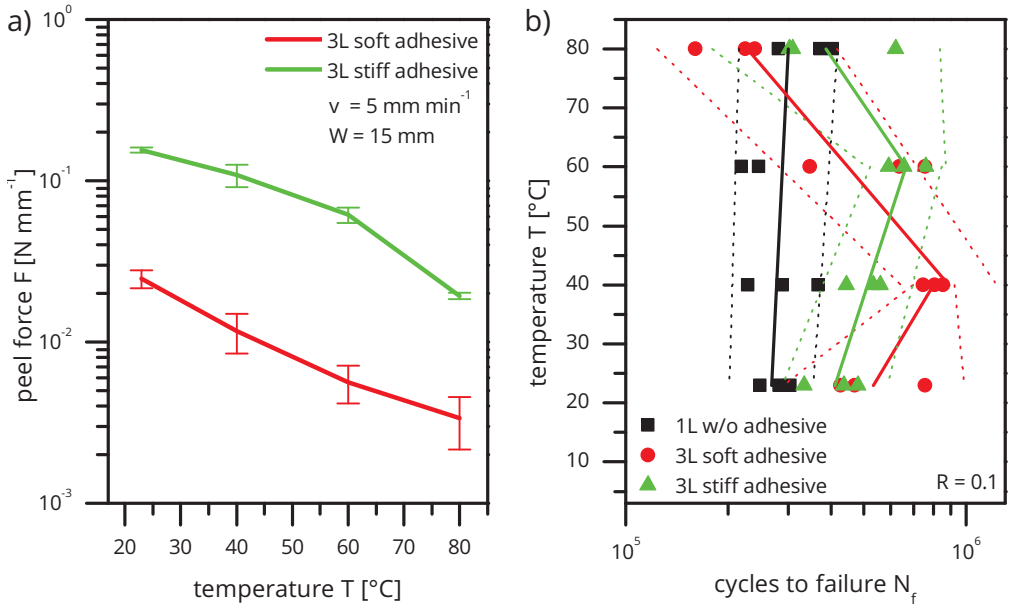

Figure 3.41: Results of a) T-peel test with an evaluation of the peelforce F vs. temperature T and b) Wöhler tests with the cycles to failure N_f vs. temperature T with the same apparent stresses in both the monolayer and the outer layers of the multilayer films.

der of magnitude. Details regarding the measurement method in DMA shear mode of miniature loudspeaker laminates are explained in section 4.3.3.

For fatigue tests DENT specimens were cut along the machine direction of the films and laminates with a geometry of 15 mm $\times$ 45 mm $\times$ 0.5 mm (width W $\times$ clamping length Z $\times$ crack length a) and tested at a frequency of 100 Hz. Results of Wöhler tests with the cycles to failure N_f as a function of the temperature T at a fixed load are shown in Figure 3.43). In order to obtain an estimation of the contribution of the adhesive layer in the fatigue behavior, along with the two 3-layer laminates also comparative tests with only one 8 mm thick PEEK outer layer were performed. The stress for the PEEK monolayer was chosen to match the calculated loads in the 3-layer laminates in their outer layers, when the adhesive layer is neglected.

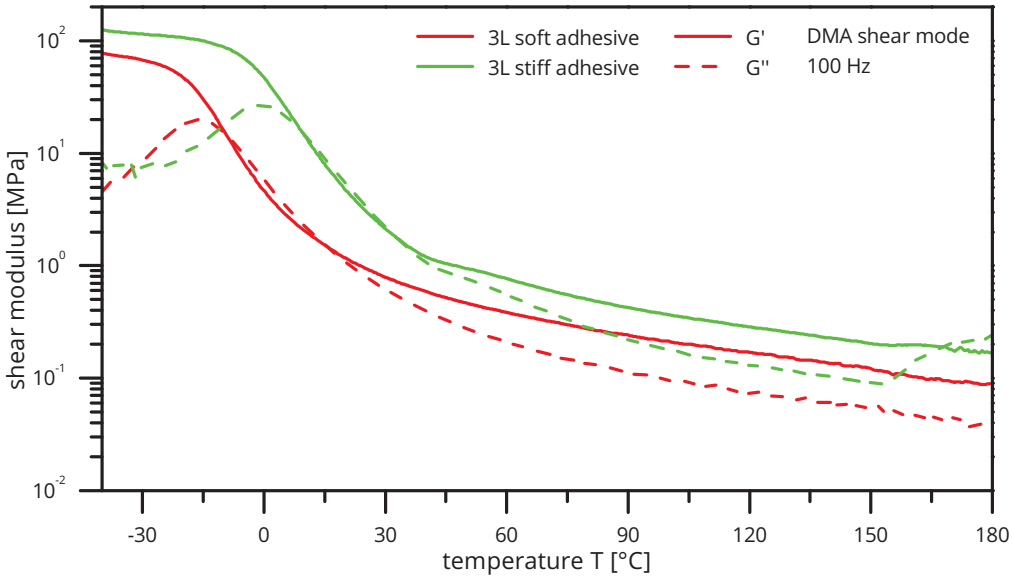

Figure 3.42: Results of temperature dependent dynamic mechanical analysis (DMA) tests in shear mode of **3L$_{46}$**-PEEK$_8$I$_{30}$ with a soft and **3L$_{46}$**-PEEK$_8$I$_{30}$ with a stiff adhesive damping layer for a frequency f of 100 Hz.

Therefore the remaining differences in the cycles to failure N_f reflect the contribution of the adhesive layers.

Whereas for the monolayer almost constant N_f was found over all temperatures a significant temperature effect was revealed for the 3-layer laminates. At 23 °C both 3-layer laminates showed similar N_f which were already above values found for the monolayer. At 40 °C and 60 °C for the 3-layer laminates with a soft and a stiff adhesive, respectively, a maximum in their crack growth resistance was found and a significant decrease above those temperatures. If one neglected the one measurement of the multilayer with a soft adhesive at 60 °C with N_f of approximately $3 \cdot 10^5$, both multilayers would have exhibited their maximum at 60 °C. At 80° for both laminates the effect of the additional adhesive layer almost vanished and values in the region of the monolayer were observed. But still a small difference remained with slightly lower values for the 3-layer laminate with soft adhesive than for the monolayer and slightly higher values for the 3-layer laminate with the stiff

adhesive. Compared to the temperature dependent peel tests, no direct correlation could be observed with the Wöhler tests.

In order to obtain a more detailed picture, besides the standard Wöhler evaluation with the cycles of crack growth N_f, also the cycles of crack growth initiation N_{cgi} and the cycles of crack growth $N_{cg} = N_f - N_{cgi}$ were analyzed with the results depicted in Figure 3.43. Although the evaluation of the cycles of crack growth N_{cg} vs. temperature T (Figure 3.43b) revealed more or less the same picture as the evaluation of the cycles to failure N_f, but with the exception at 60 °C where the advantage of the multilayers begin to vanish in N_{cg} due to the beginning of higher scatter. In contrast, in the cycles of crack growth initiation N_{cgi} significant differences were found. Here for all films with rising temperatures also constant rising N_{cgi} was found up to 60 °C with an approximately constant five-fold advantage for the multilayer over the monolayer films. Therefore the advantage of the multilayers in N_f at 60 °C stems from longer crack growth initiation times. At 80 °C the advantage vanished almost completely. In summary, at both stages, crack growth initiation and crack growth itself, up to a temperature of 60 °C the multilayers exhibited a higher fatigue strength than the monolayer PEEK film. At 80 °C the advantage vanished with even lower N_{cg} of the multilayer laminate with a soft adhesive damping layer.

In Figures 3.44, 3.45a) and 3.45b) results of the temperature dependent fatigue crack growth (FCG) evaluations are depicted where apparent stress intensities ΔK_{app} for the outer layers in the multilayer films were calculated by neglecting the adhesive damping layers in the calculation. An indication that LEFM should be applicable to these PEEK films was obtained in monotonic tests in section 3.4.1 were a similar PEEK monolayer film showed brittle fatigue modes. For the multilayer laminates apparent stress intensities ΔK_{app} were calculated by neglecting the adhesive damping layers. For the monolayer in Figure 3.44 only a slight advantage in crack growth resistance was found at 80° compared to tests at room temperature, but there were no further differentiations between tests at different temperatures.

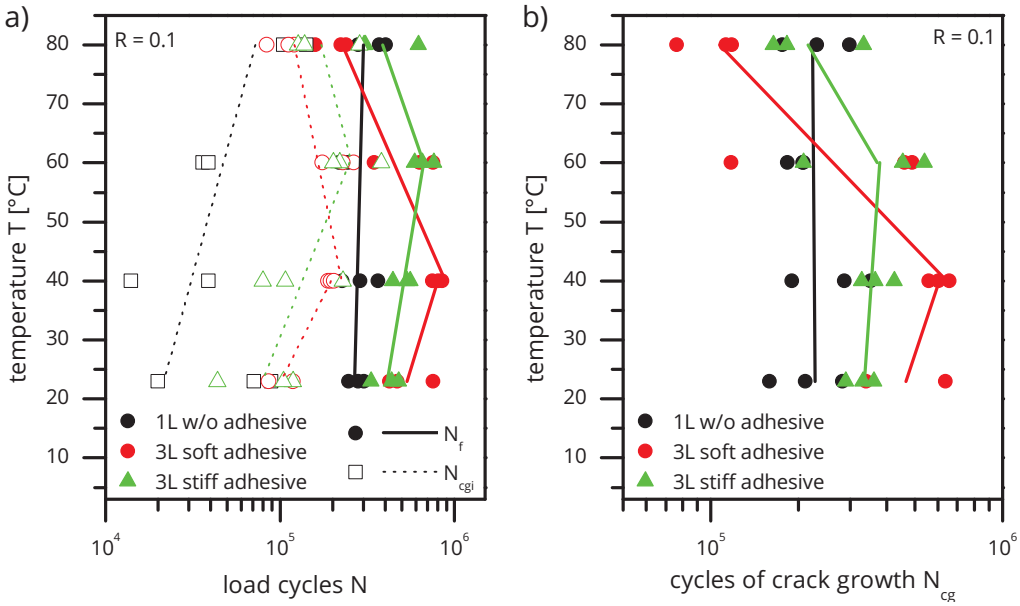

Figure 3.43: Results of Wöhler tests with a) the cycles to crack growth initiation N_{cgi} and the cycles to failure N_f and b) the cycles of crack growth $N_{cg} = N_f - N_{cgi}$ vs. temperature T with the same apparent stresses in both the monolayer and the outer layers of the multilayer films for probabilities of 50 %.

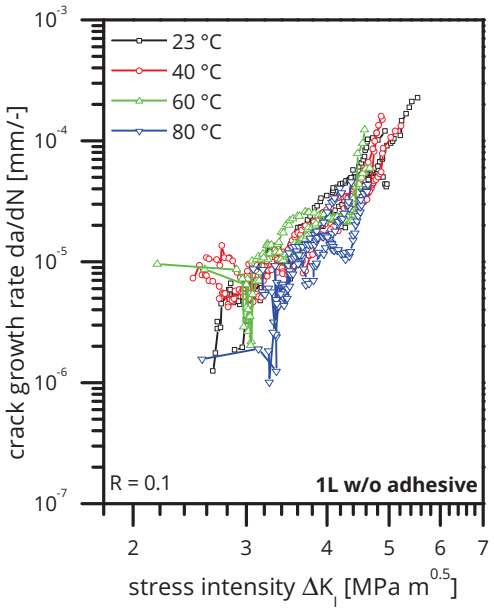

Figure 3.44: Results of temperature dependent FCG tests for a 8 µm thick PEEK film **1L$_8$**-PEEK$_8$ at temperatures from 23 °C to 80 °C.

In contrast **3L$_{46}$**-PEEK$_8$I$_{30}$ with a soft adhesive revealed a significant temperature effect with similar crack growth rates da/dN at the same stress intensities ΔK for tests at 23 °C and 40 °C but a decreasing crack growth resistance at higher temperatures. For **3L$_{46}$**-PEEK$_8$J$_{30}$ also no temperature dependence of the FCG curves was found.

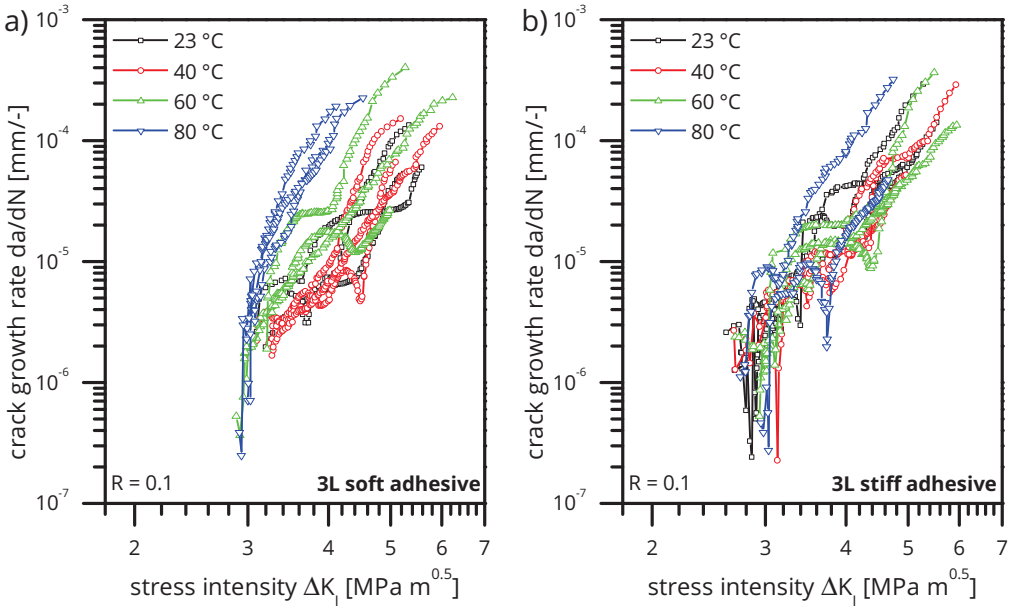

Figure 3.45: Results of temperature dependent FCG tests for 3-layer PEEK laminates with the load averaged over the whole cross section of the laminates a) **3L$_{46}$**-PEEK$_8$I$_{30}$ with a soft adhesive and b) **3L$_{46}$**-PEEK$_8$J$_{30}$ with a stiff adhesive at temperatures from 23 °C to 80 °C.

A comparison of FCG curves of the mono- and 3-layer films at the same temperatures is shown in Figure 3.46. Both at 23 °C and 40 °C the 3-layer laminates revealed an advantage in crack growth resistance compared to the monolayer film. The difference further increased at 40 °C with also better results for **3L$_{46}$**-PEEK$_8$I$_{30}$ with a soft adhesive compared to **3L$_{46}$**-PEEK$_8$J$_{30}$ with a stiff adhesive. At 60 °C almost identical results were observed for all films and at 80 °C the monofilm was clearly better. Here slightly better results for **3L$_{46}$**-PEEK$_8$J$_{30}$ with a stiff adhesive compared to **3L$_{46}$**-PEEK$_8$I$_{30}$ with the

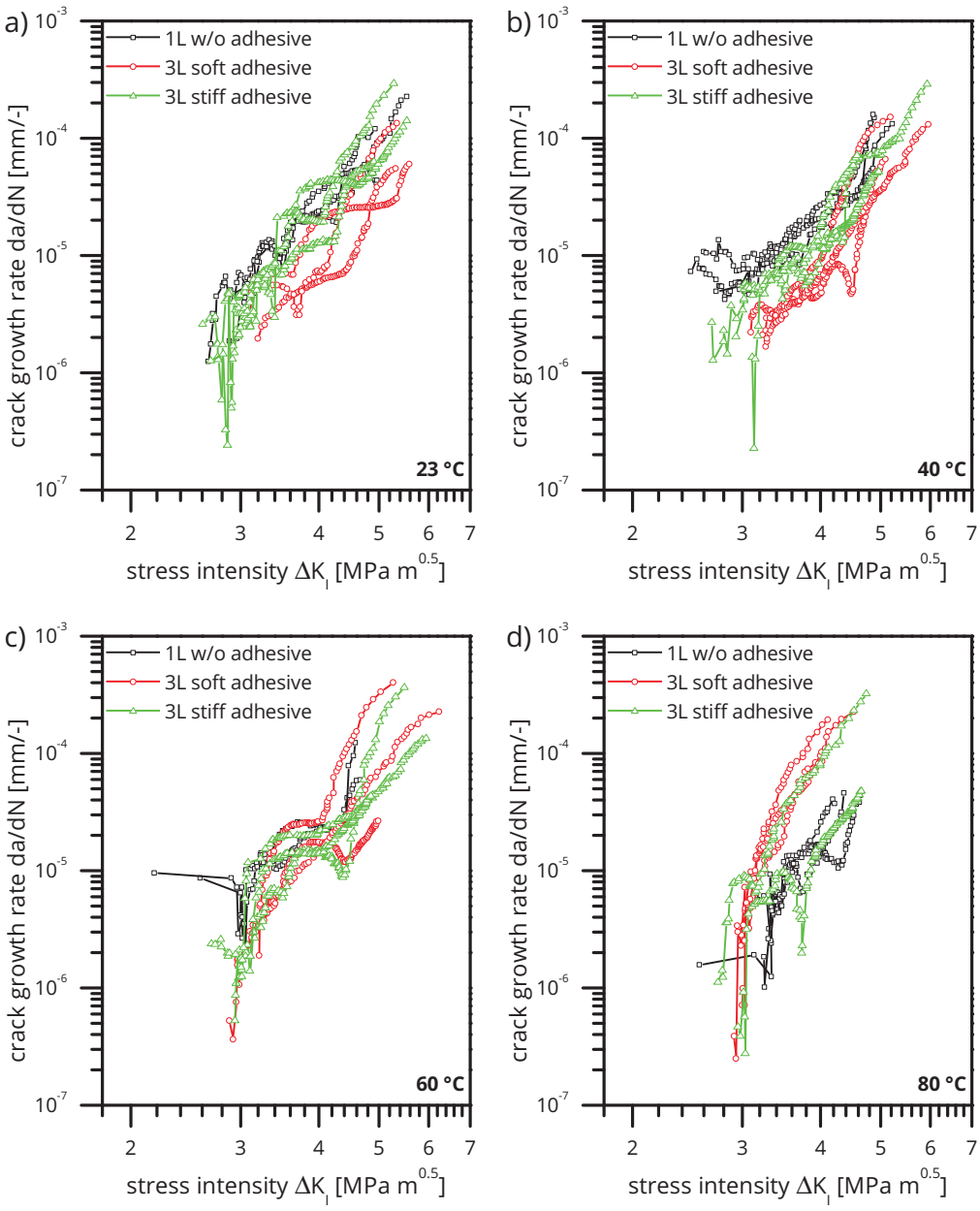

Figure 3.46: Results FCG tests at temperatures of a) 23 °C, b) 40 °C, c) 60 °C and d) 80 °C for a PEEK monolayer film **1L$_8$**-PEEK$_8$, a 3-layer PEEK laminate with a soft adhesive **3L$_{46}$**-PEEK$_8$I$_{30}$ and a 3-layer PEEK laminate with a stiff adhesive **3L$_{46}$**-PEEK$_8$J$_{30}$ where the calculation of the stress in the 3-layer laminates was regarded to the cross section of the PEEK outer layers.

soft adhesive were measured. In conclusion the FCG evaluations fitted well to the evaluation of the cycles of crack growth N_{cg} from the temperature dependent Wöhler tests where similar results were obtained but with a clearer differentiation in the latter.

Usually one would expect a decreasing fatigue strength with rising temperatures, since the additional energy for chain disentanglement and therefore also the craze stability lowers with increasing temperature [158]. Such results for amorphous polyether imide (PEI), polyether sulfone (PES) and polysulfone (PSU) were reported by Novotny [158]. A similar behavior of a rising fatigue strength than with the PEEK monofilm was reported in section 3.4.3 for semicrystalline PET films, where a maximum in the fatigue resistance was found at the glass transition. Also Karger-Kocsis and Friedrich, Novotny and Rae et al. reported either a constant fracture toughness, a maximum in the crack growth resistance or even an increasing fracture toughness of PEEK over temperature [140], [142], [158]. Plummer et al. concluded from transmission electron microscopic evaluations with semicrystalline PEEK that in this material instead of disentanglement crazing, crazing due to chain scission occurs at room temperature which might give way to shear deformation at temperatures near T_G [161], [162].

An indication for a change in the fracture process of the 3-layer laminates was obtained by polarization microscopic evaluations of the broken surfaces, shown in Figures 3.52 to 3.55. In all samples significant contributions from shear bands and even crack growth in the shear bands were observed, which often led to crack growth in a zig-zag pattern and revealed magenta colored birefringence effects. Since the crack deviated from the crack plane mode II fracture was superimposed according to Equations 3.10 and 3.11. This behavior is regarded as the cause for the significant scatter obtained in the FCG curves. With further crack growth, the broken surfaces changed significantly. The transition to cyan in the monolayer and green colored cracked surfaces in the multilayers led to the conclusion that also the stress states changed. Here also increasing global plastic deformation took place which

showed as diamond-shaped deformed zones which were too big to fit in the micrographs. Furthermore, beginning with this zone small ridges formed which were interpreted as stop bands. Confirmation for the hypothesis of the formation of shear bands was achieved with a micrograph of **1L$_8$**-PEEK$_8$ from a stopped fatigue test at a crack length of 0.5 mm, shown in Figure 3.47. Here a distinct deformation zone along the crack path which was related to a

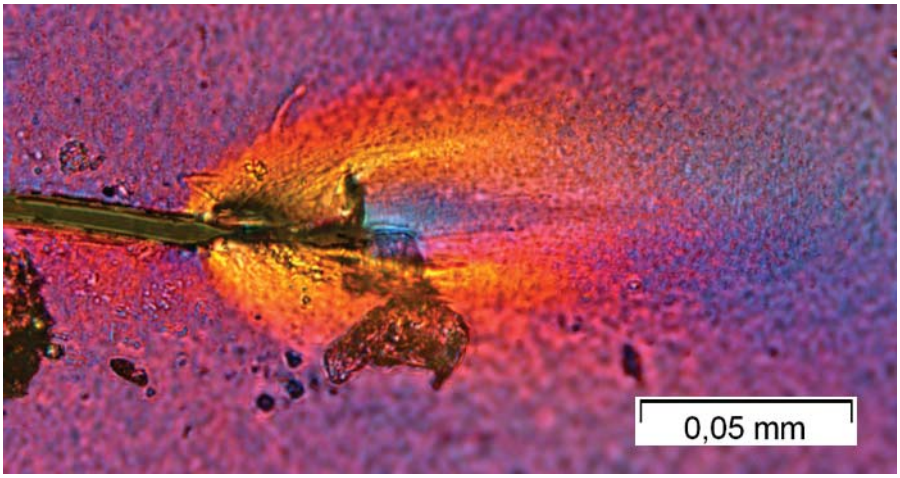

Figure 3.47: Polarized light microscopic image of **1L$_8$**-PEEK$_8$ from a stopped fatigue test.

craze zone and two distinct zones of shear deformation symmetrically above and below the craze zone were found. Similar features in bulk specimens were described by Takemori as epsilon crack tip zones, which only occur at short cracks near the free surface and lead to discontinuous crack growth (DCG). There the σ_{xx} term is reduced due to the near surface and a strong shear component superimposes the dilational stress which favors crazing. Not only additional energy is consumed in forming the shear bands which leads to stabilization of the crack, but also ΔK_I is reduced. If the epsilon crack tip zone is once formed at a short crack, it stabilizes the cracks and allows DCG to continue up to higher apparent ΔK_I values [163], [164]. Both stopping marks and strong indications of shear bands were also found in the micrographs of the PEEK films.

In the monolayer PEEK film across all tested temperatures the relative position of the shear dominated zones did not move, but its intensities decreased at higher temperatures. This was in good accordance with the fatigue tests, where the fatigue strength of the monolayer film was constant over temperature. In contrast in both 3-layer laminates the shear bands continued over longer crack paths than in the monolayer from 23 °C to 60 °C and then almost vanished at 80 °C. This again fitted well to the fatigue results where up to 60 °C a higher fatigue strength was measured for the multilayer films, but the advantage vanished at 80 °C. In addition to the fact that most of the fatigue life takes place at the beginning of the crack path, it was concluded that the shear bands dominated the fatigue performance of the observed mono- and multilayer PEEK films. Therefore the occurrence of the shear bands over a longer crack path in the multilayer PEEK films than in the monolayer films is regarded as cause for their better fatigue performance.

In order to obtain an estimation of the influence of delamination effects on the fatigue behavior of the investigated films, calculations of the adhesive fracture energy G_A from delamination tests and the energy release rate G from fatigue tests were done, with the fundamental background described in sections 3.2.2 and 3.2.1.3. For the calculation of the energy release rates G using Equation 3.13 ΔK values from FCG tests before ultimate failure were taken using the apparent stress intensities ΔK_{app} of the PEEK outer layers from the multilayer films. According to theory the stress intensities before ultimate failure should best match the monotonic fracture toughness K_{IC} and therefore should be comparable with the adhesive fracture energy G_A from monotonic delamination tests. The latter was calculated according to the method described in section 3.3.6. A comparison of the energy release rate G from fatigue tests and the adhesive fracture energy G_A from delamination tests is shown in Figure 3.48. As can be clearly seen there is a significant difference in the calculated energy values with significantly lower energies for the delamination processes. Furthermore the delamination energies G_A decrease about one order of magnitude between 23 °C and

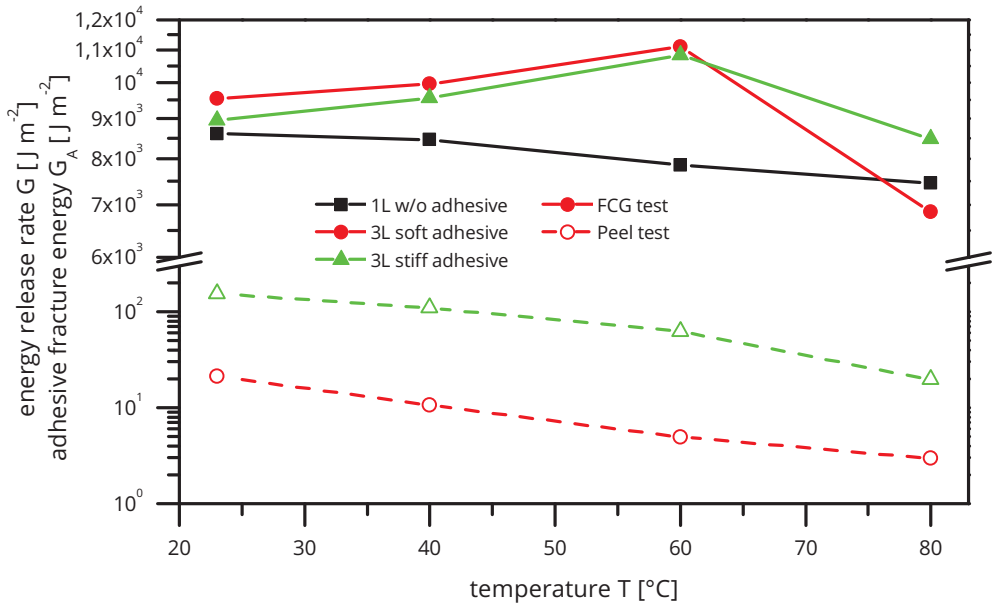

Figure 3.48: Comparison of the adhesive fracture energy G_A from T-peel tests with the energy release rate G from FCG tests with the stress in the 3-layer laminates regarded to the overall thickness of the laminates, both at temperatures from 23 °C to 80 °C.

80 °C and the energy release rates G reflect the results from fatigue tests with a higher fatigue strength from 23 °C to 60 °C. Since G_A was at significantly lower levels in theory, delamination between the layers should have occurred before crack growth. However the situation is more complicated, because these processes act in different directions. Whereas crack growth acts along the width of the samples, delamination occurs in the thickness direction. Furthermore the delamination process is thought to be induced by the stiffness differences between the soft damping and the stiff outer layers. As a result when the laminates are loaded in tension in the fatigue tests or under bending deformation in application the stiffness difference leads also to a difference in the stresses σ_{yy} in each layer according to Figures 3.5 and 3.2. This stress difference then might lead to a delamination stress in the thickness direction σ_{zz}. Since during the fatigue tests and also in the micrographs no delaminations were visible, it was concluded that

delamination processes did not contribute to the fatigue behavior of the investigated multilayer films.

For this reason the second process of crack bridging which might be involved here could give a better explanation. Here, as described in section 3.2.1.6, crack tunneling in the stiff outer layers occurs which leads to crack bridging by the remaining adhesive which shields the crack tip. This behavior was clearly observed throughout all temperatures in the fatigue tests of the multilayer laminates. Examples for a lagging behind crack growth in the damping adhesives are shown for both multilayer films in Figure 3.49 for temperatures of 40 °C. This contribution from crack bridging might have

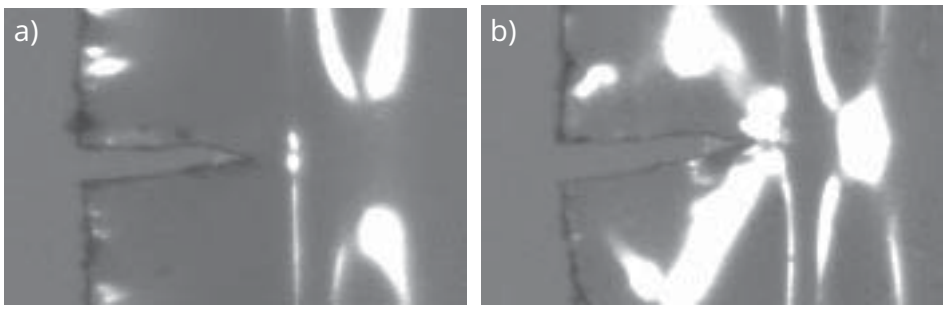

Figure 3.49: Pictures taken during fatigue tests at 40 °C of the crack tips in a) **3L$_{46}$**-PEEK$_8$I$_{30}$ with a soft adhesive at 220 000 cycles and b) **3L$_{46}$**-PEEK$_8$J$_{30}$ with a stiff adhesive at 137 000 cycles, both at a crack length of 1.2 mm.

additionally shielded the cracks in the multilayer films which therefore again favored discontinuous crack growth and consequently the occurrence of shear zones according to the theory of the epsilon crack tip zones. The clarification of the described effects would be an interesting topic for further research.

In conclusion the effect of delamination on the fatigue behavior of multilayer films for miniature loudspeakers was investigated. This was done by comparing the fracture energies from delamination (G_A) and fatigue processes (G). Temperature dependent monotonic delamination tests and also temperature dependent fatigue tests were performed and then evaluated

regarding the involved dissipated energies in the corresponding fracture processes. In a comparison of the adhesive fracture energy G_A from delamination and the energy release rate G from fatigue tests it was revealed that G_A exhibited values up to 100 times lower than G. Therefore delamination should have occured at significantly lower loads than fatigue crack growth, but delamination never was observed during the fatigue tests. Furthermore no correlation between fatigue and delamination test results was found. However still significant differences remained between the fatigue behavior of the multilayer films and comparative tests with only one of their stiff monolayers without an adhesive. Polarized light microscopic evaluations of the broken samples revealed a change of birefringence effects directly at the cracked surfaces over temperature in accordance to the fatigue results. These birefringence effects were attributed to shear deformations, which are described in the literature to shield the crack tips and as a consequence yield a higher crack growth resistance.Furthermore in the optical documentation of the crack growth kinetics, throughout all temperatures it was observed that crack growth in the adhesive damping layers lagged behind. It was concluded that this might be attributed to the process of crack bridging, which may be involved. Here the remaining adhesive might have additionally shielded the cracks in the stiff outer layers and consequently favored the formation of the described shear bands.

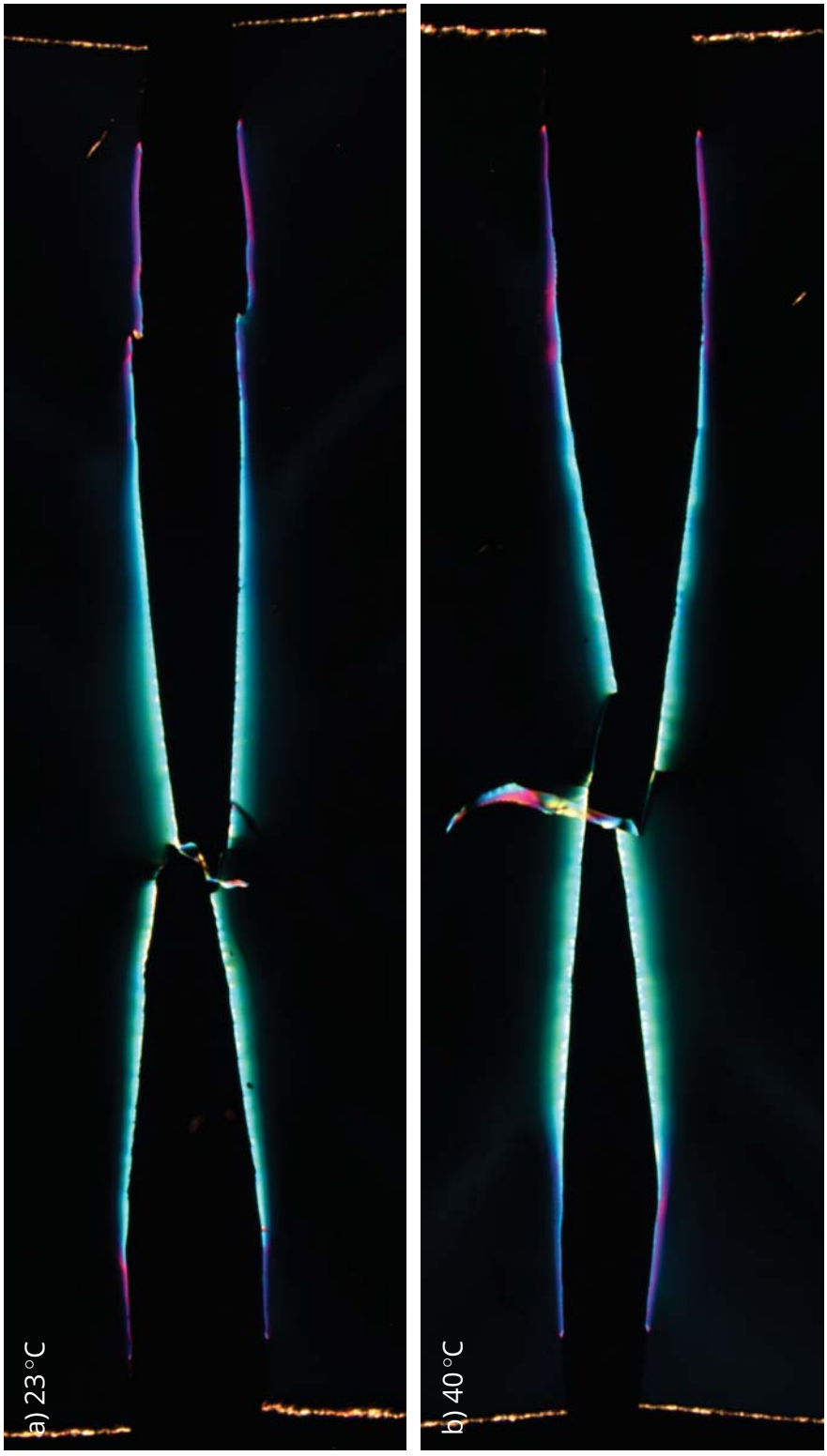

Figure 3.50: Polarized light microscopic images of fracture surfaces from temperature dependent fatigue tests with **1L$_8$**-PEEK$_8$ at a) 23 °C and b) 40 °C.

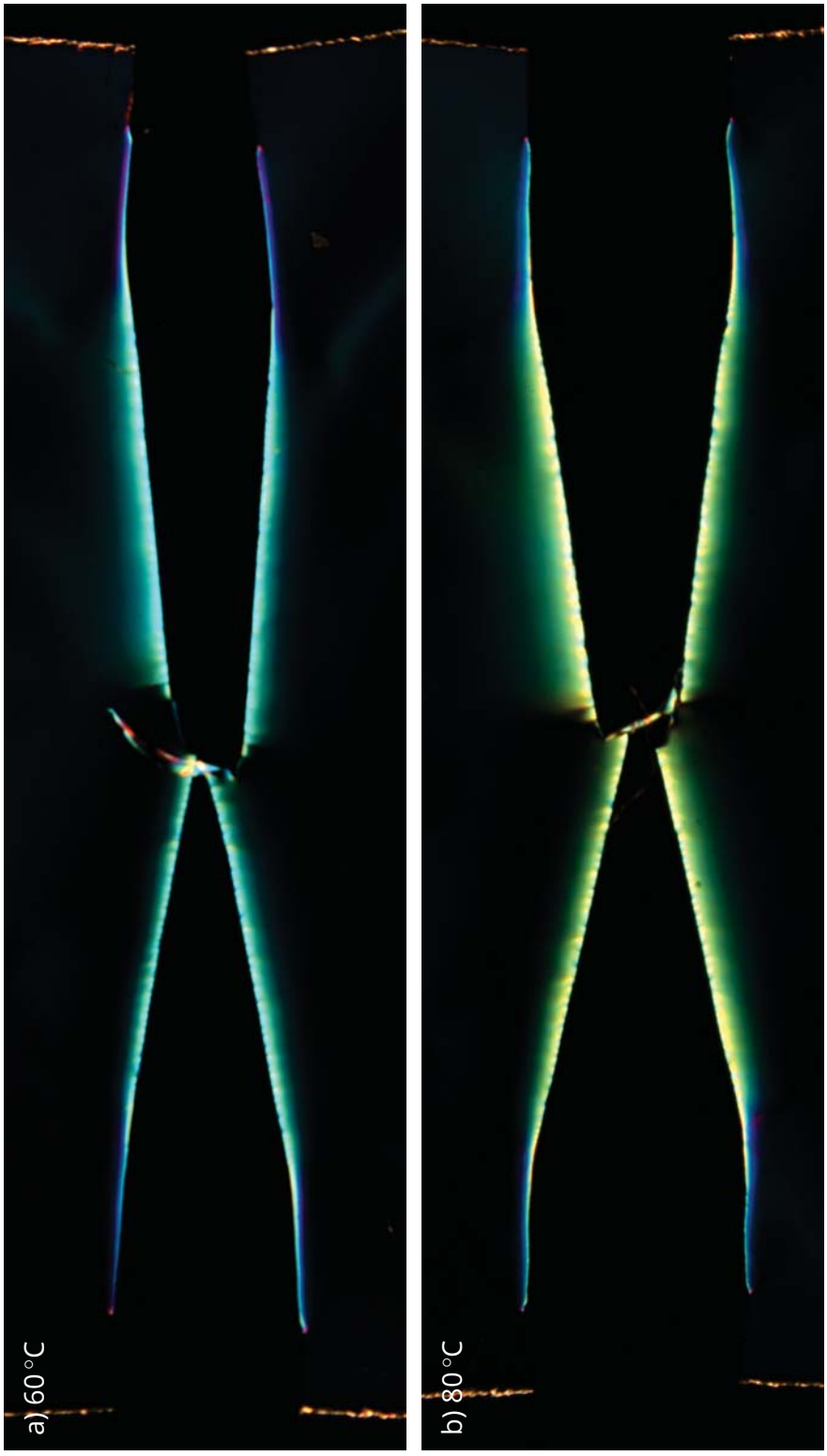

Figure 3.51: Polarized light microscopic images of fracture surfaces from temperature dependent fatigue tests with **1L$_8$**-PEEK$_8$ at a) 60 °C and b) 80 °C.

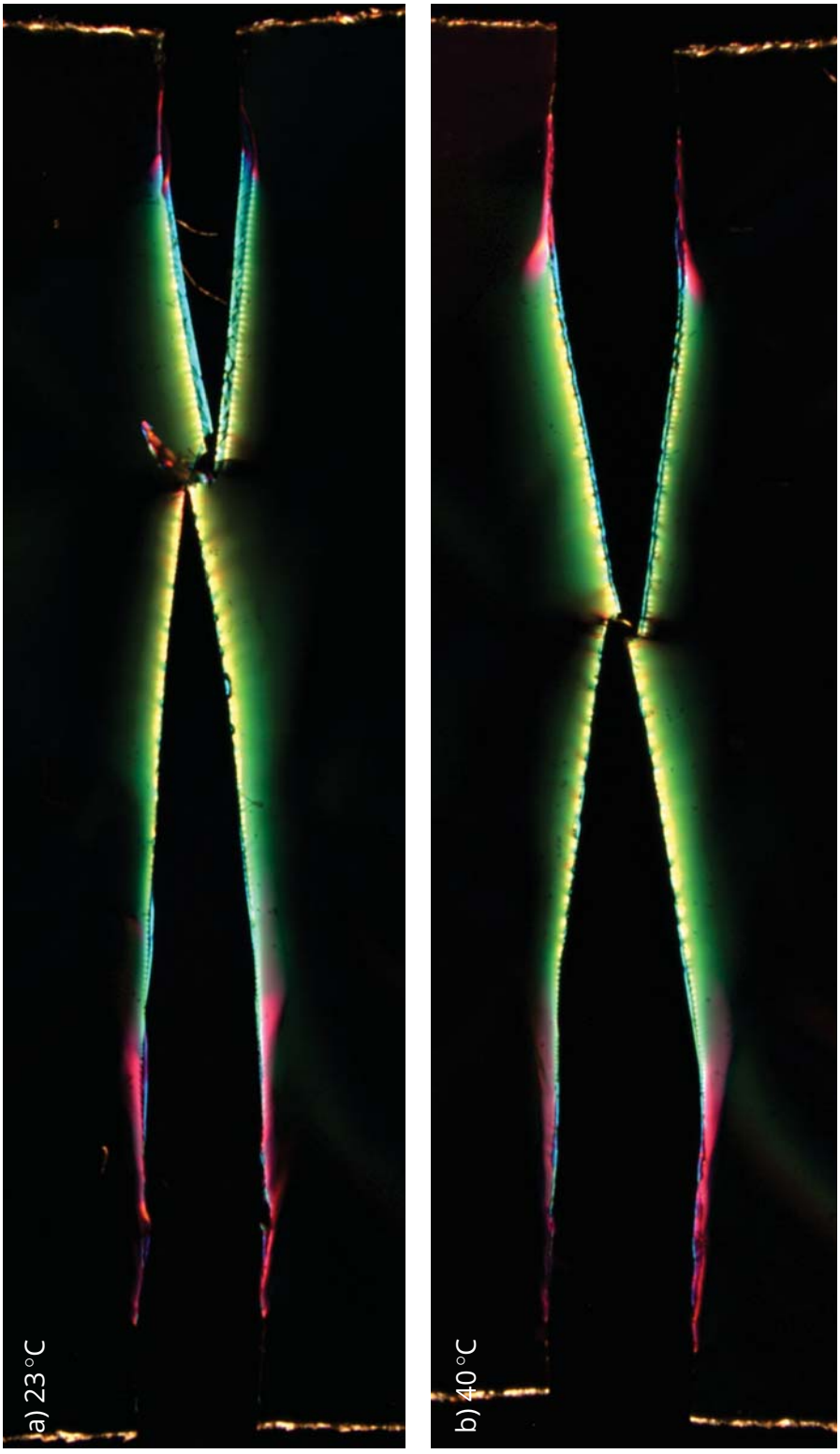

Figure 3.52: Polarized light microscopic images of fracture surfaces from temperature dependent fatigue tests with **3L$_{46}$**-PEEK$_{8}$I$_{30}$ containing a soft adhesive at a) 23 °C and b) 40 °C.

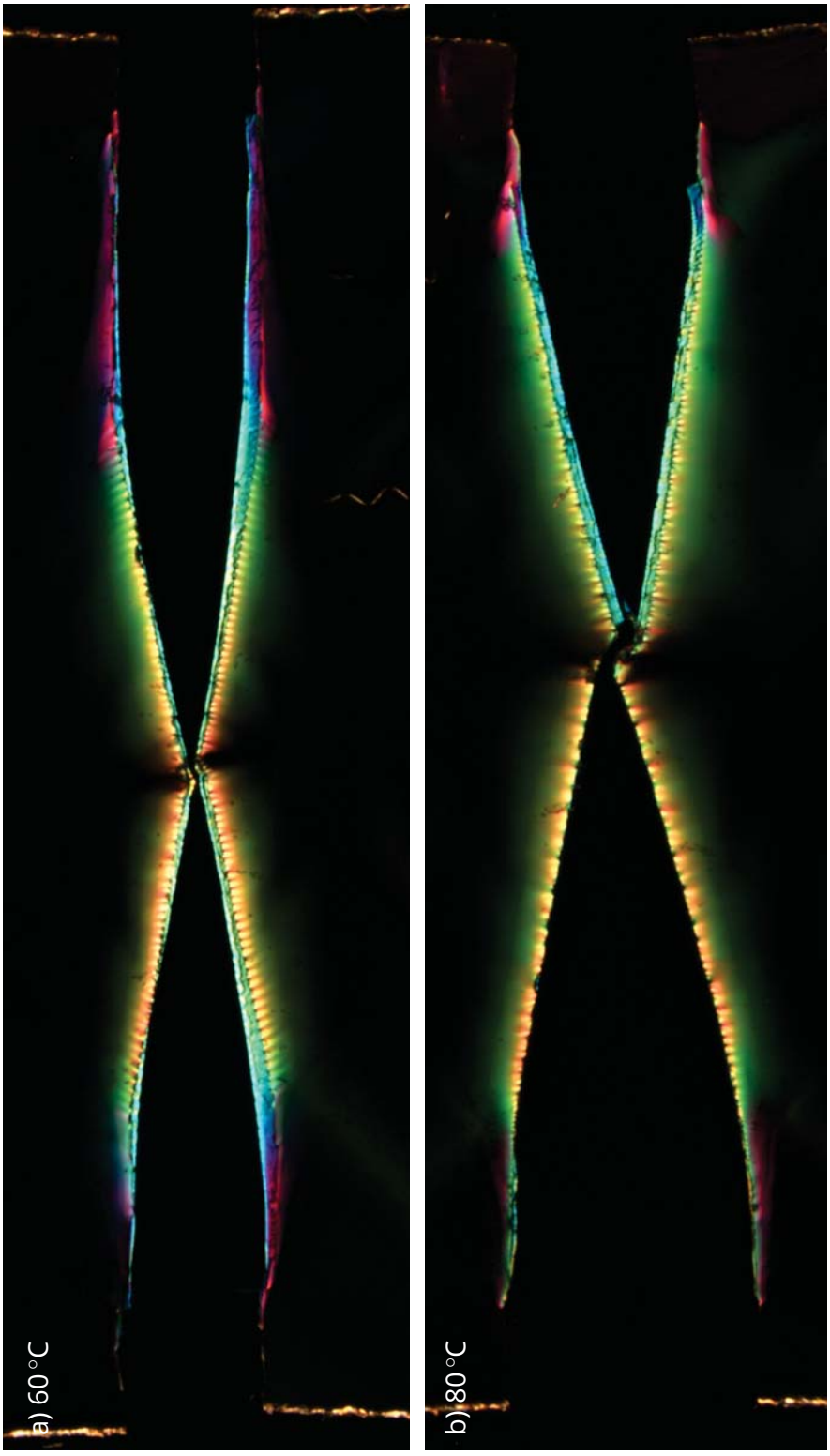

Figure 3.53: Polarized light microscopic images of fracture surfaces from temperature dependent fatigue tests with $\mathbf{3L_{46}}$-$PEEK_{8|30}$ containing a soft adhesive at a) 60 °C and b) 80 °C.

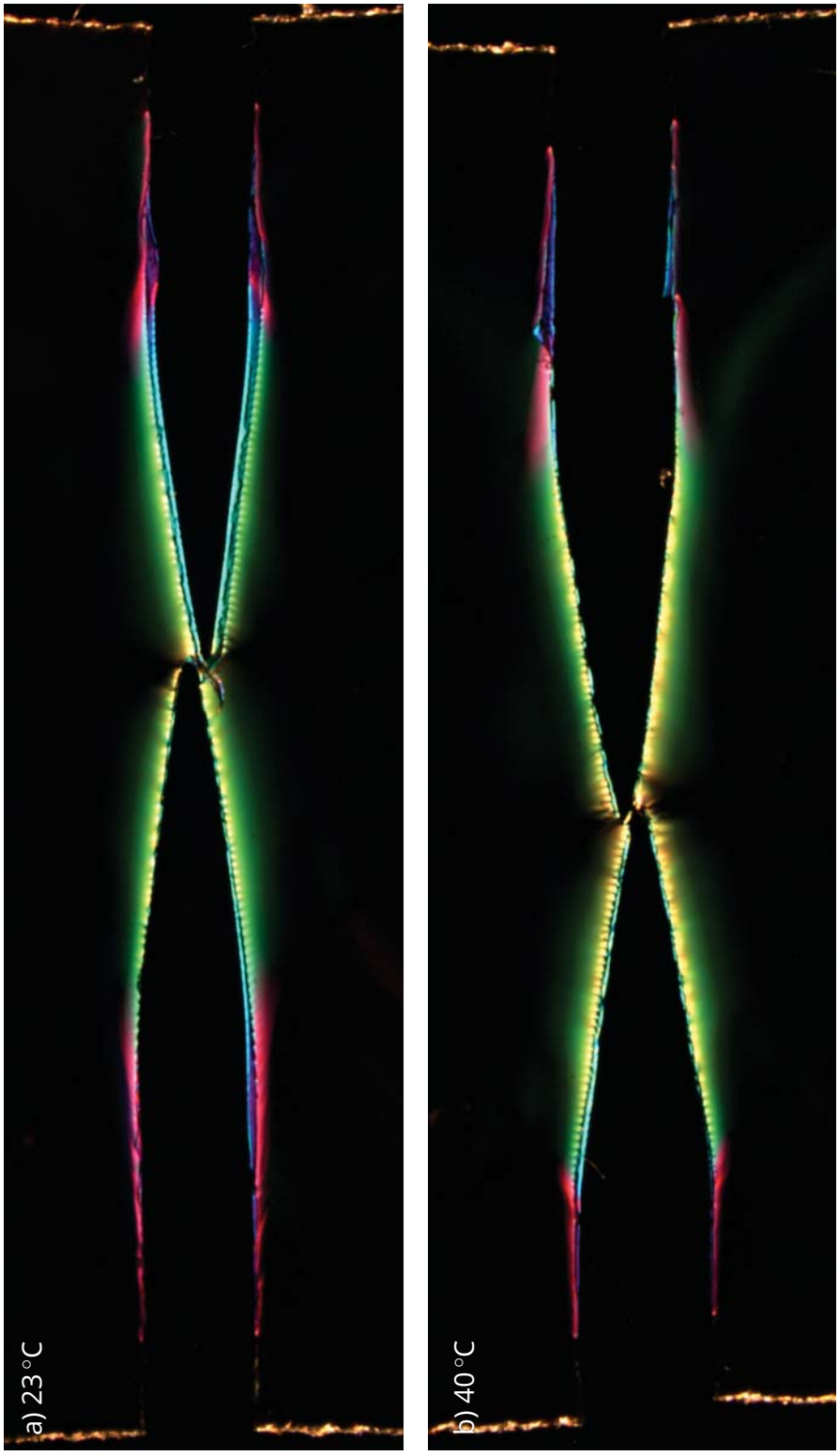

Figure 3.54: Polarized light microscopic images of fracture surfaces from temperature dependent fatigue tests with **3L$_{46}$**-PEEK$_{8J30}$ containing a stiff adhesive at a) 23 °C and b) 40 °C.

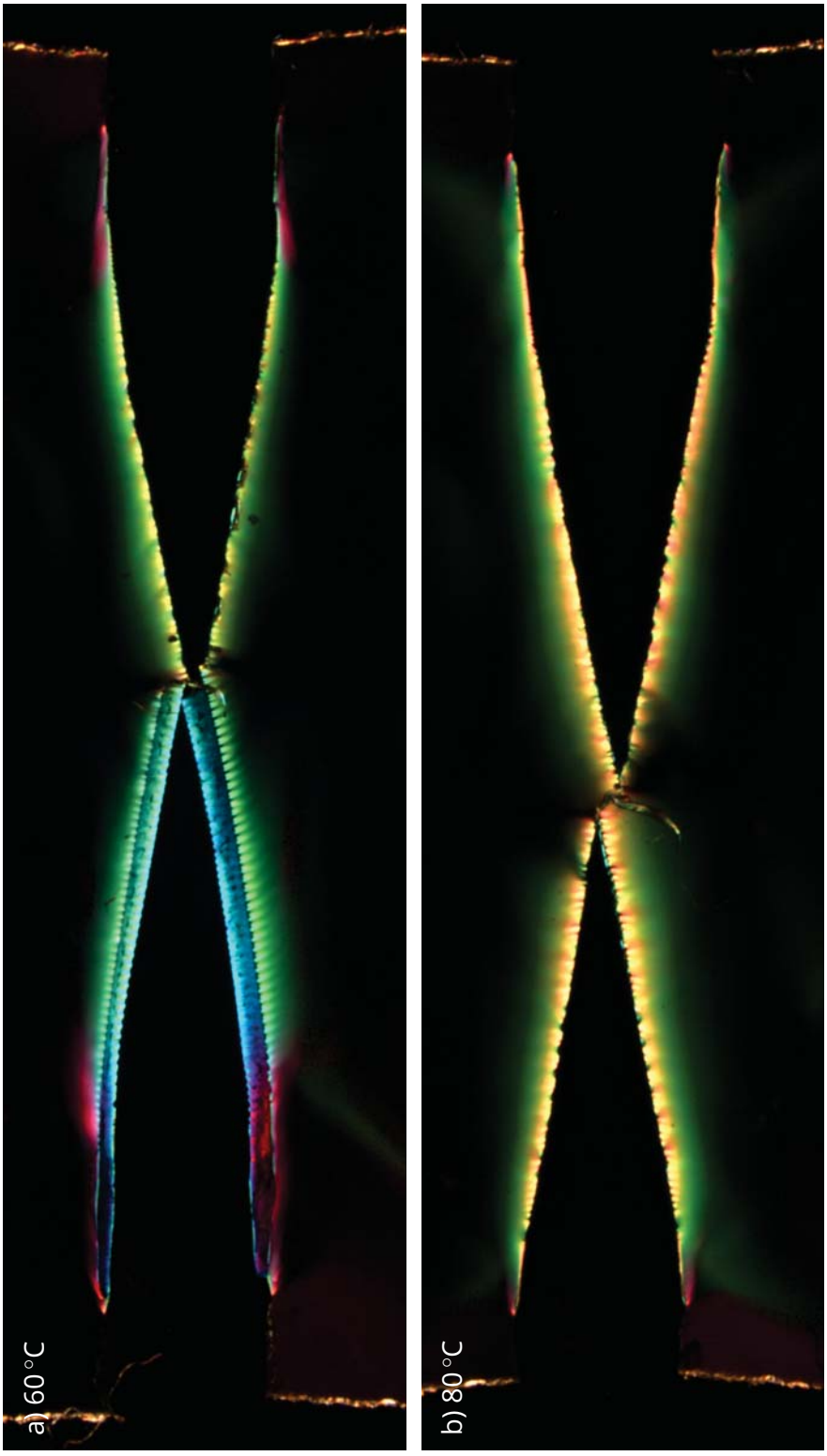

Figure 3.55: Polarized light microscopic images of fracture surfaces from temperature dependent fatigue tests with $\mathbf{3L_{46}}$-$PEEK_{8|30}$ containing a stiff adhesive at a) 60 °C and b) 80 °C.

3.4.5 Effect of anisotropy

Whereas state of the art PAR films exhibit a quasi-isotropic material behavior due to their production process of solvent casting, films with higher fracture toughness such as PEN, PEEK and PET are mainly produced via extrusion as explained in section 2.2. One main advantage is the economic efficiency of this process but this is accompanied by a strong anisotropic material behavior of these films. In order to achieve thicknesses down to the single value µm region the melt has to be drawn after the die. Due to the drawing process molecules are strongly oriented in the machine direction (i. e. extrusion direction). This also has a strong impact on the fracture and fatigue behavior of these films. Therefore, by measuring in machine direction, cracks have to grow perpendicular to the molecular orientation, whereas by measuring in transverse direction cracks grow parallel to the molecular orientation. Consequently the films show a higher fracture toughness when cracks have to grow perpendicular to the molecular orientation, as found by Maspoch et al. for PET films and Hashemi for high impact polystyrene (HIPS) films, both evaluated by EWF, Wu and Schultz for fracture toughness measurements with oriented PEEK samples and by Knapp et al. for high frequency fatigue tests with thin extruded films [43], [141], [165], [166].

In order to achieve a better understanding of the direction-dependent fatigue behavior of extruded films Wöhler and fatigue crack growth (FCG) tests with 3-layer laminates with PEEK outer layers (**3L$_{46}$**-PEEK$_8$L$_{30}$) using DENT specimens were carried out. They were prepared with a geometry of 15 mm $\times$ 45 mm $\times$ 0.5 mm (width W $\times$ clamping length Z $\times$ crack length a). The specimens were cut and tested in 0°, 45° and 90° to the machine direction. The tests and evaluations were then performed according to section 3.3.4 for three load levels $\Delta\sigma$ of 9.2 MPa, 11.5 MPa and 14.3 MPa at room temperature (23 °C). An overview of the laminate design is given in Table 3.5.

Table 3.5: Test materials.

Laminate	Layer type		Thickness t [µm]	
	1/3	2	1/3	2
3L$_{46}$-PEEK$_8$L$_{30}$	PEEK	adhesive L	8	30

Results of the direction dependent Wöhler tests are shown in Figure 3.56a) with fits for probabilities of failure of 5 %, 50 % and 95 % based on the $\arcsin\sqrt{P}$ method [126]–[128]. Whereas for tests in 0° and 45° to the extrusion direction only a minor load dependence of the cycles to failure N_f was found, the results in 90° showed a clear load dependence and also significantly higher scatter. Furthermore, in concordance with the literature, with the crack plane parallel to the processing direction in the 90° tests, significantly earlier failure occurred than when the crack had to grow perpendicular to the molecular orientation as in 0° tests. The results in 45° lay in between with a rather constant ratio of one order of magnitude lower N_f than in 0°.

In the evaluation of fatigue crack growth curves in Figure 3.56b) a different picture was found than in Wöhler tests. An indication that LEFM should be applicable to these PEEK films was obtained in monotonic tests in section 3.4.1 where a similar PEEK monolayer film showed brittle fatigue modes. For the multilayer films an apparent stress intensity was calculated for the whole cross section of the specimens. Since cracks left the crack planes in 0° and 45° tests the requirements of pure mode I loads are not met for the calculation of the stress intensities according to Equations 3.31 and 3.33. Nevertheless to ease the comparison throughout the tests in different load directions the deviations of crack growth out of the crack plane were neglected for the calculation of ΔK. In the FCG curves scatter was found in all test directions. In 0° tests FCG curves similar to those in the literature (Figure 3.14) were found with accelerating crack growth at low stress intensities ΔK followed by a region of stable crack growth and finally unstable

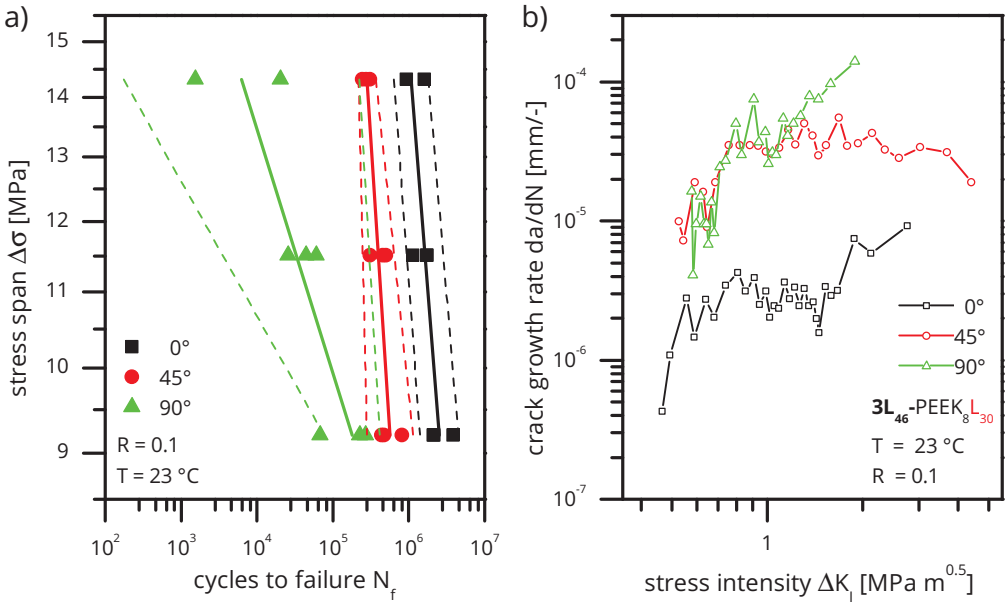

Figure 3.56: Results of direction dependent a) Wöhler tests and b) FCG tests with **3L$_{46}$**-PEEK$_8$L$_{30}$ with the load in 0°, 45° and 90° to the extrusion direction.

crack growth at high ΔK values. A similar behavior was obtained in 90° tests but at significantly higher crack growth rates and only a short period of stable crack growth from 0.7 MPa m$^{0.5}$ to 1.1 MPa m$^{0.5}$. In 45° nearly identical FCG curves as in 90° tests were found up to ΔK values of approximately 1.1 MPa m$^{0.5}$. Here also at low stress intensities ΔK crack growth accelerated, followed by a region of stable crack growth. But in contrast to the tests in 0° and 90° instead of the following unstable region beginning at approximately 1.6 MPa m$^{0.5}$ and 1.1 MPa m$^{0.5}$, respectively, in 45° tests the stable crack growth region reached up to ΔK values of 4.4 MPa m$^{0.5}$ with a final failure immediately following.

The reason for the differences in Wöhler and FCG tests was found in the optical documentation of the crack growth kinetics, which are depicted in Figures 3.57 and 3.58. Typically for tests with crack growth perpendicular to the molecular orientation, the specimen showed a ductile behavior with meander-like formations of the crack path in tests at 0° (Figure 3.57a). Since

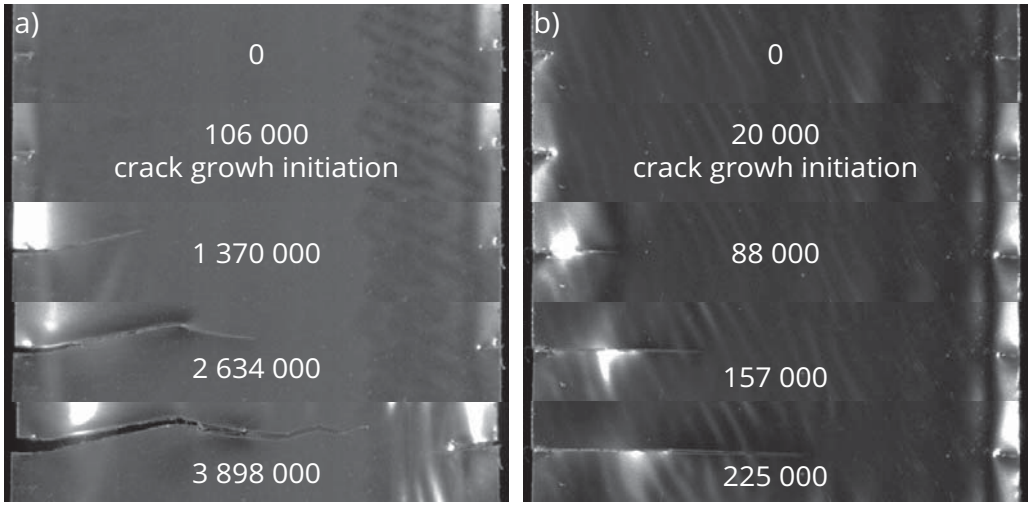

Figure 3.57: Optical documentation of the fatigue crack growth behavior with the load in a) 0° and b) 90° to the machine direction of the films and with a DENT geometry at a start value of ΔK = 0.38 MPa m$^{0.5}$, respectively.

the crack deviated from the crack plane mode II fracture was superimposed according to Equations 3.10 and 3.11. Since the crack growth changed its direction several times this resulted also in changing crack growth rates at each direction change as shown in the FCG evaluation in Figure 3.56b. Furthermore stop and go mechanisms occurred which led to further scatter. Also early crack growth initiation was revealed and therefore the fracture process was dominated by crack growth. In contrast at 90° (Figure 3.57b) a predominately brittle fatigue behavior was observed with crack growth strictly perpendicular to the load direction and also early crack growth initiation. Also here stop and go mechanisms occurred which led to scatter in the FCG evaluation.

In the tests with the extrusion direction of the films at 45° to the load direction a very interesting phenomenon was observed with crack growth at a strict angle throughout the test up until failure (Figure 3.58). Since the cracks were deflected at both sides, it was possible for them to grow until they nearly aligned one above the other before ultimate failure occurred.

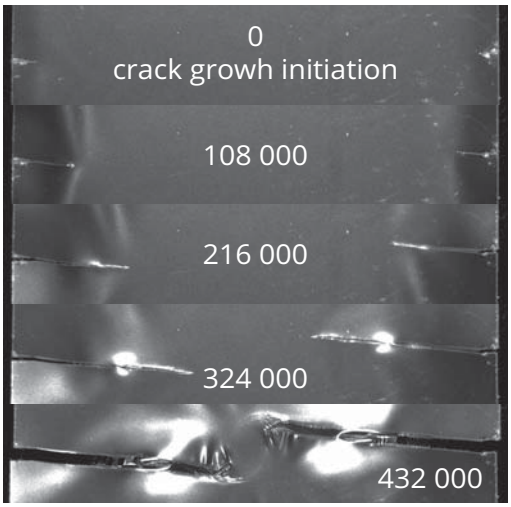

Figure 3.58: Optical documentation of the fatigue crack growth behavior with the load in 45° to the machine direction of the films and with a DENT geometry at a start value of ΔK = 0.38 MPa m$^{0.5}$.

Thus no unstable crack growth in the FCG curves occurred. The deflection of the crack growth path is thought to have resulted from a balance between the direction of the lowest crack growth resistance parallel to the molecular orientation at 45° to the load direction and the load direction itself. Additionally, due to the strong anisotropic material properties and the mismatch of load and molecular orientation in the 45° tests mode II loading of the cracks was superimposed and therefore also contributed to the balance. Induced from the deflection of the cracks along the molecular orientation they experienced almost the same low crack growth resistance as in the 90° tests. As a result the differences in the Wöhler curves between 45° and 90° tests resulted from significantly longer stable crack growth in the 45° samples.

In conclusion the anisotropic fracture toughness of extruded films described in the literature was also verified in this test for the fatigue behavior of thin PEEK laminates. The anisotropy is thought to have been induced by the extrusion process followed by drawing of the films which leads to a predominant molecular orientation in the machine direction. Furthermore

a deviation between results in Wöhler and FCG tests occurred in tests with the load at 45° to the processing direction. Whereas in Wöhler tests curves for the 45° were right in between the results for tests in 0° and 90°, in the FCG evaluations the 45° tests revealed the same low crack growth resistance results as tests at 90°. It was possible to attribute the latter effect to the deflection of crack growth along the molecular orientation, which also led to a similar low crack growth resistance as at 90° where crack growth occurred parallel to the molecular orientation. Finally it was possible to explain the differences between Wöhler and FCG curves between 45° and 90° tests with a significantly longer stable crack growth in the 45° samples.

3.5 Summary

A good fracture and fatigue behavior of thin polymer films for miniature speaker membranes is one of their main requirements. In monotonic pretests with double edge notched tension (DENT) specimens the films exhibited brittle fracture modes, therefore the usually applied testing method of essential work of fracture (EWF) was not applicable. Since also no differentiation between laminates was found, which showed a distinct differentiation in component tests, a cyclic fatigue test based on linear elastic fracture mechanics (LEFM) was implemented which operates at a frequency of 100 Hz. Additionally an optical system was attached to track the crack growth kinetics. The crack growth resistance of the thin films then was characterized with Wöhler and fatigue crack growth (FCG) tests.

By applying the crack tip similitude concept the applicability of LEFM for the cyclic fatigue of PAR, PC, PEI, PESU and PET films was checked. For this fatigue crack growth (FCG) tests with DENT and center cracked tension (CCT) specimens were performed and compared to see if, according to the crack tip similitude concept, matching FCG curves were found. In a next step process zone sizes of DENT and CCT specimens where the tests were

stopped after crack growth initiation were measured using polarized light microscopy and compared to theoretical values. For PAR, PESU and PET films matching FCG curves were obtained between both specimen geometries, respectively, but PC and PEI films showed significant deviations. Although process zones sizes in DENT specimens were discernible in PAR, PC and PEI and in CCT specimens only in PEI, these measured sizes matched well to theoretical values. In order to clarify the reason for the deviations in the FCG curves in PC in a next step simulations were done to determine the global and local stress distributions in the specimens and at the crack tips. Here it was found that in the PC films the K controlled region stretches up to approximately 0.25 mm behind the crack tip at ΔK=1 MPa m$^{0.5}$. Since plastic zone sizes at the same ΔK values are of a similar size, the requirement for LEFM of only a small scale plasticity might not be upheld for PC.

The effect of the temperature in the range between −20 °C to 100 °C to the fatigue behavior of PET films was evaluated with Wöhler and FCG curves with DENT specimens. Below the glass transition of PET a maximum of its crack growth resistance was revealed at 60 °C in Wöhler tests followed by a sharp decrease at higher temperatures. In FCG curves up to 80 °C, nearly identical curves were obtained with also a sharp decrease at higher temperatures. Similar results were reported by Novotny for other semicrystalline polymers and this was subsequently attributed to an increased mobility in their amorphous regions which led to an increased crack tip plasticity and consequently to a higher crack growth resistance [158]. Polarized light microscopic images of the fracture surfaces revealed a significant increase of plastic deformations at both the fracture surfaces and across the specimens. The first was ascribed to the increased crack tip plasticity, which contributed to an increased fatigue strength. However the latter phenomenon, especially found at elevated temperatures above the glass transition T_G is thought to stem from material softening at T_G and therefore a loss in fatigue strength. This was found to match findings from the literature, where in EWF tests PET

films exhibited a maximum of the non essential work of fracture w_p between 60 °C to 100 °C, which is ascribed to plastic deformations [26], [38], [41].

The effect of the multilayer design of state of the art miniature loudspeaker laminates was investigated by comparing the fracture energies involved in the fatigue and the delamination processes in PEEK multilayer films. Therefore temperature-dependent fatigue crack growth tests were performed with DENT specimens. It was found that, compared to a PEEK monolayer films without adhesive, an increase in crack growth resistance has been obtained in the multilayer laminates. In a next step the energy release rate G was calculated from ΔK values before ultimate failure. In order to evaluate the delamination behavior, T-peel tests with film strips were done and the associated adhesive fracture energy G_A was calculated. In the comparison of both energy values it was found that the G_A values were 10 to 1000 times lower than G values from fatigue tests and therefore delamination might have occurred at significantly lower loads than crack growth. But delaminations were not observed during fatigue tests and therefore were regarded as insignificant for the fatigue behavior. The occurrence of shear bands and discontinuous crack growth (DCG) in polarized light microscopic evaluations of the fracture surfaces correlated well to the temperature-dependent advantage of the multilayer over the monolayer films. Furthermore crack bridging due to slower crack growth in the adhesive damping layers was observed. This is thought to have additionally shielded the cracks and consequently contributed to the occurrence of DCG and shear bands. As a result a higher crack growth resistance of the multilayer compared to the monolayer PEEK films was measured.

The effect of anisotropic fatigue behavior of thin films induced by the process of extrusion was determined by Wöhler and fatigue crack growth tests with PEEK multilayer films. DENT specimens were cut and tested at 0°, 45° and 90° to the processing direction. As described in the literature the highest crack growth resistance was measured with 0° specimens where the cracks had to grow perpendicular to the molecular orientation and the lowest at 90°

with the crack growing parallel to the molecular orientation. Whereas Wöhler curves of 45° samples were right in between the 0° and 90° tests, in the FCG experiments the 45° samples showed the same low crack growth resistance as 90° samples but with significantly longer stable crack growth. The reason for this behavior was revealed in the optical documentation where crack growth in the 45° samples was deflected by the molecular orientation and therefore the cracks revealed stable crack growth up until the crack fronts were nearly vertically aligned. Consequently the deflection of crack growth resulted in the same low crack growth resistance but higher cycles to failure due to longer stable crack growth than in 90°.

References

[14] J. P. Trotignon, J. Verdu, C. Martin, and E. Morel, "Fatigue behaviour of some temperature-resistant polymers," *Journal of Materials Science*, vol. 28, no. 8, pp. 2207–2213, 1993, ISSN: 0022-2461. DOI: 10.1007/BF00367585.

[16] Victrex plc, *Victrex PEEK polymer for films*.

[18] K. Humer, E. K. Tschegg, and H. W. Weber, "Tensile, fracture and thermal properties of polyarylates at room and cryogenic temperatures," *Cryogenics*, vol. 33, no. 7, pp. 686–691, 1993, ISSN: 0011-2275. DOI: 10.1016/0011-2275(93)90020-0.

[23] S. Hashemi and D. O'Brien, "The essential work of plane-stress ductile fracture of poly(ether-ether ketone) thermoplastic," *Journal of Materials Science*, vol. 28, no. 15, pp. 3977–3982, 1993, ISSN: 0022-2461. DOI: 10.1007/BF00351217.

[26] A. Pegoretti and T. Ricco, "Rate and temperature effects on the plane stress essential work of fracture in semicrystalline pet," in *Fracture of polymers, composites, and adhesives II*, ser. ESIS publication, Blackman, B. R. K, A. Pavan, and J. G. Williams, Eds., vol. 32, Amsterdam and Boston: Elsevier, 2003, pp. 89–100, ISBN: 9780080441955. DOI: 10.1016/S1566-1369(03)80086-9.

[28] S. Hashemi, "Fracture toughness evaluation of ductile polymeric films," *Journal of Materials Science*, vol. 32, pp. 1563–1573, 1997, ISSN: 0022-2461. DOI: 10.1023/A:1018582707419.

[30] T. Bárány, T. Czigány, and J. Karger-Kocsis, "Application of the essential work of fracture (ewf) concept for polymers, related blends and composites: A review," *Progress in Polymer Science*, vol. 35, no. 10, pp. 1257–1287, 2010, ISSN: 00796700. DOI: 10.1016/j.progpolymsci.2010.07.001.

[34] S. Hashemi, "Plane-stress fracture of polycarbonate films," *Journal of Materials Science*, vol. 28, pp. 6178–6184, 1993, ISSN: 0022-2461. DOI: 10.1007/BF00365040.

[38] A. Arkhireyeva and S. Hashemi, "Determination of fracture toughness of poly (ethylene terephthalate) film by essential work of fracture and j integral measurements," *Plastics, Rubber and Composites*, vol. 30, no. 7, pp. 337–350, 2001. DOI: 10.1179/146580101322913257.

[39] A. Arkhireyeva and S. Hashemi, "Fracture behaviour of polyethylene naphthalate (pen)," *Polymer*, vol. 43, no. 2, pp. 289–300, 2002, ISSN: 00323861. DOI: 10.1016/S0032-3861(01)00623-1.

[41] S. Hashemi and A. Arkhireyeva, "Influence of temperature on work of fracture parameters in semi-crystalline polyester films," *Journal of Macromolecular Science, Part B*, vol. 41, no. 4, pp. 863–880, 2002. DOI: 10.1081/MB-120013070.

[42] S. Hashemi, "Effect of temperature on fracture toughness of an amorphous poly(ether-ether ketone) film using essential work of fracture analysis," *Polymer Testing*, vol. 22, no. 5, pp. 589–599, 2003, ISSN: 01429418. DOI: 10.1016/S0142-9418(02)00162-9.

[43] S. Hashemi, "Work of fracture of high impact polystyrene (hips) film under plane stress conditions," *Journal of Materials Science*, vol. 38, no. 14, pp. 3055–3062, 2003, ISSN: 0022-2461. DOI: 10.1023/A:1024752508458.

[52] M. E. Light and A. J. Lesser, "Effect of test conditions on the essential work of fracture in polyethylene terephthalate film," *Journal of Materials Science*, vol. 40, no. 11, pp. 2861–2866, 2005, ISSN: 0022-2461. DOI: 10.1007/s10853-005-2430-9.

[54] H. Zhao and R. K. Li, "Fracture behaviour of poly(ether ether ketone) films with different thicknesses," *Mechanics of Materials*, vol. 38, no. 1-2, pp. 100–110, 2006, ISSN: 01676636. DOI: 10.1016/j.mechmat.2005.05.013.

[74] D. Broek, *Elementary engineering fracture mechanics*. M. Nijhoff, 1982, ISBN: 9789024726561.

[75] R. W. Hertzberg, *Deformation and fracture mechanics of engineering materials*, 4th ed. New York: John Wiley & Sons, 1996, ISBN: 0471012149.

[76] R. W. Hertzberg and J. A. Manson, *Fatigue of engineering plastics*. New York: Academic Press, 1980, ISBN: 9780123435507.

[77] W. Brostow and R. D. Corneliussen, *Failure of plastics*. Munich, DE: Carl Hanser Verlag, 1986, ISBN: 3446141995.

[78] T. L. Anderson, *Fracture mechanics: Fundamentals and applications*, 3rd ed. Boca Raton, FL: Taylor & Francis, 2005, ISBN: 9780849316562.

[79] D. Gross and T. Seelig, "Lineare bruchmechanik," in *Bruchmechanik*, Springer Berlin Heidelberg, 2011, pp. 65–149, ISBN: 978-3-642-10196-0. DOI: 10.1007/978-3-642-10196-0_4.

[80] J. Larmor, "The influence of flaws and air-cavities on the strength of materials," *Philosophical Magazine Series 5*, vol. 33, no. 200, pp. 70–78, 1892, ISSN: 1941-5982. DOI: 10.1080/14786449208620233.

[81] A. A. Griffith, "The phenomena of rupture and flow in solids," *Philosophical Transactions of the Royal Society A: Mathematical, Physical and Engineering Sciences*, vol. 221, no. 582-593, pp. 163–198, 1921, ISSN: 1364-503X. DOI: 10.1098/rsta.1921.0006.

[82] H. M. Westergaard, "Bearing pressures and cracks: Bearing pressures through a slightly waved surface of trhough a nearly flat part of a cylinder, and related problems of cracks," *Journal of applied mechanics*, vol. 49, pp. 49–53, 1939.

[83] I. N. Sneddon, "The distribution of stress in the neighbourhood of a crack in an elastic solid," *Proceedings of the Royal Society A: Mathematical, Physical and Engineering Sciences*, vol. 187, no. 1009, pp. 229–260, 1946, ISSN: 1364-5021. DOI: 10.1098/rspa.1946.0077.

[84] G. R. Irwin, "Analysis of stresses and strains near the end of a crack traversing a plate," *J. appl. Mech*, 1957.

[85] M. L. Williams, "On the stress distribution at the base of a stationary crack," *Journal of applied mechanics*, vol. 24, pp. 109–114, 1957.

[86] C. E. Inglis, "Stress in a plate due to the presence of sharp corners and cracks," *Transaction of Naval Architects (Trans. Roy. Inst. Naval Architects)*, vol. 60, pp. 219–241, 1913.

[87] J. G. Williams, "Introduction to linear elastic fracture mechanics," in *Fracture mechanics testing methods for polymers, adhesives, and composites*, ser. ESIS publication, D. R. Moore, A. Pavan, and J. G. Williams, Eds., vol. 28, Amsterdam and New York: Elsevier, 2001, pp. 3–10, ISBN: 9780080436890. DOI: 10.1016/S1566-1369(01)80024-8.

[88] G. R. Irwin, "Onset of fast crack propagation in high strength steel and aluminum alloys," in *Sagamore Research Conference Proceedings*, vol. 2, 1956, pp. 289–305.

[89] Y. Murakami, *Stress intensity factors handbook*. Oxford: Pergamon Press, 1987.

[90] G. R. Irwin, "Fracture mode transition for a crack traversing a plate," *Journal of Basic Engineering*, vol. 82, no. 2, p. 417, 1960. DOI: 10.1115/1.3662608.

[91] F. A. McClintock and G. R. Irwin, "Plasticity aspects of fracture mechanics," in *Fracture toughness testing and its applications*, J. R. Low and W. F. Brown, Eds., ser. ASTM STP 381, Philadelphia, PA: American Society for Testing and Materials, 1965, pp. 84–113, ISBN: 978-0-8031-0105-0.

[92] D. S. Dugdale, "Yielding of steel sheets containing slits," *Journal of the Mechanics and Physics of Solids*, vol. 8, no. 2, pp. 100–104, 1960, ISSN: 00225096. DOI: 10.1016/0022-5096(60)90013-2.

[93] W. F. J. Brown and J. E. Srawley, Eds., *Plane Strain Crack Toughness Testing of High Strength Metallic Materials*, ser. ASTM STP 410, Philadelphia, PA: American Society for Testing and Materials, 1966, ISBN: 978-0-8031-6215-0. DOI: 10.1520/STP410-EB.

[94] American Society for Testing and Materials ASTM E 399-12e3, *Standard test method for linear-elastic plane-strain fracture toughness kic of metallic materials*, West Conshohocken, PA, 2012. DOI: 10.1520/E0399.

[95] American Society for Testing and Materials ASTM D5045-99(2007)e1, *Test methods for plane-strain fracture toughness and strain energy release rate of plastic materials*, West Conshohocken, PA, 2007. DOI: 10.1520/D5045-99R07E01.

[96] S. Hashemi and Z. Yuan, "Fracture of poly(ether-ether ketone) films," *Plastics, Rubber and Composites Processing and Applications*, vol. 21, no. 3, pp. 151–161, 1994.

[97] D. R. Bloyer, Venkateswara Rao, K. T., and R. O. Ritchie, "Laminated nb/nb3al composites: Effect of layer thickness on fatigue and fracture behavior," *Materials Science and Engineering: A*, vol. 239-240, pp. 393–398, 1997, ISSN: 0921-5093. DOI: 10.1016/S0921-5093(97)00608-4.

[98] D. R. Bloyer, R. O. Ritchie, and Venkateswara Rao, K. T., "Fracture toughness and r-curve behavior of laminated brittle-matrix composites," *Metallurgical and Materials Transactions A*, vol. 29, no. 10, pp. 2483–2496, 1998, ISSN: 1073-5623. DOI: 10.1007/s11661-998-0220-0.

[99] D. R. Bloyer, R. O. Ritchie, and Venkateswara Rao, K. T., "Fatigue-crack propagation behavior of ductile/brittle laminated composites," *Metallurgical and Materials Transactions A*, vol. 30, no. 3, pp. 633–642, 1999, ISSN: 1073-5623. DOI: 10.1007/s11661-999-0055-3.

[100] R. R. Adharapurapu, K. S. Vecchio, F. Jiang, and A. Rohatgi, "Effects of ductile laminate thickness, volume fraction, and orientation on fatigue-crack propagation in ti-al3ti metal-intermetallic laminate composites," *Metallurgical and Materials Transactions A*, vol. 36, no. 6, pp. 1595–1608, 2005, ISSN: 1073-5623. DOI: 10.1007/s11661-005-0251-8.

[101] T. Fett and D. Munz, *Stress intensity factors and weight functions*, ser. International series on advances in fracture. Southampton, UK and Boston, Mass. USA: Computational Mechanics Publications, 1997, ISBN: 978-1853124976.

[102] B. N. Cox and D. B. Marshall, "Stable and unstable solutions for bridged cracks in various specimens," *Acta Metallurgica et Materialia*, vol. 39, no. 4, pp. 579–589, 1991, ISSN: 09567151. DOI: 10.1016/0956-7151(91)90126-L.

[103] B. N. Cox and C. S. Lo, "Load ratio, notch, and scale effects for bridged cracks in fibrous composites," *Acta Metallurgica et Materialia*, vol. 40, no. 1, pp. 69–80, 1992, ISSN: 09567151. DOI: 10.1016/0956-7151(92)90200-X.

[104] F. Erdogan and P. F. Joseph, "Toughening of ceramics through crack bridging by ductile particles," *Journal of the American Ceramic Society*, vol. 72, no. 2, pp. 262–270, 1989. DOI: 10.1111/j.1151-2916.1989.tb06112.x.

[105] R. M. Foote, Y.-W. Mai, and B. Cotterell, "Crack growth resistance curves in strain-softening materials," *Journal of the Mechanics and Physics of Solids*, vol. 34, no. 6, pp. 593–607, 1986, ISSN: 00225096. DOI: 10.1016/0022-5096(86)90039-6.

[106] A. C. Kaya and F. Erdogan, "Stress intensity factors and cod in an orthotropic strip," *International Journal of Fracture*, vol. 16, no. 2, pp. 171–190, 1980, ISSN: 0376-9429. DOI: 10.1007/BF00012620.

[107] F. Zok and C. L. Hom, "Large scale bridging in brittle matrix composites," *Acta Metallurgica et Materialia*, vol. 38, no. 10, pp. 1895–1904, 1990, ISSN: 09567151. DOI: 10.1016/0956-7151(90)90301-V.

[108] American Society for Testing and Materials ASTM D1876-08, *Test method for peel resistance of adhesives (t-peel test)*, West Conshohocken, PA, 2008. DOI: 10.1520/D1876-08.

[109] A. J. Kinloch, C. C. Lau, and J. G. Williams, "The peeling of flexible laminates," *International Journal of Fracture*, vol. 66, no. 1, pp. 45–70, 1994, ISSN: 0376-9429. DOI: 10.1007/bf00012635.

[110] D. R. Moore and J. G. Williams, *A protocol for determination of the adhesive fracture toughness by peel testing of flexible laminates*, 2000.

[111] D. R. Moore and J. G. Williams, "Peel testing of flexible laminates," in *Fracture mechanics testing methods for polymers, adhesives, and composites*, ser. ESIS publication, D. R. Moore, A. Pavan, and J. G. Williams, Eds., vol. 28, Amsterdam and New York: Elsevier, 2001, pp. 203–223, ISBN: 9780080436890. DOI: 10.1016/S1566-1369(01)80035-2.

[112] D. R. Moore, "Peel strength and adhesive fractur toughness," in *The application of fracture mechanics to polymers, adhesives and composites*, ser. ESIS publication, D. R. Moore, Ed., vol. 33, Amsterdam and Boston: Elsevier, 2004, pp. 131–136, ISBN: 9780080553078.

[113] L. F. Kawashita, D. R. Moore, and J. G. Williams, "Protocols for the measurement of adhesive fracture toughness by peel tests," *The Journal of Adhesion*, vol. 82, no. 10, pp. 973–995, 2006. DOI: 10.1080/00218460600876142.

[114] D. R. Moore, "An introduction to the special issue on peel testing," *International Journal of Adhesion and Adhesives*, vol. 28, no. 4-5, pp. 153–157, 2008, ISSN: 0143-7496. DOI: 10.1016/j.ijadhadh.2007.01.001.

[115] D. R. Moore and J. G. Williams, *A protocol for determination of the interfacial work of fracture by peel testing of flexible laminates*. [Online]. Available: https://workspace.imperial.ac.uk/meadhesion/Public/ESIS%20peel%20protocol%20(June%2007)-revised%20Nov%202010.pdf.

[116] M. A. Meyers and K. K. Chawla, *Mechanical behavior of materials*, 2nd ed. Cambridge and New York: Cambridge University Press, 2009, ISBN: 9780511455575.

[117] J. P. Benthem and W. T. Koiter, "Asymptotic approximations to crack problems," in *Methods of analysis and solutions of crack problems*, ser. Mechanics of Fracture, G. C. Sih, Ed., vol. 1, Dordrecht: Springer Netherlands, 1973, pp. 131–178, ISBN: 978-90-481-8246-6. DOI: 10.1007/978-94-017-2260-5_3.

[118] C. E. Feddersen, "Discussions to: Okabe's strain crack toughness testing of metallic materials," in *Plane Strain Crack Toughness Testing of High Strength Metallic Materials*, W. F. J. Brown and J. E. Srawley, Eds., ser. ASTM STP 410, Philadelphia, PA: American Society for Testing and Materials, 1966, p. 77, ISBN: 978-0-8031-6215-0.

[119] H. Tada, "A note on the finite width corrections to the stress intensity factor," *Engineering Fracture Mechanics*, vol. 3, no. 3, pp. 345–347, 1971. DOI: 10.1016/0013-7944(71)90043-9.

[120] G. Pinter, *Fracture mechanics of plastics and composites*.

[121] E. Haibach, *Betriebsfestigkeit: Verfahren und Daten zur Bauteilberechnung*. 2006.

[122] Deutsches Institut für Normung DIN 50100:1978-02, *Testing of materials; continuous vibration test; definitions, symbols, procedure, evaluation*, Berlin, 1978.

[123] A. Wöhler, "Versuche über die festigkeit der eisenbahnwagenachsen," *Zeitschrift für Bauwesen*, vol. 10, pp. 160–161, 1860.

[124] O. H. Basquin, "The exponential law of endurance tests," in *Proc. ASTM*, vol. 10, 1910, pp. 625–630.

[125] American Society for Testing and Materials ASTM E 739 - 91, *Practice for statistical analysis of linear or linearized stress-life (s-n) and strain-life (-n) fatigue data*, West Conshohocken, PA, 1991. DOI: 10.1520/E0739-10.

[126] D. Dengel, "Die arc sin p-transformation—ein einfaches verfahren zur grafischen und rechnerischen auswertung geplanter wöhlerversuche," *Materialwissenschaft und Werkstofftechnik*, vol. 6, no. 8, pp. 253–261, 1975.

[127] D. Dengel, "Empfehlungen für die statistische abschätzung des zeit- und dauerfestigkeitsverhaltens von stahl," *Materialwissenschaft und Werkstofftechnik*, vol. 20, no. 3, pp. 73–81, 1989.

[128] D. Dengel and M. Karim Khani, "Arc sin p- transformation - an effective tool for graphical and numerical evaluation of planned wöhler experiments," *International Journal of Fracture*, vol. 80, no. 4, pp. 339–351, 1996, ISSN: 0376-9429. DOI: 10.1007/BF00018511.

[129] P. C. Paris and F. Erdogan, "A critical analysis of crack propagation laws," *Journal of Basic Engineering*, vol. 85, no. 4, pp. 528–533, 1963. DOI: 10.1115/1.3656900.

[130] L. Castellani and M. Rink, "Fatigue crack growth of polymers," in *Fracture mechanics testing methods for polymers, adhesives, and composites*, ser. ESIS publication, D. R. Moore, A. Pavan, and J. G. Williams, Eds., vol. 28, Amsterdam and New York: Elsevier, 2001, pp. 91–97, ISBN: 9780080436890. DOI: 10.1016/S1566-1369(01)80029-7.

[131] American Society for Testing and Materials ASTM E 647-00, *Standard test method for measurement of fatigue crack growth rates*, West Conshohocken, PA, 2000. DOI: 10.1520/E0647.

[132] M. Berer and G. Pinter, "Determination of crack growth kinetics in non-reinforced semi-crystalline thermoplastics using the linear elastic fracture mechanics (lefm) approach," *Polymer Testing*, vol. 32, no. 5, pp. 870–879, 2013, ISSN: 01429418. DOI: 10.1016/j.polymertesting.2013.03.022.

[133] M. Berer, G. Pinter, and M. Feuchter, "Fracture mechanical analysis of two commercial polyoxymethylene homopolymer resins," *Journal of Applied Polymer Science*, vol. 131, no. 19, n/a, 2014, ISSN: 00218995. DOI: 10.1002/app.40831. [Online]. Available: http://dx.doi.org/10.1002/app.40831.

[134] International Organisation for Standardisation ISO 15850:2002, *Plastics - determination of tension-tension fatigue crack propagation - linear elastic fracture mechanics (lefm) approach*, Berlin, DE, 2002. [Online]. Available: http://www.beuth.de/de/norm-entwurf/iso-15850-dam-1/140493051.

[135] M. M. Novotny, "Fatigue crack propagation in engineering thermoplastics - effects of temperature and short fiber reinforcement," PhD thesis, University of Leoben, Leoben, AUT, 1997.

[136] B.-A. Zahnt, "Fatigue behavior of discontinous glassfiber reinforced plastics: Characterization methods, material laws and structureal-property-relationships," PhD thesis, Montanuniversität Leoben, Austria, 2003.

[137] L. F. Kawashita, *Ic peel*, 2007. [Online]. Available: http://www3.imperial.ac.uk/pls/portallive/docs/1/17285696.XLS.

[138] A. Arkhireyeva and S. Hashemi, "Effect of temperature on work of fracture parameters in poly(ether-ether ketone) (peek) film," *Engineering Fracture Mechanics*, vol. 71, no. 4–6, pp. 789–804, 2004. DOI: 10.1016/S0013-7944(03)00010-9.

[139] D. P. Jones, D. C. Leach, and D. R. Moore, "Mechanical properties of poly(ether-ether-ketone) for engineering applications," *Polymer*, vol. 26, pp. 1385–1393, 1985, ISSN: 00323861.

[140] J. Karger-Kocsis and K. Friedrich, "Temperature and strain-rate effects on the fracture toughness of poly(ether ether ketone) and its short glass-fibre reinforced composite," *Polymer*, vol. 27, no. 11, pp. 1753–1760, 1986, ISSN: 00323861. DOI: 10.1016/0032-3861(86)90272-7.

[141] G.-M. Wu and J. M. Schultz, "Fracture behavior of oriented poly(ether-ether-ketone) (peek)," *Polymer Engineering & Science*, vol. 29, no. 6, pp. 405–414, 1989, ISSN: 00323888. DOI: 10.1002/pen.760290609.

[142] P. J. Rae, E. N. Brown, and E. B. Orler, "The mechanical properties of poly(ether-ether-ketone) (peek) with emphasis on the large compressive strain response," *Polymer*, vol. 48, no. 2, pp. 598–615, 2007, ISSN: 00323861. DOI: 10.1016/j.polymer.2006.11.032.

[143] K. Friedrich, "Stress corrosion crack propagation in glass fibre reinforced/thermoplastic pet," *Journal of Materials Science*, vol. 16, no. 12, pp. 3292–3302, 1981, ISSN: 0022-2461. DOI: 10.1007/BF00586289.

[144] K. Friedrich, "Microstructural efficiency and fracture toughness of short fiber/thermoplastic matrix composites," *Composites Science and Technology*, vol. 22, no. 1, pp. 43–74, 1985, ISSN: 02663538. DOI: 10.1016/0266-3538(85)90090-9.

[145] T. J. Pecorini and R. W. Hertzberg, "The fracture toughness and fatigue crack propagation behaviour of annealed pet," *Polymer*, vol. 34, no. 24, pp. 5053–5062, 1993, ISSN: 00323861. DOI: 10.1016/0032-3861(93)90248-9.

[146] J. J. Osorio-Ramos, E. R. García, V. Cortés-Suarez, and E. Rocha-Rangel, "Fracture mechanics of recycled pet-based composite materials reinforced with zinc particles," in *Processing and Properties of Advanced Ceramics and Composites V*, N. P. Bansal, J. P. Singh, S. W. Ko, R. H. R. Castro, G. Pickrell, N. J. Manjooran, K. M. Nair, and G. Singh, Eds., Hoboken, NJ, USA: John Wiley & Sons, Inc, 2013, pp. 55–62, ISBN: 9781118744109. DOI: 10.1002/9781118744109.ch6.

[147] Goodfellow Cambridge Ltd., *Polyethylene naphthalate (PEN): Material information*. [Online]. Available: http://www.goodfellow.com/E/Polyethylene-naphthalate-Film.html.

[148] R. W. Lang, W. Balika, and G. Pinter, "Applicability of linear elastic fracture mechanics to fatigue in amorphous and semi-crystalline polymers," in *The application of fracture mechanics to polymers, adhesives and composites*, ser. ESIS publication, D. R. Moore, Ed., vol. 33, Amsterdam and Boston: Elsevier, 2004, pp. 83–92, ISBN: 9780080553078.

[149] R. H. Dodds, T. L. Anderson, and M. T. Kirk, "A framework to correlate a/w ratio effects on elastic-plastic fracture toughness (j c)," *International Journal of Fracture*, vol. 48, no. 1, pp. 1–22, 1991, ISSN: 0376-9429. DOI: 10.1007/BF00012499.

[150] K. Friedrich, "Crazes and shear bands in semi-crystalline thermoplastics," in *Crazing in Polymers*, ser. Advances in Polymer Science, H.-H. Kausch, Ed., vol. 52-53, Springer Berlin / Heidelberg, 1983, pp. 225–274, ISBN: 978-3-540-12571-6. DOI: 10.1007/BFb0024059. [Online]. Available: http://dx.doi.org/10.1007/BFb0024059.

[151] N. J. Mills, "Dugdale yielded zones in cracked sheets of glassy polymers," *Engineering Fracture Mechanics*, vol. 6, no. 3, pp. 537–549, 1974. DOI: 10.1016/0013-7944(74)90010-1.

[152] P. S. Theocaris and E. E. Gdoutos, "The size of plastic zones in cracked plates made of polycarbonate," *Experimental Mechanics*, vol. 15, no. 5, pp. 169–176, 1975, ISSN: 0014-4851. DOI: 10.1007/BF02319142.

[153] R. Fraser and I. Ward, "Temperature dependence of craze shape and fracture in polycarbonate," *Polymer*, vol. 19, no. 2, pp. 220–224, 1978, ISSN: 00323861. DOI: 10.1016/0032-3861(78)90043-5.

[154] G. L. Pitman and I. Ward, "Effect of molecular weight on craze shape and fracture toughness in polycarbonate," *Polymer*, vol. 20, no. 7, pp. 895–902, 1979, ISSN: 00323861. DOI: 10.1016/0032-3861(79)90130-7.

[155] P.-P. Cortet, L. Vanel, and S. Ciliberto, "Dynamical law for slow crack growth in polycarbonate films," *Physical Review Letters*, vol. 99, no. 20, 2007, ISSN: 0031-9007. DOI: 10.1103/PhysRevLett.99.205502.

[156] H. F. Brinson, "The ductile fracture of polycarbonate," *Experimental Mechanics*, vol. 10, no. 2, pp. 72–77, 1970, ISSN: 0014-4851. DOI: 10.1007/BF02320135.

[157] K. Noda, A. Takahara, and T. Kajiyama, "Fatigue failure mechanisms of short glass-fiber reinforced nylon 66 based on nonlinear dynamic viscoelastic measurement," *Polymer*, vol. 42, no. 13, pp. 5803–5811, 2001, ISSN: 00323861. DOI: 10.1016/S0032-3861(00)00897-1. [Online]. Available: http://www.sciencedirect.com/science/article/pii/S0032386100008971.

[158] M. M. Novotny, "Ermüdungsrissausbreitung in technischen thermoplasten - einfluss der temperatur und der kurzfaserverstärkung," PhD thesis, University of Leoben, Leoben, AUT, 1997.

[159] G. Oreski and G. M. Wallner, "Delamination behaviour of multi-layer films for pv encapsulation," *Solar Energy Materials and Solar Cells*, vol. 89, no. 2-3, pp. 139–151, 2005. DOI: 10.1016/j.solmat.2005.02.009.

[160] H. Zhou, "Interlayer delamination and adhesion of coextruded films," *Journal of Applied Polymer Science*, vol. 92, no. 6, pp. 3901–3909, 2004, ISSN: 00218995. DOI: 10.1002/app.20419.

[161] C. J. G. Plummer and H.-H. Kausch, "Deformation of thin films of poly(ether ether ketone)," *Polymer*, vol. 34, no. 2, pp. 305–311, 1993, ISSN: 00323861. DOI: 10.1016/0032-3861(93)90081-K. [Online]. Available: http://www.sciencedirect.com/science/article/pii/003238619390081K.

[162] C. J. G. Plummer, N. Cudré-Mauroux, and H.-H. Kausch, "Deformation and entanglement in semicrystalline polymers," *Polymer Engineering & Science*, vol. 34, no. 4, pp. 318–329, 1994, ISSN: 00323888. DOI: 10.1002/pen.760340414. [Online]. Available: http://dx.doi.org/10.1002/pen.760340414.

[163] M. T. Takemori and D. S. Matsumoto, "An unusual fatigue crack-tip plastic zone: The epsilon plastic zone of polycarbonate," *Journal of Polymer Science: Polymer Physics Edition*, vol. 20, no. 11, pp. 2027–2040, 1982, ISSN: 00981273. DOI: 10.1002/pol.1982.180201105.

[164] M. T. Takemori, "Competition between crazing and shear flow during fatigue," in *Crazing in Polymers Vol. 2*, ser. Advances in Polymer Science, H.-H. Kausch, Ed., vol. 91/92, Springer Berlin / Heidelberg, 1990, pp. 263–300, ISBN: 978-3-540-51306-3. DOI: 10.1007/BFb0018023. [Online]. Available: http://dx.doi.org/10.1007/BFb0018023.

[165] M. L. Maspoch, V. Hénault, D. Ferrer-Balas, J. I. Velasco, and O. O. Santana, "Essential work of fracture on pet films: Influence of the thickness and the orientation," *Polymer Testing*, vol. 19, no. 5, pp. 559–568, 2000, ISSN: 01429418. DOI: 10.1016/S0142-9418(99)00026-4.

[166] G. Knapp, G. Oreski, and G. Pinter, "New method of characterizing the fatigue behavior of thin films for acoustic applications at high frequencies," in *Proceedings 71st Annual Technical Conference - ANTEC 2013*, vol. 2, Brookfield: Society of Plastics Engineers, 2013, pp. 1600–1604, ISBN: 978-1-63266-530-0. [Online]. Available: http://legacy.4spe.org/conferences/antec2013/papers/1591442.pdf.

4 Damping characterization of thin polymer films for acoustic applications

4.1 Introduction

The damping behavior of thin polymer films used as membranes in miniature loudspeakers is one of their key features in order to guarantee an excellent sound quality and protect the speaker from high dynamic loads at resonance (section 2.4). In order to ensure a good speaker design, therefore, knowledge of the damping behavior is indispensable. Since state of the art systems cannot provide detailed insights into the damping behavior of these films at application-relevant conditions over a wide frequency and temperature range (section 2.4.2), in this work new methods are introduced to overcome this drawback. In section 4.2 the theoretical background of passive damping designs is explained and effects of different design parameters are discussed. Furthermore the frequency-temperature dependence of glass and secondary transitions is explained. Based on this in section 4.3, new methods based on dynamic mechanical analysis (DMA) are introduced for the characterization of the damping behavior of thin miniature speaker films with the frequency and temperature dependent mechanical loss factor $\tan\delta(f,T)$. For comparative studies of different damping designs, the methods of dynamic mechanical analysis (DMA) in ”speaker” mode is introduced in section 4.3.2, where, based on a dual cantilever setup, the specimen is formed to mimic the supports of miniature speakers. Consequently in this

test the specimens are tested under bending deformations similar to the conditions in application. Furthermore in section 4.3.3 a setup in DMA shear mode is presented for an optimized characterization of constrained layer damping (CLD) laminates where damping occurs due to shear deformation of the adhesive damping layer. In application, damping has to be ensured at up to 1000 Hz but the DMA setups are not capable of performing tests at these conditions. Thus the theoretical approach of time temperature superposition principle (TTSP) is used to perform extrapolations as described in section 4.3.4. In a last step the damping behavior is evaluated with the normalized loss factor over the application relevant temperatures $\overline{tA}$ which is explained in section 4.3.5. Different damping designs such as a monolayer film, a free layer damping (FLD) and a constrained layer damping (CLD) laminate are characterized in DMA "speaker" mode in section 4.4.1. The influence of different polymers as constraining layers in CLD laminates in the evaluation in DMA shear mode is discussed in section 4.4.2. Finally the effect of the damping layer thickness in CLD laminates is determined in DMA shear mode in section 4.4.3.

4.2 Background

The basic concepts of passively damped structures and therefore also for membranes in miniature loudspeakers, are the concepts of free layer damping (FLD) and constrained layer damping (CLD) which first were theoretically described by Plass, Ross, Kerwin and Ungar at the end of the 1950's [64], [167]–[173]. Since then they gained wide recognition due to its excellent damping performance and ease of applicability especially in the automotive, aircraft, railway and marine industries [59], [174]–[187]. In Figure 4.1 the basic concept of damping under bending loads like those in the loudspeaker membrane supports for a) an undamped monolayer structure, b) a free layer damping design and c) a constrained layer damping design are shown schematically.

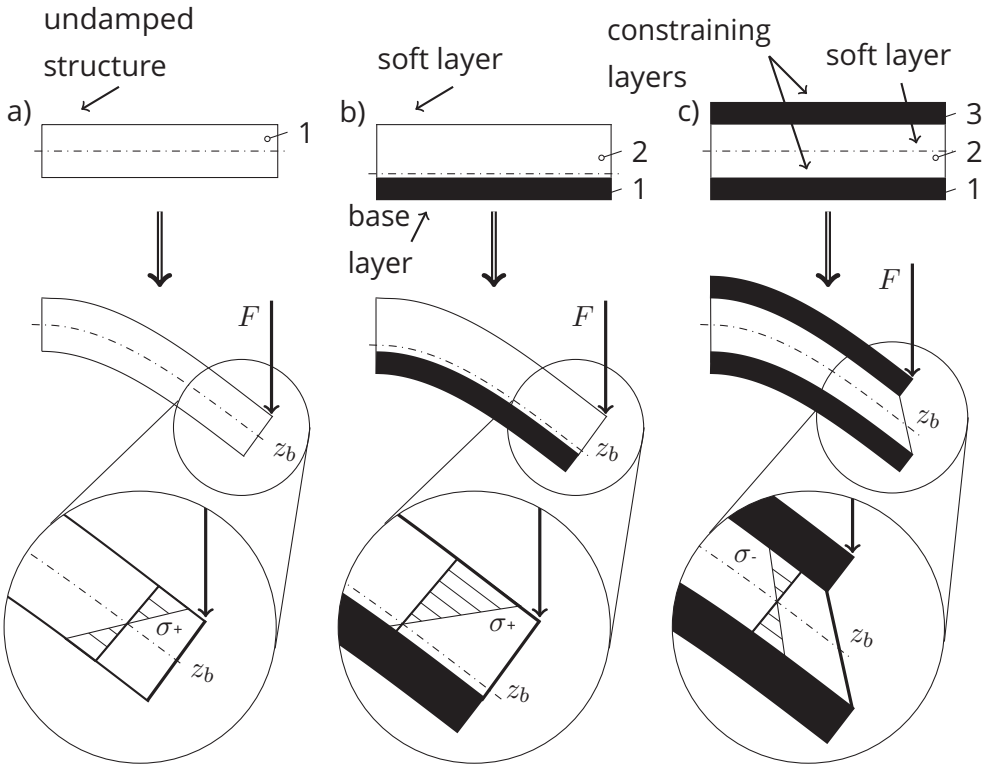

Figure 4.1: Schematic comparison of the load conditions in bending beams as a) undamped structure, b) with a free layer damping (FLD) design and c) a constrained layer damping (CLD) design, according to [169], [188].

In order to achieve a better understanding of the composite damping behavior of the loudspeaker laminates, a theoretical model has been established. In a first step the laminate is simplified as a series-parallel array of springs where each spring stands for a separate energy-storage mechanism. Bending of the laminate consequently corresponds to a deformation x of the spring array relative to its base, resulting also in a deflection of each spring. In a cyclic deformation the stored energy W_i and dissipated energy D of each spring with a given stiffness K_i and loss factor η_i by a deflection of x_i can be calculated as follows [64]:

$$W_i = \frac{K_i x_i}{2} \tag{4.1}$$

$$D_i = 2\pi\eta_i W_i \tag{4.2}$$

Based on the definition of the loss factor, the composite loss factor η of all springs is found by summation of them and therefore also the loss factor of the laminate is obtained by [64], [172], [189]:

$$\eta = \frac{\sum D_i/2\pi}{\sum W_i} = \frac{\sum \eta_i K_i x_i^2}{\sum K_i x_i^2} \tag{4.3}$$

In order to achieve a significant damping effect, the part corresponding to the dissipated energy $\sum \eta_i K_i x_i^2$ of the ith damping element has to be a significant fraction of the total dissipated energy. As a consequence, the damping element not only has to provide a high loss factor η_i but also an adequate stiffness K_i and has to be positioned in the right place to experience significant deformation x_i [64], [172], [190]. Since usually the contribution of the stiff supporting structures to the dissipated energy is negligible, Equation 4.3 is reduced with the damping layer referred as layer 1 to:

$$\eta = \frac{\sum \eta_1 W_1}{\sum W_i} = \frac{\eta_1}{1 + \dfrac{W_2 + W_3 + ...}{W_1}} \tag{4.4}$$

Therefore the composite loss factor η always is lower than the loss factor of the damping element η_1 but could be optimized by adjusting its stiffness K_1 and position and therefore its deflection x_1 to obtain a larger contribution to the total stored energy $\sum W_i$ [64].

4.2.1 Undamped structures

In a monolayer structure the monolayer has to fulfill both tasks: to provide a high fracture toughness to resist high dynamic loads and to provide an adequate damping behavior. The damping capacity is solely dependent on the inherent mechanical loss factor of the material. Furthermore in the application temperature range a constant stiffness of the membrane is required in order to ensure also a constant dynamical behavior and resonant frequency f_R. Therefore polymers with glass transition temperatures T_G below the application temperature range are preferred because above T_G, the material behavior is more constant [189]. Since the inherent damping capacity of thin polymer films is very low, this design is only used in basic applications.

4.2.2 Free layer damping (FLD)

A more sophisticated approach is the concept of free layer damping (FLD) (Figure 4.1b). Here on a stiff base structure a softer viscoelastic material (VEM) as a damping layer is applied. When this structure is bent the damping layer undergoes a bending deformation which is shifted into the tensile stress region and damping is provided via viscoelastic dissipation [62], [64], [189]–[191]. Based on Equation 4.1, the composite loss factor η for a laminate with a damping layer softer than the base layer follows as

$$\eta = \frac{\beta_2}{1 + \frac{E_1}{E_2}\frac{H_1^3/H_2}{H_2^2 + 12H_{12}^2}} = \frac{\beta_2}{1 + \frac{1}{e_2 h_2(3 + 6h_2 + 4h_2^2)}} \tag{4.5}$$

where $\beta_2 =$ loss factor of the damping layer

$e_2 = \frac{E_2}{E_1} =$ ratio of moduli of elasticity

$h_2 = \frac{H_2}{H_1} =$ ratio of thicknesses [64]

Therefore the composite stiffness and also damping performance depends on the height ratio h_2 and stiffness ratio e_2 of the base structure and the damping layer and the loss factor β_2 of the VEM [64], [178], [189]. Since the highest damping values occur at T_G of the damping layer, an appropriate damping layer has to exhibit it's T_G in the application temperature range of the loudspeaker [189].

4.2.3 Constrained layer damping (CLD)

The most effective passive damping design is the concept of constrained layer damping (CLD). Here a soft viscoelastic material is constrained by two stiff outer layers. Due to the relative motion of the constraining layers the VEM exhibits a shear deformation. Hence damping is provided via energy dissipation due to the viscoelastic nature of the damping material, as shown in Figure 4.1c. For this case the composite loss factor η is given by

$$\eta = \frac{\beta_2 Y X}{1 + (2+Y)X + (1+Y)(1+\beta_2^2)X^2} \tag{4.6}$$

with the stiffness parameter Y

$$\frac{1}{Y} = \frac{E_1 H_1^3 + E_3 H_3^3}{12 H_{31}^2} \left(\frac{1}{E_1 H_1} + \frac{1}{E_3 H_3} \right) = \frac{1 + e_3 h_3^3}{12 h_{31}^2} \left(1 + \frac{1}{e_3 h_3} \right) \tag{4.7}$$

where $E_1, E_3 =$ elastic moduli of the stiff elastic layers

$H_1, H_3 =$ thicknesses of the stiff elastic layers

$H_{31} = H_2 + \dfrac{H_1 + H_3}{2} =$ distance of the neutral axis between the stiff elastic layers

$e_3 = \dfrac{E_3}{E_1} =$ ratio of moduli of elasticity

$h_3 = \dfrac{H_3}{H_1} =$ ratio of thicknesses

and the shear parameter X [64]

$$X = \frac{G'_2}{p^2 H_2}\left(\frac{1}{E_1 H_1} + \frac{1}{E_3 H_3}\right) \tag{4.8}$$

where $G'_2 =$ storage shear modulus

$p = \frac{2\pi}{\lambda} =$ wavenumber

$\lambda =$ wavelength of the flexural vibration of the laminate

For a symmetrical design with layers with identical stiffness ($e_3 = 1$) and thickness ($h_3 = 1$) as constraining layers, Equations 4.7 and 4.8 are simplified as follows

$$Y = 3\left(\frac{H_2}{H_1} + 1\right)^2 \tag{4.9}$$

$$X = \frac{G'_2}{p^2 H_2}\frac{2}{E_1 H_1} \tag{4.10}$$

Where the stiffness parameter Y therefore is reduced to a geometric parameter. The shear parameter X depends strongly on the storage shear modulus G'_2 of the damping layer and its thickness and the thickness H_1 and tensile modulus E_1 of the stiff elastic layers [64], [192]. As a result the composite loss factor η, depends not only on the loss factor of the damping layer β_2 but also on its shear modulus and thickness and the tensile modulus and thickness of the stiff elastic constraining layers [64], [193] Also here T_G of the damping layer should lie within the application temperature range of the loudspeaker [189].

4.2.4 Interrelation between different damping measures

In Equation 4.3 it was shown that the mechanical loss factor is defined the as ratio of the dissipated and stored energy during deformation of the material. Therefore it also corresponds to other damping mechanisms besides viscous

damping. Consequently for small damping other measures of damping such as $\tan\delta$ from forced frequency DMA, decay experiments with the logarithmic decrement Λ and the quality factor Q relate to each other at resonance as shown in Equation 4.11 [61], [64], [172], [190].

$$\eta = \tan\delta = \frac{\Lambda}{\pi} = \frac{1}{Q} \tag{4.11}$$

with the phase angle δ between induced load and the corresponding reaction of the material. Whereas $\eta = \tan\delta$ applies for all frequencies, the correlation $\eta = \frac{1}{Q}$ is only valid at resonance [172]. This does not imply that with different measurement methods the same quantitative values are obtained, but at least they should be comparable in a qualitative manner as long as results are not influenced by other effects.

4.2.5 Frequency-temperature behavior of glass and secondary transitions

In polymers besides of the main transition, which is also called glass or α-transition, where large parts of the main chain achieve mobility, also smaller secondary transitions often are found, where only local motions in the main chain, locally restricted side chain motions, motions in parts of the side chains or effects between the polymer and small dissolved molecules in the polymer occur [194], [195]. When there are more of them they are denoted with successive greek letters β, γ, θ. Whereas a glass transition shows a curved course in an Arrhenius plot with the inverse transition temperature over $\log$ frequency, the secondary relaxations exhibit steeper slopes with a linear behavior in an Arrhenius plot [195].

For the description of the temperature frequency-dependence of the glass transition (α-transition, T_G) in polymers the semi-empirical WLF-approach named after Williams, Landel and Ferry is applicable:

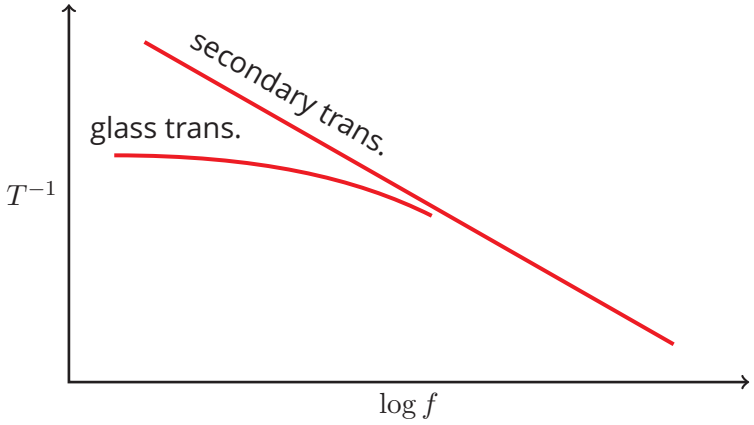

Figure 4.2: Schematic of an Arrhenius plot with an indication of the course of a glass transition and a secondary transition, according to [195].

$$\log a_T = \log f - \log f_R = \frac{c_1 \cdot (T - T_R)}{c_2 + (T - T_R)} \tag{4.12}$$

with the shift factor a_T, the reference frequency f_R, reference temperature T_R and the material constants c_1 and c_2 [70], [194], [196]–[198]. Since c_2 also depends on T_R and T_∞ (Equation 4.13), this simplifies Equation 4.12 to Equation 4.14 where T_∞ is the only remaining independent variable which is the temperature where $\log a_T$ becomes infinite [196], [198]–[200]. As a result the other parameters can easily be obtained in a least-squares fit [198], [200].

$$c_2 = T_R - T_\infty \tag{4.13}$$

$$c_1 = \frac{\log a_T \cdot (T - T_\infty)}{(T - T_R)} \tag{4.14}$$

For describing the time-temperature behavior of secondary transitions, a modified Arrhenius approach is applicable as follows:

$$f = f_0 \cdot e^{\left(\frac{E_a}{RT}\right)} \tag{4.15}$$

with the activation energy E_a and f_0 a frequency which, according to Heijboer, is equal for a great majority of secondary transitions in amorphous polymers with $\log f_0$ 13.5 $\pm$ 1.0 [70], [194], [195], [197], [198], [201].

Fit parameters for WLF and Arrhenius fits and calculated activation energies E_A for the corresponding glass and secondary transitions, respectively, for some state of the art vibration damping polymers from the literature are given in Tables 4.1 and 4.2 [197].

Table 4.1: Comparison of the glass transition temperatures T_G and fit parameters from WLF fits for state of the art vibration damping materials for constrained layer designs with a nitril rubber, a blend of nitril rubber, polyvinyl acetate (PVA) and polystyrene (PS) and a proprietary composition [197]

Material	Polymer(s)	T_G [°C]	c_1	c_2[K]	T_∞[K]
Paracril-BJ	nitril rubber	−3.9	10.86	104.8	164.45
Blend	nitril rubber, PVA, PS	54.4	16	222.2	105.35
Soundcoat N5	proprietary	25	20	210	88.15

Table 4.2: Comparison of the secondary transition temperatures T_t and fit parameters from Arrhenius fits for state of the art vibration damping materials for constrained layer damping (butyl rubber, acrylic adhesives) and free layer damping designs (LD-400, Antivibe) [197]

Material	Polymer	T_t [°C]	E_A at [kJ mol^{-1}]
	butyl rubber	4.4	36.95
3M-467	acrylic adhesive	23.9	43.88
3M ISD-110	acrylic adhesive	−3.9	37.88
LD-400	proprietary	15.6	101.62
Antivibe DS	proprietary	26.7	73.91

4.3 Methodology

4.3.1 Objectives

The initial situation for the characterization of loudspeakers membranes directly with films are their low thickness of about 50 µm, different damping designs, a temperature range in application from 0 °C to 60 °C and the highest loads above 100 Hz. Consequently the main challenges in characterizing their damping behavior are the handling of the thin films, achieving an appropriate reproducibility in experiments in application near conditions over both a wide temperature and a wide frequency range. Since the method of forced frequency dynamic mechanical analysis (DMA) seemed most promising to fulfill these requirements, especially in performing measurements over a wide temperature and frequency range, this was chosen as the starting point for further investigations [73], [202]–[204].

In different damping designs of loudspeaker membranes such as undamped films, FLD and CLD laminates, the damping is provided by different deformation modes of their damping layers. Hence the flexibility of commercially available DMAs in performing experiments in different deformation modes is of great importance for establishing optimized methods for damping characterization [73], [202]–[204]. Although in application the membrane has to provide its damping under bending deformation for which the FLD and CLD designs are optimized (chapter 4.2), in CLD laminates damping occurs through shear deformation of the adhesive damping layer when the structure is bent. Furthermore two of the main influences on the composite damping performance are the loss factor $\tan\delta$ and thickness of the damping layer h_2 [64], [172], [189], [190], [193], [197]. Since the shear deformation mode is one of the basic deformation modes in dynamic mechanical analysis (DMA) this approach seems appropriate for an optimized damping characterization of CLD laminates. In FLD laminates, damping occurs through extension of the damping layer thus DMA shear mode is not subjected as

applicable to characterize the damping behavior of them [59], [168], [189]. Therefore to mimic the load conditions in application appropriately, DMA experiments have to be performed under bending deformation of the films. Furthermore to achieve a comparable evaluation of the damping performance between different designs they also have to be tested under the same load conditions as in application. Since measurements under the standard bending deformation mode in DMA with thin loudspeaker films are not easily performed because these films are not stiff enough a more sophisticated approach is needed for the characterization of their damping performance under bending deformation[188], [205]. The resulting main challenges for the damping characterization of loudspeaker membranes are:

- implementation of a DMA-setup in shear mode optimized for the characterization of CLD laminates,
- implementation of a DMA-setup in bending mode for:
  - characterizing the damping behavior of FLD laminates,
  - comparing different damping designs.
- achieving an appropriate reproducibility,
- performing experiments at conditions near to application over both wide temperature and frequency ranges.

4.3.2 Dynamic mechanical analysis (DMA) in bending mode

Since the loudspeaker films have to provide the damping under bending deformations it is most obvious to characterize their damping behavior in DMA bending mode too. In preliminary tests using a DMA 8000 (Perkin Elmer Inc., Waltham, USA) the standard bending mode setup was changed by clamping the film specimen at the outer fixtures with a clamping length

of 12 mm and loading the specimen with an edge in the middle (Figure 4.3a). Resulting from the thinness and therefore also low stiffness of the films, a tensile instead of bending deformation occurred which led to poor results. To overcome this in a next step the geometry of the membranes of miniature speakers was mimicked with film samples as shown schematically in Figure 4.3b. Compared to the miniature speakers in Figure 1.1 here the stiffening element is replaced by the fixture at the drive shaft in the middle, the loudspeaker membrane and the specimen are both fixed at the outer side by the frame and the outer fixtures, respectively, and the bead in between takes up the vertical displacement. As a result, this setup mimics the geometry of miniature loudspeaker beads which enables to directly measure the dynamic mechanical behavior of the laminates under bending deformation over both frequency and temperature. Therefore this measurement mode is called DMA "speaker" mode [188], [205].

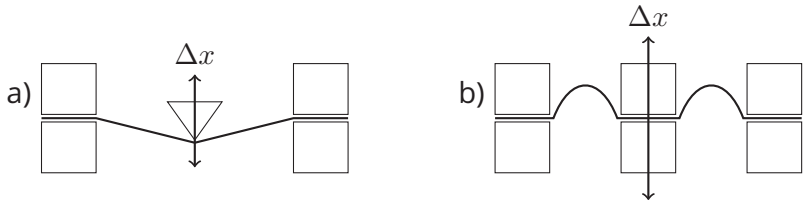

Figure 4.3: Schematics of the DMA setups with a) a modified standard bending mode with the specimen clamped at the outer fixtures and b) mimicked miniature loudspeaker surrounds by forming beads out of miniature loudspeaker film samples, according to [205].

One advantage in doing this is, as already pointed out, that the test is nearer to the application but with the trade off of a complex geometry which could not be described with simple equations. Therefore the modulus of the material cannot be calculated easily. On the other hand the mechanical loss factor $\tan\delta$ still can be determined since its calculation is based on the phase angle δ which is independent of the geometry and is directly measured during the experiments [73], [188], [202], [205].

One of the main requirements to achieve reproducible results is a reproducible bead geometry. In order to fulfill this requirement the following method was developed. The base for this was a dual cantilever setup where the specimen is clamped symmetrically both at the drive shaft and the outer fixtures with a clamping length Z of 3.4 mm in between. Before attaching the specimen in a first step the drive shaft was raised exactly 0.95 mm above the test plane. Then the specimen was placed, with additional clamps at the ends, in the setup in order to obtain a reproducible preload and alignment. In a next step the specimen was clamped at the drive shaft and outer fixtures. With this procedure a defined excessive length of the specimen between the drive shaft and the outer fixtures was obtained without introducing irreversible strain into the material (Figure 4.4a). When the drive shaft was lowered back to the test plane this resulted in a defined and reproducible bead geometry (Figure 4.4b) [188], [205].

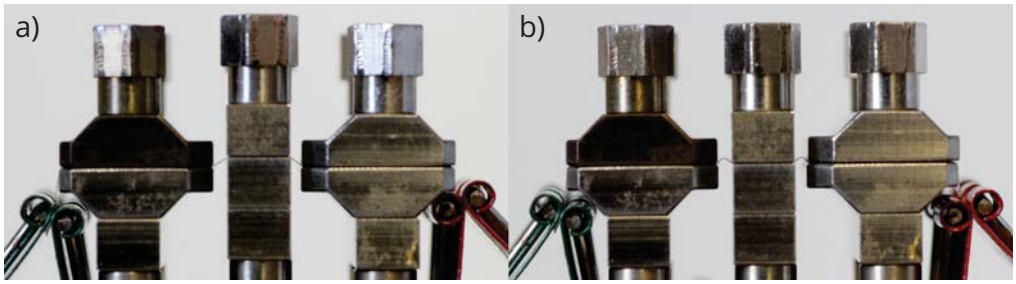

Figure 4.4: Methodology to replicable mimic a loudspeaker support geometry by a) raising the drive shaft before clamping the specimen and with b) the resulting specimen geometry, according to [188], [205].

In order to ensure a signal with enough strength in the DMA, the maximum width B of 12 mm for the specimen was used. The film stripes were cut with a commercially available roll cutter. As in loudspeakers the zero position of the oscillation was intended to be in the test plane. Since the same applies to measurements in DMA shear mode this was chosen as the control mode for the further experiments. To achieve appropriate test parameters pre-tests were performed. Therefore in a first step a displacement scan at standard conditions and 1 Hz was done. The results are shown in Figure 4.5a with the

mechanical loss factor $\tan\delta$ and the dynamic force ΔF as functions of the dynamic displacement amplitude Δx [188]. Below Δx values of 0.1 mm the

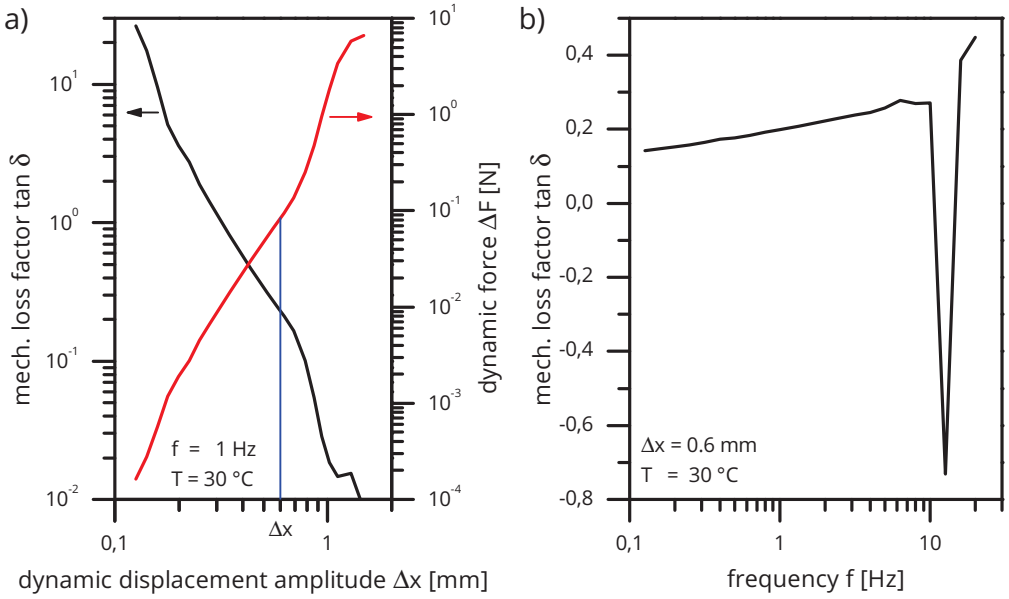

Figure 4.5: Results of a) a displacement scan at a frequency of 1 Hz with the mechanical loss factor $\tan\delta$ and the dynamic force ΔF as function of the dynamic displacement amplitude Δx and b) a frequency scan at Δx=0.6 mm with the mechanical loss factor $\tan\delta$ as function of the frequency f, both performed with a CLD laminate **3L$_{46}$**-PEEK$_8$P$_{30}$ at a temperature of 30 °C, according to [188].

signal was too low for the DMA to control the test. At 0.1 mm a resonance occurred. Between 0.3 mm to 0.7 mm a stable measurement range for both Δx and ΔF was found, which also is the application range for miniature loudspeakers. A reason for the required high displacement amplitude might be that with the mimicked speaker geometry, by exciting the drive shaft not only pure material deformation like in standard DMA setups was obtained but also a superimposed change of the bead geometry. This, combined with the low stiffness of the films, led to very high Δx values in order to achieve a signal above the detection limit of the DMA. Starting with 0.7 mm both Δx and ΔF exhibited a change in the slope. Since the films were

clamped at the beginning of the tests at a displacement of $x_0 = 0.95\,\text{mm}$, this behavior was regarded as the beginning of material deformation but in predominantly tensile mode. This assumption was verified by calculating an apparent dynamic tensile modulus E_{app} using Equations 4.16 and 4.17 with the geometric situation shown schematically in Figure 4.6.

$$E_{app} = \frac{\Delta\sigma}{\Delta\varepsilon} = \frac{\dfrac{\Delta F}{B \cdot t}}{\dfrac{\Delta l}{l_0}} \tag{4.16}$$

$$\Delta l = l - l_0 = \frac{\Delta x - x_0}{\sin\alpha} \tag{4.17}$$

with the dynamic stress and the dynamic strain amplitude $\Delta\sigma$ and $\Delta\varepsilon$, the dynamic force amplidute ΔF, the specimen width and thickness B and t, the original excessive clamping length of the specimen l_0 when brought into the setup and the elongation Δl. For the laminate **3L$_{46}$**-PEEK$_8$P$_{30}$ at a dynamic

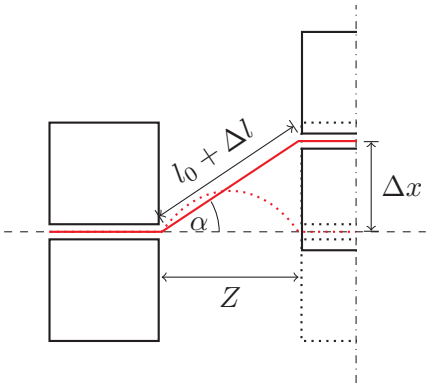

Figure 4.6: Schematic diagram for the calculation of the apparent tensile modulus E_{app} from DMA amplitude scans for dynamic displacement amplitudes Δx in the region of the drive shaft displacement where the specimens were clamped x_0 before the tests.

displacement amplitude Δx of 1.02 mm and therefore a dynamic strain $\Delta\varepsilon$ of 0.7 %, an apparent tensile modulus E_{app} of 799 MPa was determined.

This correlated well with the calculated monotonic tensile modulus for the laminate **3L$_{46}$**-PEEK$_8$P$_{30}$ of 870 MPa based on monotonic tensile tests of one of its outer layers. Consequently for the final test setup a dynamic displacement amplitude Δx of 0.6 mm was chosen in order to ensure a test above the resonance and below the region of predominant tensile deformation [188], [205].

Results of the frequency scan at Δx of 0.6 mm and standard conditions are shown in Figure 4.5b [188]. From 0.1 Hz to 5 Hz stable test conditions were found and a resonance at approximately 10 Hz. Consequently test frequencies of 0.1 Hz, 0.5 Hz, 1.0 Hz and 5.0 Hz were chosen for succeeding experiments, which were subsequently cycled during a dynamic heating segment which enabled us the recording of temperature scans at four different frequencies in one experiment. Experiments at a frequency of 10 Hz were also performed in order to obtain the temperature of the $\tan\delta$ peak at this frequency for succeeding calculations. Since at temperatures above the $\tan\delta$ peak and therefore above the glass transition of the adhesives the stiffness of the laminates decreased significantly, also a shift of the resonance occured below 10 Hz. Consequently starting with these temperatures the DMA was not able to provide stable measurement conditions at a frequency of 10 Hz. A low heating rate of 2 K min^{-1} was chosen in order to ensure a balanced temperature distribution in the sample. A more detailed damping characterization was obtained by an extended temperature range of −40 °C to 180 °C compared to the application-relevant range from 0 °C to 60 °C. In Table 4.3 an overview of the chosen test parameters is listed.

4.3.3 Dynamic mechanical analysis (DMA) in shear mode

Since in application in CLD laminates damping is provided via shear deformation of the adhesive damping layer when the structure is bent, a DMA setup in shear mode was used to characterize their damping behavior via the temperature and frequency dependent mechanical loss factor $\tan\delta(f,t)$.

Table 4.3: Test parameters for the damping characterization in DMA bending deformation.

parameter	unit	value
specimen width	[mm]	12
clamping length	[mm]	3.4
displacement amplitude	[mm]	0.6
heating rate	[K min^{-1}]	2
temperature range	[°C]	−40 to 180
test frequencies	[Hz]	0.1, 0.5, 1.0 and 5.0

The test is based on DIN EN 6721-1 on a DMA/SDTA 861^e (Mettler Toledo AG, Schwerzenbach, CH) [206]. A detailed schematic comparison of the load situation in both application and experiment is shown in Figure 4.7a and Figure 4.7b, respectively [169], [198].

In DMA shear mode usually disc shaped specimens are clamped symmetrically between two fixed outer and a central moving bracket (Figure 4.8) [198]. Consequently shear deformation occurs through oscillation of the central bracket [73], [202]. Using the geometry factor k for shear deformation of the disc shaped specimens (Equation 4.18), the resulting complex shear modulus G^* is calculated according to Equation 4.19 [198].

$$k = A \cdot \frac{2}{d} = \frac{D^2\pi}{2d} \tag{4.18}$$

$$G^* = \frac{F}{\Delta x} \cdot \frac{1}{k} \tag{4.19}$$

with the cross section A, the diameter D and the thickness d of the specimen and the applied load F and displacement Δx amplitude. Since the loudspeaker membranes are very thin and therefore exhibit a high shear stiffness especially in the glass region of the damping adhesive, an appropriate choice of the specimen geometry is crucial fur successful measurements. The upper measurement limit for a DMA is defined by the stiffness of the

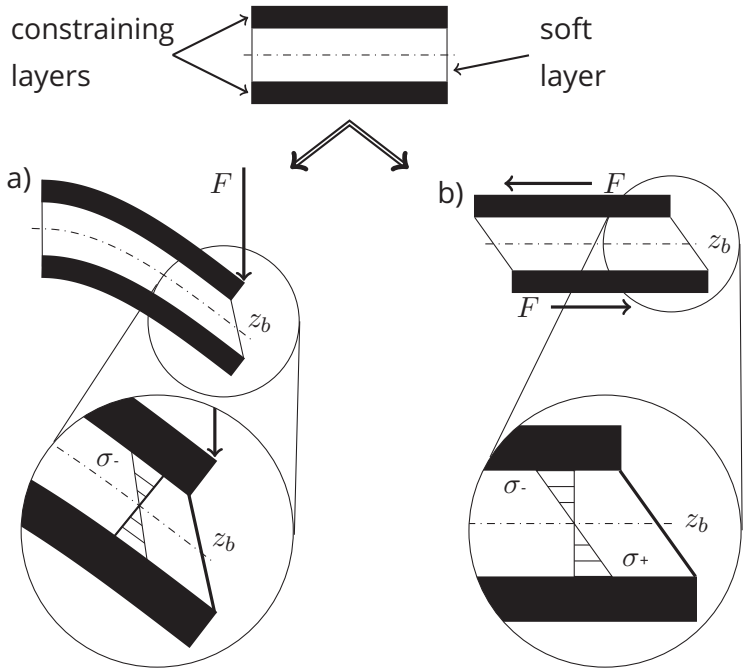

Figure 4.7: Schematic comparison of the load situations in the soft viscoelastic damping layer of constrained layer damping (CLD) laminates in both a) bending deformation in application and b) shear deformation in the DMA experiments, according to [169], [198].

test setup $F/\Delta x$ which, inserted in Equation 4.19, enables the calculation of the theoretical measurement limit of the complex shear modulus G^*_{max} [73], [198]. This should be at least five times higher than the modulus of the sample, otherwise the signal/noise ratio becomes disadvantageous leading to poor results. [73], [198], [207]. The lower measurement limit is formed by the detection limit of the DMA which is relevant in the rubber regime of the damping adhesive where its modulus drops by a factor of 10^3. To take both limits into account preliminary tests were performed and an optimized disc shaped specimen geometry with a diameter of 6 mm was developed (Figure 4.8a). By using a commercially available punch a high reproducibility of the geometry was ensured. Since the specimens are very thin, a minimal misalignment of the setup would result in contact of the specimen fixtures. Therefore 0.5 mm thick silica discs are placed between the specimen and

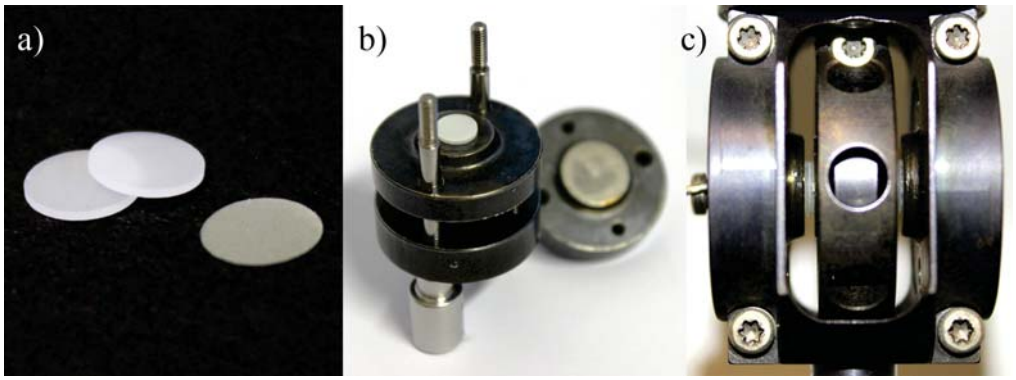

Figure 4.8: DMA setup for experiments in shear mode with loudspeaker membranes a) with disc shaped silica plates and specimen, b) with shear clamps with specimens during assembly and c) attached to the test setup, according to [198].

each the fixtures (Figure 4.8) [198], [207]. A high enough dynamic displacement amplitude Δx in the tests should guarantee a signal with enough strength above the detection limit of the DMA. On the other hand, in DMA shear mode actual material deformation takes place and therefore Δx has to be within the linear viscoelastic region of the tested material in order to measure actual material parameters. As long as the storage modulus exhibits a constant level, linear viscoelasticity prevails with the upper limit marked by a drop of the modulus [73], [198]. Consequently a displacement scan was performed with the results shown in Figure 4.9. In order to ensure stable measurements over the whole experiment, a dynamic displacement amplitude Δx of 0.4 µm was chosen. This guarantees stable experiment conditions both at low temperatures where the material exhibits a higher stiffness and therefore the area of linear viscoelasticity shifts to lower Δx values and also at higher temperatures where the material is soft and Δx has to be high enough to ensure a signal above the detection limit of the DMA [198]. With a low heating rate of 2 K min^{-1} between test temperatures from −40 °C to 220 °C, equally distributed temperatures in the specimens were ensured. The frequency range was limited by an unstable signal below 1 Hz and the measurement limit of the DMA at 200 Hz. As a consequence in the

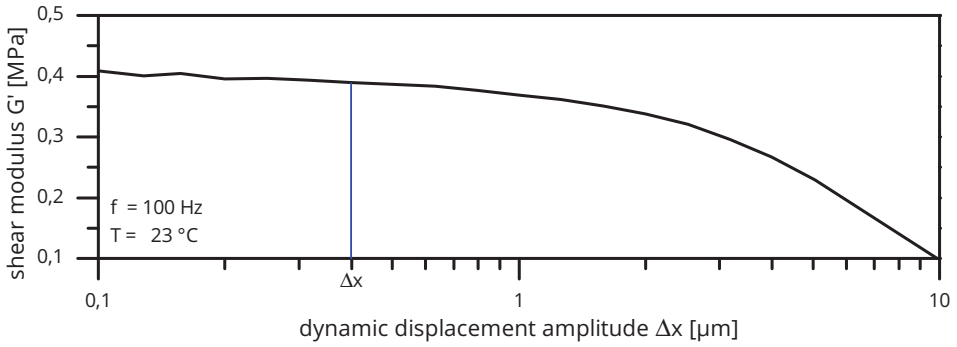

Figure 4.9: Results of a displacement scan with a CLD laminate with 10 µm thick PAR outer and 30 µm thick damping layer at a frequency of 100 Hz and a temperature of 25 °C with the storage shear modulus G' as function of the dynamic displacement amplitude Δx.

experiments during a dynamic heating segment, frequencies of 1 Hz, 10 Hz, 100 Hz and 200 Hz were subsequently cycled which enabled the recording of material parameters for multiple frequencies in one measurement run [198]. An overview of the test parameters is given in Table 4.4 [198].

Table 4.4: Test parameters for the damping characterization in DMA shear deformation [198].

parameter	unit	value
specimen diameter	[mm]	6
displacement amplitude	[µm]	0.4
heating rate	[K min^{-1}]	2
temperature range	[°C]	−40 to 220
test frequencies	[Hz]	1, 10, 100 and 200

The influence of the specimen stiffness in the glass region of the adhesive damping layer for a CLD laminate is demonstrated in Figure 4.10 with both displacement amplitude Δx and mechanical loss factor $\tan\delta$ as functions of the temperature T at frequencies of 1 and 200 Hz [198]. Below the glass transition of the damping layer the stiffness of the specimen is too high

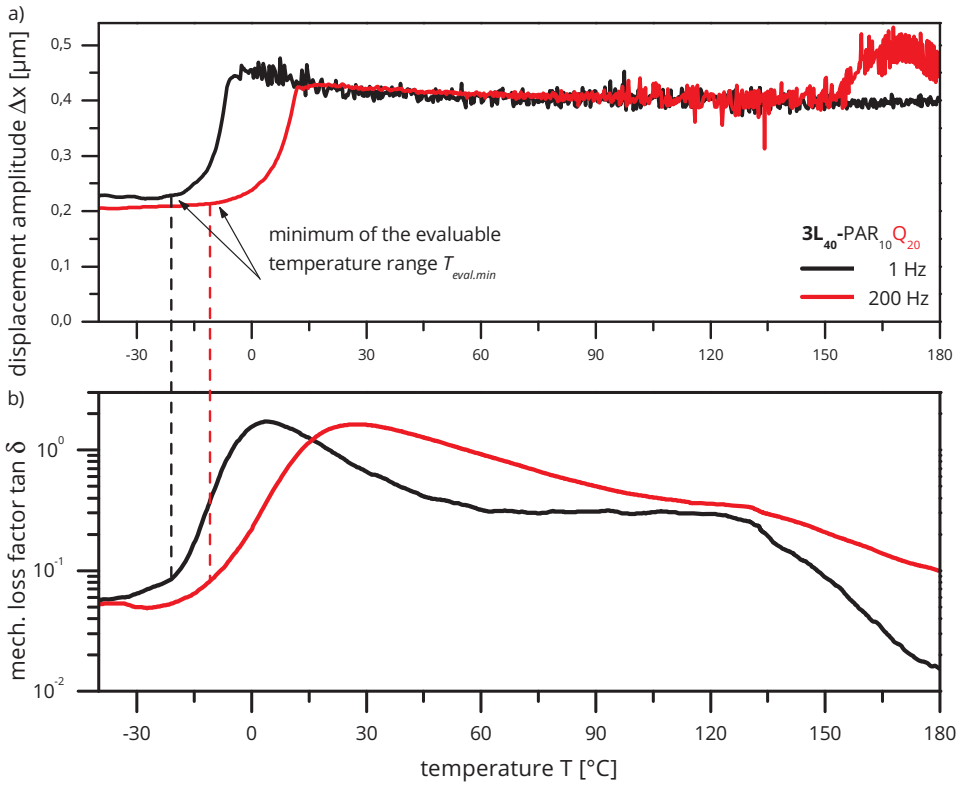

Figure 4.10: Plots of displacement amplitude Δx and mechanical loss factor $\tan\delta$ vs. temperature T for a CLD laminate to determine the minimum of the evaluable temperature range $T_{eval.min}$, according to [198].

and the load limit of the DMA is reached before the nominal displacement amplitude Δx. Here instead of the sample stiffness, the stiffness of the whole setup is measured. Above its glass transition T_G the damping layer became soft and the nominal displacement amplitude Δx was reached and therefore actual material properties are measured. This marks the lower limit of the temperature range which can be evaluated $T_{eval.min}$ [198].

4.3.4 Application of the time temperature superposition principle (TTSP)

Since both DMA methods have their measurement limits below the application frequency range of miniature speakers where the damping has to be provided at frequencies of up to 1000 Hz, it is necessary to perform extrapolations through theoretical approaches. This is done in academic research via the time-temperature superpositions principle (TTSP) which describes the correlation between the temperature and time dependence of dispersion areas in polymers [198]. For the glass transition (α-transition, T_G) in polymers the semi-empirical WLF-approach (Equation 4.12), as described in section 4.2.5, for secondary relaxations a modified Arrhenius approach (Equation 4.15) is applicable [195].

The requirement for the application of TTSP is a thermo-rheologically simple material behavior, i.e. all relaxation or retardation times in the material have to depend equally on temperature [198], [208], [209]. Several methods have been established to verify the applicability of TTSP for a certain material, such as the modified Cole-Cole plot (log M'' vs. log M'), the van Gurp plot (δ vs. M^*) and the wicket plot (log $\tan\delta$ vs. log M') with the storage modulus M', the loss modulus M'' and the complex modulus M^* [70], [198], [209]–[211]. If the requirement of thermo-rheological simplicity is fulfilled in all methods, a continuous curve in the shape of an inverse "U" is obtained [70], [198]. In this work the wicket plot was chosen, where the mechanical loss factor $\tan\delta$ is plotted as a function of the storage modulus M' on a double logarithmic scale. For all these methods the bases are isothermal frequency scans which ensure a thermal equilibrium in the specimen. An unequal temperature distribution would lead to scattered relaxation times and, as a result, a violation of TTSP. A. Moser introduced a new method based on dynamic temperature scans in multi-frequency mode. These are converted in a next step into frequency scans at each temperature. When the specimen geometry and a suitable heating rate are chosen correctly

the requirement of equilibrated temperatures throughout the specimen is fulfilled [198], [212].

4.3.5 Normalized loss factor tA

Since in miniature loudspeakers the damping performance has to be provided in the whole application range from 0 °C to 60 °C the evaluation of the peak height of the mechanical loss factor $\tan\delta$ alone is not sufficient to classify the damping performance of a laminate. Instead it is advised to calculate the area under the mechanical loss factor $\tan\delta$ in the temperature range relevant for application, called tA [189], [198]. In our work this concept was extended by normalizing tA to the evaluated temperature range which led to the integrated average of the mechanical loss factor which is "named normalized loss factor $\overline{tA}$" as shown in Equation 4.20 [198].

$$\overline{tA} = \frac{1}{T_2 - T_1} \int_{T_1}^{T_2} \tan\delta \, dT \tag{4.20}$$

with the upper and lower limits of the evaluated temperature range T_1 and T_2. As a result with the concept of $\overline{tA}$ an improved comparability is obtained compared to standard evaluations with $\tan\delta$ as a function of frequency and temperature [198].

4.4 Results and Discussion

4.4.1 Effect of damping design under bending deformation

Parts of this section have already been published in:

G. Knapp, M. Leyrer, G. Oreski, *et al.*, "Characterization of the damping behavior of thin films with dynamic mechanic analysis in bending mode,"

in *Proceedings of ASME 2014 International Mechanical Engineering Congress & Exposition (IMECE2014)*, 2014

Cited text passages, tables and figures have been marked accordingly.

The influence of the damping design on the damping behavior of loudspeaker films under bending deformation is described in this subsection. In miniature speakers the films are also loaded in bending deformation; in order to achieve a valid comparison of their damping behavior they have to be characterized under similar conditions, for which the DMA "speaker" mode is applicable, as described in section 4.3.2. For this evaluation an undamped thermoplastic elastomer (TPE) monolayer film, a 2-layer film with a free layer damping (FLD) design consisting of a PEEK base layer (PEEK) and a TPE damping layer and a 3-layer film with a constrained layer damping (CLD) design consisting of PAR constraining layers and a soft adhesive damping layer were chosen as test materials. Details regarding their composition and thickness distribution are listed in Table 4.5. Reference comparisons with experiments with the same materials in DMA shear mode were performed [188], [205].

Table 4.5: Test materials with an undampend, a FLD and a CLD design, according to [205].

laminate	design	layer type		thickness (µm)		
		1/3	2	1	2	3
1L$_{50}$-TPE(a)$_{50}$	und.	TPE(a)		50		
2L$_{38}$-PEEK$_8$TPE(b)$_{30}$	FLD	PEEK	TPE (b)	8	30	
3L$_{40}$-PAR$_{10}$Q$_{20}$	CLD	PAR	adhesive Q	10	20	10

Results for these films are shown in Figures 4.11 to 4.13 for the films **1L$_{50}$**-TPE(a)$_{50}$, **2L$_{38}$**-PEEK$_8$TPE(b)$_{30}$ and **3L$_{40}$**-PAR$_{10}$Q$_{20}$ in both DMA "speaker" mode at 0.1 Hz, 1 Hz and 5 Hz and DMA shear mode at 1 Hz, 10 Hz, 100 Hz and 200 Hz [188], [205]. In DMA "speaker" mode the undamped elastomer film (Figure 4.11a) exhibited sharp loss factor peaks between −58 °C (0.1 Hz)

and −50 °C (5 Hz) with peak values of approximately 0.4 with a sharp decline up to 0 °C where the lowest damping with values below 10^{-2} were found. Starting at 0 °C the elastomer film became too soft to ensure stable mea-

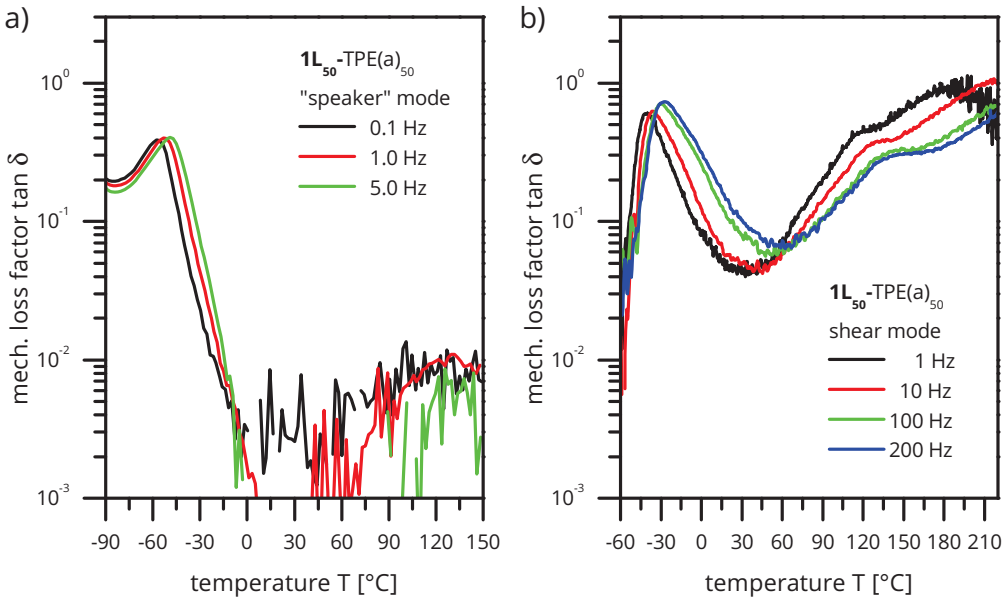

Figure 4.11: Results of **1L$_{50}$**-TPE(a)$_{50}$ with the mechanical loss factor $\tan\delta$ vs. temperature T for different frequencies in a) DMA "speaker" and b) DMA shear mode.

surement conditions, which led to high scatter in the $\tan\delta$ signal. Rising $\tan\delta$ values were also found with rising temperatures. In DMA shear mode (Figure 4.11b) also sharp loss factor peaks were observed but at higher temperatures and higher peak values than in "speaker" mode. Here the elastomeric film showed $\tan\delta$ peak temperatures beginning from −41 °C to −27 °C and peak values between 0.6 and 0.75 for frequencies from 1 Hz to 200 Hz. Frequency-dependent $\tan\delta$ minima with values from 0.045 to 0.07 occurred in the range from 30 °C to 60 °C and showed higher values with increasing frequencies. The minima were followed by a second peak with even higher $\tan\delta$ values than in the first one. It is expected that in DMA shear mode, stiffness effects to $\tan\delta$ only play a minor role compared to

DMA "speaker" mode which might explain the differences in $\tan\delta$ values at the second peak at temperatures above 60 °C.

The free layer damping (FLD) laminate (**2L$_{38}$**-PEEK$_8$TPE(b)$_{30}$) consisting of a PEEK base layer and a thermoplastic elastomer as the damping layer also exhibited sharp loss factor peaks in DMA "speaker" mode with peak values of approximately 0.3 at temperatures from −16 °C to −9 °C(Figure 4.12a) [188], [205]. Above a steady decline of $\tan\delta$ was observed which was related to

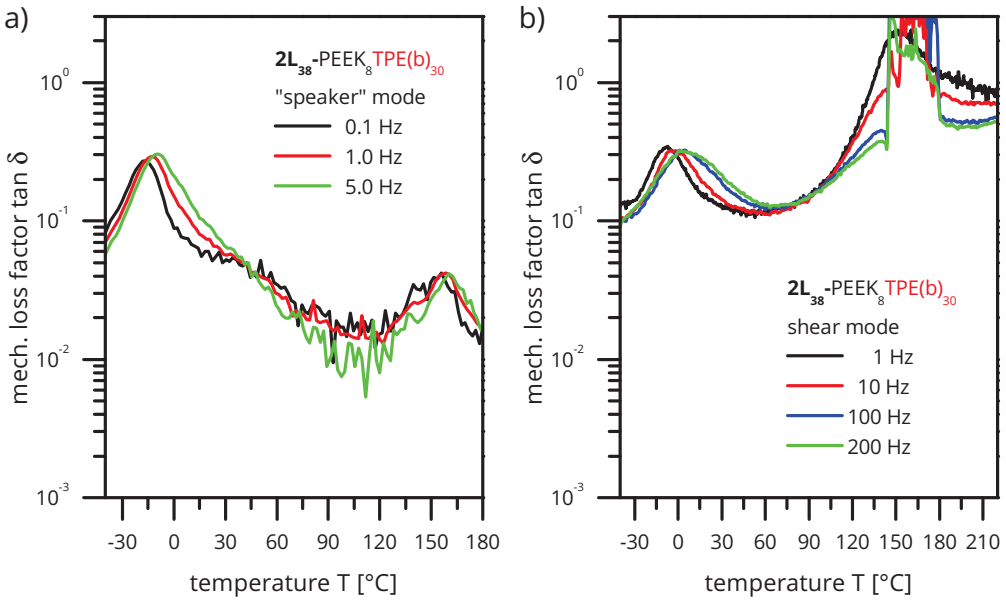

Figure 4.12: Results of **2L$_{38}$**-PEEK$_8$TPE(b)$_{30}$ with the mechanical loss factor $\tan\delta$ vs. temperature T for different frequencies in a) DMA "speaker" and b) DMA shear mode, according to [205].

a contribution of both a decreasing loss factor of the damping layer and a decreasing stiffness of the whole laminate as explained in section 4.2.2. At 160 °C further but only small peaks were found which were related to the glass transition of the PEEK outer layers. Results in DMA shear mode were very similar with similar peak heights and temperatures at the same frequencies (Figure 4.12b) [188], [205]. In contrast to the DMA "speaker" mode, in shear mode the second maximum, here at approximately 160 °C,

exhibited significantly higher $\tan\delta$ values of up to 2.3 at 1 Hz. This behavior was attributed to a combination of a shear deformation of both a softened damping and also a softened base layer, which is thought to not occur in use. Directly at the peak, the signal became too weak at 10 Hz, 100 Hz and 200 Hz which led to wrong results [205].

In tests in DMA "speaker" mode with **3L$_{40}$**-PAR$_{10}$Q$_{20}$ high peak values of $\tan\delta$ of approximately 0.6 at temperatures of the peaks ranging from 2 °C to 20 °C for frequencies of 0.1 Hz to 5 Hz were revealed (Figure 4.12a) [205]. At higher

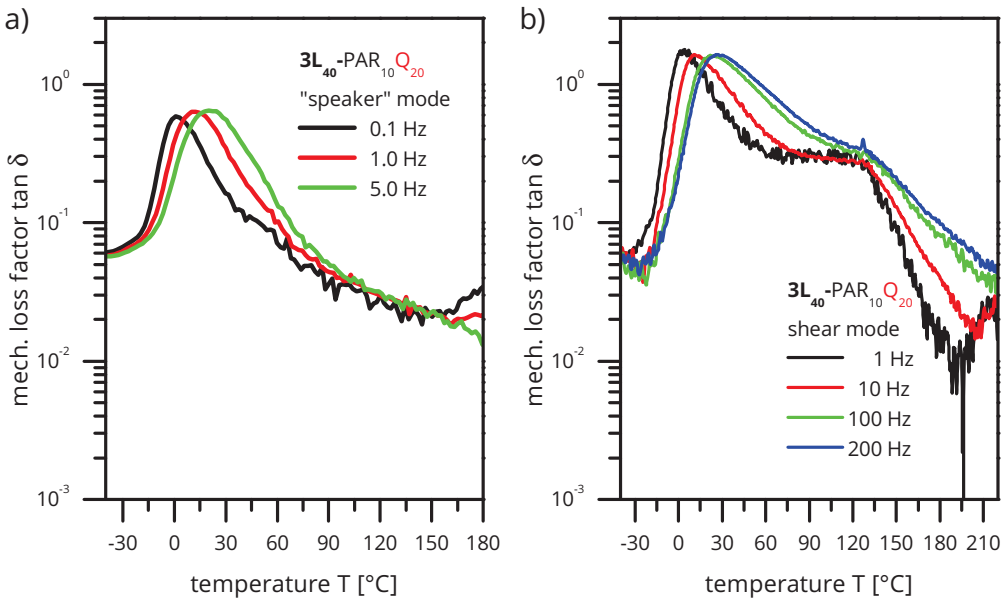

Figure 4.13: Results of **3L$_{40}$**-PAR$_{10}$Q$_{20}$ with the mechanical loss factor $\tan\delta$ vs. temperature T for different frequencies in a) DMA "speaker" and b) DMA shear mode, according to [205].

temperatures $\tan\delta$ decreased steadily down to values of approximately 0.2 at 180 °C. The same material in DMA shear mode showed significantly higher $\tan\delta$ peaks than in "speaker" mode with values of up to 1.7, which were at approximately 10 °C higher temperatures at the same frequencies (Figure 4.12b). At 1 Hz and 10 Hz above the peak up to approximately 130 °C a damping plateau was found followed by a significant drop in $\tan\delta$. Similar

to results with the FLD laminate, the difference between the measurement modes with the CLD laminate was related to additional geometric and stiffness effects in DMA "speaker" mode which may play only a minor role in DMA shear mode [205].

A comparison of $\tan\delta$ curves for each material in DMA "speaker" and shear mode at a frequency of 1 Hz is depicted in Figure 4.14. The most significant

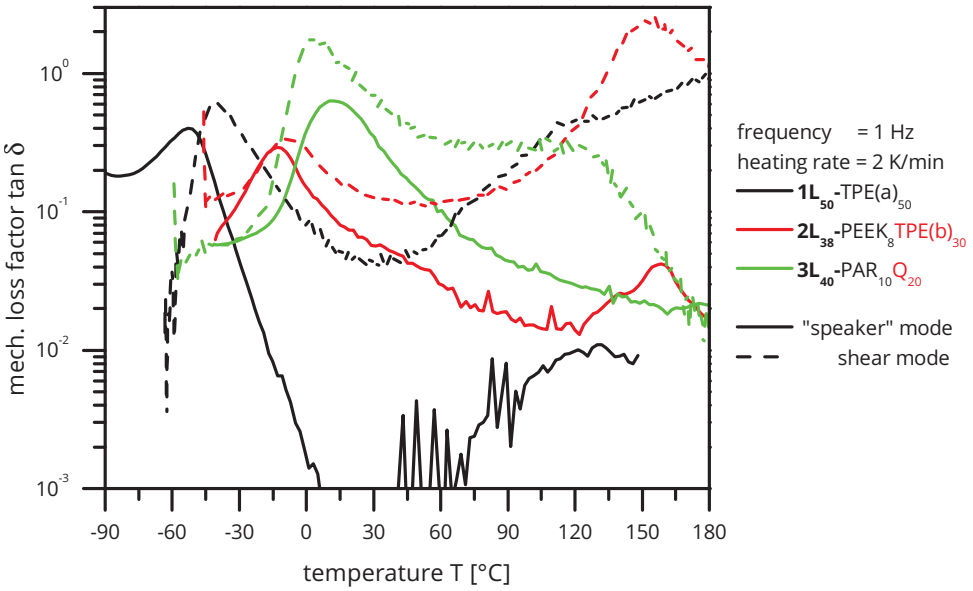

Figure 4.14: Comparison of results in a) DMA "speaker" and b) DMA shear mode with the mechanical loss factor $\tan\delta$ vs. temperature T for at a frequency of 1 Hz for all tested laminates.

differences for the undamped film **1L$_{50}$**-TPE(a)$_{50}$ between the results of the DMA "speaker" and the shear mode were the shift of the $\tan\delta$ peak to higher temperatures and the difference in the damping levels at higher temperatures with significant lower values in "speaker" mode. The FLD laminate **2L$_{38}$**-PEEK$_8$TPE(b)$_{30}$ revealed very similar values at the $\tan\delta$ peak in both test methods but also significant differences at higher temperatures. Whereas in "speaker" mode only a small peak at the glass transition of the PEEK base layer was found, in shear mode the significantly higher second peak was attributed to a superposition effect induced by the additional softening of

the PEEK base layer [205]. **3L$_{40}$**-PAR$_{10}$Q$_{20}$ with a CLD design showed qualitatively comparable results in both measurement modes despite the absence of the plateau at higher temperatures in DMA "speaker" mode. Therefore it was concluded that in DMA shear mode the inherent material damping capacity is characterized but in DMA "speaker" mode also geometric and stiffness effects are reproduced [205].

As explained in section 4.3.4, in order to perform extrapolations to higher frequencies using the time temperature superposition principle (TTSP) at first its applicability has to be verified. This is done by checking the measurements for thermorheological simplicity by calculating wicket plots with frequency dependent $\tan\delta$ curves as a function of the storage modulus G'. Since for the DMA "speaker" mode no calculation of the dynamic modulus can be done yet due to the complex geometry of the mimicked miniature speaker beads, it is also not possible to perform a wicket evaluation. Therefore the applicability of the time temperature superposition (TTSP) could not be verified yet for measurements in DMA "speaker" mode. Examples of wicket plots from measurements in DMA shear mode in the whole measured temperature range are shown in Figure 4.15 for **1L$_{50}$**-TPE(a)$_{50}$ and **2L$_{38}$**-PEEK$_8$TPE(b)$_{30}$ and in Figure 4.23a for **3L$_{40}$**-PAR$_{10}$Q$_{20}$. Since the modulus of polymers decreases over temperature, higher moduli in the wicket plots correspond to lower temperatures and therefore the plots are read from the right to the left when comparing them to temperature-dependent DMA curves. **1L$_{50}$**-TPE(a)$_{50}$ showed a double inverse "U" which was related to the occurance of two transitions; this was also obtained in temperature-dependent $\tan\delta$ curves in Figure 4.11. Up to a temperature of −33 °C curves in the wicket plot were well aligned followed by clear separated curves up to the beginning of the second transition. $T_{eval.max}$ here correlates well to the $\tan\delta$ peak temperatures of the first transition from −41 °C to −27 °C for frequencies between 1 Hz and 200 Hz. The second transition showed good alignment throughout between the curves for each temperature. Since for **1L$_{50}$**-TPE(a)$_{50}$ two transitions were revealed, which both influence the $\tan\delta$

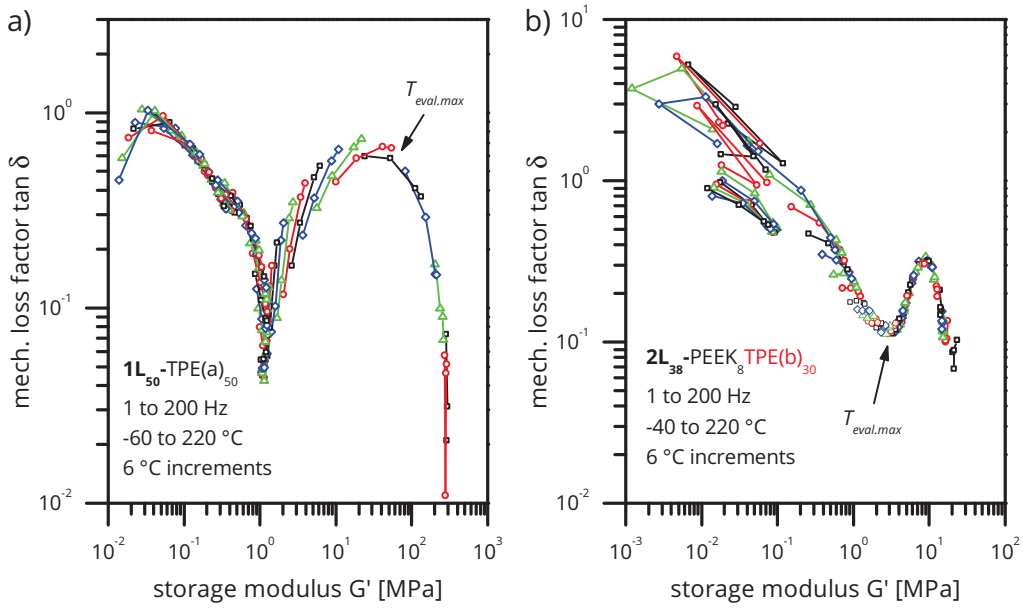

Figure 4.15: Wicket plots with the mechanical loss factor $\tan\delta$ as a function of the storage modulus G' for laminates a) **1L$_{50}$**-TPE(a)$_{50}$ and b) **2L$_{38}$**-PEEK$_8$TPE(b)$_{30}$ for temperatures ranging from −60 °C to 220 °C and −40 °C to 220 °C, respectively and frequencies from 1 Hz to 200 Hz and an evaluation of the maximum of the evaluable temperature range $T_{eval.max}$[197].

height in the temperature region in between (Figure 4.11b), the procedure described in section 4.3.4 to shift the whole curve for an estimation of the material behavior at higher frequencies is not applicable. The FLD laminate **2L$_{38}$**-PEEK$_8$TPE(b)$_{30}$ showed in DMA shear mode up to a temperature of 75 °C a standard inversed "U" shape in the wicket plot, but significant deviances above. Since its glass transition temperature T_G with 7 °C was still below $T_{eval.max}$ at the highest measurement frequency of 200 Hz, TTSP was applicable. The CLD laminate **3L$_{40}$**-PAR$_{10}$Q$_{20}$ in Figure 4.23a exhibited in DMA shear mode also a standard inversed "U" shape with beginning scatter at lower modulus levels which corresponded to a temperature of 122 °C at 200 Hz. Since its glass transition temperature T_G of 28 °C at 200 Hz was well below $T_{eval.max}$ TTSP was also applicable.

In Figure 4.16 a comparison of the measured and extrapolated temperatures of the $\tan\delta$ peaks as a function of the frequency for both DMA modes is shown, with the fit parameters c_1, c_2 and T_∞ listed in Table 4.6.

Table 4.6: Glass transitions temperatures T_G at 1 Hz and fit parameters for the WLF fit of measurements in DMA shear mode for the laminates **2L$_{38}$**-PEEK$_8$TPE(b)$_{30}$ and **3L$_{40}$**-PAR$_{10}$Q$_{20}$.

laminate	T_G[°C]	c_1	c_2[K]	T_∞[K]
2L$_{38}$-PEEK$_8$TPE(b)$_{30}$	−7.3	16.7	121.5	158.4
3L$_{40}$-PAR$_{10}$Q$_{20}$	4.3	4.8	75.5	226.3

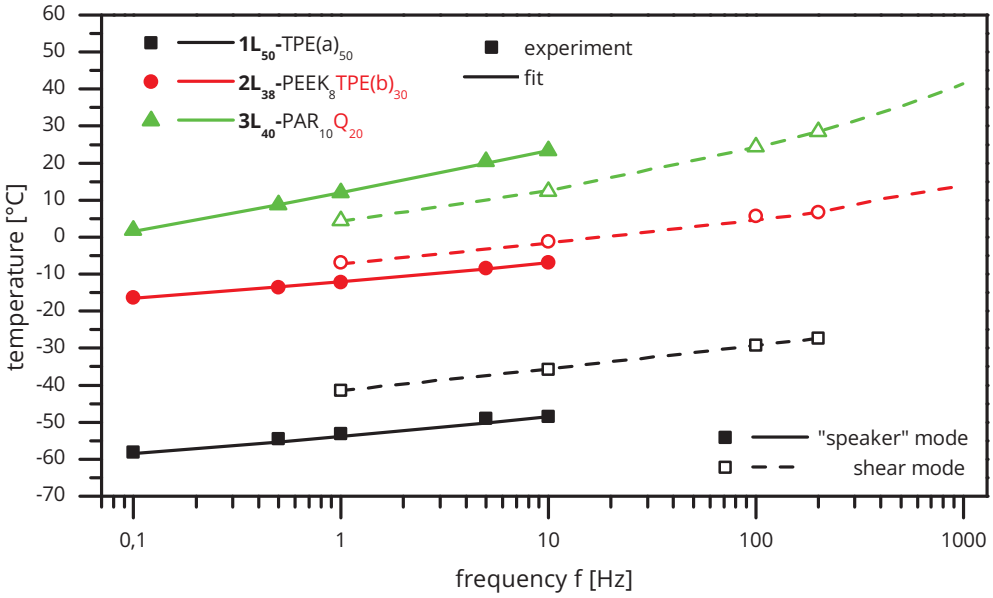

Figure 4.16: Comparison of the application of TTSP in DMA "speaker" and shear mode for all tested laminates.

Whereas for **2L$_{38}$**-PEEK$_8$TPE(b)$_{30}$ similar values for the WLF fit parameters were found as in the literature (Table 4.1), **3L$_{40}$**-PAR$_{10}$Q$_{20}$ showed significantly lower values for both c_1 and c_2 and significantly higher T_∞. All laminates showed similar slopes in the evaluation in Figure 4.16 in both "speaker" and shear mode but significant differences in the temperatures of the damping

peaks were found between the two DMA measurement modes. Throughout the frequency range the elastomeric monolayer exhibited approximately 12 °C lower temperatures of the $\tan\delta$ peaks in "speaker" mode. A similar picture was observed for the FLD laminate but here with a more moderate difference with approximately 5 °C lower temperatures of the peaks in "speaker" mode. The opposite behavior was exhibited by the CLD laminate **3L$_{40}$**-PAR$_{10}$Q$_{20}$ with approximately 10 °C higher temperatures of the $\tan\delta$ peaks in "speaker" mode. At first this behavior was attributed to an eventual hysteretic heat up in DMA shear mode due to the high maximum test frequency of 200 Hz. Therefore additional experiments with all three test materials in DMA shear mode were conducted with the same temperature program but this time only at a frequency of 1 Hz. It was proposed that if a hysteretic heat up occurs, a shift of the low frequency curves from experiments where the frequencies are cycled between 1 Hz to 200 Hz may be detected compared to experiments at only 1 Hz. The comparison revealed nearly identical curves and therefore it was concluded that the shift in Figure 4.16 might not be attributed to a hysteretic heat up but rather to other effects for which further investigations have to be made.

Finally results for a comparison of the normalized loss factor $\overline{tA}$ in the application-relevant temperature range from 0 °C to 60 °C as a function of the frequency f are shown in Figure 4.17. Whereas for all materials lower damping values were measured in DMA "speaker" than in shear mode, the qualitative rankings are the same in both methods throughout the measured frequency ranges. Consistent with the literature in both methods, the ranking in damping performance undamped $<$ FLD $<$ CLD was obtained [189].

The following conclusions are drawn from the results with different damping designs. In experiments with CLD laminates in DMA shear mode only the adhesive damping layer is characterized as long as temperatures are well below the glass transition of the outer layers. They remain therefore stiff and have only a negligible influence on the measurement. Hence DMA

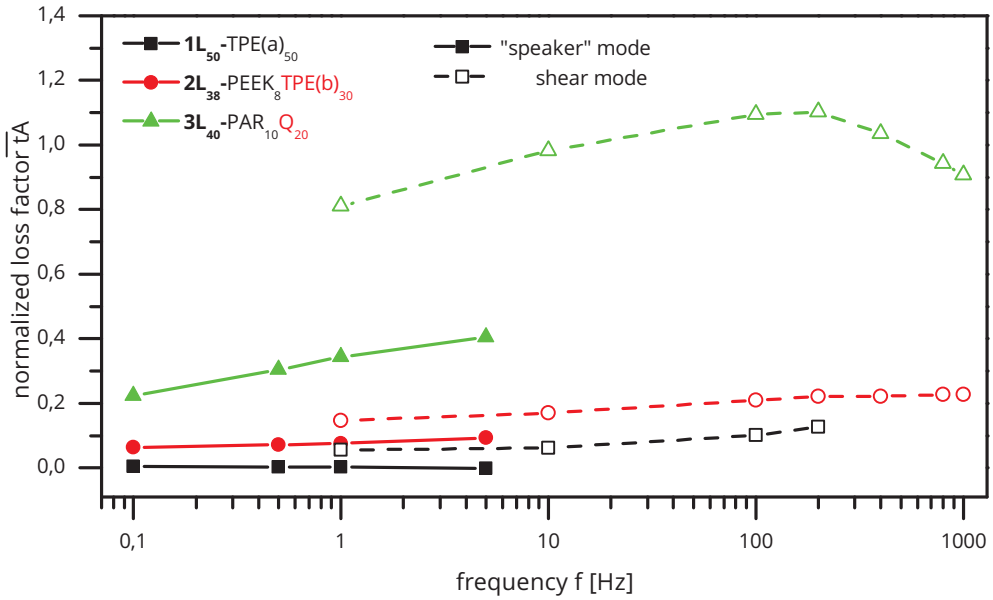

Figure 4.17: Comparison of the $\overline{tA}$ evaluation in DMA "speaker" and shear mode as function of the frequency in the temperature range from 0 °C to 60 °C for all tested laminates.

shear mode is optimized for the characterization of the damping behavior of adhesive damping layers in CLD laminates since here both in application and experiments the same damping mechanism prevails in the laminate. On the other hand in application in FLD laminates, damping occurs due to extension and compression of the damping layer. Although this is not reproduced in DMA shear mode, the DMA "speaker" mode is optimized in order to match the application as closely as possible. Therefore the "speaker" mode is eligible not only to perform a ranking of different damping designs but also to optimize their composite design since here also geometric and stiffness effects, as described in section 4.2 are reproduced. Still there is room for further optimization especially for the characterization of thin monolayer films, which only exhibit low stiffness leading to results of lower quality especially above their glass transition. Furthermore the test frequency range has to be extended in order to obtain an improved comparability with applications where the resonance frequency f_R occurs at frequencies of

up to 1000 Hz [188], [205]. In conclusion whereas the DMA shear mode is applicable only for the damping characterization of CLD laminates, with the DMA "speaker" mode different damping designs can be evaluated regarding their damping performance.

4.4.2 Effect of outer layers in CLD laminates in DMA shear mode

Parts of this section have already been published in:

G. Knapp, G. Oreski, and G. Pinter, "Method to characterize the damping behavior of thin passively constrained layer laminates using dynamic mechanical analysis (DMA) in shear mode," *Polymer Testing*, 2015, ISSN: 01429418. DOI: 10.1016/j.polymertesting.2015.01.011.

Cited text passages, tables and figures have been marked accordingly.

In this part the influence of different outer layers in CLD laminates on the damping characterization in DMA shear mode of their damping layers is evaluated. Cuillery et al. reported a significant decrease of the damping performance with decreasing adhesion between layers for CLD laminates with metal/polymer/metal design consisting of 200 µm thick stainless steel sheets and a 300 µm thick styrene-ethylene/butylene-sterene triblock polymer [213]. In order to investigate whether adhesion is also of significance in miniature speaker laminates, five different laminates with a symmetrical design and damping layer thicknesses of 20 µm to 30 µm with three different types of stiff outer layers and damping adhesives, respectively, were chosen as test materials. An extreme example with inferior adhesion was used with laminate **3L$_{135}$**-PET(e)$_{55}$R$_{20}$RF$_{60}$, which consists of a siliconized PET and a release film as outer layers. A detailed overview of the composition of the tested laminates is given in Table 4.7 [198].

Altough the thickness of the damping layer has a significant influence on the damping performance of CLD laminates as discussed in section 4.2.3, **3L$_{50}$**-

Table 4.7: Test materials with five variations of constraining and damping layers, according to [198].

Laminate	Layer type			Thickness [µm]		
	1	2	3	1	2	3
3L$_{40}$-PAR$_{10}$Q$_{20}$	PAR	adhesive Q	PAR	10	20	10
3L$_{44}$-PET(d)$_{12}$Q$_{20}$	PET	adhesive Q	PET	12	20	12
3L$_{40}$-PAR$_{10}$R$_{20}$	PAR	adhesive R	PAR	10	20	10
3L$_{135}$-PET(e)$_{55}$R$_{20}$RF$_{60}$	siliconized PET	adhesive R	release film	55	20	60
3L$_{50}$-PAR$_{10}$S$_{30}$	PAR	adhesive S	PAR	10	30	10

PAR$_{10}$S$_{30}$ with a 30 µm thick damping layer, compared to a damping layer thickness of 20 µm in the other laminates in this section, was included in the comparison since it exhibits a secondary loss peak compared to the standard glass transitions in the laminates with adhesives Q and R. The influence of the damping layer thickness is then discussed in detail in section 4.4.3. Since in pretests it was found that the adhesive damping layers exhibited 10^3 to 10^5 times lower moduli than the stiff outer layers, it was expected that in DMA shear mode alone the dynamic mechanical behavior of the soft adhesive damping layers and their adhesion to the outer layers would be characterized. Therefore also varying moduli and also varying thicknesses of the outer layers should have only minor influence on the results in DMA shear mode.

Results for all tested laminates for the mechanical loss factor $\tan\delta$ as a function of temperature T and frequencies of 1 Hz, 10 Hz, 100 Hz and 200 Hz are shown in Figures 4.18 and 4.19 [198]. For the laminates with adhesives type Q and R sharp $\tan\delta$ maxima were found which was related to their glass transitions. For all of them with increasing frequency both a shift of the peak to higher temperatures and a broadening was found. Also above the damping peak a plateau starting at approximately 60 °C at 1 Hz was

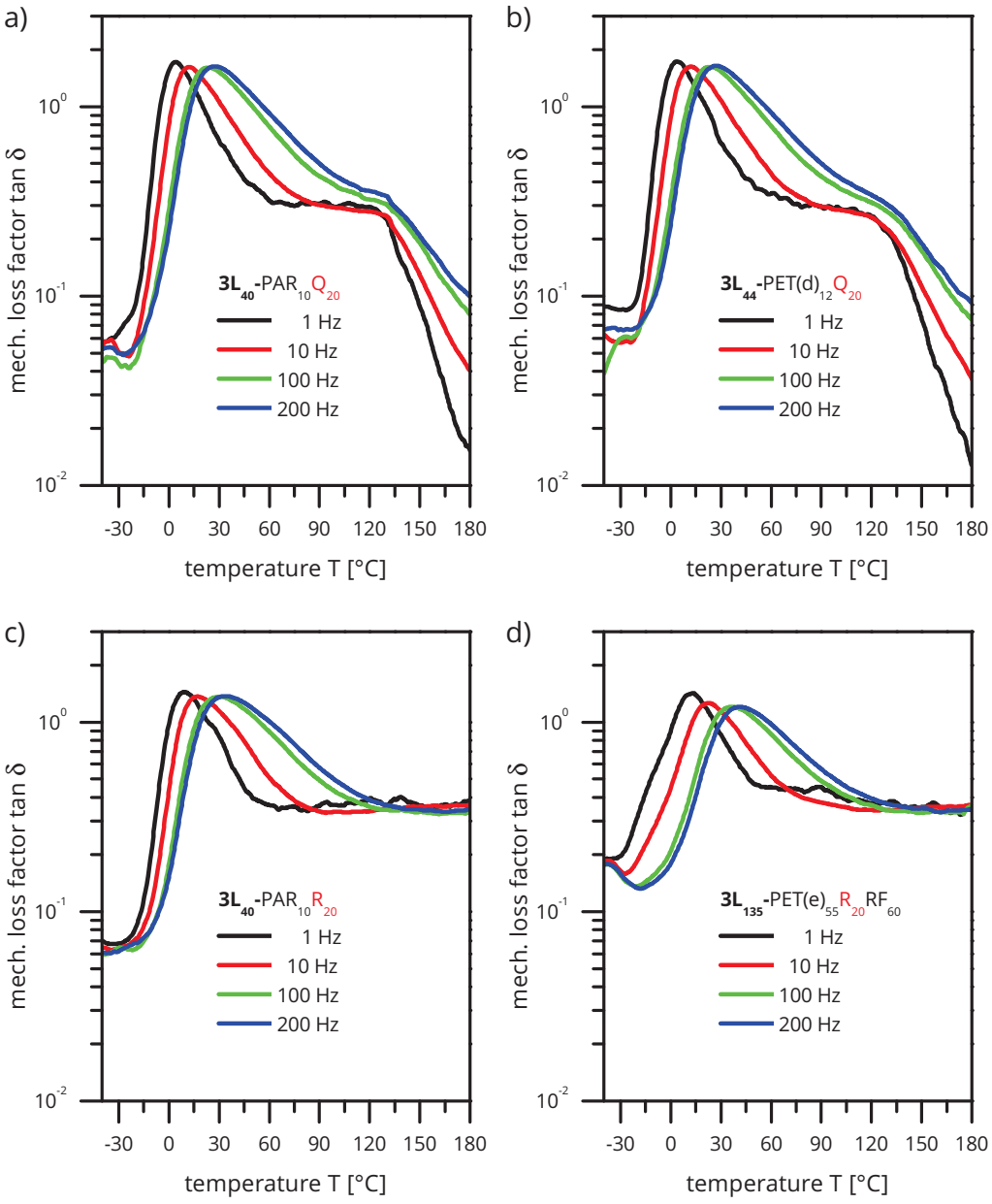

Figure 4.18: Results with the mechanical loss factor $\tan\delta$ vs. temperature T for frequencies of 1 Hz to 200 Hz for laminates a) **3L$_{40}$**-PAR$_{10}$Q$_{20}$, b) **3L$_{44}$**-PET(d)$_{12}$Q$_{20}$, c) **3L$_{40}$**-PAR$_{10}$R$_{20}$ and d) **3L$_{135}$**-PET(e)$_{55}$R$_{20}$RF$_{60}$, according to [198]

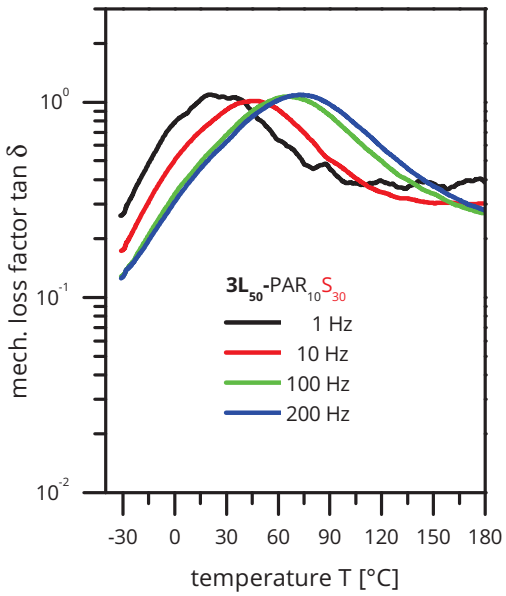

Figure 4.19: Results with the mechanical loss factor $\tan\delta$ vs. temperature T for frequencies of 1 Hz to 200 Hz for laminate **3L$_{50}$**-PAR$_{10}$S$_{30}$, according to [198].

observed. Solely laminates with adhesive type Q exhibited a sharp decrease at about 120 °C. An almost different behavior was found for laminate **3L$_{50}$**-PAR$_{10}$S$_{30}$ with a significantly wider damping peak but at lower $\tan\delta$ levels. Also laminate **3L$_{50}$**-PAR$_{10}$S$_{30}$ has exhibited a plateau at low damping levels above the peak [198].

Comparisons between results of laminates with the same damping adhesives but different outer layers are shown in Figure 4.20 [198]. The laminates, both consisting of adhesive type Q and PAR (**3L$_{40}$**-PAR$_{10}$Q$_{20}$) and PET (**3L$_{44}$**-PET(d)$_{12}$Q$_{20}$) outer layers, respectively, revealed only negligible differences (Figure 4.20a) [198]. In contrast the laminates with adhesive type R and PAR (**3L$_{40}$**-PAR$_{10}$R$_{20}$) and siliconized PET and a release film (**3L$_{135}$**-PET(e)$_{55}$R$_{20}$RF$_{60}$) as outer layers revealed significant differences with a lower damping peak for **3L$_{135}$**-PET(e)$_{55}$R$_{20}$RF$_{60}$. This was regarded as the result of inferior adhesion between the damping and outer layers in **3L$_{135}$**-PET(e)$_{55}$R$_{20}$RF$_{60}$ [198], [213]. This might lead to poor coupling between the stiff outer and the soft

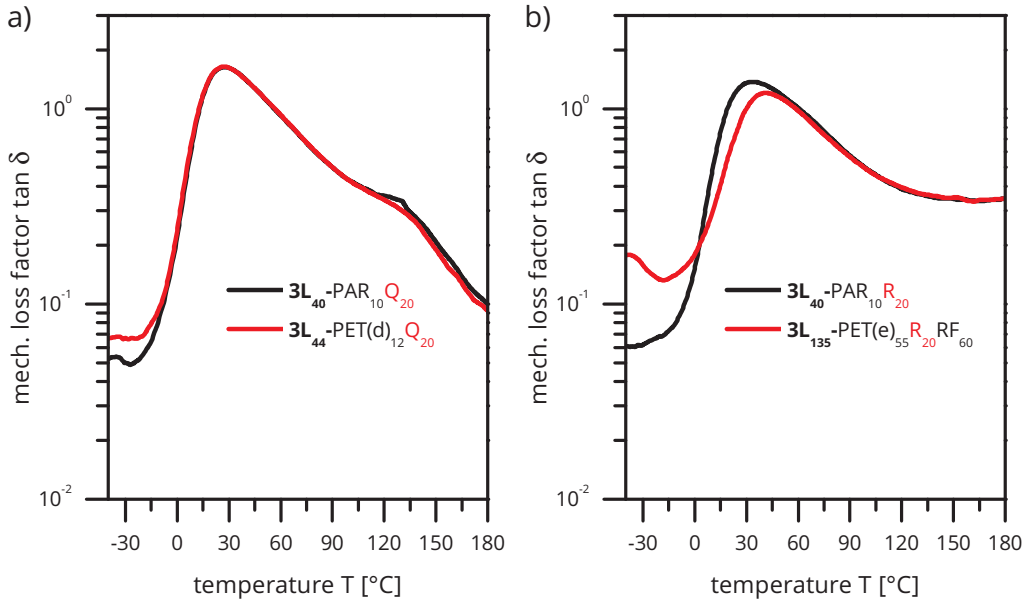

Figure 4.20: Comparison of results with the mechanical loss factor $\tan\delta$ vs. temperature T for a frequency of 200 Hz for laminates with the same damping adhesives but different constraining layers, respectively, according to [198].

damping adhesive and a low amount of dissipated energy. The difference in $\tan\delta$ between **3L$_{40}$**-PAR$_{10}$R$_{20}$ and **3L$_{135}$**-PET(e)$_{55}$R$_{20}$RF$_{60}$ below the damping peak was below $T_{eval.min}$ and consequently of no significance [198].

Since the experimental setup has a frequency limit of 200 Hz but in loudspeakers the damping performance has to be provided at their resonance frequency f_R at up to 1000 Hz, extrapolations using the WLF and a modified Arrhenius approach were done (see also section 4.3.4). The time-temperature behavior of all tested laminates is depicted in Figure 4.21 with the temperature of the $\tan\delta$-peak as a function of the frequency. Moreover analogous results in the comparison of $\tan\delta$ vs. temperature curves between laminates with the same damping adhesive (Figure 4.20) were found in the evaluation of the time-temperature behavior of the $\tan\delta$-maxima (Figure 4.21) [198]. Although between laminates with the same damping adhesive Q and technical polymers as outer layers differences were insignifi-

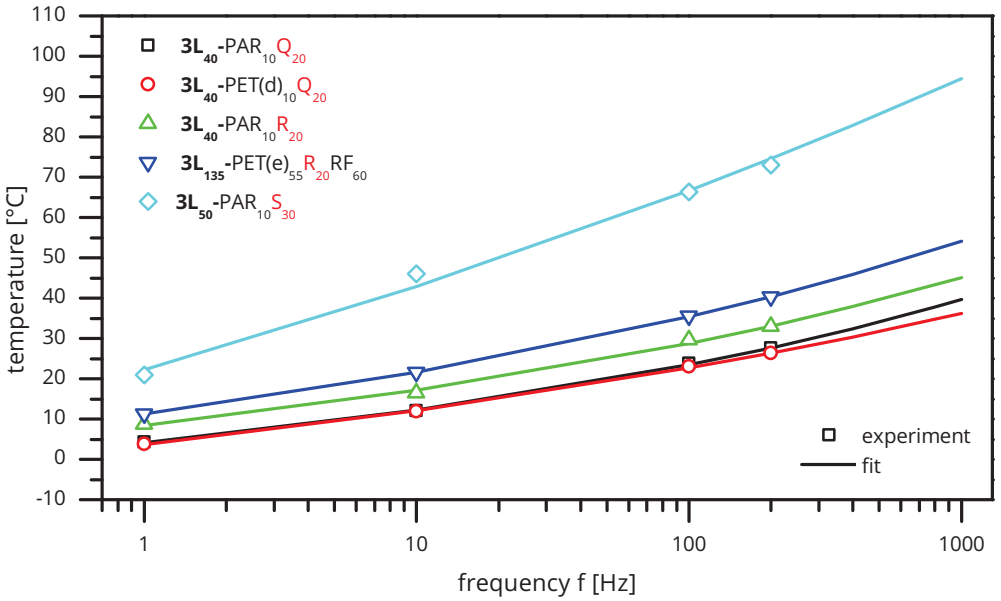

Figure 4.21: Comparison of the measured and extrapolated temperatures of the $\tan\delta$ peaks as function of the frequency for all tested laminates, according to [198].

cant, for laminates with adhesive R and PAR or siliconized PET and a release film as outer layers for the latter a shift towards higher temperatures was observed [198]. Except for laminate **3L$_{50}$**-PAR$_{10}$S$_{30}$ all other laminates showed a curved behavior in Figure 4.21 which is associated with a glass transition T_G, which is usually described in academic research with the semi-empirical WLF approach (Equation 4.12) [198]. In contrast **3L$_{50}$**-PAR$_{10}$S$_{30}$ exhibited a significantly steeper gradient with a nearly linear behavior and a more pronounced frequency-dependence. In the literature such behavior is explained by an occurrence of a secondary instead of a glass transition which is subsequently described with a modified Arrhenius approach [194], [195], [198]. A similar behavior was reported by Jones for acrylic vibration damping adhesives for CLD designs [197]. The corresponding fit parameters are listed in Table 4.8. Compared to WLF fit parameters from the literature, in Table 4.1 significantly lower c_1 and c_2 and significantly higher T_∞ values were calculated [197]. **3L$_{50}$**-PAR$_{10}$S$_{30}$ also exhibited a relatively high activation

Table 4.8: Fit parameters for the WLF and Arrhenius fits of measurements in DMA shear mode.

laminate	WLF fit parameters			Arrhenius fit parameters	
	c_1	c_2[K]	T_∞[K]	E_A [kJ mol^{-1}]	$\log f_0$
3L$_{40}$-PAR$_{10}$Q$_{20}$	4.8	75.5	226.3		
3L$_{44}$-PET(d)$_{12}$Q$_{20}$	7.9	101.6	197.9		
3L$_{40}$-PAR$_{10}$R$_{20}$	5.9	89.5	216.8		
3L$_{135}$-PET(e)$_{55}$R$_{20}$RF$_{60}$	5.3	90.7	222.8		
3L$_{50}$-PAR$_{10}$S$_{30}$				90	15.8

energy E_A compared to values from the literature listed in Table 4.2 [197]. $\log f_0$ matched quite well the range for secondary relaxations between 12 to 15 reported by Heijboer [194], [195], [201].

The consequence of different transitions to the time-temperature behavior of loss factor $\tan\delta$-maxima is shown in Figure 4.22 with the mechanical loss factor $\tan\delta$ as a function of the temperature for laminates **3L$_{40}$**-PAR$_{10}$Q$_{20}$ and **3L$_{50}$**-PAR$_{10}$S$_{30}$ for frequencies of 1 Hz and 100 Hz [198]. Whereas in laminate **3L$_{40}$**-PAR$_{10}$Q$_{20}$ exhibiting a glass transition the $\tan\delta$-peak shifted by 19 °C from 1 Hz to 100 Hz for laminate **3L$_{50}$**-PAR$_{10}$S$_{30}$ with a secondary transition a shift of 44 °C was found [198].

Since TTSP is only valid for thermo-rheologically simple materials, i. e. materials where all relaxation or retardation times depend equally on temperature, it is advised to check its applicability (see also section 4.3.4) [197], [198]. Here this is done by applying the wicket plot where the mechanical loss factor $\tan\delta$ is plotted against the storage modulus G', as shown in Figure 4.23 and 4.24 for temperatures from −40 °C to 220 °C in increments of 10 °C and a frequency range from 1 Hz to 200 Hz [198]. The occurrence of significant scatter or other deviations of the standard bent curve were set as limits for the applicability of TTSP. Since each point in the wicket plot also refers to a dedicated temperature this enables the evaluation of the maximum of

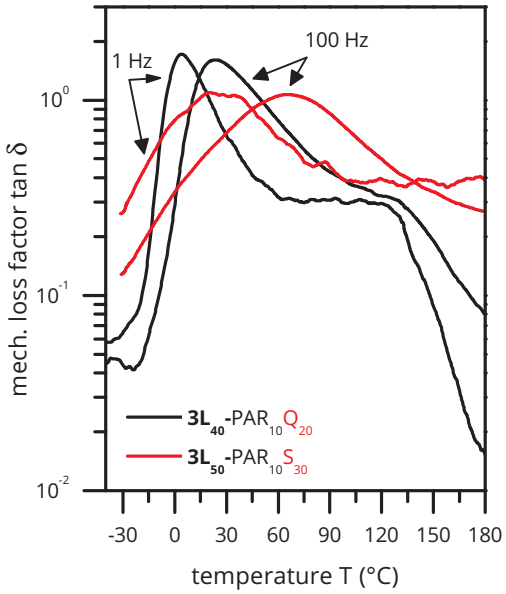

Figure 4.22: Comparison of the temperature-frequency dependence of a glass and a secondary transition for laminates **3L$_{40}$**-PAR$_{10}$Q$_{20}$ and **3L$_{50}$**-PAR$_{10}$S$_{30}$, respectively, with the mechanical loss factor $\tan\delta$ as function of the temperature T at frequencies of 1 and 10 Hz, according to [198].

the evaluable temperature range for TTSP, which here is called $T_{eval.max}$. For example both laminates **3L$_{40}$**-PAR$_{10}$Q$_{20}$ and **3L$_{44}$**-PET(d)$_{12}$Q$_{20}$ exhibited a similar behavior in the wicket plots with a standard inverted "U" shape down to regions of low modulus. The beginning of this region corresponds to a temperature of 120 °C in both laminates [198].

A comparison of the glass transition temperatures for laminates with adhesives Q and R and secondary transition temperatures for **3L$_{50}$**-PAR$_{10}$S$_{30}$ and the upper temperature limits for the application of TTSP $T_{eval.max}$ for 200 Hz is listed in Table 4.9 [198]. Taken into consideration that the transition temperatures were at significantly lower temperatures as $T_{eval.max}$ at the corresponding frequencies at all laminates, TTSP was assumed to be applicable for each material [198].

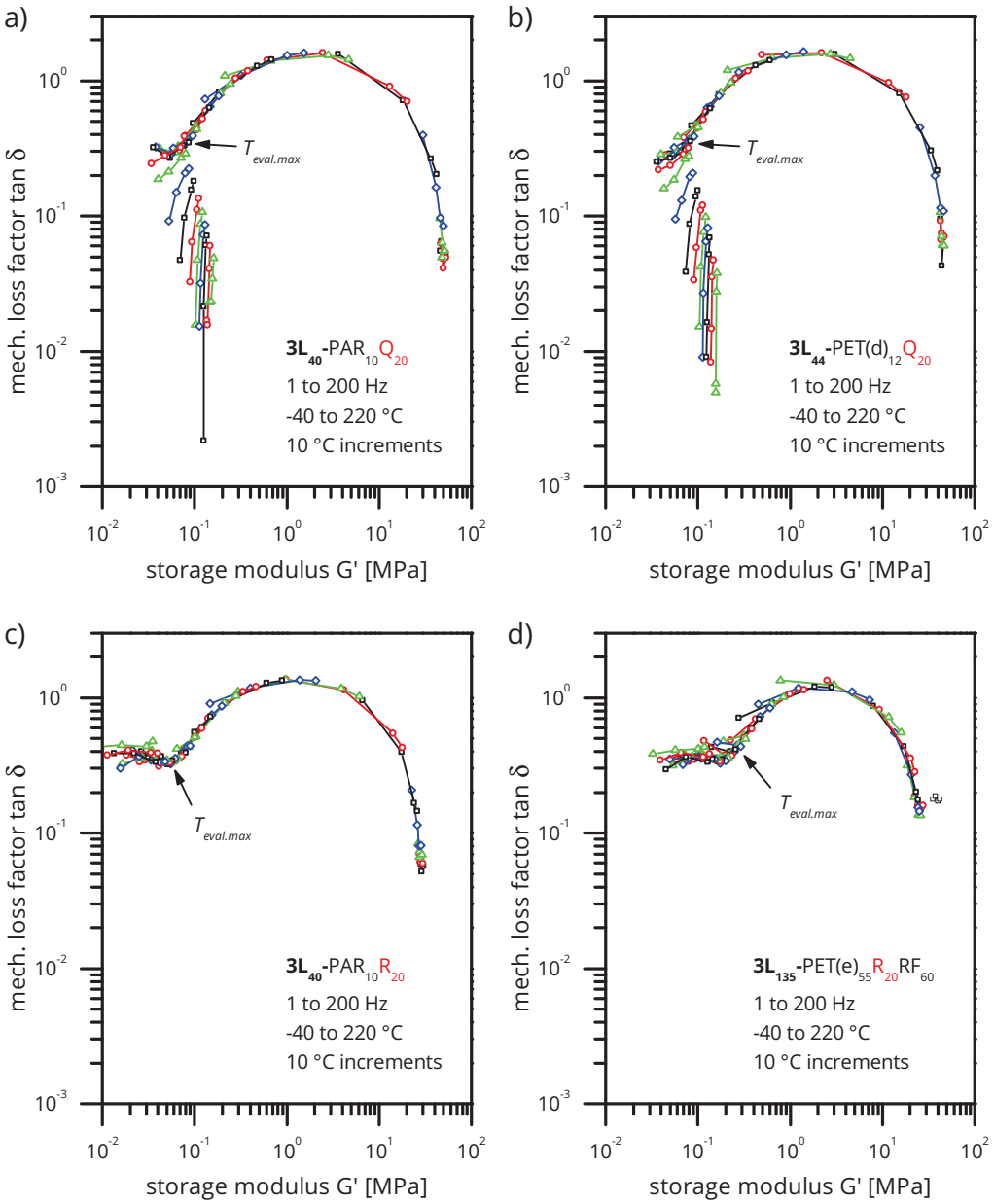

Figure 4.23: Wicket plots with the mechanical loss factor $\tan\delta$ as a function of the storage modulus G' for laminates a) **3L$_{40}$**-PAR$_{10}$Q$_{20}$, b) **3L$_{44}$**-PET(d)$_{12}$Q$_{20}$, c) **3L$_{40}$**-PAR$_{10}$R$_{20}$ and d) **3L$_{135}$**-PET(e)$_{55}$R$_{20}$RF$_{60}$ for temperatures ranging from −40 °C to 220 °C and frequencies from 1 Hz to 200 Hz and an evaluation of the maximum of the evaluable temperature range $T_{eval.max}$, according to [197], [198].

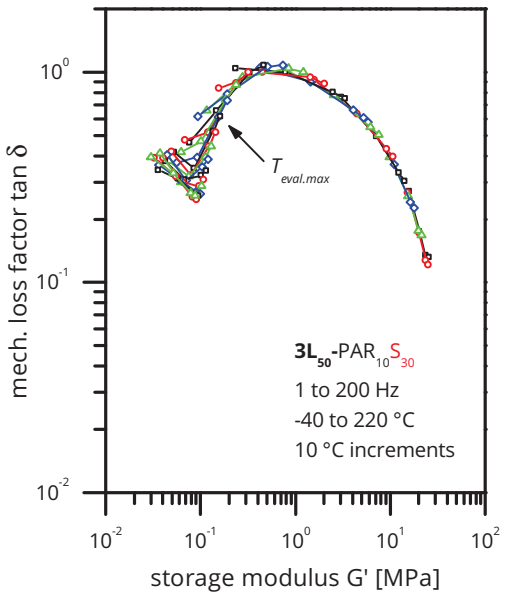

Figure 4.24: Wicket plot with the mechanical loss factor $\tan\delta$ as a function of the storage modulus G' for laminate **3L$_{50}$**-PAR$_{10}$S$_{30}$ for temperatures ranging from −40 °C to 220 °C and frequencies from 1 Hz to 200 Hz and an evaluation of the maximum of the evaluable temperature range $T_{eval.max}$, according to [197], [198].

In order to overcome the measurement limit of 200 Hz of the DMA the information gained from the application of TTSP was used to estimate the $\tan\delta$-peak temperatures at application-relevant frequencies of up to 1000 Hz. In a next step $\tan\delta$-curves were shifted empirically from measurements at 200 Hz to 1000 Hz which is shown for the laminate **3L$_{40}$**-PAR$_{10}$Q$_{20}$ in Figure 4.25 [198]. Because the shift was within the same order of magnitude, only minor errors are assumed to come from this method [198].

Since in miniature loudspeakers a good damping behavior is required over both a wide temperature and frequency range, the usage of the $\tan\delta$-peak as ranking tool is not sufficient. Instead for such applications in the literature it is proposed to evaluate the area under the loss factor tA in the application-relevant temperature and frequency range [189], [198]. In this work furthermore tA was normalized to the application temperature range

Table 4.9: Overview of the transition temperatures T_t and the maximum of the evaluable temperature range $T_{eval.max}$ according to the evaluation using the wicket plot for 200 Hz, according to [198].

laminate	T_t [°C]	$T_{eval.max}$ [°C]
3L$_{40}$-PAR$_{10}$Q$_{20}$	28	122
3L$_{44}$-PET(d)$_{12}$Q$_{20}$	26	121
3L$_{40}$-PAR$_{10}$R$_{20}$	33	141
3L$_{135}$-PET(e)$_{55}$R$_{20}$RF$_{60}$	40	145
3L$_{50}$-PAR$_{10}$S$_{30}$	75	98

resulting in the normalized mechanical loss factor $\overline{tA}$ (see also section 4.3.5). In order to obtain a prediction of the temperatures which prevail in miniature loudspeakers in application, thermographic measurements were done with an IR-camera and a miniature speaker under a voltage signal derived from application. Based on this the upper limit of the application temperature range was considered as 60 °C. The lower limit was set to 0 °C since the lowest application temperatures for the speakers are approximately at −20 °C to −10 °C and a certain heat up by the voice coil was also taken into account. Results of $\overline{tA}$ as a function of the frequency f for a temperature range of 0 °C to 60 °C are shown in Figure 4.26 [198]. At high frequencies significant differences in the ranking of the damping behavior of the tested laminates were found compared to results at 1 Hz. Thus it was concluded that an evaluation at only 1 Hz would not have been sufficient to achieve a proper correlation between experimental results to the damping behavior at application. Also here between laminates **3L$_{40}$**-PAR$_{10}$Q$_{20}$ and **3L$_{44}$**-PET(d)$_{12}$Q$_{20}$ with the same damping adhesive type Q but different technical polymers as outer layers only minor differences in the damping evaluation were found. In contrast laminates **3L$_{40}$**-PAR$_{10}$R$_{20}$ and **3L$_{135}$**-PET(e)$_{55}$R$_{20}$RF$_{60}$ with the same damping adhesive type R but PAR as outer layers in **3L$_{40}$**-PAR$_{10}$R$_{20}$ and siliconized PET and a release film in **3L$_{135}$**-PET(e)$_{55}$R$_{20}$RF$_{60}$ revealed the most significant differences in the damping behavior in this evaluation with a lower damp-

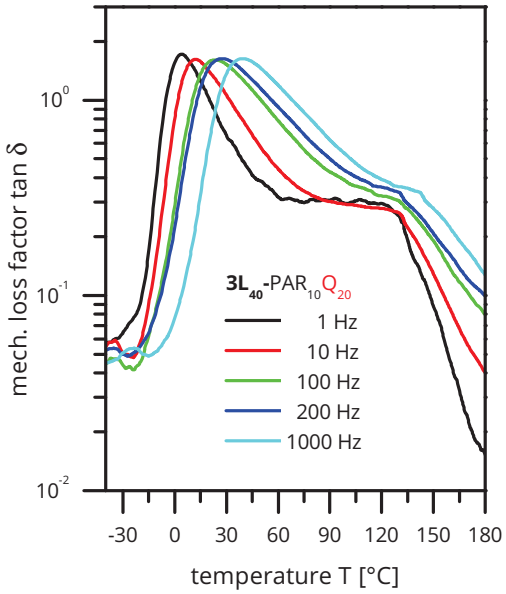

Figure 4.25: Results with the mechanical loss factor $\tan\delta$ vs. temperature T for frequencies of 1 Hz to 200 Hz and an extrapolation to 1000 Hz via the WLF approach for laminate **3L$_{40}$**-PAR$_{10}$Q$_{20}$, according to [198].

ing level for **3L$_{135}$**-PET(e)$_{55}$R$_{20}$RF$_{60}$ over the whole frequency range. The reason for this deviation is found in the comparison between temperature dependent $\tan\delta$ curves of both laminates with adhesive R in Figure 4.20b) where lower damping levels for laminate **3L$_{40}$**-PAR$_{10}$R$_{20}$ were found [198]. This was regarded to stem from an inferior adhesion between the damping adhesive and the outer layers, which were a siliconized PET and a release film. Finally laminate **3L$_{50}$**-PAR$_{10}$S$_{30}$ showed the lowest $\overline{tA}$-values because the main part of its $\tan\delta$-peak was above application relevant temperatures especially at high frequencies. In contrast, the laminates **3L$_{40}$**-PAR$_{10}$Q$_{20}$ and **3L$_{44}$**-PET(d)$_{12}$Q$_{20}$ featured the best damping behavior for the application in miniature loudspeakers with the highest $\overline{tA}$ values [198].

The influence of the chosen evaluation temperature range to the normalized loss factor $\overline{tA}$ as a function of the frequency is depicted in Figure 4.27 [198]. A shift of the evaluation range followed a change in the slope of the $\overline{tA}$ over frequency curves, but an extension of the temperature range yielded lower

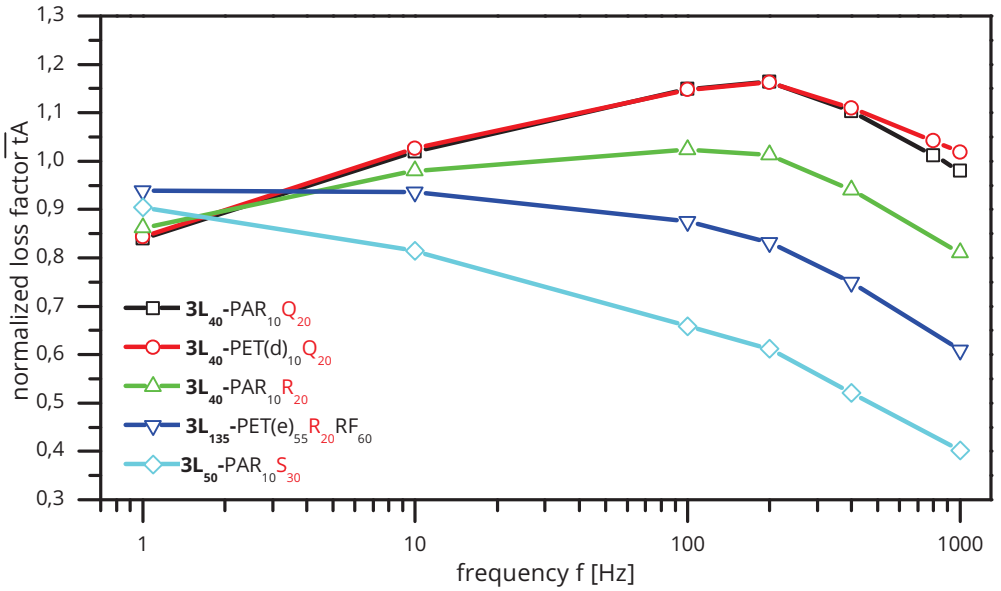

Figure 4.26: Results for the evaluation of $\overline{tA}$ as function of the frequency in the temperature range from 0 °C to 60 °C for all tested laminates, according to [198].

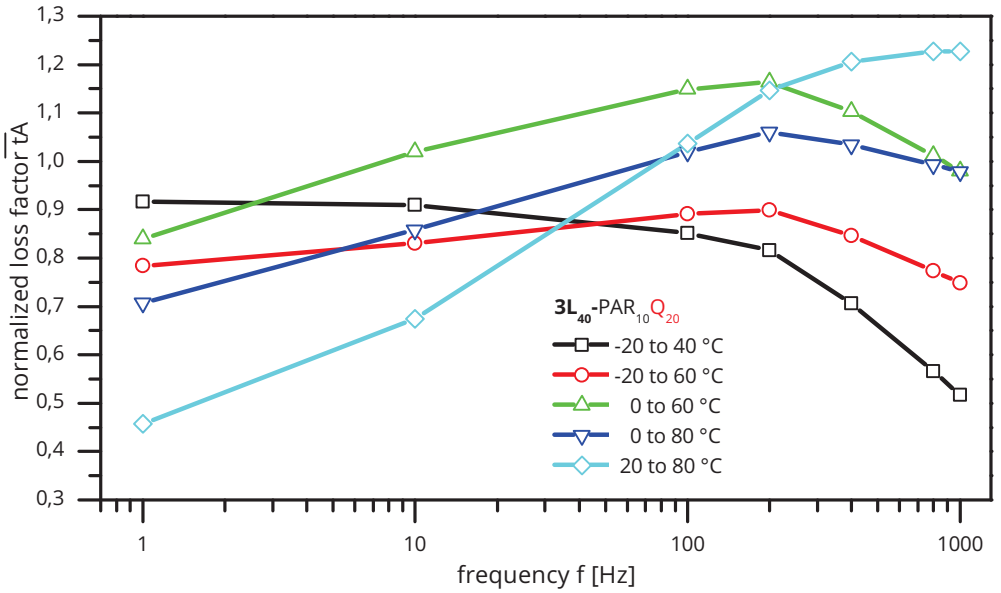

Figure 4.27: Results with the evaluation of $\overline{tA}$ as function of the frequency for temperature ranges of 60 °C and 80 °C, starting from −20 °C, 0 °C and 20 °C for a temperature range of 60 °C and −20 °C and 0 °C for a range of 80 °C, according to [198].

$\overline{tA}$ values over the whole frequency range. As shown quite large differences are obtained by changing the evaluation range. Therefore it is mandatory to fit this method well to the application in order to obtain a valid correlation between specimen and component tests [198].

In conclusion, in this section the influence of the constraining layers of CLD laminates on the damping characterization of their damping layers in DMA shear mode was investigated. For two laminates consisting of the same damping layer Q but PAR (**3L$_{40}$**-PAR$_{10}$Q$_{20}$) and PET (**3L$_{44}$**-PET(d)$_{12}$Q$_{20}$) constraining layers, respectively, no effect due to different outer layers was observed. In contrast in the comparison of laminates with a damping layer R and one with PAR (**3L$_{40}$**-PAR$_{10}$R$_{20}$) and the other witch siliconized PET and a release film as outer layers (**3L$_{135}$**-PET(e)$_{55}$R$_{20}$RF$_{60}$) for the latter lower temperature dependent $\tan\delta$ values were measured directly at the $\tan\delta$ peak. This was ascribed to an inferior adhesion behavior between the layers in **3L$_{135}$**-PET(e)$_{55}$R$_{20}$RF$_{60}$. A significantly broader $\tan\delta$ peak compared to the other laminates was found for laminate **3L$_{50}$**-PAR$_{10}$S$_{30}$ but at lower damping levels. In a next step the applicability of TTSP was verified by wicket plots and subsequently extrapolations to application relevant frequencies of 1000 Hz were performed. Here laminate **3L$_{50}$**-PAR$_{10}$S$_{30}$ showed a stronger frequency-temperature dependence than the other laminates, which was thought to stem from a secondary loss peak compared to standard glass transitions in laminates with adhesives Q and R. In a final step the damping performance of the laminates was evaluated with the normalized loss factor $\overline{tA}$ in the application relevant temperature range of 0 °C to 60 °C. The laminates with adhesive Q showed the best and laminate **3L$_{50}$**-PAR$_{10}$S$_{30}$ the worst damping behavior. Finally the effect of the evaluation temperature range for $\overline{tA}$ was investigated with the conclusion that the temperature range has to be well fitted to the application in order to obtain a meaningful correlation between tests on the film level and the application.

Concluding the findings on the effect of the constraining layers on the damping layer characterization in DMA shear mode it was found that as

long as sufficient adhesion is guaranteed between the constraining and the damping layers in CLD laminates there is no influence on the evaluation of the damping performance in DMA shear mode.

4.4.3 Effect of the damping layer thickness in CLD laminates

Despite the mechanical loss factor $\tan\delta$ of the adhesive damping layer, its thickness h_2 is one of the main influences on the damping performance of constrained layer damping (CLD) laminates, as explained in section 4.2.3 [59], [197]. The resulting composite loss factor is governed by two main effects. With thinner damping layers a lower amount of volume contributes in storing and dissipating strain energy. And with lower thicknesses higher shear strain levels occur in the damping layer when the structure is bent [193]. Nashif reported results for CLD structures with various configurations of constrained and damping layer thicknesses, where both $\tan\delta$ peak height and temperature were affected by the damping layer thickness, but no explanation for the temperature dependence was given [59]. Also Teng and Hu described the correlation between damping layer thickness and composite loss factor [214]. Darrouj and Faulkner investigated effects of different metal sheets as constraining layers and the thickness of the rubber damping layer to the composite loss factor in a CLD design. They observed that an optimum thickness of the damping layer can be found [215]. Bourahla et al. and Cuillery et al. also found a proportional increase of the loss factor height and and peak temperature with increasing damping layer thicknesses with CLD beams consisting of stainless steel sheets, epoxy adhesive and copoly(ethylene-vinyl acetate) (EVA) layers, respectively [216], [217].

Since no information about the influence of the thickness of the damping layer in thin polymeric CLD laminates like the ones used in miniature loudspeakers was found this topic is investigated in this section. Four laminates consisting of the same 8 µm thick PEEK (PEEK) outer layers and the same damping adhesive type P with thicknesses of 10 µm, 30 µm, 50 µm

and 100 µm were tested in DMA shear mode regarding $\tan\delta$ as a function of both frequency f and temperature T. Details about their composition are listed in Table 4.10.

Table 4.10: Test materials with an undampend, a FLD and a CLD design.

laminate	layer type		thickness [µm]	
	1&3	2	1&3	2
3L$_{26}$-PEEK$_8$P$_{10}$	PEEK	adhesive P	8	10
3L$_{46}$-PEEK$_8$P$_{30}$	PEEK	adhesive P	8	30
3L$_{66}$-PEEK$_8$P$_{50}$	PEEK	adhesive P	8	50
3L$_{116}$-PEEK$_8$P$_{100}$	PEEK	adhesive P	8	100

Results for the laminates with different damping layer thicknesses h_2 for the mechanical loss factor $\tan\delta$ as a function of temperature T and frequencies of 1 Hz, 10 Hz, 100 Hz and 200 Hz are shown in Figures 4.28 and a comparison of them at 1 Hz and 200 Hz in Figure 4.29. For all laminates sharp frequency dependent $\tan\delta$ maxima were found which was related to their glass transitions. **3L$_{26}$**-PEEK$_8$P$_{10}$ exhibited its maximum approximately 5 °C higher throughout all frequencies. Above the glass transition for all laminates a plateau was observed which was limited by a frequency dependent loss factor $\tan\delta$ decrease beginning at approximately 170 °C at 200 Hz. Consistent with the literature for higher damping layer thicknesses h_2 higher damping levels were observed throughout the measurement range.

The dependence of the loss factor peak height and peak temperature of the damping layer thickness h_2 for frequencies of 1 Hz, 10 Hz, 100 Hz and 200 Hz is depicted in Figure 4.30. For all measured frequencies a nearly identical behavior was found with a linear increase over the logarithmic thickness scale for damping layer thicknesses h_2 from 10 µm to 50 µm and more shallow gradients up to 100 µm (Figure 4.30a). But not only did the height of the peak change with the damping layer thickness, also the temperature of the peak as shown in Figure 4.30b. Throughout the measured

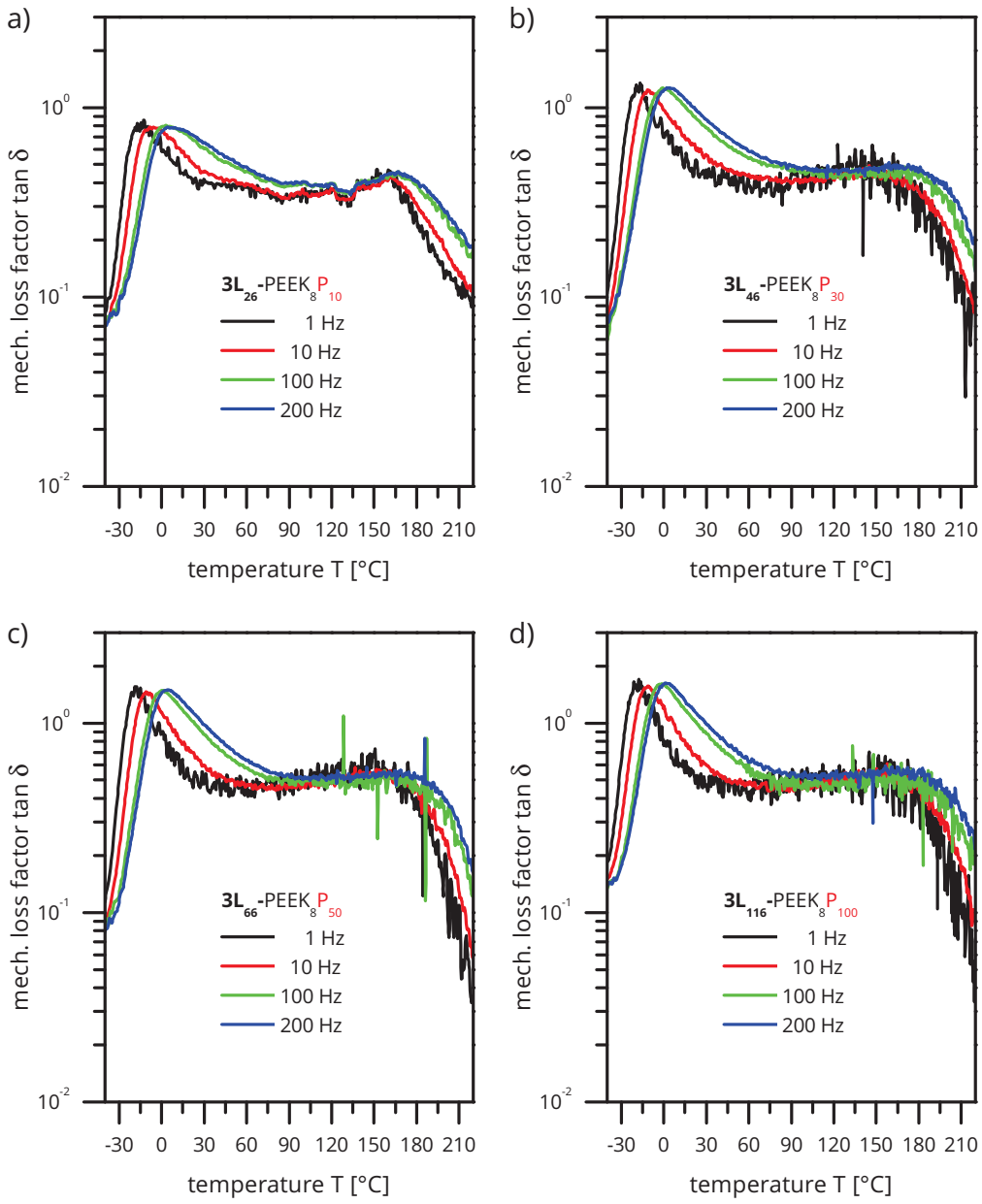

Figure 4.28: Results with the mechanical loss factor $\tan\delta$ vs. temperature T for frequencies of 1 Hz to 200 Hz for laminates with the same damping adhesive P with thicknesses of a) 10 µm, b) 30 µm, c) 50 µm and d) 100 µm.

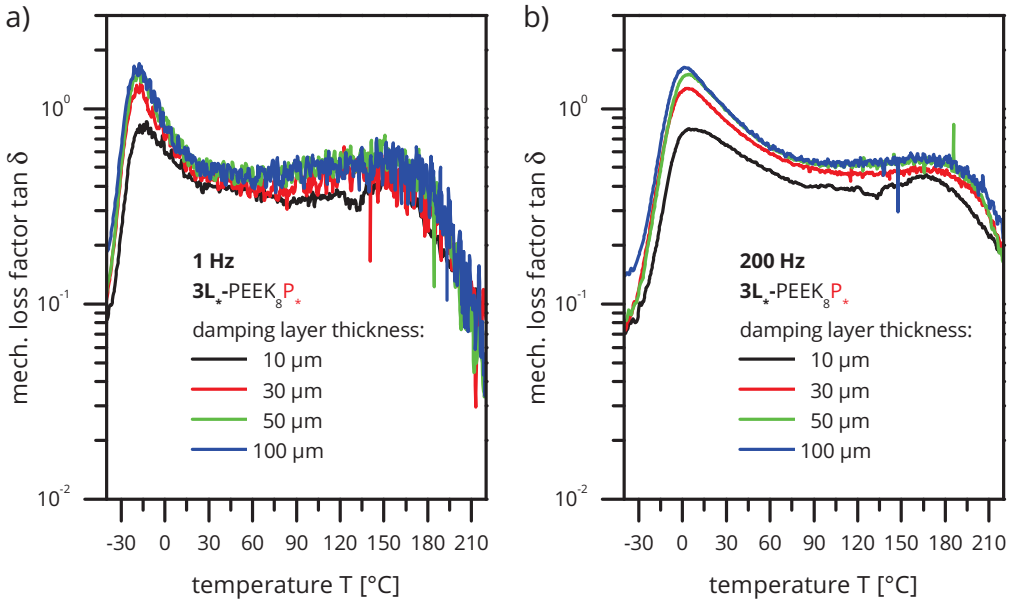

Figure 4.29: Comparison of results with the mechanical loss factor $\tan\delta$ vs. temperature T for a frequency of a) 1 Hz and b) 200 Hz for laminates with the same damping adhesive with different thicknesses of 10 µm, 30 µm, 50 µm and 100 µm.

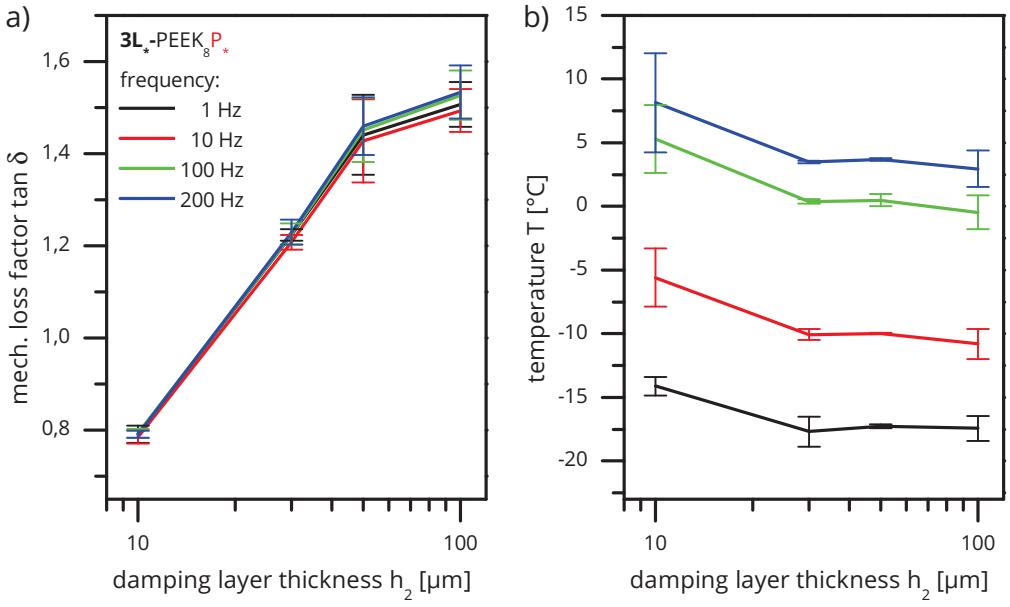

Figure 4.30: Dependence of a) peak height of the damping layer thickness h_2 and b) the loss factor peak temperature for frequencies of 1 Hz, 10 Hz, 100 Hz and 200 Hz.

frequency range a reciprocal correlation between the mean of the $\tan\delta$ peak temperatures and the damping layer thicknesses was observed but with significant scatter. Similar results were reported by Nashif for CLD structures with various configurations of constrained and damping layer thicknesses, but no explanation for the temperature dependence was given [59]. From Bourahla et al. this behavior was ascribed to an interphase effect [216]. Cuillery et al. attributed the temperature shift of multilayer CLD beams to a structural effect [217]. Whereas the loss factor height dependence from the damping layer thickness is sufficiently explained by the theoretical concept of the constrained layer damping (CLD) design, described in section 4.2, for the results presented here of the temperature dependence from the damping layer thickness in miniature speakers laminates it is thought, that it stems from two main effects. For one the sharpness of the peak in **3L$_{26}$**-PEEK$_8$P$_{10}$ decreased and therefore became more round compared to the other laminates which led to a slight increase of the $\tan\delta$ peak temperature because of the asymmetric $\tan\delta$ peak shapes. And due to the large stiffness differences between the stiff constraining and the soft adhesive layers of up to a factor of 10^5, an interphase region between the layers might have formed if sufficient adhesion occurred. In this region of a certain thickness the shear deformation in the soft adhesive layer might have been constrained which was suspected to have led to a stiffer material behavior and therefore a lower damping capacity. Bhattacharya et al. also found an increase in T_G of 4 °C in DMA measurements of a 1.5 mm thick blend of carboxylated nitrile rubber and epichlorohydrin rubber after moulding it to a 1.5 mm thick aluminum foil on one side. This increase was related to a interphase effect due to strong adhesion between the aluminum foil and the rubber which lead to restrictions of the molecular mobility in the vicinity of the interphase [218]. If its assumed that the thickness of an interphase between the adhesive and the outer layers remained constant with varying adhesive layer thicknesses then the volume fraction of the interphase increased compared to the total thickness of the adhesive damping layer. As a result interphase effects became more dominant.

In order to check the applicability of the time temperature superposition principle (TTSP) and therefore the validity to perform extrapolations to higher frequencies wicket plots were calculated, which are shown in Figure 4.31 [197]. For all damping layer thicknesses similar inversed "U" shaped curves were obtained with beginning scatter at approximately 100 °C which was taken as maximum of the evaluable temperature range $T_{eval.max}$ for TTSP. All laminates had their glass transitions T_G at significantly lower temperatures than $T_{eval.max}$, as shown in Table 4.11, which therefore yielded applicability of TTSP. Since with increasing damping layer thickness the loss factor $\tan\delta$

Table 4.11: Overview of the glass transitions temperatures T_G and the maximum of the evaluable temperature range $T_{eval.max}$ according to the evaluation using the wicket plot for 200 Hz.

h_2 [µm]	T_G [°C]	$T_{eval.max}$ [°C]
10	8	100
30	3	102
50	4	102
100	3	99

increased in the temperature dependent evaluations (Figures 4.28 and 4.29), also in the wicket plots the loss factor height increased. As a result the inversed "U" grew with higher damping layer thicknesses.

The dependence of the temperature on the loss factor peak of the frequency and the application of TTSP in order to perform an extrapolation to application relevant frequencies of up to 1000 Hz is shown in Figure 4.32 with the accompanying fit parameters from the WLF fits in Table 4.12. For damping layer thicknesses h_2 ranging from 30 µm to 100 µm nearly identical temperatures of the $\tan\delta$ peaks were found. In contrast here for the laminate with h_2 of 10 µm the shift of the $\tan\delta$ peak of approximately 5 °C was even more obvious. A significant thickness influence of the WLF fit parameters was observed with both decreasing c_1 and c_2 values and increasing T_∞ with increasing thickness. As a consequence the frequency-temperature depen-

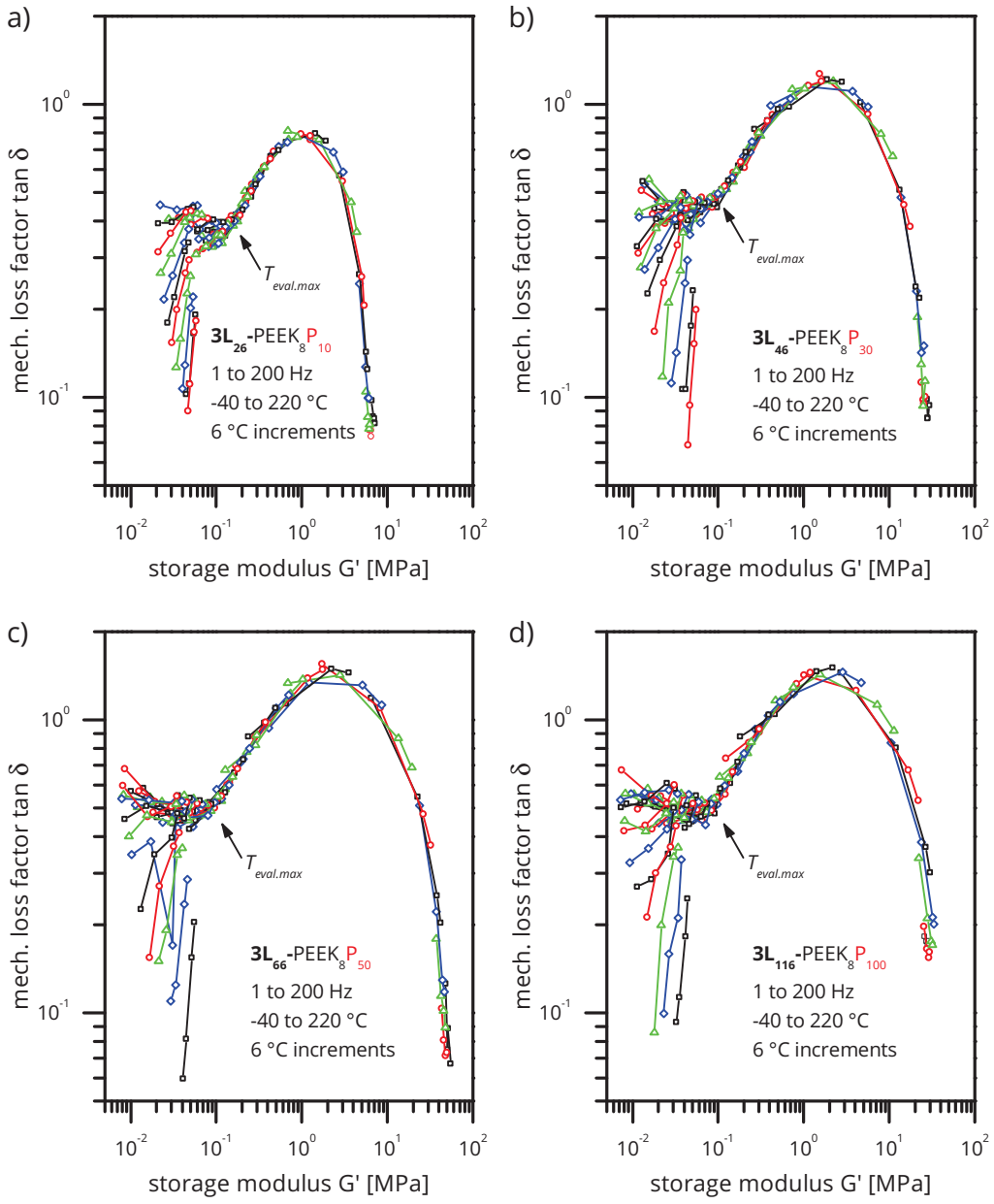

Figure 4.31: Wicket plots with the mechanical loss factor $\tan\delta$ as a function of the storage modulus G' for laminates with the same damping adhesive P with thicknesses of a) 10 µm, b) 30 µm, c) 50 µm and d)100 µm for temperatures ranging from −40 °C to 220 °C and frequencies from 1 Hz to 200 Hz and an evaluation of the maximum of the evaluable temperature range $T_{eval.max}$[197].

Table 4.12: Fit parameters for the WLF fit of measurements in DMA shear mode for laminates with the same damping adhesive P with damping layer thicknesses h_2 from 10 µm to 100 µm.

h_2 [µm]	c_1	c_2[K]	T_∞[K]
10	18.4	190.2	91.1
30	16.2	166.4	110.3
50	6.5	81.2	195.7
100	5.2	65.9	210.2

dence also increased with rising h_2. This behavior was also believed to stem from interphase effects. In the interphase the molecular motion in the damping adhesive might be constrained due to strong adhesion to the outer layers which might have led to a weaker frequency-temperature dependence of its glass transition. In the thinner laminates the relative volume fraction of the interphase in relation to the total damping adhesive might be higher, and subsequently interphase effects might be more pronounced. Compared to WLF fit values from the literature (Table 4.1) the calculated values from these tests were in a similar range at h_2 of 10 µm and 30 µm, but at 50 µm and 100 µm significantly lower c_1 and c_2 values and significantly higher T_∞ values were determined [197].

Finally an evaluation of the normalized loss factor $\overline{tA}$ evaluated in the application relevant temperature range for miniature speakers from 0 °C to 60 °C is shown as a function of the frequency f in Figure 4.33a and the damping layer thickness h_2 in Figure 4.33b. At low frequencies and low damping layer thicknesses low damping levels were also found. For all laminates the highest damping levels were found at an extrapolated frequency of 1000 Hz which ranged from 0.65 for **3L$_{26}$**-PEEK$_8$P$_{10}$ up to 1.15 for **3L$_{116}$**-PEEK$_8$P$_{100}$. At 1 Hz very similar values of approximately 0.5 were observed for all damping layer thicknesses.

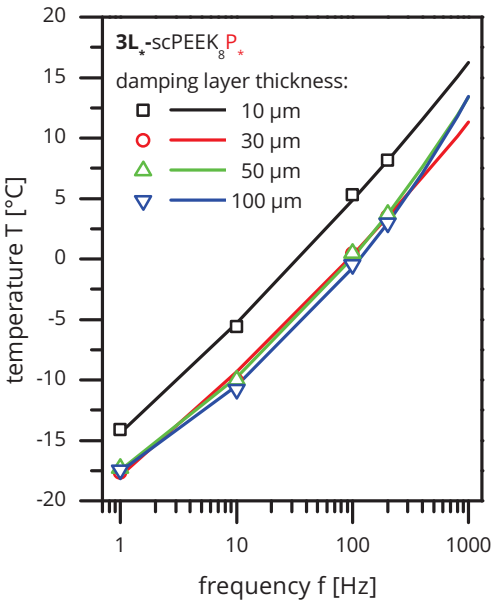

Figure 4.32: Comparison of the measured and extrapolated temperatures of the $\tan\delta$ peaks as function of the frequency for all tested laminates

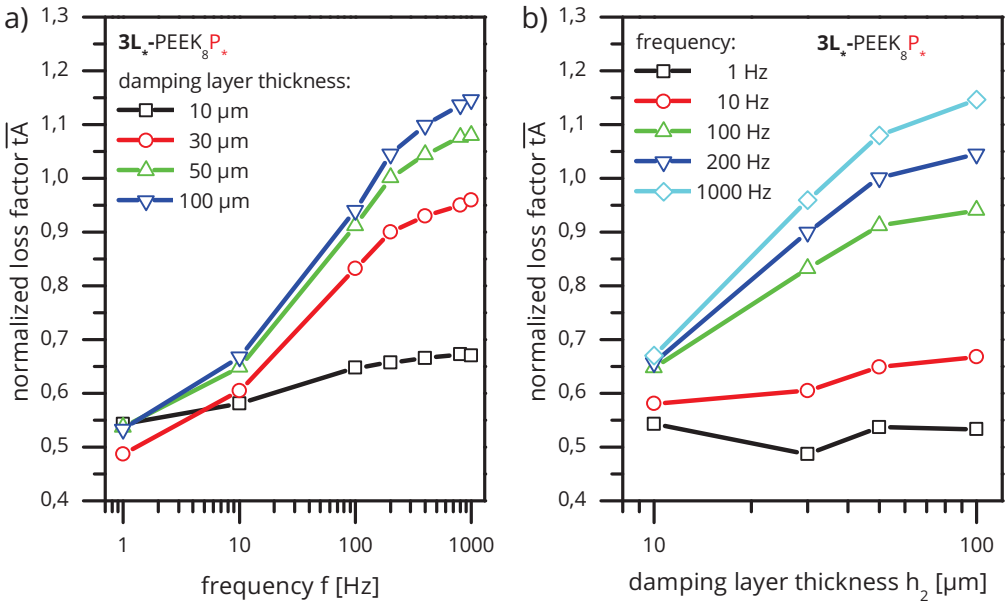

Figure 4.33: Results with the evaluation of $\overline{tA}$ as function of the a) the frequency f and b) the damping layer thickness h_2 for a temperature range of 0 °C to 60 °C.

In conclusion the influence of the damping layer thickness on the damping behavior of CLD laminates was successfully evaluated. With a decreasing damping layer thickness a lower loss factor $\tan\delta$ values, a shift of the $\tan\delta$ peak to higher temperatures and a weaker frequency-temperature dependence was found. Whereas the loss factor height dependence was ascribed to geometrical effects as explained by the concept of the constrained layer damping (CLD) design, the two latter effects were thought to stem from two main influences. A flattening of the $\tan\delta$ curves occurred with decreasing damping layer thicknesses which led to rounder peaks and therefore to a temperature shift because of the asymmetric $\tan\delta$ peak shapes. And a strong adhesion of the damping to the constraining layer the molecular mobility in the interphase might have been constrained which would have led to higher activation energies and therefore also higher temperatures needed for the glass transition in the interphase region. Furthermore it was thought that the constrained conditions in the interphase also led to a weaker frequency-temperature dependence. With lower damping layer thicknesses it was expected that the volume fraction of the interphase and therefore its influence on the composite behavior increased.

In further steps TTSP was verified by wicket plots and subsequently extrapolations to application-relevant frequencies for miniature loudspeakers of up to 1000 Hz were performed. Finally the damping performance as a function of both damping layer thickness and frequency was evaluated using the normalized loss factor $\overline{tA}$ in the application-relevant temperature range from 0 °C to 60 °C. Also here an increase of the damping performance at higher damping layer thicknesses was registered.

4.5 Summary

In order to determine the damping behavior at application relevant conditions of thin polymer membranes used in miniature speakers new methods

were successfully established based on forced frequency dynamic mechanical analysis (DMA). Since in application the damping in the membrane has to be provided under bending deformations, in a first step a DMA setup was introduced which mimics the same load conditions. Because of the thinness of the membranes of under 50 µm, their stiffness is too low for standard DMA test setups in bending mode. To overcome this drawback in DMA "speaker" mode the geometry of miniature speaker surrounds are replicated with the film specimen in a setup derived from DMA dual cantilever mode.The composite loss factor of laminates is measured in DMA "speaker" mode and not only the loss factor of the damping layer is measured but also geometric and stiffness effects due to the specific passive damping designs are covered. This enables us to perform comparative measurements between different damping designs.

In the constrained layer damping (CLD) design, damping occurs by shear deformation of a soft middle damping layer due to a relative motion of two stiff outer constraining layers when the structure is bent. Based on this a setup optimized for characterizing the damping behavior of adhesive layers in CLD laminates in DMA shear mode was designed. Since both methods are limited in their frequency range the theoretical approach of time temperature superposition principle (TTSP) was applied to extend the evaluation range to application-relevant conditions of up to 1000 Hz. In a final step the frequency-dependent normalized mechanical loss factor in the application-relevant temperature range from 0 °C to 60 °C $\overline{tA}$ was calculated which enabled us to also take the damping distribution over temperature into account.

Comparative experiments with an undamped film, a free layer damping (FLD) and a constrained layer damping (CLD) laminate were performed in DMA "speaker" and shear mode. Since in DMA shear mode for the undamped elastomeric film and the FLD laminate effects at higher temperatures were found which is not expected to occur in application it was concluded that this testing mode is only applicable for optimized tests with CLD laminates.

On the other hand in DMA ”speaker” mode in accordance with the literature for the undamped film, the lowest and for the CLD laminate the highest damping performances were observed. The ”speaker” mode best resembles the application and this method is eligible for comparative rankings between different passive damping designs.

In DMA shear mode the effect of different polymers in the outer layers was observed. It was found that as long sufficient adhesion is guaranteed with this test method solely the performance of the damping layer is determined and therefore could be specifically optimized. Finally in DMA shear mode the effect of the damping layer thickness on the damping performance was investigated. In accordance with the literature, with thicker damping layers higher damping levels were measured. An observed shift of T_G to higher temperatures with lower damping layer thicknesses, which was accompanied by a weaker frequency-temperature dependence, was thought to stem from effects from an interphase. Here, according to Bhattacharya et al., the molecular mobility might be constrained in the vicinity of the interphase due to strong adhesion to the outer layers, which might lead to higher glass transition temperatures [218].

References

[59] A. D. Nashif, D. I. G. Jones, and J. P. Henderson, *Vibration damping*. New York: Wiley, 1985, ISBN: 0471867721.

[61] W. Klippel, *Distributed mechanical parameters describing vibration and sound radiation of loudspeaker drive units*, Dresden, DE. [Online]. Available: https://www.klippel.de/fileadmin/klippel/Files/Know_How/Literature/Papers/Distributed%20parameter.pdf.

[62] H. Oberst and K. Frankenfeld, “Über die dämpfung der biegeschwingungen dünner bleche durch festhaftende beläge,” *Acustica*, vol. 2, no. 4, pp. 181–194, 1952.

[64] E. E. Ungar, “Damping of panels,” in *Noise and vibration control*, L. L. Beranek, Ed., New York: McGraw-Hill, 1971, pp. 434–474, ISBN: 0-9622072-0-9.

[70] American Society for Testing and Materials ASTM E 756 - 05, *Test method for measuring vibration-damping properties of materials*, West Conshohocken, PA, 2010. DOI: 10.1520/E0756-05R10.

[73] G. W. Ehrenstein, G. Riedel, and P. Trawiel, *Thermal analysis of plastics: Theory and practice*. Munich: Carl Hanser Verlag, 2004, ISBN: 978-1569903629.

[167] H. J. J. Plass, “Damping of vibrations in elastic rods and sanwich structures by incorporation of additional viscoelastic material,” in *Proceedings of the Midwestern Conference on Solid Mechanics*, 1957, p. 48.

[168] D. Ross, E. E. Ungar, and E. M. Kerwin, “Damping of plate flexural vibrations by means of viscoelastic laminae,” *Structural damping*, vol. 3, pp. 44–87, 1959.

[169] E. M. Kerwin, “Damping of flexural waves by a constrained viscoelastic layer,” *The Journal of the Acoustical Society of America*, vol. 31, no. 7, p. 952, 1959, ISSN: 00014966. DOI: 10.1121/1.1907821.

[170] E. M. Kerwin, “Ideal spaced damping treatments for flexural waves,” *The Journal of the Acoustical Society of America*, vol. 31, no. 6, p. 846, 1959, ISSN: 00014966. DOI: 10.1121/1.1936164.

[171] E. E. Ungar, “Loss factors of viscoelastic systems in terms of energy concepts,” *The Journal of the Acoustical Society of America*, vol. 34, no. 7, p. 954, 1962, ISSN: 00014966. DOI: 10.1121/1.1918227.

[172] E. E. Ungar and J. A. Zapfe, “Structural damping,” in *Noise and Vibration Control Engineering*, I. L. Vér and L. L. Beranek, Eds., Hoboken, NJ, USA: John Wiley & Sons, Inc, 2005, pp. 579–609, ISBN: 9780470172568. DOI: 10.1002/9780470172568.ch14.

[173] B. M. Shafer, "An overview of constrained-layer damping theory and application," in *ICA 2013 Montreal*, ser. Proceedings of Meetings on Acoustics, ASA, 2013. DOI: 10.1121/1.4800606.

[174] U. Sorathia, W. Yeager, and T. Dapp, "Advanced damping materials for marine applications," in *Sound and vibration damping with polymers*, ser. ACS Symposium Series, R. D. Corsaro and L. H. Sperling, Eds., vol. 424, Washington, DC: American Chemical Society, 1990, pp. 382–396, ISBN: 9780841212800. DOI: 10.1021/bk-1990-0424.ch021.

[175] C. B. Smith and N. M. Wereley, "Composite rotorcraft flexbeams with viscoelastic damping layers for aeromechanical stability augmentation," in *M3D III: Mechanics and Mechanisms of Material Damping*, ser. ASTM STP 1304, A. Wolfenden and V. K. Kinra, Eds., West Conshohocken, PA: ASTM International, 1997, pp. 62–77, ISBN: 978-0-8031-2417-2. DOI: 10.1520/STP11739S.

[176] S. Cervello, G. Donzella, A. Pola, and M. Scepi, "Analysis and design of a low-noise railway wheel," *Proceedings of the Institution of Mechanical Engineers, Part F: Journal of Rail and Rapid Transit*, vol. 215, no. 3, pp. 179–192, 2001, ISSN: 0954-4097. DOI: 10.1243/0954409011531503.

[177] E. Balmes and S. Germes, *Tools for viscoelastic damping treatment design. application to an automotive floor panel*, International seminar on modal analysis, Ed., Leuven, 2002. [Online]. Available: http://www.sdtools.com/pdf/isma02_damp.pdf.

[178] M. D. Rao, "Recent applications of viscoelastic damping for noise control in automobiles and commercial airplanes," *Journal of Sound and Vibration*, vol. 262, no. 3, pp. 457–474, 2003, ISSN: 0022-460X. DOI: 10.1016/S0022-460X(03)00106-8.

[179] J. Flint, *A Review of Theories on Constrained Layer Damping and Some Verification Measurements on Shim Material*. Warrendale, PA: SAE International, 2003. DOI: 10.4271/2003-01-3321.

[180] R. D. Buehrle, J. Klos, and G. P. Gibbs, "Damped windows for aircraft interior noise control," in *Proceedings of the International Conference on Noise Control Engineering 2004*, 2004, pp. 899–910. [Online]. Available: http://www.ingentaconnect.com/content/ince/incecp/2004/00002004/00000001/art00107.

[181] M. Triches Jr, Gerges, S. N. Y., and R. Jordan, "Reduction of squeal noise from disc brake systems using constrained layer damping," *Journal of the Brazilian Society of Mechanical Sciences and Engineering*, vol. 26, no. 3, pp. 340–348, 2004, ISSN: 1678-5878. DOI: 10.1590/S1678-58782004000300011.

[182] E. Balmes and S. Germes, "Design strategies for viscoelastic damping treatment applied to automotive components," in *22nd IMAC Conference & Exposition 2004*, Bethel, Connecticut: Society for Experimental Mechanics, 2004, ISBN: 9781604238020. [Online]. Available: http://www.sdtools.com/pdf/imac04_damp.pdf.

[183] R. Kristensen, K. Nielsen, and L. Mikkelsen, "Numerical studies of shear damped composite beams using a constrained damping layer," *Composite Structures*, vol. 83, no. 3, pp. 304–311, 2008, ISSN: 02638223. DOI: 10.1016/j.compstruct.2007.04.025.

[184] C. A. Gallimore, "Passive viscoelastic constrained layer damping application for a small aircraft landing gear system," PhD thesis, Virginia Polytechnic Institute and State University, Blacksburg, 2008. [Online]. Available: http://scholar.lib.vt.edu/theses/available/etd-10102008-124400/unrestricted/Thesis_CraigGallimore_Rev1.pdf.

[185] T. Proulx, Ed., *Structural Dynamics, Volume 3*, ser. Conference Proceedings of the Society for Experimental Mechanics Series. New York, NY: Springer New York, 2011, ISBN: 978-1-4419-9833-0. DOI: 10.1007/978-1-4419-9834-7.

[186] V. R. Deulgaonkar, S. P. Kallurkar, and A. G. Mattani, "Review and diagnostics of noise and vibrations in automobiles," *International Journal of Modern Engineering Research (IJMER)*, vol. 1, no. 2, pp. 242–246, 2011.

[187] R. M. Glaese, M. Sheehan, L. M. Stepp, R. Gilmozzi, and H. J. Hall, "Vibration mitigation for wind-induced jitter for the giant magellan telescope," in *SPIE Astronomical Telescopes + Instrumentation*, ser. SPIE Proceedings, SPIE, 2012, p. 84440V. DOI: 10.1117/12.926337.

[188] M. Leyrer, "Charakterisierung des dynamisch mechanischen verhaltens von dünnen folien unter biegebelastung," Bachelor Thesis, University of Leoben, Leoben, AUT, 2015.

[189] L. H. Sperling, "Sound and vibration damping with polymers," in *Sound and vibration damping with polymers*, ser. ACS Symposium Series, R. D. Corsaro and L. H. Sperling, Eds., vol. 424, Washington, DC: American Chemical Society, 1990, pp. 5–22, ISBN: 9780841212800. DOI: 10.1021/bk-1990-0424.ch001.

[190] E. M. Kerwin and E. E. Ungar, "Requirements imposed on polymeric materials by structural damping applications," in *Sound and vibration damping with polymers*, ser. ACS Symposium Series, R. D. Corsaro and L. H. Sperling, Eds., vol. 424, Washington, DC: American Chemical Society, 1990, pp. 317–345, ISBN: 9780841212800. DOI: 10.1021/bk-1990-0424.ch017.

[191] H. Oberst, G. W. Becker, and K. Frankenfeld, "Über die dämpfung der biegeschwingungen dünner bleche durch fest haftende beläge ii," *Acustica*, no. 2, pp. 433–444, 1954. [Online]. Available: http://www.ingentaconnect.com/content/dav/aaua/1954/00000004/A00104s1/art00007.

[192] W. A. Driscoll, S. M. Heilmann, and J. K. Rasmussen, "Vibration-damping constrained-layer constructions," *The Journal of the Acoustical Society of America*, vol. 77, no. 2, p. 777, 1985, ISSN: 00014966. DOI: 10.1121/1.392328.

[193] B. R. Sher and R. Moreira, "Dimensionless analysis of constrained damping treatments," *Composite Structures*, vol. 99, pp. 241–254, 2013, ISSN: 02638223. DOI: 10.1016/j.compstruct.2012.11.037.

[194] F. R. Schwarzl, *Polymermechanik: Struktur und mechanisches Verhalten von Polymeren*. Springer, 1990, ISBN: 9783540519652.

[195] J. Heijboer, "Secondary loss peaks in glassy amorphous polymers," *International Journal of Polymeric Materials*, vol. 6, no. 1-2, pp. 11–37, 1977. DOI: 10.1080/00914037708075218.

[196] M. L. Williams, R. Landel, and J. D. Ferry, "The temperature dependence of relaxation mechanisms in amorphous polymers and other glass-forming liquids," *Journal of the American Chemical Society*, vol. 77, no. 14, pp. 3701–3707, 1955.

[197] D. I. G. Jones, *Handbook of viscoelastic vibration damping*. Chichester and New York: J. Wiley, 2001, ISBN: 9780471492481.

[198] G. Knapp, G. Oreski, and G. Pinter, "Method to characterize the damping behavior of thin passively constrained layer laminates using dynamic mechanical analysis (DMA) in shear mode," *Polymer Testing*, 2015, ISSN: 01429418. DOI: 10.1016/j.polymertesting.2015.01.011.

[199] Miller, A. A., "Free volumes in polystyrene and polyisobutylene," *Journal of Polymer Science Part A: General Papers*, vol. 2, no. 3, pp. 1095–1103, 1964, ISSN: 1542-6246. DOI: 10.1002/pol.1964.100020307.

[200] J. D. Ferry, *Viscoelastic properties of polymers*, 3rd. New York: John Wiley & Sons, Inc, 1980, ISBN: 9780471048947.

[201] J. Heijboer, "Molecular origin of relaxations in polymers," *Annals of the New York Academy of Sciences*, vol. 279, no. 1, pp. 104–116, 1976, ISSN: 1749-6632. DOI: 10.1111/j.1749-6632.1976.tb39700.x. [Online]. Available: http://dx.doi.org/10.1111/j.1749-6632.1976.tb39700.x.

[202] K. P. Menard, *Dynamic Mechanical Analysis: A practical introduction*. 2008.

[203] Mettler-Toledo AG, *Dma/sdta861e product brochure*, Mettler-Toledo AG, Ed., Schwerzenbach, CH, 9/2011. [Online]. Available: http://us.mt.com/us/en/home/supportive_content/product_documentation/product_brochures/dma_brochure/_jcr_content/download/file/file.res/51725063C_V09.11_DMASDTA861B_Bro_e.pdf.

[204] I. PerkinElmer, *Dma 8000: Dynamic mechanical analyzer*, I. PerkinElmer, Ed., Waltham, USA. [Online]. Available: http://www.perkinelmer.com/cmsresources/images/44-74431bro_dma8000.pdf.

[205] G. Knapp, M. Leyrer, G. Oreski, and G. Pinter, "Characterization of the damping behavior of thin films with dynamic mechanic analysis in bending mode," in *Proceedings of ASME 2014 International Mechanical Engineering Congress & Exposition (IMECE2014)*, 2014.

[206] International Organization for Standardization ISO 6721-1, *Plastics - determination of dynamic mechanical properties - part 1: General principles*, Berlin, 2011. [Online]. Available: http://www.beuth.de/en/standard/din-en-iso-6721-1/142846302?SearchID=523142314.

[207] M. Schubnell, "Measurement of thin films in shear by dma," *Mettler Toledo thermal analysis UserCom*, vol. 29, no. 29, pp. 14–17, 2009. [Online]. Available: http://us.mt.com/us/en/home/supportive_content/matchar_apps/MatChar_UC293.html#.

[208] N. W. Tschoegl, W. G. Knauss, and I. Emri, "The effect of temperature and pressure on the mechanical properties of thermo- and/or piezorheologically simple polymeric materials in thermodynamic equilibrium – a critical review," *Mechanics of Time-Dependent Materials*, vol. 6, no. 1, pp. 53–99, 2002, ISSN: 1385-2000. DOI: 10.1023/A:1014421519100.

[209] U. D. Çakmak and Z. Major, "Experimental thermomechanical analysis of elastomers under uni- and biaxial tensile stress state," *Experimental Mechanics*, vol. 54, no. 4, pp. 653–663, 2014, ISSN: 0014-4851. DOI: 10.1007/s11340-013-9820-8.

[210] E. R. Harrell and N. Nakajima, "Modified cole–cole plot based on viscoelastic properties for characterizing molecular architecture of elastomers," *Journal of Applied Polymer Science*, vol. 29, no. 3, pp. 995–1010, 1984, ISSN: 00218995. DOI: 10.1002/app.1984.070290327.

[211] M. van Gurp and J. Palmen, "Time-temperature superposition for polymer blends," *Rheological Bulletin*, vol. 67, no. 1, pp. 5–8, 1998. [Online]. Available: www.rheology.org/SoR/publications/rheology_b/jan98/van_Gurp%26Palmen.PDF.

[212] A. Moser, "Zeit-temperatur-verschiebung von thermoplastischen polymeren werkstoffen," Master's thesis, University of Leoben, Leoben, 2013. [Online]. Available: https://online.unileoben.ac.at/mu_online/wbAbs.showThesis?pThesisNr=36420&pOrgNr=&pPersNr=149386.

[213] P. Cuillery, J. Tatibouet, and M. Mantel, "Relationship between interfacial phenomena and viscoelastic behavior of laminated materials," *Journal of Adhesion Science and Technology*, vol. 12, no. 3, pp. 271–292, 1998, ISSN: 0169-4243. DOI: 10.1163/156856198X00876.

[214] T.-L. Teng and N.-K. Hu, "Analysis of damping characteristics for viscoelastic laminated beams," *Computer Methods in Applied Mechanics and Engineering*, vol. 190, no. 29-30, pp. 3881–3892, 2001, ISSN: 00457825. DOI: 10.1016/S0045-7825(00)00305-4.

[215] M. N. Darrouj and R. G. Faulkner, "Optimum design of constrained layer damping panels," *Materials & Design*, vol. 10, no. 4, pp. 202–208, 1989, ISSN: 02613069. DOI: 10.1016/S0261-3069(89)80006-8.

[216] H. Bourahla, J. Lenoir, M. Romand, and J. Chauchard, "Influence de l'epaisseur de l'adhésif et du vieillissement sur les propriétés mécaniques dynamiques d'un assemblage: Adhésif structural/acier inoxydable," *Angewandte Makromolekulare Chemie*, vol. 178, no. 1, pp. 47–62, 1990. DOI: 10.1002/apmc.1990.051780104.

[217] P. Cuillery, R. Gaertner, J. Tatibouet, and M. Mantel, "Structural effects on dynamic features of sandwich metal/polymer/metal," *Journal of Applied Polymer Science*, vol. 65, no. 12, pp. 2493–2505, 1997, ISSN: 00218995. DOI: 10.1002/(SICI)1097-4628(19970919)65:12<2493::AID-APP20>3.0.CO;2-0. [Online]. Available: http://dx.doi.org/10.1002/(SICI)1097-4628(19970919)65:12<2493::AID-APP20>3.0.CO;2-0.

[218] T. Bhattacharya, D. K. Tripathy, and S. K. De, "Dynamic mechanical studies on the adhesion between aluminium and rubber," *Journal of Adhesion Science and Technology*, vol. 6, no. 10, pp. 1165–1178, 1992, ISSN: 0169-4243. DOI: 10.1163/156856192X00269.

5 Conclusion and Outlook

One of the greatest challenges in research and development of miniature loudspeakers is the acquisition of high quality test data. If at all possible obtaining these is both time consuming and costly since at first test loudspeakers have to be produced. Therefore to test new or optimize existing materials, first test loudspeakers have to be built on a fully automatic production line. Then in a next step component tests are performed, which are also neither time nor cost efficient, especially not for an early selection of materials or if information at different test conditions are needed. Additionally, since the dynamic behavior between different miniature speaker geometries often differs significantly, test results which were acquired with one defined loudspeaker geometry are probably not applicable for other geometries.

In order to increase both the time and cost efficiency in research and development, the typical test pyramid was established. Starting with coupon tests where actual material behavior with generic test specimens often is measured at each level of the pyramid, the complexity of the tested structure, the tests themselves and therefore the costs rise, with component tests sitting on top. In this thesis the goal was to establish tests at the bottom of the test pyramid in order to obtain a detailed insight into structure property relationships of the loudspeaker laminates by variation of specific test parameters in a time and cost efficient manner. Therefore after evaluation of the application-relevant boundary conditions, tests on the specimen level were set up to match the application conditions as closely as possible with

the ultimate goal of measuring actual material parameters. This then enables us to predict effects on the dynamic miniature speaker behavior even with different loudspeaker geometries if the application-relevant boundary conditions are known.

Since a good fatigue performance of the miniature loudspeaker membranes is one of their key requirements, a test was set up to characterize this using generic film specimens which where pre-edged before testing using templates and a razorblade. Since the goal of this was not only to rank different laminates but also to achieve a deeper insight into the processes taking place during fatigue of the laminates, the method was split up into a stress-based approach with Wöhler tests and a fracture mechanical approach with fatigue crack growth tests. The first allows us to evaluate the ratio between the amount of the service life until first crack growth occurs and the time until final failure. This information is also helpful for a material selection, because beginning crack growth may already worsen the acoustics. In the second fracture mechanical approach the crack growth kinetics are characterized, which is actual material data, if the requirements for the theoretical concepts on which the tests are based upon are met. Although this was done by using specimens which were pre-edged with razorblades, it was frequently found that shortly after the tests were started cracks already grew a small distance, which was related to a sharpening of the cracks before actual stable crack growth occurred at significantly higher cycles. This is thought to also take place in the loudspeaker membranes where, starting from inherent failures, cracks begin to grow. According to the crack tip similitude concept the same crack growth rates then are found both in the loudspeakers and in the test specimens when the same local load conditions occur at the crack tip. Also the same should hold when different specimen geometries are tested. Thus in a first step the applicability of linear elastic fracture mechanics (LEFM) to describe the cyclic fatigue behavior of thin miniature loudspeaker films was studied by applying the crack tip similitude concept in the form of comparing the fatigue crack growth behavior of two different specimen geometries

and measured process zone sizes with theoretical values. Whereas LEFM seemed applicable for PAR, PESU and PET films, in PC and PEI films significant deviations were found. Finally it was possible to ascribe the deviations in PC to the occurrence of large process zones by which the requirement of small scale plasticity in LEFM might not have been fulfilled. All in all it was concluded that with the established method, valid predictions regarding the fatigue behavior of miniature loudspeaker membranes are possible.

With the established fatigue test setup, then three major effects were studied. First of all the temperature dependency of the fatigue behavior of PET films was investigated. Here a fracture toughness maximum at 60 °C was observed, which was in good correlation with the onset of the glass transition of PET from DMA experiments in tensile mode. The maximum was thought to stem from increased mobility at the glass transition of the amorphous phases which led to an increased crack tip plasticity and therefore to a higher crack growth resistance. As a result it was concluded that in order to determine the application limits of such films, the onset of the glass transition is a good measure. Since PET films are comparably cheap but exhibit a high fracture toughness it is also concluded that they may be a cost efficient alternative for loudspeaker designs where application temperatures do not exceed 60 °C.

In a next step the effect of the multilayer design was investigated with 3-layer laminates consisting of a symmetrical design with two of the same stiff outer layers and a soft damping adhesive in between. In theory, in loudspeaker membranes cracks starting in one stiff outer layer have to first nucleate in the second too and then crack growth in them may be shielded by the remaining soft damping adhesive. The second mechanism was regarded as responsible for an increase in the measured fracture toughness of two 3-layer laminates compared to their monolayer without adhesive in fatigue tests with DENT specimens. It was also shown that delamination processes play only a minor role for the fatigue behavior of the multilayer laminates. In

conclusion with a multilayer design the fracture toughness of the miniature speaker membranes is significantly improved.

Finally in the evaluation of the anisotropic fatigue behavior of a PEEK 3-layer film it was found that a predominant molecular orientation in machine direction induced by the extrusion process of its outer layers significantly influences its fatigue behavior. Crack growth rates in tests with specimens which were cut out at 45° orientation relative to the process direction were dominated by the lowest crack growth resistance parallel to the molecular orientation. In conclusion this may affect the fatigue behavior of miniature speakers in such way that the lowest crack growth resistance in anisotropic loudspeaker laminates governs the fracture toughness of these films.

In the second part of the work characterization methods of the damping behavior of the loudspeaker membranes directly at the film level were introduced. Also here the tests were designed along the test pyramid with the DMA shear mode at the bottom. It was shown that the only additional factor influencing the results of the damping characterization, despite the mechanical loss factor $\tan\delta$ of the adhesive, was the film's thickness. This then allows a focused development of the damping adhesives without further superimposed effects. The next level in the testing pyramid is the DMA "speaker" mode. Here not only the damping behavior of the adhesive was characterized but also stiffness effects from the whole laminate contributed to the resulting damping performance. With this, further optimization of the laminate design is possible. Furthermore comparative tests between different membrane designs are possible, such as monolayers, free layer damping and constrained layer damping designs. In conclusion test methods were established which enable the quantification of the major effects on the damping performance of miniature speaker laminates. These are, first the damping designs of the membrane. Besides that, the loss factor of the damping layer is one of the main factors. Furthermore the film's thickness and also the thickness and stiffness ratios between the damping and the

base or constraining layers have a significant contribution to the damping performance of the membranes.

The methods introduced in this thesis are an excellent starting point for future developments of new test methods to fill the gap between coupon and component tests. One promising concept are tests based on the introduced methods, but with thermoformed laminates with a loudspeaker geometry. This would allow going into even more detail into the already obtained results and to study further effects. For example in the fatigue tests, investigations regarding the influence of the renucleation of cracks in the second outer layer would be possible either by optical methods or by monitoring the dynamic compliance of the speakers. If crack growth occurs the compliance changes accordingly. Also the observations about the effect of anisotropic fatigue behavior of extruded films on the fatigue behavior of the miniature loudspeakers could be further detailed. Finally the effect of different speaker geometries and therefore different biaxial stress states in the laminates could be examined.

For the damping characterization several interesting topics could be covered. First of all the influence of the stiffness ratios to the damping performance of the films could be studied in even more detail. Since also a whole speaker exhibits a higher stiffness than a small specimen, higher test frequencies will be reached than in the DMA ”speaker” mode and the signal would be clearer at temperatures above the $\tan\delta$ maximum. Consequently this would ease experiments with elastomeric monolayer films. One of the key features would be that the beginning of nonlinear damping would be observable which has a direct effect on sound distortion and therefore acoustic quality of a speaker [1]–[3]. Finally the effect of different miniature speaker designs could be studied in an efficient manner.

References

[1] S. J. Pawar, S. Weng, and J. Huang, "Total harmonic distortion improvement for elliptical miniature loudspeaker based on suspension stiffness nonlinearity," *IEEE Transactions on Consumer Electronics*, vol. 58, no. 2, pp. 221–227, 2012, ISSN: 0098-3063. DOI: 10.1109/TCE.2012.6227416.

[2] C. Chang, S. J. Pawar, S. Weng, Y. Shiah, and J. Huang, "Effect of nonlinear stiffness on the total harmonic distortion and sound pressure level of a circular miniature loudspeaker-experiments and simulations," *IEEE Transactions on Consumer Electronics*, vol. 58, no. 2, pp. 212–220, 2012, ISSN: 0098-3063. DOI: 10.1109/TCE.2012.6227415.

[3] W. Klippel, *Nonlinear damping in micro-speakers*, Dresden, DE. [Online]. Available: http://www.klippel.de/fileadmin/klippel/Files/Know_How/Literature/Papers/Nonlinear%20Damping%20in%20Micro-Speakers_Klippel.pdf.